Experimental investigation of porosity, surface area, and gas diffusivity impacts on methanogenic activity within porous media: implications for underground hydrogen storage

Von der Fakultät für Georessourcen und Materialtechnik der
Rheinisch-Westfälischen Technischen Hochschule Aachen

zur Erlangung des akademischen Grades eines

Doktors der Naturwissenschaften

genehmigte Dissertation

vorgelegt von

Saeed Khajooie, M.Sc.

Berichter: Herr Univ.-Prof. Dr. rer. nat. Ralf Littke
Herr Prof. Dr. rer. nat. Andreas Busch

Tag der mündlichen Prüfung: 11.10.2024

To my beloved wife, Pari,

and our son, Nick, who inspire me every day

Abstract

The transition from fossil fuels to renewable energy sources has significantly increased interest in large-scale hydrogen (H_2) storage within subsurface formations. This strategy addresses the intermittency issues of renewable energy caused by atmospheric fluctuations, leading to an imbalance in energy supply and demand. Surplus energy can be converted to H_2 via water electrolysis and then stored in various geological formations, including depleted oil and gas reservoirs, saline aquifers, and salt caverns. However, injecting H_2 into subsurface formations may stimulate microbial metabolism, potentially leading to the irreversible conversion of H_2 into byproducts like CH_4, H_2S, and acetic acid, posing risks of H_2 contamination and equipment corrosion. Despite these challenges, the potential to convert H_2 into CH_4 through biological processes, a technique known as bio-methanation, presents an opportunity for sustainable underground methane production.

This work aimed to explore the impact of pore characteristics on methanogenic activity within porous media. The model organism was *Methanothermococcus thermolithotrophicus*, a strain of methanogenic *Archaea*. Reservoir analogues from the Cretaceous (Bentheim Sandstone, Obernkirchen Sandstone, Anröchter Grün Limestone) and Triassic (Red and Grey Weser Sandstone) were selected for this study based on their differences in porosity (8-24 %). The results of Chapter 2 demonstrate the influence of sand particles, rock fragments, and porous rocks on methanogenic activity, setting the stage for detailed experimental investigations. Measurements on water-saturated rock specimens revealed a strong correlation between microbial activity and pore volume. Additionally, the higher activities observed in intact rocks compared to their corresponding bulk solutions (8-10 times higher) indicate that the available surface area for microbial colonization is a crucial factor in controlling microbial activity when the amount of substance is constant. With the cell size of the utilized *Archaea* ranging from 1 to 2 µm, only pores larger than this threshold are accessible. This conclusion is further supported by increased activities in the presence of sand particles and rock fragments compared to their respective bulk solutions, as well as variations in activities within water-saturated rocks with similar pore volumes. In Chapter 3, various techniques including mercury injection capillary pressure (MICP), nuclear magnetic resonance (NMR), scanning electron microscopy (SEM), and X-ray micro-computed tomography (µCT) were employed to assess the impact of surface area quantitatively. The specific surface area of accessible pores obtained from MICP, NMR,

and SEM revealed strong correlations with the normalized microbial activity, confirming the role of surface area in accelerating methanogenic reactions. The normalization procedure accounts for pore volume and gas-liquid interfacial area. The impact of interfacial area and, consequently, mass transfer flux has been observed through the higher activity of Grey Weser sandstone compared to Bentheim sandstone, as measured in the test conducted on rocks with similar pore volumes. Grey Weser sandstone exhibits a lower specific surface area of accessible pores but a larger interfacial area. Chapter 4 examines the effective diffusivity of gas in water-saturated rock specimens, a crucial parameter in governing gas-liquid mass transfer. The rate of methanogenic reactions depends on the amount of H_2 and CO_2 molecules in the aqueous phase, suggesting an indirect influence of the mass transfer process on microbial activity. The experiments were conducted using the pressure decay technique under initial pressure and temperature of 1.0 MPa and 35°C, respectively. The analyzed rock specimens exhibited effective H_2 diffusivity ranging from $0.8 \cdot 10^{-9}$ to $2.9 \cdot 10^{-9}$ m²/s, which is higher than the respective values for CH_4 and CO_2, ranging from $0.3 \cdot 10^{-9}$ to $0.9 \cdot 10^{-9}$ m²/s. Additionally, it was observed that effective diffusivities positively correlate with other rock properties such as porosity, permeability, and mean pore radius.

The findings of this thesis hold significant implications for integrating pore characteristics into existing kinetic microbial growth models such as the Monod or Contois (Muloiwa et al., 2020), enabling more accurate estimations of microbial activities during both underground hydrogen storage and underground bio-methanation.

Zusammenfassung

Der Übergang von fossilen Brennstoffen zu erneuerbaren Energiequellen hat das Interesse an der großtechnischen Speicherung von Wasserstoff (H_2) in unterirdischen Formationen erheblich gesteigert. Diese Strategie verursacht Probleme, die mit der nicht dauerhaften Verfügbarkeit der erneuerbaren Energien zusammenhängen, die durch atmosphärische Schwankungen verursacht werden und zu einem Ungleichgewicht von Energieangebot und -nachfrage führen. Überschüssige Energie kann durch Wasserelektrolyse in H_2 umgewandelt und anschließend in verschiedenen geologischen Formationen, einschließlich erschöpfter Öl- und Gasreservoire, salzhaltiger Aquifere und Salzkavernen, gespeichert werden. Das Einbringen von H_2 in unterirdische Formationen kann jedoch den mikrobiellen Stoffwechsel anregen, was möglicherweise zu einer irreversiblen Umwandlung von H_2 in Nebenprodukte wie CH_4, H_2S und Essigsäure führt und das Risiko von H_2-Verlusten sowie der Korrosion von Anlagen birgt. Trotz dieser Herausforderungen bietet das Potenzial zur Umwandlung von H_2 in CH_4 durch biologische Prozesse, eine Technik bekannt als Bio-Methanisierung, auch eine Chance für die nachhaltige unterirdische Methanproduktion.

Diese Arbeit zielte darauf ab, den Einfluss von Poreneigenschaften auf die methanogene Aktivität innerhalb poröser Medien zu untersuchen. Als Modellorganismus diente Methanothermococcus thermolithotrophicus, ein Stamm methanogener Archaeen. Für diese Studie wurden Reservoir-Analoga aus der Kreidezeit (Bentheim Sandstein, Obernkirchen Sandstein, Anröchter Grünstein) und der Trias (Roter und Grauer Wesersandstein) aufgrund ihrer Unterschiede in der Porosität (8-24%) ausgewählt. Die Ergebnisse von Kapitel 2 zeigen den Einfluss von Sandpartikeln, Gesteinsfragmenten und allgemein porösen Gesteinen auf die methanogene Aktivität, was die Grundlage für detaillierte experimentelle Untersuchungen bildet. Messungen an wassergetränkten Gesteinsproben ergaben eine starke Korrelation zwischen mikrobieller Aktivität und Porenvolumen. Darüber hinaus deuten die höheren Aktivitäten in intakten Gesteinen im Vergleich zu entsprechenden Bulk-Lösungen (8-10 mal höher) darauf hin, dass die verfügbare innere Oberfläche bei der mikrobiellen Kolonisierung ein entscheidender Faktor zur Kontrolle der mikrobiellen Aktivität ist, wenn die Stoffmenge konstant bleibt. Mit einer Zellgröße der verwendeten Archaeen von 1 bis 2 µm sind nur Poren zugänglich, die größer als diese Schwelle sind. Diese Schlussfolgerung wird durch erhöhte Aktivitäten in Anwesenheit von Sandpartikeln und Gesteinsfragmenten im Vergleich zu ihren jeweiligen Bulk-Lösungen sowie durch Variationen der Aktivitäten in wassergetränkten Gesteinen mit

ähnlichen Porenvolumina weiter untermauert. In Kapitel 3 wurden verschiedene Techniken, einschließlich Quecksilber-Injektionskapillardruck (MICP), Kernspinresonanz (NMR), Rasterelektronenmikroskopie (REM) und Röntgen-Mikrocomputertomographie (µCT), angewendet, um den Einfluss der Oberfläche quantitativ zu bewerten. Die spezifische Oberfläche der zugänglichen Poren, die durch MICP, NMR und REM bestimmt wurde, zeigte starke Korrelationen mit der normalisierten mikrobiellen Aktivität und bestätigte die Rolle der inneren Oberfläche bei der Beschleunigung methanogener Reaktionen. Das Normalisierungsverfahren berücksichtigt das Porenvolumen und die Gas-Flüssigkeits-Grenzfläche. Der Einfluss der Grenzfläche und damit des Massentransfers wurde durch die höhere Aktivität von Grauer Wesersandstein im Vergleich zu Bentheim Sandstein bei gleichem Porenvolumen beobachtet. Grauer Wesersandstein weist eine geringere spezifische Oberfläche der zugänglichen Poren, aber eine größere Grenzfläche auf. Kapitel 4 untersucht die effektive Diffusivität von Gas in wassergetränkten Gesteinsproben, einen entscheidenden Parameter für die Steuerung des Gas-Flüssigkeits-Stoffübergangs. Die Rate der methanogenen Reaktionen hängt von der Menge der H_2- und CO_2-Moleküle in der wässrigen Phase ab, was auf einen indirekten Einfluss des Massentransfers auf die mikrobielle Aktivität hindeutet. Die Experimente wurden mit der Druckabfalltechnik bei einem initialen Druck von 1,0 MPa und einer Temperatur von 35 °C durchgeführt. Die analysierten Gesteinsproben zeigten effektive H_2-Diffusivitäten im Bereich von $0{,}8 \cdot 10^{-9}$ bis $2{,}9 \cdot 10^{-9}$ m²/s, was höher ist als die entsprechenden Werte für CH_4 und CO_2, die im Bereich von $0{,}3 \cdot 10^{-9}$ bis $0{,}9 \cdot 10^{-9}$ m²/s liegen. Darüber hinaus wurde beobachtet, dass effektive Diffusivitäten positiv mit anderen Gesteinseigenschaften wie Porosität, Permeabilität und mittlerem Porenradius korrelieren.

Die Erkenntnisse dieser Arbeit haben bedeutende Implikationen für die Integration von Poreneigenschaften in bestehende kinetische Modelle des mikrobiellen Wachstums wie die Monod- oder Contois-Modelle (Muloiwa et al., 2020) und ermöglichen genauere Schätzungen der mikrobiellen Aktivitäten während sowohl der unterirdischen Wasserstoffspeicherung als auch der unterirdischen Bio-Methanisierung.

Acknowledgements

I wish to extend my deepest gratitude to Prof. Ralf Littke for the invaluable opportunity to work as a research assistant and pursue my PhD at his institute at RWTH Aachen University. His trust, support, and the independence he granted me in my research have been invaluable. I deeply appreciate the time he dedicated to discussing my work, as well as his encouragement and motivation throughout my academic journey.

A heartfelt appreciation goes to my direct advisor, Dr. Garri Gaus, who sparked my interest in the field hydrogen storage. He imparted his valuable experiences in the laboratory and provided me with an excellent opportunity to develop my skills in conducting laboratory research and developing new ideas in the field petrophysical studies. I would like to thank him for his continuous support and encouragement and for always being available to discuss scientific challenges and offer insightful guidance. His time and efforts in reviewing my research writing and securing opportunities for collaboration with universities and research institutes have enriched my work immensely. Dr. Gaus has been more than just an advisor; he has been a friend who supported me during personal challenges, and his unique sense of humor made difficult times bearable.

I would also like to thank Prof. Andreas Busch for accepting the role of co-examiner and for taking the time to read and discuss my thesis.

Special thanks go to my former colleague, Timo Seemann, who advised and supported me in acquiring supplementary data to enhance my research. His ideas during our scientific discussions and his feedbacks on my writings have significantly improved my publications and thesis. Special appreciation goes to Anja Bettina Dohrmann from the Federal Institute for Geosciences and Natural Resources (BGR) for her support in preparing the materials needed for my experiments and for providing valuable insights into microbiology, which greatly assisted me in interpreting data and writing the discussion. I am also grateful to Dr. Hannes Claes from KU Leuven, Dr. Jop Klaver from Pondera Consult, Dr. Mathias Nehler, and Dr. Benedikt Ahrens from the Fraunhofer Research Institution for their support in conducting supplementary measurements as well as their valuable feedback on my publications. A heartfelt thanks to Patrick Thelen for his technical expertise in setting up new equipment and his commitment to maintaining our laboratory operations. I also sincerely appreciate our enriching conversations about fatherhood and children. Michelle Gumb is especially thanked for her administrative support and for addressing bureaucratic challenges.

Further appreciation goes to all my current and former colleagues at the institute, particularly Dr. Sebastian Grohmann, Dr. Steffen Nolte, Dr. Alireza Baniasad, Dr. Sebastian Amberg, Dr. Linda Burnaz, Mutuma Mbui, Leidy Castro Vera, Arysthasya Arysanto, and Donka Macherey. Their support created a wonderful working environment, and our discussions about challenges and discoveries were incredibly motivating. I cherish the moments we shared over the past three years, which would have been far less enjoyable without all of you.

In acknowledging the support, I received during my PhD, I must express my sincere gratitude to my little family for their indispensable role throughout this journey. My deepest gratitude to my beloved wife, Pari, and our son, Nick, who are the greatest blessings and motivations in my life. Nick's presence has brought immense joy and inspiration to us. I am profoundly thankful to Pari, for her love, understanding, patience, and encouragement, which have provided me with the peace of mind to flourish in my academic pursuits. Pari and I have faced many challenges since starting our new lives in Germany, and her unwavering support in every matter has been the foundation of my achievements, especially during the growth of our son in the past two years. This thesis is as much a testament to her love and support as it is to my academic efforts.

Yours sincerely,
Saeed

Table of contents

List of Tables

Chapter 2: Methanogenic conversion of hydrogen to methane in reservoir rocks: an experimental study of microbial activity in water-filled pore space

Chapter 3: Methanogenic activity in water-saturated reservoir analogues for underground hydrogen storage: The role of surface area

Chapter 4: Exploring effective diffusion coefficients in water-saturated reservoir rocks via pressure decay technique: Implications for Underground Hydrogen Storage

List of Figures

Chapter 1: Introduction

Chapter 2: Methanogenic conversion of hydrogen to methane in reservoir rocks: an experimental study of microbial activity in water-filled pore space

Chapter 3: Methanogenic activity in water-saturated reservoir analogues for underground hydrogen storage: The role of surface area

Chapter 4: Exploring effective diffusion coefficients in water-saturated reservoir rocks via pressure decay technique: Implications for Underground Hydrogen Storage

Appendices

List of abbreviations and symbols

Symbol	Definition	Unit
A	Total surface area of solids	m^2
a	Slope of correlations between normalized H_2 consumption rates and specific surface area	$mM \cdot m^2/(h \cdot cm^3 \cdot cm^2 \cdot g)$
$A_{interfacial}$	Interfacial area between liquid and gas phases	cm^2
b	Intercept of correlations between normalized H_2 consumption rates and specific surface area	$mM/(h \cdot cm^3 \cdot cm^2)$
C	Molar concentration	mol/m^3 or M
C_{H2}	Consumed H_2 concentration	mM
C_{CH4}	Generated CH_4 concentration	mM
d	Pore diameter	µm
D	Gas diffusion coefficient in water	m^2/s
D_{eff}	Effective gas diffusion coefficient in water-saturated rock	m^2/s
F_s	Pore shape factor	-
h_L	Height of water column in diffusion cell	m
h_G	Height of gas column in diffusion cell	m
H_{cc}	Henry's constant for gas/water system, C/ρ_g	-
m	Mass of rock specimen	g
MICP	Mercury Injection Capillary Pressure	-
Mw	Molecular weight	kg/kgmol
n	Number of moles	mol
N	Amount of diffused gas into water	mol

Symbol	Definition	Unit
NMR	Nuclear Magnetic Resonance	-
N_∞	Maximum amount of diffused gas into water	mol
P	Gas pressure	Pa
P_c	Capillary pressure	MPa
P_j	Gas pressure in the sample container of microbial activity setup	bar
P_{ref}	Gas pressure in the reference cell	bar
P_{tot}	Total pressure of gas mixture	bar
P_{H_2}	H_2 partial pressure	bar
P_{CO_2}	CO_2 partial pressure	bar
P_{CH_4}	CH_4 partial pressure	bar
P_{H_2o}	H_2O vapor pressure	bar
r_0	Radius of rock specimen	m
R	Universal gas constant	m^3·Pa/(K·mol)
R_{H_2}	Rate of H_2 consumption	mM/h
R_{H_2} (normalized)	Rate of H_2 consumption normalized by pore volume and interfacial area	mM/(h·cm^3·cm^2)
S	Pore surface area	μm^2
SEM	Scanning Electron Microscopy	-
SSA	Specific surface area	m^2/g
SPV	Specific pore volume	cm^3/g
T	Temperature	K
T_{2s}	Surface transversal relaxation time	s
T_{eq}	Required time to reach pressure equilibrium in microbial activity test	h
V	Gas volume	m^3
V_b	Bulk volume of rock specimen	cm^3
V_i	Cumulative pore volumes corresponding to pore throat diameters of d_i	mL/g
V_j	Volume of sample container in microbial activity setup	cm^3
V_p	pore volume of rock specimen	cm^3
V_{ref}	Volume of reference cell	cm^3

Symbol	Definition	Unit
Δt_j	Time interval between pressure recording steps in sample container of microbial activity setup	h
Δt_{ref}	Time interval between pressure recording steps in reference cell of microbial activity setup	h
Z	Gas compressibility factor	-
α	Volume ratio of the liquid phase to gas phase	-
α_n	Positive roots of the first kind of Bessel function of zero order	-
β	Rate coefficient of pressure decay	kg/m^3
γ	Exponent factor indicating the rate of pressure decay	1/s
γ_{Hg}	Air/mercury surface tension	N/m
ε	Tortuosity	-
θ_{Hg}	Air/mercury contact angle	degree
λ	root of characteristic function	-
μ	Gas viscosity	Pa·s
µCT	X-ray micro-computed tomography	-
ρ	Transversal surface relaxivity	µm/s
ρ_{bulk}	Bulk density of rock specimen	g/cm^3
ρ_g	Molar gas density	mol/m^3
ρ_{g0}	Initial gas density	kg/m^3
$\rho_{g\infty}$	Gas density at equilibrium condition	kg/m^3
σ	Standard deviation	-
ϕ	porosity	%

Chapter 1

1.Introduction

1.1. Underground hydrogen storage

The combustion of fossil fuels for energy supply releases an enormous amount of greenhouse gases into the atmosphere, making global warming a major environmental concern (Liebscher et al., 2016; Metz et al., 2005). Therefore, the energy transition towards renewable, carbon-free or carbon-neutral energy sources is indispensable to decarbonize energy systems, reduce greenhouse gas emissions and combat progressive global warming (Dopffel et al., 2021; van Renssen, 2020). Solar and wind plants are significant contributors to this energy transition, substantially rising in importance over the past decade in many countries (European Commission, 2021). The share of solar and wind energy sources is projected to increase significantly by 2050, rising from 12% in 2022 to 52% in the Stated Policies Scenario (STEPS), 65% in the Announced Pledges Scenario (APS), and 74% in the Net Zero Emissions (NZE) scenario. STEPS reflects current energy, climate, and related industrial policies, while APS assumes the full and timely achievement of all national energy and climate objectives declared by governments. The NZE scenario aims to limit global warming to 1.5°C by 2050 (Figure 1.1) (IEA, 2023).

However, the major drawback of these renewable energy sources is their reliance on seasonal variations in atmospheric events (e.g. daylight amount and intensity, wind force), which leads to an imbalance between supply and demand. One approach to balancing this discrepancy is to store the excess energy generated when there is an oversupply of renewables and release it during times when renewables are in short supply (Heinemann et al., 2021). Storage technologies such as batteries, compressed air, capacitors, flywheels

and pumped hydropower plants are effective on a small scale, typically in the MWh range, and provide short-term support to the energy system (Figure 1.2) (Liebscher et al., 2016; Muhammed et al., 2022).

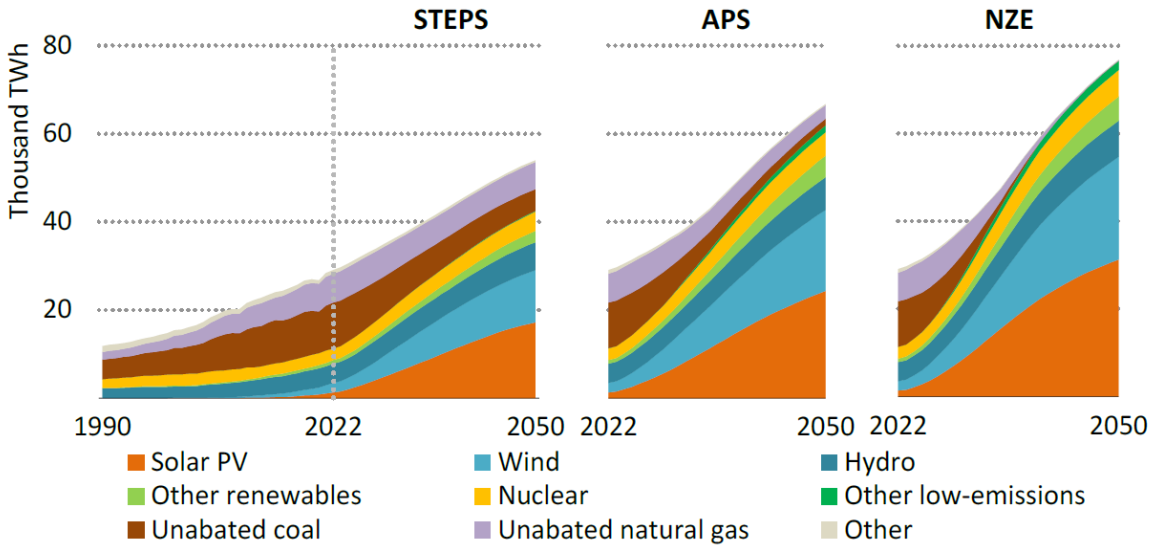

Figure 1.1. Growth of renewable energy sources is projected to increase significantly across various scenarios: by 2.4 times under the Stated Policies Scenario (STEPS) by 2030, 2.7 times under the Announced Pledges Scenario (APS), and to triple under the Net Zero Emissions (NZE) scenario. Solar and wind power are anticipated to drive 95% of this growth, with their combined share in global electricity generation rising from 12% to approximately 30% by 2030 (after IEA (2023)).

With anticipated excess energy ranging from GWh to TWh, the conversion of surplus electricity into hydrogen (H_2) as an energy carrier using power-to-gas technology has attracted significant attention as a promising solution (Gahleitner, 2013; Mouli-Castillo et al., 2021). The H_2 produced can either be stored for future use or converted into methane (CH_4) through biological processes. Consequently, the H_2 storage remains an active area of research. H_2 has a higher energy density per mass at 143 MJ/kg compared to CH_4's 55.6 MJ/kg, yet its lower density (0.084 kg/m³ at 20°C and 0.1 MPa) results in a volumetric energy density that is one-third that of CH_4 (Mazloomi & Gomes, 2012). Consequently, the storage of H_2 on a scale ranging from GWh to TWh demands extensive storage volumes, far beyond the capacity of surface storage facilities such as pipelines or tanks (Figure 1.2) (Hashemi et al., 2021; Heinemann et al., 2021). Subsurface geological formations, including depleted hydrocarbon reservoirs, aquifers, and salt caverns provide the required capacity for large-scale H_2 storage, crucial for ensuring mid- to long-term stability in the energy grid and fulfilling seasonal energy demands (Liebscher et al., 2016). Salt caverns offer the advantage of frequent injection-withdrawal cycles and high flow rates, making them well-suited to quickly meet fluctuations in energy demand. Nevertheless, the

utilization of salt caverns is constrained by its smaller capacity compared to porous formations, as well as the scarcity of suitable salt deposits for cavern construction, typically ranging from 100,000 to 1,000,000 m³ (Bünger et al., 2016; Panfilov, 2016). For instance, salt deposits in Germany are predominantly located in the northern regions, specifically within the Upper Permian (Zechstein) formations. These deposits include significant structures like the Gorleben and Morsleben salt domes (Mertineit & Schramm, 2019). Depleted hydrocarbon reservoirs and porous aquifers, on the other hand, offer substantial storage capacities and significant potential for local positioning compared to caverns, making them a viable choice for long-term energy supply (Zivar et al., 2021).

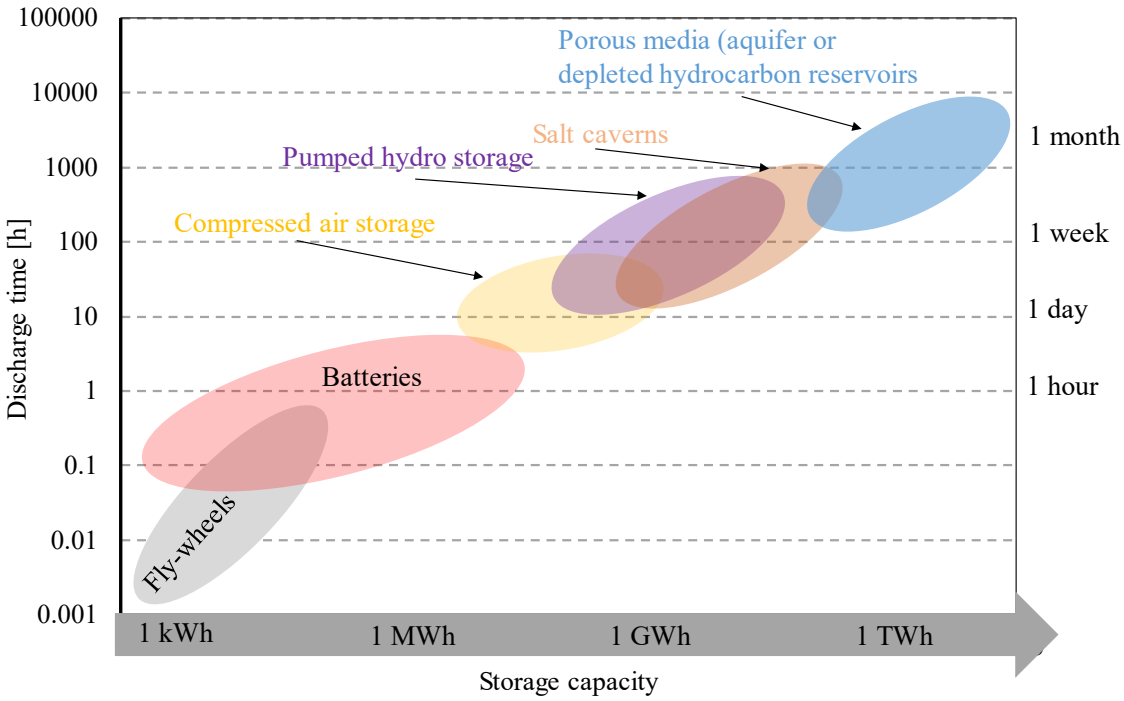

Figure 1.2. Comparison of discharge times and storage capacities across various energy storage systems, including surface facilities like flywheels, batteries, compressed air storage, and pumped hydro storage, alongside subsurface H_2 storage in geological formations like salt caverns and porous rocks (modified after Edlmann et al. (2021); Teske et al. (2017)).

The storage of natural gas, town gas, and CO_2 in geological formations has been in practice for decades, but its application to H_2 storage is a recent development (Heinemann et al., 2018). The experiences gained during underground storage of natural gas and CO_2 can be generally utilized as an analogy for H_2. However, the transfer of this knowledge to pore-scale processes such as geochemistry, geomechanics, hydrogeology, and microbial activity is constrained by the distinct physical and chemical properties of H_2, which differ significantly from those of other stored gases (Figure 1.3).

H_2 is a highly reactive compound (Osman et al., 2022) that can initiate abiotic reactions with dissolved ions, such as sulfate in formation water, or with minerals in the rock matrix. These minerals include iron-bearing minerals (e.g., hematite, goethite, Fe^{3+}-bearing clays, and micas) (Hassanpouryouzband et al., 2022a), sulfur-bearing minerals (e.g., pyrite) (Reitenbach et al., 2015), and carbonate minerals (Marton Berta et al., 2018). These reactions result in the formation of H_2S, as well as mineral dissolution or precipitation within both the reservoir rock and the caprock. The generation of H_2S reduces the quality of stored H_2 and alters the pore water pH (Truche et al., 2013), thereby triggering further fluid-rock interactions. In addition, mineral precipitation in reservoir rock can reduce the permeability, while mineral dissolution in the caprock may create migration pathways, compromising the sealing integrity (Hassanpouryouzband et al., 2022a). Furthermore, the dissolution of minerals affects the mechanical properties of both reservoir and caprock (Dabbaghi et al., 2024). These consequences significantly influence various aspects of H_2 storage; however, their extent and kinetics remain subjects of debate, necessitating experimental studies under conditions typical of subsurface storage (Thüns et al., 2019; Truche et al., 2009).

Cyclic injection and production of H_2 in subsurface formations cause periodic fluctuations in the effective stress within the reservoir and adjacent fault zones. These alterations in stress regime can lead to reservoir compaction, resulting in reduced porosity and permeability at the pore scale (Dautriat et al., 2011; Ostermeier, 1995), as well as subsidence and induced seismicity at the surface (Suckale, 2009, 2010). Additionally, an increase in pore pressure within the reservoir rock applies buoyancy-driven forces to the overlying caprock, disturbing its stress equilibrium. The caprock's response to periodic stress loading and unloading can lead to the creation and propagation of cracks and fractures, compromising its sealing integrity (Ramesh Kumar et al., 2023). Moreover, the induced stress can contribute to faults reactivation, potentially affecting their stability and sealing (Zeng et al., 2023). Despite these effects, research on the impact of cyclical injection-production on the mechanical properties of reservoir rocks and faults remains significantly scarce (Heinemann et al., 2021). Furthermore, geochemical reactions of H_2 with load-bearing minerals may lead to their dissolution, consequently intensifying both elastic and inelastic reservoir deformation driven by cyclical stress alterations (Schimmel et al., 2022).

The complexity of displacement patterns during H_2 flow in porous media, combined with the trapping mechanisms, introduces further challenges for UHS. The unfavorable viscosity and density contrast between H_2 and water causes instability in the displacement front (Lysyy et al., 2022), resulting in the formation of viscous fingering (Berg & Ott, 2012; Paterson, 1983) and gravity tongues (Nijjer et al., 2022). Additionally, the heterogeneity of rock formations leads to flow channeling along high-permeability layers, further complicating these patterns (Nijjer et al., 2019). The associated residual trapping and permanent H_2 loss due to uncontrolled lateral spreading negatively impact the economic feasibility of storage (Carden & Paterson, 1979; Heinemann et al., 2021). The movement of the H_2 plume during injection and withdrawal, and its distribution within the reservoir, are governed by the interplay of gravitational, capillary, and viscous forces. This interaction affects multiphase flow parameters, including relative permeability and capillary pressure (Boon & Benson, 2021; Krevor et al., 2012; Pini et al., 2012). To best knowledge of author, only two experimental studies have been conducted to determine these parameters for the H_2-brine system under various conditions (Boon & Hajibeygi, 2022; Yekta et al., 2018). Therefore, further investigations are needed to gain a comprehensive understanding of fluid dynamics to mitigate associated uncertainties. Another challenge in H_2 transport arises from its higher diffusivity compared to other stored gases such as CH_4 and CO_2. However, studies have shown that H_2 loss due to pure diffusion through caprock or the lateral boundaries of reservoirs typically ranges from 0.2% to 3% over the storage lifetime (Carden & Paterson, 1979; Hassannayebi, 2019). Despite this, diffusion becomes particularly significant when coupled with biotic processes, as it governs the gas-liquid mass transfer essential for providing H_2 molecules in the aqueous phase for microbial reactions. The conversion of H_2 by microorganisms into other byproducts maintains or even enhances the concentration gradient, thereby facilitating a continuous diffusive flow (Jensen et al., 2021). Experimental studies (Strauch et al., 2023) determining H_2 diffusivities in liquid-saturated rocks are very limited, highlighting the need for further research.

The injection of H_2 into subsurface porous media has the potential to stimulate H_2 consuming microbial processes, leading to its permanent conversion into various byproducts such as CH_4, hydrogen sulfide (H_2S), acetic acid, and others (Dopffel et al., 2021; Heinemann et al., 2021).

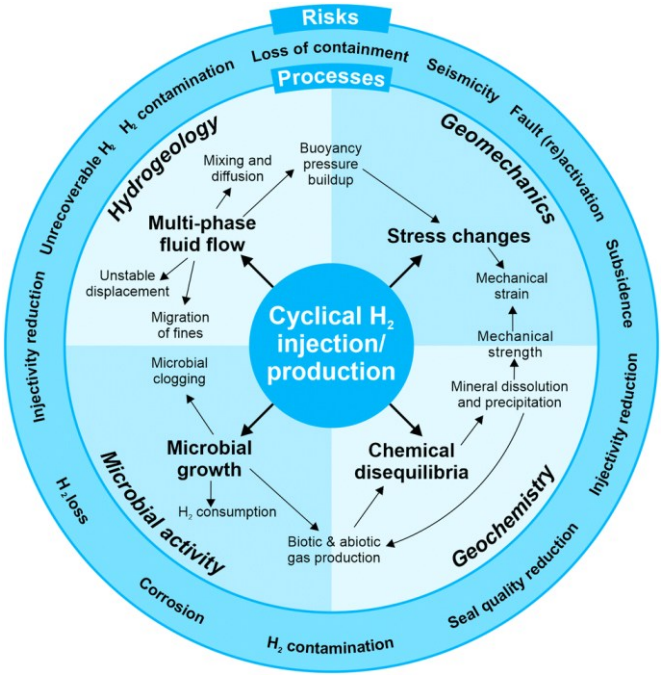

Figure 1.3. Key processes and associated risks involved in underground H_2 storage, which must be addressed to effectively evaluate the opportunities and challenges (after Heinemann et al. (2021)).

The desirability of these microbial reactions depends on the objectives of the storage project; nevertheless, it is crucial to understand their reaction kinetics and identify the controlling parameters. For underground H_2 storage initiatives, conducting a quantitative analysis of H_2 conversion is crucial to measure the extent of H_2 loss and evaluate the associated risks on the project's viability (Reitenbach et al., 2015). In the context of bio-methanation, investigating microbial activity is fundamental to determining the efficiency of CH_4 production (Amez et al., 2021; Strobel et al., 2020). Previous experiments examining H_2 consumption rates due to biotic processes have largely been conducted in the absence of porous media (Ivanova et al., 2007; Kashefi & Lovley Derek, 2000; Krumholz Lee et al., 1999; Robinson & Tiedje, 1984; Smatlak et al., 1996). The limited research on biotic activities within porous media has overlooked the influence of pore characteristics on these processes (RAG Austria AG, 2020, 2021). Nevertheless, research in other fields has highlighted the influence of surface area and mass transfer between liquid and gas phases on microbial activities (Ahmerkamp et al., 2020; Baek et al., 2021; Burkhardt et al., 2015; Mills, 2003; Yang et al., 2020; Yuan et al., 2012). Thus, this study investigates the influence of pore characteristics, specifically porosity and surface area, on microbial activity during Underground Hydrogen Storage (UHS). Additionally, it seeks to assess the effective gas diffusivity in water-saturated rock, a crucial parameter in determining mass transfer flux that impacts H_2 supply for microbial reactions. Through this research, we aim

to deepen our understanding of the complex interactions between microbial processes and the properties of porous media.

1.2. Types of hydrogen

Hydrogen, though the most abundant element (H) in the universe, is relatively rare in its gaseous form (H_2) in natural environment on Earth and requires either artificial production (Balat, 2008; Baykara, 2018) or the exploration of natural H_2 in subsurface formations (Blay-Roger et al., 2024). For decades, it was believed that the natural formation of H_2 was minimal and dispersed too quickly to be significant (Blay-Roger et al., 2024), and the commercial viability of these resources remains to be established (Jackson et al., 2024). Consequently, various processes have been developed for artificial H_2 generation, including electrolysis, thermolysis, steam methane reforming (SMR), pyrolysis, and gasification, to facilitate the energy transition. These processes utilize various sources for H_2, including water, natural gas, biomass, and coal. The necessary electrical energy is supplied by a range of sources, encompassing nonrenewable, nuclear, and renewable energies such as solar, wind, geothermal, and hydropower. H_2 is renowned as a clean energy source because its combustion yields water as a byproduct (Das & Veziroğlu, 2001). Nevertheless, the production of H_2 is not always environmentally friendly due to associated pollutants, suggesting that it is not entirely clean. As a result, H_2 is classified by different symbolic colors based on the energy source and extraction method used, which indicates its environmental impact (Dawood et al., 2020; Yu et al., 2021). There is no standard color specification in the literature, but the most common types of H_2 are green, blue, and grey (Figure 1.4). H_2 derived from water electrolysis using renewable energy is termed "green" due to its lack of CO_2 emissions. Both grey and blue types come from fossil fuels via steam methane reforming, but blue H_2 production is integrated with CO_2 capture and sequestration, aiming to reduce or eliminate carbon emissions (Dawood et al., 2020; Energiewende, 2021; Hage et al., 2020). The required CO_2 capture rate to transition from grey to blue H_2 has not yet been established. However, reported maximum capture rates are 70% for SMR alone, and 90% when including post-combustion CO_2 capture (Newborough & Cooley, 2020). Other color codes used in the literature to describe H_2 derived from various sources or processes include black, brown, turquoise, orange, pink, yellow, and red (Figure 1.4) (Incer-Valverde et al., 2023). H_2 created from the gasification of bituminous coal and lignite coal is classified according to their respective colors, black and brown. Additionally, H_2 generated from biomass gasification is also classified as brown H_2. These

types are the most environmentally damaging due to their high CO_2 emissions, placing them at the opposite end of the H_2 spectrum from green H_2 (Dodgshun; Incer-Valverde et al., 2023; Shiva Kumar & Lim, 2022). Nevertheless, some researchers classify any H_2 produced from fossil fuels as grey H_2, including black and brown, which can be converted to blue H_2 by coupling with CO_2 capture and sequestration (Dash et al., 2023; Moreno-Brieva et al., 2023). The pyrolysis of CH_4 is an innovative technology that has been developed, producing turquoise H_2 and refractory carbon (Amin et al., 2011). This technology has the potential to be recognized as low-emission if renewable energy is used for the thermal process and the resulting carbon is stored permanently, without being used for further processing (Schneider; Van de Riet & Bais). H_2 can also be obtained through water electrolysis or thermochemical processes utilizing nuclear energy, referred to by red and pink colors, respectively. However, there is debate regarding the assignment of color codes to these types, with some authors referring to H_2 produced from both processes as purple (Ajanovic et al., 2022; Dash et al., 2023; Incer-Valverde et al., 2023). Yellow H_2 is a subset of green H_2, produced via electrolysis powered by solar energy. This distinction highlights the particular renewable energy source used in its production (Williams, 2022; Willige, 2022). Unlike green H_2, which is derived from surplus renewable energy, yellow H_2 depends on solar energy that could otherwise, at least partially, fulfill regular electricity demands. Consequently, fossil fuels might be used to make up for this shortfall. As a result, producing yellow H_2 under these circumstances increases the grid's emission factor and cannot be considered carbon neutral (Liponi et al., 2023). The other type of electrolytic H_2 is produced using grid electricity derived from a combination of renewable energy sources and fossil fuels. Some authors refer to this type as orange, while others classify it as yellow (Dodgshun; Incer-Valverde et al., 2023; Lubbe et al., 2023). An overview of the color codes for different types of H_2, based on the energy source, H_2 source, processes, and CO_2 emissions, is presented in Figure 1.4.

"White" refers to naturally occurring geogenic H_2, which can either seep to the surface or accumulate within geological formations to create H_2 deposits (Aimikhe & Eyankware, 2023; Yedinak, 2022). The recent occurrences of natural H_2 in many locations have prompted extensive research to explore the various elements contributing to H_2 generation in subsurface formations. These elements include generation, migration, trapping, and accumulation, forming a hydrogen system analogous to the hydrocarbon system (Prinzhofer et al., 2018; Zhao et al., 2023) (Figure 1.5).

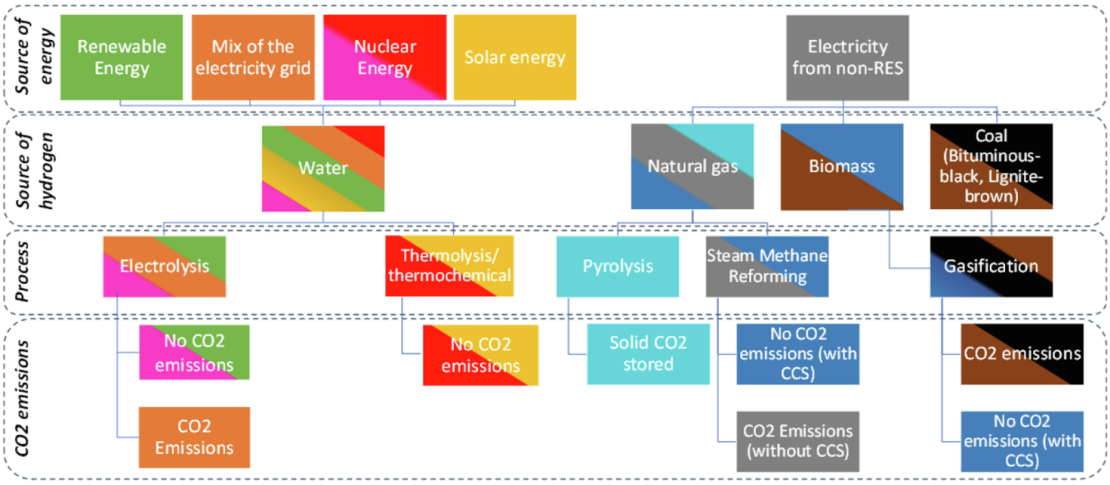

Figure 1.4. Overview of the energy sources, H_2 sources, production processes, and associated emissions for various types of H_2, represented by symbolic colors: green, orange, red, pink, blue, grey, turquoise, brown, black, and yellow (after Incer-Valverde et al. (2023)).

However, these geological systems exhibit two main differences. As shown in Figure 1.5, the kitchen of the hydrogen system is typically situated in the basement, distinct from the sedimentary basin where H_2 migrates and accumulates (Jackson et al., 2024). This source rock provides favorable conditions for H_2-generating mechanisms involving minerals (Milkov, 2022), which are the primary source of natural H_2 (Prinzhofer et al., 2018). Conversely, hydrocarbons primarily originate from the thermal cracking of organic matter, and therefore all components of hydrocarbon systems, including generation, occur within the basin itself (Jackson et al., 2024). Although some studies suggest that H_2 can be produced from the late cracking of organic matter during metagenesis (Horsfield et al., 2022; Mahlstedt et al., 2022), it is likely to be consumed by microorganisms present in the source rocks or upper formations during migration (Milkov, 2022). Moreover, the timelines required for various events in these systems differ significantly. The timescale for hydrocarbon generation and accumulation is in the order of 10's to 100's of millions of years, whereas the lifespan of a hydrogen system ranges from 10 to 100 years (Bachaud et al., 2017; Prinzhofer et al., 2018; Tissot & Welte, 2013).

Several mechanisms have been proposed to explain the genesis of natural H_2, classified into abiotic and biotic processes. Biotic processes, such as the anaerobic decomposition of organic matter and fermentative processes, typically occur under conditions conducive to microbial life. In contrast, abiotic mechanisms, such as water-rock interactions involving Fe^{2+}-bearing minerals, water radiolysis, and degassing from the mantle, produce H_2 over a

wider temperature range (up to 600°C) (Gregory et al., 2019; Milkov, 2022; Zgonnik, 2020).

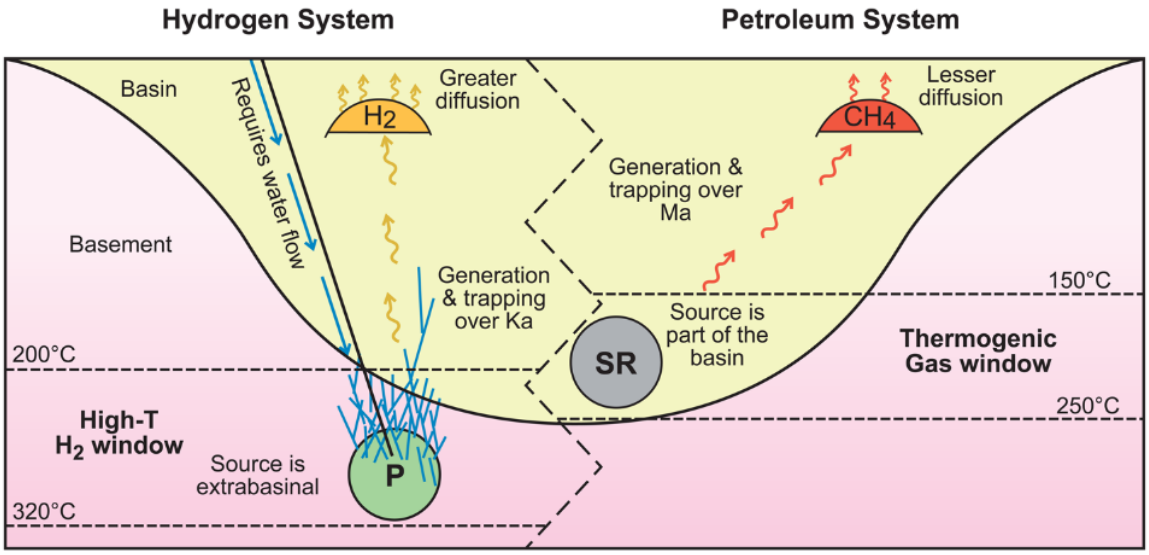

Figure 1.5. Comparison of hydrogen and hydrocarbon systems, highlighting the location of source rocks relative to the sedimentary basin. The hydrocarbon source rock (SR) is located within the basin, while the H_2 source rock (Protolith (P)) is situated in the basement beneath the sedimentary basin (after Jackson et al. (2024)).

The most significant and well-understood water-rock interaction is serpentinization (Jackson et al., 2024). This occurs when water interacts with ultramafic rocks, such as peridotite (primarily composed of the mineral olivine containing Fe^{2+}). This process, typically occurring at temperatures between 210 and 300°C, results in the oxidation of the rocks into serpentine and the generation of H_2 (Zgonnik, 2020). The dominant presence of peridotite in the Earth's upper mantle suggests a significant potential for H_2 production through this mechanism (Zhao et al., 2023). The oxidation of peridotite yields 2-4 kg of H_2 per m^3, theoretically producing up to 10^8 Mt of H_2 from an estimated 10^{12} Mt of peridotite in the Earth's mantle (Blay-Roger et al., 2024).

The migration from the kitchen to the upper layers occurs through permeable pathways and fractures, following mechanisms similar to those of hydrocarbon gases. These mechanisms include advection in the gas phase or solution due to pressure gradients, as well as diffusion resulting from concentration gradients (Jackson et al., 2024). H_2 may subsequently accumulate in a geological trap, which could be structural, stratigraphic, or a combination of both types, forming deposits (Blay-Roger et al., 2024; Maiga et al., 2024). Alternatively, it may dissipate into the atmosphere via seepages, giving rise to circular depressions known as fairy circles, which are valuable indicators for exploration (Wang et al., 2023). The density and size of these structures can vary, with diameters ranging from 1 meter in

Australia (Figure 1.6) to up to 8 kilometers in Mali (Blay-Roger et al., 2024). The sealing mechanism for trapping H_2 is similar to that of hydrocarbon systems, relying on high capillary forces in the pores of low-permeability rocks overlying the deposits (Hutchinson Ian et al., 2024). However, the migration continues by molecular diffusion of H_2 through impermeable rocks. While the diffusion coefficient of H_2 in pure water is 2.8 time larger than that of methane (Muhammed et al., 2022), its low solubility compared to methane (Kaye & Laby, 1928) acts counteractive resulting in an insignificant diffusive flux in comparison to the potential volume of a commercial accumulation (Monge & Vayssaire, 2022).

The H_2 reservoirs discovered worldwide exhibit variable concentrations. Nearly pure H_2 deposits are found in Brazil (Cathles & Prinzhofer, 2020), Mali (Prinzhofer et al., 2018), and Oman (Neal & Stanger, 1983). Accumulations with concentrations ranging from 50% to 92% are located in the USA (Guélard et al., 2017; Morrill et al., 2013), Canada (Sherwood Lollar et al., 2006), and Germany (Erdmann, 1910).

1.3. Microbial activity in porous media in the context of UHS

Subsurface formations host a diverse community of microorganisms, including bacteria and Archaea (Hoehler & Jørgensen, 2013). The abundance of microbial cells ranges from 10^4 to 10^8 cells per gram of rock, estimating a total population of $2 \cdot 10^{29}$ to $6 \cdot 10^{29}$ cells within the continental subsurface (Dutta et al., 2018). Microbial metabolism is influenced by environmental conditions such as temperature, pressure, pH, and salinity, as well as the presence of electron donors and acceptors necessary for respective reactions (Thaysen et al., 2021). The H_2-consuming microbes with specific enzymes (hydrogenases) catalyze the breakdown of H_2 into protons and electrons, providing energy for biotic processes to occur at temperatures of subsurface formations (Gregory et al., 2019; Hagemann et al., 2016; Wait & Wait, 2011). Therefore, the presence of H_2 within subsurface formations serves as an energy source for biotic reactions, potentially enhancing microbial activity (Reitenbach et al., 2015). The primary biotic processes relevant to H_2 storage include methanogenesis, acetogenesis, sulfate reduction, and iron (III) reduction. Methanogenic *Archaea* transform carbon dioxide present in reservoir fluids into CH_4 at optimal temperatures between 30 and 40°C (Heinemann et al., 2021; Panfilov, 2016). Nevertheless, certain studies have documented their ability to survive at elevated temperatures, reaching up to 122 °C (Lovley & Goodwin, 1988; Magot et al., 2000; Takai et al., 2008).

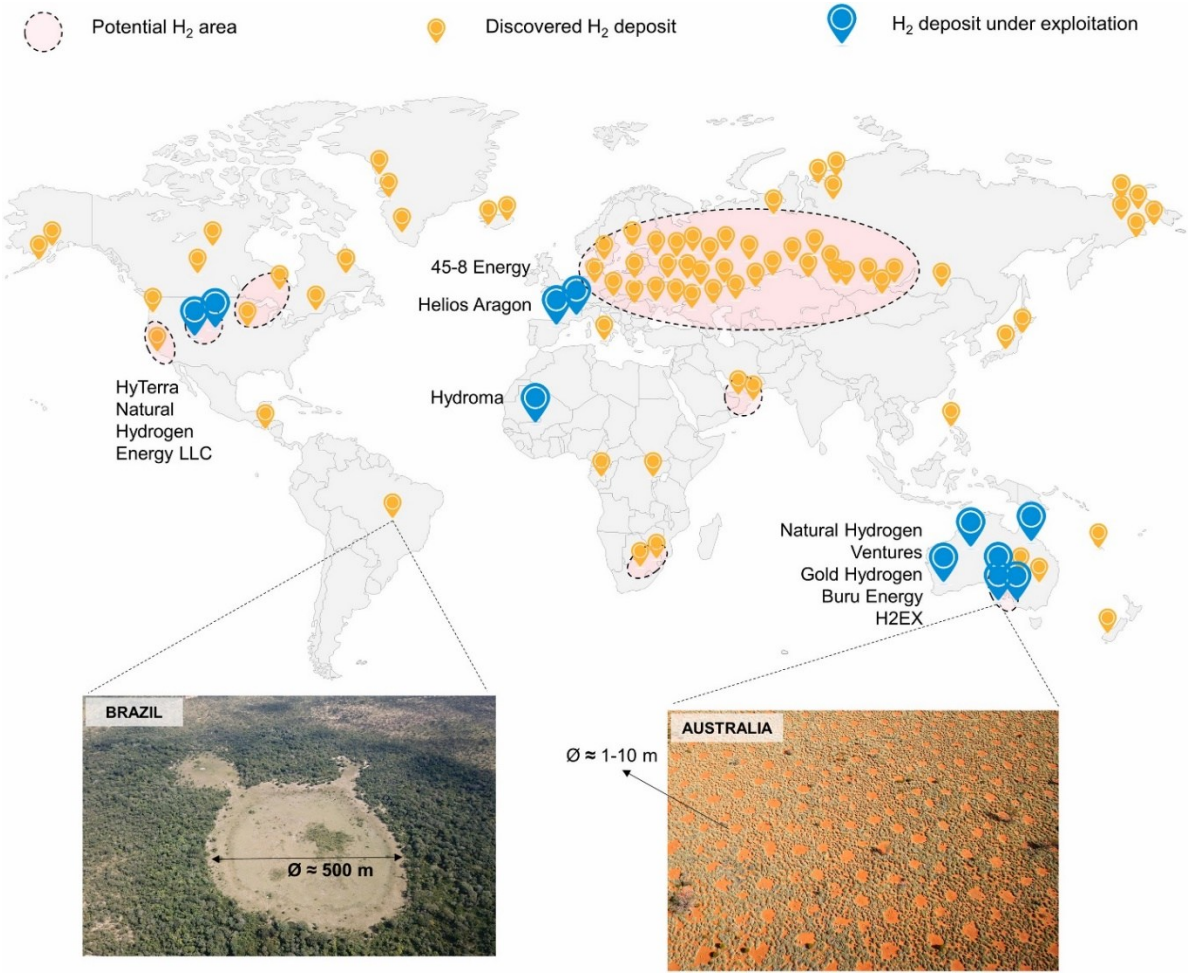

Figure 1.6. Worldwide distribution of natural H_2 deposits categorized into potential areas, discovered areas, and areas under exploitation. Two images display fairy circles in Brazil and Australia, highlighting variations in their density and diameter (after Blay-Roger et al. (2024)).

The methanogenic reaction is as follows (Zivar et al., 2021):

$$CO_2+4H_2 \rightarrow CH_4+2H_2O \quad (1.1)$$

The acetogenesis process occurs in the presence of acetate as an electron acceptor, converting it into acetic acid as follows (Zivar et al., 2021):

$$2CO_2 + 4H_2 \rightarrow CH_3COOH + 2H_2O \quad (1.2)$$

Sulfate reduction involves utilizing sulfate obtained from the dissolution of anhydrite as an electron acceptor, leading to the generation of H_2S (Hemme & van Berk, 2018). While the optimum temperature for the activity of sulfate-reducing bacteria is typically around 38°C (Bernardez et al., 2013), documented cases have shown activity at higher temperatures, reaching levels as high as 110°C (Jørgensen et al., 1992; Machel, 2001). The resultant H_2S

causes corrosion in downhole and surface facilities, posing a significant risk to operational safety (Zivar et al., 2021). The sulfate reducer reaction is shown below (Zivar et al., 2021):

$$SO_4^{2-} + 5H_2 \rightarrow H_2S + 4H_2O \quad (1.3)$$

In reservoir rocks containing Fe_2O_3, iron-reducing bacteria catalyze its conversion to Fe_3O_4 through the following reaction (Zivar et al., 2021):

$$3Fe_2O_3 + H_2 \rightarrow Fe_3O_4 + H_2O \quad (1.4)$$

1.4. Pore characteristics influencing the microbial activity within porous media

To the best of the author's knowledge, the relationship between pore characteristics and microbial activity during underground H_2 storage to date remains unexplored. Nonetheless, numerous studies have examined the effects of surface area and gas-liquid mass transfer on bacterial growth and the kinetics of microbial reactions in alternative environments. In the mid-1930s, microbiologists recognized that bacteria exhibit a pronounced tendency to adhere to particles or surfaces. Observations showed that an increase in the surface-to-volume ratio, referred to as the "bottle effect", significantly enhanced bacterial growth in storage containers or in the presence of surfaces and particles. This phenomenon was attributed to the adsorption of nutrients by these surfaces, thereby creating a more conducive environment for bacterial proliferation, ultimately leading to microbial colonization (Stark, 1938; Waksman & Carey, 1935a; Zobell & Anderson, 1936). The stimulating effect of surface area on microbial growth was further validated by an investigation of sandy sediments collected from the subtidal North Sea. The research aimed to ascertain how various grain properties such as size, sphericity, and surface-to-volume ratio affect cell abundance. For this purpose, the sediments were sorted into five different grain sizes, ranging from 227 to 882 µm. The findings indicated a strong correlation between the available surface area and cell abundance (Ahmerkamp et al., 2020). Furthermore, the production of biogas through anaerobic digestion in the microbial reactors benefits from increased surface area, leading to enhanced energy output. A thorough review of multiple experimental studies demonstrated a strong correlation between the CH_4 generation rates and the ratio of electrode surface area to reactor volume, referred to as the S/V ratio (Baek et al., 2021). Moreover, an effective strategy for improving biogas recovery from organic waste treatment and carbon dioxide methanation involves the use of carrier

materials such as polypropylene rings and glass rings. The increased surface area of these materials provides more sites for bacterial adhesion, resulting in immobilization of microorganisms and their subsequent rapid proliferation (Li et al., 2018; Yang et al., 2020). Additionally, ceramics and biochar are frequently employed as carrier materials owing to their substantial specific surface areas (M. Lu et al., 2013; Wang et al., 2017; Zhao et al., 2016). For instance, an experimental study examined the impact of incorporating corn straw biochar into a bio-methanation reactor, revealing a significant 70% increase in CH_4 production (Yang et al., 2020).

The rate of gas-liquid mass transfer is another factor affecting microbial reactions, as microorganisms can only convert H_2 molecules in the aqueous phase (Osman et al., 2022). This suggests that the reaction rates are limited by the availability of dissolved H_2. The transfer rate is governed by the concentration gradient, the mass transfer coefficient, and the interfacial area between the liquid and gas phases. The driving force behind mass transfer is the concentration gradient between the gas-liquid interface and the bulk liquid (Jensen et al., 2021). The relatively low solubility of H_2, which determines its concentration at the interface, constrains mass transfer and acts as a bottleneck for microbial reactions (Porté et al., 2019; Szuhaj et al., 2016). To address this, various bioreactor configurations have been developed to increase the interfacial area, thereby enhancing bioenergy production. These include bubble dispersion reactors, membrane reactors, and trickle bed reactors (Ale Enriquez & Ahring, 2023; Jensen et al., 2021). The bubble dispersion reactor improves gas-liquid contact by generating small-diameter bubbles that permeate the culture broth (Villadsen et al., 2011a). In the membrane reactor, a porous tubular membrane is integrated, allowing the substrate gas to diffuse through the membrane into the liquid broth, meaning the interfacial area primarily depends on the membrane's surface (Ale Enriquez & Ahring, 2023; Nock et al., 2019). The trickle bed reactor uses a porous carrier material, forming a thin liquid layer on the carrier's surface to expand the gas-liquid contact area (Burkhardt et al., 2015; Dupnock & Deshusses, 2019). The two-film theory provides a framework for gas-liquid mass transfer (Lewis & Whitman, 1924), suggesting that the mass transfer coefficient reflects the total resistance caused by stationary gas and liquid films around the interface. The contribution from the gas side is insignificant, especially for gases with low solubility, such as H_2. Given that the mass transfer coefficient on the liquid side is directly proportional to the gas diffusion coefficient in the liquid, accurately determining this parameter is crucial (Jensen et al., 2021). The H_2 diffusivity in water has been

extensively investigated and documented in the literature (Gertz, 1954; Gubbins et al., 1966; Jähne et al., 1987; Vivian & King, 1964; Wise & Houghton, 1966). However, understanding of the effective diffusivity of H_2 in water-saturated rocks remains limited. The only experimental study, conducted by Strauch et al. (2023) measured the H_2 diffusivity in water-saturated Bentheim sandstone at ambient pressure and temperature, revealing a value of $1.6 \cdot 10^{-9}$ m^2/s. Moreover, the diffusion of gas molecules into the overlying caprock and underlying aquifer can lead to gas loss, potentially compromising sealing efficiency and the feasibility of subsurface H_2 storage (Fleury et al., 2009; Reitenbach et al., 2015). While several studies have shown that diffusive loss can reach up to 3% (Carden & Paterson, 1979; Hassannayebi, 2019), accurately determining the diffusion coefficient is essential for generating the critical data required in modeling efforts to precisely estimate gas loss.

1.5. Microbial activity in underground hydrogen storage projects

The storage of pure H_2 is currently limited to four salt caverns, including Teeside in the UK, and Clemens, Moss Bluff, and Spindletop in the USA (Zivar et al., 2021). Due to the scarcity of facilities dedicated to storing pure H_2, insights into its behavior within subsurface formations are primarily derived from the storage of so-called town gas, containing 16-50% H_2 (Liebscher et al., 2016). Two additional projects utilizing salt caverns for storage have been implemented in Kiel, Germany, and STOPIL-H2, France. Experiences with H_2 storage in salt caverns have revealed no detectable microbial consumption of H_2. The lack of microbial activity in these formations is not surprising, attributed to the high salinity of the brine, which limits the diversity and abundance of microorganisms (Dopffel et al., 2021). Increased salt content induces osmotic stress in cells, implying that only those microorganisms equipped with isosmotic intracellular mechanisms can thrive in this environment (Oren, 2001; Oren, 2006). The majority of hydrogenotrophic methanogens, sulfate reducers, and homoacetogens thrive in slightly halophilic environments (0.2-0.5 M NaCl), although certain strains exhibit resilience to salinities as high as 4.4 M NaCl (Thaysen et al., 2021). Despite the reduced diversity and abundance, halophilic microbes have the potential to be introduced through the water used in cavern dissolution or during extended operational periods (Mouser et al., 2016; Vreeland et al., 1998). This highlights the importance of investigating biological processes within salt caverns, particularly in the presence of sulfate, as it increases the likelihood of microbial H_2S formation at the brine-gas interface (Hemme & van Berk, 2017).

An examination of town gas storage in a saline aquifer at Lobodice, Czech Republic revealed the activity of H_2-consuming microbes. Over a seven-month testing phase, it was reported that H_2 was microbially converted into CH_4 and H_2S at 35°C. This transformation resulted in a decrease in H_2 concentration from 54 vol.% to 37 vol.%, accompanied by a decline in pressure and an increase in the abundance of methanogenic *Archaea* cells. Furthermore, an experimental study conducted on methanogenic bacteria extracted from formation fluid samples of this reservoir conclusively demonstrated their role in converting H_2 into CH_4. Additionally, isotopic analysis of the resulting CH_4 confirmed its biological origin (Šmigáň et al., 1990). Similarly, the town gas storage in the Lower Jurassic sandstone aquifer at Ketzin, operational from 1964 to 2004, experienced several challenges. These included H_2 loss, pressure reduction, changes in gas composition, corrosion of downhole facilities, and altered permeability. Further investigations of the caprock and wells confirmed their structural integrity and sealing capabilities, suggesting that identified issues were likely attributed to chemical and biological processes. The rate of H_2 loss was recorded at 8 million m^3 annually, accounting for 61% of the H_2 stored. Additionally, analysis of the gas composition revealed alterations due to the consumption of CO and the production of CO_2, H_2, H_2S, and CH_4. Nevertheless, it remains unclear which microbial processes, if any, might have contributed to these alterations (Liebscher et al., 2016; Marcogaz, 2017). Another town gas storage containing 50-60% H_2 in a saline aquifer operated from 1956 to 1972 in Beynes, France. While some reports indicated no issues such as H_2 loss or alterations in gas composition during its 18 years of operation (Foh et al., 1979), other researchers noted significant microbial activity leading to changes in the gas composition (Albes et al., 2014; Panfilov, 2016).

Three projects have investigated H_2 storage in depleted hydrocarbon reservoirs, albeit at a field test scale (Dopffel et al., 2021; Strobel et al., 2020). During the Underground Sun Storage project, a mixture containing 10% H_2 and 90% natural gas was injected into the Lehen-002 sandstone reservoir in Vöcklabruck, Austria, and stored for four months. It was observed that 18% of the injected H_2 was unrecoverable, with losses being attributed to diffusion, solubility, and microbial conversion processes. In addition, DNA and RNA analyses indicated shifts in the microbial community of the formation water, highlighting the stimulation of methanogenesis, acetogenesis, and sulfate reduction processes. This finding revealed that methanogenic reaction can initiate at very low CO_2 concentrations, resulting in an increase in CH_4 and a decrease in CO_2 from 0.2% to 0.05%. Additionally,

fluid samples collected during the withdrawal period showed the generation of up to 100 mg/L of acetate and the complete depletion of sulfate, from approximately 20 mg/L to 0 mg/L, underscoring the impact of microbial metabolism. The H_2S produced likely reacted with iron, leading to no detection in the withdrawn gas. Prior to commencing field tests, laboratory experiments were conducted to establish a crucial foundation for their execution. This experimental phase involved incubating cores extracted from the reservoir under anaerobic conditions along with formation water. The findings consistently indicated the presence and activity of methanogenesis, acetogenesis, and sulfate reduction processes (Dopffel et al., 2021; Pichler, 2019; RAG Austria AG, 2020). The project's findings suggest that geo-methanation is potentially feasible in this reservoir. This led to the subsequent "Underground Sun Conversion (USC)" project, which focused exclusively on investigating geo-methanation through experimental studies, microbial process simulations, and field tests. One of the laboratory tests aimed to investigate a stable geo-methanation process by performing repeated conversion cycles of a gas mixture containing 10%-40% H_2 and 2.5%-10% CO_2, with methane as the make-up gas, over a period of 300 days. The findings demonstrated that increasing the H_2 concentration up to 30% resulted in a longer reaction time for complete conversion. The observed discrepancy in the test with 40% H_2 and 10% CO_2 could be attributed to the high dissolution of CO_2 in the fluid, which led to a reduction in pH and adversely affected the methanogenic reaction. Building on the insights gained from laboratory tests and simulations, 16 field tests were conducted using a gas mixture composed of 10-20% H_2 and 2.5% CO_2, and 77.5-87.5% natural gas. Results of the field tests revealed that H_2 conversion rates differ between the areas near the wellbore and the deep reservoir. This discrepancy is attributed to the superior supply of feed gas to microbes near the wellbore. Furthermore, the tests highlighted a noticeable heterogeneity in the distribution of microbial activity within the withdrawal gas. In one region, the composition of the withdrawal gas showed little to no change compared to the injected gas, while in another region, significant changes were observed. Furthermore, in addition to methanation, the occurrence of other biotic processes such as sulfate reduction and homoacetogenesis was identified. This was evidenced by the presence of H_2S in the produced gas and acetate in the reservoir brine (RAG Austria AG, 2021). In 2010, HyChico launched a pilot project in a depleted gas reservoir to store H_2 sourced from a nearby wind park in Argentina. Multiple injection-withdrawal cycles were conducted using a 10% H_2 and natural gas mixture, with subsequent analyses tracking changes in reservoir properties and gas composition. It was observed that some amount of H_2 was biologically converted

into CH_4. Following this, HyChico initiated a collaborative project with the French Geological Survey (BRGM) to explore underground bio-methanation further. Preliminary results suggest that the reservoir conditions are conducive to methanation processes (Pérez et al., 2016). Investigation of microbial activity during these projects revealed significant uncertainties regarding the behavior of microorganisms within porous media, indicating the need for further research in this area.

1.6. Main objectives and structure of the dissertation

The dissertation was composed of five principal chapters, starting with an introduction. Chapters two to four thoroughly explored various pore characteristics influencing microbial activity within porous media, each presented as a research article. The final chapter, Chapter five, concludes the dissertation with a general summary and future outlook. The objectives and scope of each chapter are outlined below.

Chapter 2 *was published* similarly as Khajooie, S., Gaus, G., Dohrmann, A. B., Krüger, M., & Littke, R. (2024). Methanogenic conversion of hydrogen to methane in reservoir rocks: An experimental study of microbial activity in water-filled pore space. *International Journal of Hydrogen Energy*, *50*, 272-290.

In this publication, the activity of methanogenic *Archaea* within water saturated reservoir rocks, as well as inoculated media containing sand particles and rock fragments, were experimentally studied and compared to values obtained in bulk solutions. *Methanothermococcus thermolithotrophicus* was selected as the model organism due to its relatively high activity and growth rate. Five rock samples from the Cretaceous (Bentheim Sandstone, Obernkirchen Sandstone, and Anröchter Grün Limestone) and the Triassic (Red and Grey Weser Sandstone) were chosen as reservoir analogues for UHS. Measured activities in the water-saturated pore space of the respective rocks with identical bulk volumes varied between 1.22 and 0.17 H_2 mM/h correlating with the pore volume. Furthermore, the results indicated that activities in the water-filled pore space of the selected rocks were higher by a factor of 8-10 compared to activities in bulk solutions. This observation supports the notion that the surface area available for microorganism colonization is a potential factor in controlling microbial activity when the amount of substance is held constant. This is further evidenced by the measured activities in inoculated media containing sand particles and rock fragments, as well as in rocks with similar pore volume.

Chapter 3 *was published* as Khajooie, S., Gaus, G., Seemann, T., Klaver, J., Claes, H., Nehler, M., Ahrens, B., & Littke, R. (2024). Methanogenic activity in water-saturated reservoir analogues for underground hydrogen storage: The role of surface area. *International Journal of Hydrogen Energy, 90, 171-190.*

The primary objective of this publication was to quantitatively analyze the stimulating effect of surface area on microbial activities documented in Chapter 2. To achieve this, the specific surface areas of examined reservoir analogues for UHS including, Bentheim, Obernkirchen, Red Weser, and Grey Weser sandstones were determined. These measurements were carried out using various techniques, including mercury injection capillary pressure (MICP), nuclear magnetic resonance (NMR), scanning electron microscopy (SEM), and X-ray micro-computed tomography (μCT). The findings revealed that microbial activity was enhanced exclusively within pores of sufficient size to facilitate microbial traversal and colonization. This phenomenon is attributed to the cell size of *Methanothermococcus thermolithotrophicus*, which typically ranges from 1 to 2 μm, suggesting that only pores exceeding this threshold are available to the proliferation of this particular microorganism. The impact of surface area on microbial activity was examined, with the effects of other influencing factors, including pore volume and gas-liquid interfacial area, being normalized. Correlations with the surface areas of accessible pores, determined through MICP, NMR, and SEM techniques, were revealed by the normalized values. Moreover, this study has established an empirical correlation to estimate the H_2 conversion rates within porous media by considering various pore characteristics, including pore volume, gas-liquid interfacial area, and specific surface area.

Chapter 4 *was published* as Khajooie, S., Gaus, G., Seemann, T., Ahrens, B., Tian, H., & Littke, R. (2025). Exploring effective diffusion coefficients in water-saturated reservoir rocks via pressure decay technique: Implications for Underground Hydrogen Storage. *Transport in Porous Media,152 (2), 12.*

This paper investigates the diffusion coefficients of various gases in both water and water-saturated reservoir analogues using the pressure decay technique. The study is driven by the existing knowledge gap in experimental effective diffusivities for H_2, CH_4, and CO_2 within water-saturated reservoir rocks. Additionally, it aims to assess the accuracy of the pressure decay method for measuring the diffusion coefficients of low-solubility gases such as H_2. To provide additional data for evaluating the accuracy of the employed technique, the diffusion coefficients of He and Ar in water were also measured and compared with

literature values. The observed gas diffusivities in water for H_2, He, and CH_4 are consistent with published values determined by gas concentration measurements. Furthermore, the measured effective diffusivities exhibit correlations with various pore characteristics, including porosity, permeability, and mean pore diameter. It has also been demonstrated that porous media serve as baffles or obstacles, impeding density-driven convection flow and making diffusive transport the dominant mechanism. Therefore, the diffusivities of CO_2 and Ar in water, which remain inconclusive due to the prevalence of convective transport, can be achieved by assessing the effective diffusivity within porous media characterized by known tortuosity values.

Chapter 5 discusses the outcomes of the preceding research, emphasizing the relationship between significant observations and providing conclusive insights. Additionally, suggestions for prospective future work are presented. The impact of pore volume and surface area on microbial activity within porous media is discussed. Additionally, the significance of the diffusion coefficient in gas-liquid mass transfer, which facilitates the supply of H_2 to microorganisms in the aqueous phase, is clarified. The potential for expansion of this research lies in the utilization of various microbial cultures derived from the formation water of potential H_2 reservoirs. A better understanding of the impact of native microorganisms and their natural cell abundance on H_2 conversion rates is provided by this investigation. Additionally, the effects of surface area can be more accurately investigated by conducting microbial activity tests on porous ceramics with similar porosity and dimensions but varying pore sizes. This allows for the isolation of the impact of pore volume and interfacial area, with the sole focus being on the effect of surface area. Furthermore, the impact of surface area and gas-liquid interfacial area can be more thoroughly investigated by visualizing microbial colonies within porous media using advanced imaging techniques such as micro-computed tomography (μCT), scanning electron microscopy (SEM), and optical microscopy. Moreover, the incorporation of pore characteristics into existing growth rate models, such as the Monod equation, is identified as a potential area for future research.

Chapter 2

2.Methanogenic conversion of hydrogen to methane in reservoir rocks: an experimental study of microbial activity in water-filled pore space

Keywords: Underground hydrogen storage, methanogenesis, microbial activity, pore volume, surface area

This chapter is a modified version of the publication: Khajooie, S., Gaus, G., Dohrmann, A. B., Krüger, M., & Littke, R. (2024). Methanogenic conversion of hydrogen to methane in reservoir rocks: An experimental study of microbial activity in water-filled pore space. International Journal of Hydrogen Energy, 50, 272-290. https://doi.org/10.1016/j.ijhydene.2023.07.065.

Abstract

Underground hydrogen storage can lead to the activation of methanogenic *Archaea*, demanding to quantify microbial activities within the pore space to evaluate potential hydrogen conversion rates. This study presents a method to determine microbial activities within various water-saturated reservoir rocks, inoculated media containing sand particles and rock fragments as well as bulk solution, by monitoring pressure and gas composition. Measured activities in water-saturated rock specimens with identical bulk volumes varied between 0.15 and 1.28 mM H_2/h correlating with pore volume. Additionally, the results reveal that activities within intact rocks are 8-10 times higher than in corresponding bulk solutions. This observation demonstrates that the surface area available for microorganism colonization is another potential factor controlling microbial activity when the substance amount is held constant. This notion is supported by activities measured in inoculated media containing sand particles and rock fragments, as well as in rocks with similar pore volumes.

2.1. Introduction:

The shift from fossil fuels to renewable energy sources to decarbonize energy systems and reduce greenhouse gas emissions in line with environmental concerns regarding global warming has recently attracted significant attention. Underground hydrogen storage (UHS) is considered a viable option to solve one of the main problems of renewable energy, namely the mismatch between energy production and consumption due to seasonal atmospheric fluctuations (Heinemann et al., 2021; Muhammed et al., 2022; Zivar et al., 2021). The surplus renewable electricity could potentially be converted to hydrogen as an energy carrier via water electrolysis, and then stored in various geological formations including depleted oil and gas reservoirs, saline aquifers, and salt caverns and released back to the energy system at times of peak demand (Díaz-Abad et al., 2019; Osman et al., 2022; Tarkowski, 2019). In comparison to surface storage options, subsurface formations have the advantage of being capable of storing larger amounts of hydrogen. Nevertheless, a number of physiochemical properties of pure hydrogen including its low density, low viscosity, high diffusivity, and high reactivity with rock minerals and other fluids may pose risks to the efficiency of hydrogen storage in porous reservoirs which must be taken into consideration (Bo et al., 2021; Ebigbo et al., 2013; Thiyagarajan et al., 2022).

Hydrogen-loss during injection, storage and withdrawal stages may substantially affect the feasibility of hydrogen storage in porous geological formations and must be evaluated and quantified. It may occur due to processes such as molecular diffusion, viscous fingering, and capillary trapping (Hagemann et al., 2015; Hemme & van Berk, 2018; Paterson, 1983). Another potential risk of hydrogen-loss in subsurface formations arises from geochemical reactions of dissolved and gaseous hydrogen with minerals and in-situ fluids (Bo et al., 2021; Reitenbach et al., 2015). Additionally, hydrogen may be lost due to biotic reactions (Dohrmann & Krüger, 2023; Dopffel et al., 2021).

The presence of hydrogen in porous media can trigger microbial metabolism, since hydrogen is an effective electron donor, that provides the required energy for several biotic processes in subsurface formations including iron (III) reduction, sulfate reduction, methanogenesis (Muhammed et al., 2022; Thaysen et al., 2021) or acetogenesis (Dopffel et al., 2021; Gregory et al., 2019). The primary effect of biotic reactions on subsurface hydrogen storage is permanent hydrogen-loss caused by hydrogen oxidation in conjunction with sulfate or carbon dioxide reduction to generate hydrogen sulfide, methane or acetate (Gregory et al., 2019; Hagemann, 2017; Panfilov, 2016). An investigation of microbial activity in several hydrogen-rich town gas storages has demonstrated that at some facilities no evidence of detectable hydrogen consumption was apparent (Beynes, France), while at others a reduction of hydrogen from 54 vol.% to 37 vol.%, coupled with a decrease of carbon dioxide and increase of methane, was observed during a seven month testing phase (Lobodice, the Czech Republic) (Liebscher et al., 2016; Šmigáň et al., 1990; Strobel et al., 2020). In addition, it was determined that methanogenic *Archaea* with concentrations of 10^3-10^4 cells/mL were present in the Lobodice town gas storage, facilitating the loss of hydrogen and generation of methane (Šmigáň et al., 1990). Methanogenesis has also been observed in some natural gas storage sites following the artificial addition of hydrogen and carbon dioxide such as the Underground Sun Storage (USS) and Underground Sun Conversion (USC) projects in Austria and the HyChico project in Argentina. It was reported that in the USS project about 3% of hydrogen was lost and converted to methane during storage and withdrawal periods (four and three months, respectively) (Hagemann, 2017; RAG Austria AG, 2020, 2021; Reitenbach et al., 2015).

Several studies investigating microbial hydrogen consuming processes likely to happen during UHS were conducted to determine hydrogen consumption under various hydrogen and substrate concentrations, temperatures and availabilities of organic material. Hydrogen

consumption rates of iron (III) reducers, sulfate reducers, methanogens and homoacetogens were reported to be 0.0005-0.22, 0.0005-13, 0.0008-0.58 and 0.02-0.5 mM/h, respectively (Kashefi & Lovley Derek, 2000; Krumholz Lee et al., 1999; Robinson & Tiedje, 1984). In the context of the USS project, an experimental study was conducted on sandstone cores extracted from a biogenic natural gas reservoir known as the Haller series. These rock samples were carefully inoculated with fresh formation water obtained from the Lehen-002 reservoir to ensure the preservation of the original microbial communities. The experiments were carried out under a pressure of 4.5 MPa and a temperature of 45 °C. Gas mixtures consisting of 4-10% hydrogen and 0.3-2.5% carbon dioxide in methane were introduced into the system. The objective of the study was to investigate the activities of hydrogen-consuming microorganisms present in the formation water which was achieved by closely monitoring changes in the concentrations of hydrogen, carbon dioxide, and methane, while conducting hydrochemical and molecular biological analyses. The results revealed the presence and activity of methanogenic and sulfate-reducing microorganisms (RAG Austria AG, 2020). Additionally, another series of experiments was conducted using the same rock samples, along with sintered ceramic discs and Grey Berea sandstone, as part of the UCS project. These follow-up investigations aimed to evaluate the hydrogen conversion potential of methanogenic *Archaea* within the native microbial communities of the reservoir brine. These subsequent experiments were performed under a pressure of 4.0 MPa and a temperature of 40 °C. Gas mixtures containing 10-40% hydrogen and 2.5-10% carbon dioxide, with methane or helium as a make-up gas, were introduced into the system. The observed consumption of hydrogen and carbon dioxide, coupled with the generation of methane within the bioreactors, provided confirmation of the presence and activity of methanogens. Importantly, the overall consumption and generation patterns remained consistent throughout repetitive cycles, even when different gas mixtures were employed. These findings indicate the long-term sustainability of the geo-methanation process (RAG Austria AG, 2021). Furthermore, a few studies addressed the effect of grain size on cell population and respiration rates (Dang & Lovell Charles, 2015; Mendoza-Lera et al., 2017). A study performed on sediments from the North Sea revealed that the surface area of the sediments per volume significantly affected cell abundance, oxygen consumption, and denitrification rates (Ahmerkamp et al., 2020). It should be noted that the importance of surface area in enhancing microbial activity has been acknowledged by microbiologists since the 1930s (Stark et al., 1938; Waksman & Carey, 1935b; Zobell & Anderson, 1936).

In this study, we aimed to understand the impact of particle and rock properties, such as specific surface area and pore volume on hydrogen consumption rates during methanogenesis. The microbial activities were monitored by evaluating pressure profiles and gas compositions. We conducted experiments on sand particles immersed in inoculated medium and intact rock specimens taken from outcrops of four sandstones and one carbonate formation saturated with the same medium.

2.2. Theoretical background:

2.2.1. Methanogenic reaction

Hydrogenotrophic prokaryotes are crucial to biotic processes in UHS, as they initiate and catalyze the reactions of hydrogen as an electron donor with the proper electron acceptors such as sulfate or carbon dioxide. Multiple hydrogenotrophic reactions are considered to be important in the presence of high concentrations of hydrogen in porous formations which are extensively discussed in the literature (Dopffel et al., 2021; Hagemann et al., 2014; Panfilov, 2016; Thaysen et al., 2021). The process investigated in this study is hydrogenotrophic methanogenesis. Here, hydrogen and carbon dioxide are metabolized by methanogenic *Archaea* to generate methane and water:

$$CO_2+4H_2 \rightarrow CH_4+2H_2O \quad (2.1)$$

According to experimental and field data, the optimum pressure and temperature for the activity of methanogens are 9.0 MPa and 30-40 ºC respectively (Heinemann et al., 2021; Panfilov, 2016). Nevertheless, it was observed that some species remain alive even at higher temperatures up to 122 °C (Lovley & Goodwin, 1988; Magot et al., 2000; Takai et al., 2008). The strain used in this study grows most efficiently at around 65 ºC (Huber et al., 1982).

2.2.2. Normalization of the pressure profiles with the head space volume

The pressure decay induced by methanogenic activity in sample chambers containing rock specimens or fluid samples is comparable only when headspace volumes are similar. In order to account for variations in headspace volumes, the pressure profiles need to be normalized to the corresponding headspace volumes. According to Boyle's law (equation (2.2)) an increase in volume will result in a decrease in pressure. This implies that adjusting the volume of a sample container to a reference volume will cause a corresponding change

in pressure based on their respective volumes. Over a specific time period, the pressure drops in both containers are similarly related as expressed in equation (2.3). For experiments performed in this study this means that within a given time interval, the measured pressure reduction in the sample container with larger headspace than the reference container would be lower than that in reference container under otherwise identical boundary conditions.

$$P_i V_i = P_{ref} V_{ref} \tag{2.2}$$

$$\frac{\Delta P_j V_j}{\Delta t_j} = \frac{\Delta P_{ref} V_{ref}}{\Delta t_{ref}} \tag{2.3}$$

where, P_j, V_j and P_{ref}, V_{ref} are pressures [bar] and volumes [cm^3] in sample and reference containers, respectively and Δt_i and Δt_{ref} representing the time intervals [h] between a pressure recording step at headspace volume V_j and V_{ref}, respectively

As an alternative approach, the effect of variable headspace can be explained by considering a given pressure drop in both containers and adjusting the required time intervals accordingly. When the headspace volume in the sample container is larger than that of the reference container, a longer time will be required for a particular pressure reduction. Consequently, the correction of the time interval for a given pressure drop can be used to account for variable headspace volumes as follow:

$$\frac{V_j}{\Delta t_j} = \frac{V_{ref}}{\Delta t_{ref}} \tag{2.4}$$

$$\Delta t_{ref} = \frac{V_j \Delta t_j}{V_{ref}} \tag{2.5}$$

The headspace volume of any container can be considered as reference volume, and the time intervals between pressure steps in all other containers will then have to be corrected accordingly.

2.2.3. Calculation of gas composition based on pressure data

The pressure profile during the methanogenic reaction can be converted to fractional values of hydrogen, carbon dioxide, methane and water vapor by combination of Dalton's and ideal gas laws. The total pressure (P_{tot}) of a gas mixture is equivalent to the summation of the partial pressures (P_x) of constituent gases as stated by Dalton's law (Ross, 2012), which in this case it is written as:

$$P_{tot} = P_{H_2} + P_{CO_2} + P_{CH_4} + P_{H_2O} \quad (2.6)$$

Since the temperature is constant during the process, it is assumed that the partial pressure of water remains constant and can thus be calculated using the Antoine equation (Antoine, 1891):

$$\log_{10}(P_{H2O}) = A - (B / (T + C)) \quad (2.7)$$

Here, P_{H2O} is the water vapor pressure or partial pressure [bar] and T is the temperature [K]. A, B and C are the coefficients of Antoine equation equivalent to 4.6543, 1435.264 and -64.848 respectively, which were determined by Stull (1947) for the temperature range of 255.9 to 373 ºK. In the methanogenic reaction (equation (2.1)), one mole of CH_4 is generated for each mole of CO_2 consumed; thus, the reduction in partial pressure of CO_2 can be assumed to be compensated by the generation of CH_4 and its initial value remains unchanged. Consequently, P_{H_2} can be expressed as:

$$P_{H_2} = P_{tot} - P_{H_2O} - P_{CO_2/CH_4} = P_{tot} - P_{H_2O} - P_{CO_2,ini} \quad (2.8)$$

In this study, the initial fraction of H_2 and CO_2 are 80% and 20%, respectively, and $P_{CO_2,ini}$ is given by:

$$P_{CO_2,ini} = 0.2 * (P_{tot,ini} - P_{H_2O}) \quad (2.9)$$

As the exerted pressure by each component in a gas mixture is proportional to its number of moles or concentration, the partial pressure can be transformed to the gas concentration by rearranging the ideal gas law:

$$PV = nRT \rightarrow \frac{n}{V} = \frac{P}{RT} = C \quad (2.10)$$

where, P is the pressure [Pa], V the volume [m^3], n the number of moles [mole], T the temperature [K], R the universal gas constant [8.314 m^3·Pa/(K·mol)] and C the concentration [mol/m^3]. The concentration of water vapor and H_2 is calculated using their partial pressures whereas that of CO_2 corresponds to one quarter of H_2. As the stoichiometric number of CO_2 and CH_4 are equivalent in the methanogenic reaction, the CH_4 concentration will be equal to the reduction of CO_2. Finally, gas fractions can subsequently be obtained by normalizing each gas concentration to the total concentration and compared to data gathered by mass spectrometry.

2.3. Materials:

2.3.1. Samples

In this study, plugs taken from four sandstone formations with different pore characteristics, as well as a carbonate were investigated as analogues of tight to permeable hydrogen reservoirs. Cylindrical plugs (diameter ≈ 29 mm) were taken from outcrop blocks of the Lower Cretaceous Bentheim sandstone (Lower Saxony Basin, Germany), the Triassic Weser sandstone (Lower Solling Formation of the Reinhardswald Basin, Germany), the Upper Cretaceous Anröchter Grün limestone (Westphalian Cretaceous Bay, Germany), and the Lower Cretaceous Obernkirchen sandstone (Lower Saxony Basin, Germany). Bentheim, Grey and Red Weser and Obernkirchen sandstones consist mainly of quartz and feldspar (83.77-98.77 wt%), while the Anröchter Grün specimen consists of a mixture of quartz and feldspar (39.86 wt%) as well as calcite (38.35 wt%). Clay contents of these rocks ranged between 1.22 wt.% and 16.59 wt.% consisting of variable amounts of kaolinite, muscovite, smectite, chlorite and glauconite minerals. Additionally, apatite (4.91 wt.%) and hematite (0.1 wt.%) occur in the Anröchter Grün, as well as hematite (1.4 wt.%) in the Red Weser. Porosity and specific surface area values ranged between 8.0% to 22.7% and 0.2 to 4.8 m^2/g, respectively (Table 2.1).

Table 2.1. Summary of mineral composition (XRD measurement), porosity (He-pycnometry) and specific surface area (BET technique) for the sample used in this study. The specific surface area measurements were conducted on dried and crushed rock samples (250-600 µm).

Sample	Quartz-Feldspar	Clays	Calcite	Apatite	Hematite	Porosity	Specific surface area
	[wt.%]					[%]	[m^2g^{-1}]
Bentheim Sandstone	98.8	1.2	0.0	0.0	0.0	22.7	0.2
Red Weser Sandstone (RWS)	83.8	14.8	0.0	0.0	1.4	16.0	0.9
Grey Weser Sandstone (GWS)	88.9	11.1	0.0	0.0	0.0	8.0	1.3
Obernkirchen Sandstone (OBK)	91.8	8.2	0.0	0.0	0.0	18.5	0.7
Anröchter Grün	39.9	16.6	38.5	4.9	0.1	12.4	4.8

2.3.2. Microorganisms and Methanogenium medium

Methanothermococcus thermolithotrophicus (DSM 2095) was obtained from the German Collection of Microorganisms and Cell Cultures GmbH (Braunschweig, Germany) and was grown under anaerobic and pressurized conditions (80% H_2/ 20% CO_2) either on methanogenium medium 141 or a modified version of it (skinny 141) containing lesser amounts of yeast extract (0.2 g) and trypticase peptone (1 g) and no cysteine or Na_2S to

minimize sulfide precipitation. *M. thermolithotrophicus* is a hydrogenotrophic methanogenic Archaeon first described by Huber et al. (1982). *M. thermolithotrophicus* is anaerobic and forms highly motile cocci with a diameter of up to 1.5 µm occurring singly and in pairs. They stain Gram-negative and the cell envelope is composed predominately of protein in several subunits based on thin section analyses. This species grows over a wide range of temperatures between 30 and 70 ºC, with highest rates at approximately 65 ºC. At the optimal temperature, *M. thermolithotrophicus* is capable of doubling in 55 minutes indicating a rapid growth rate that makes it suitable for biochemical experiments under laboratory timescales besides its autotrophic characteristics. Additionally, its high pressure tolerance makes it an ideal candidate to study microbial rock interactions (Bernhardt et al., 1988a; 1988b).

2.4. Methods:

2.4.1. Mass spectrometry

The methanogenic reaction (equation (2.1)) was tracked in a closed system by monitoring the pressure profile with a pressure transducer and the gas composition with a mass spectrometer. Mass spectrometry (MS) has been employed in several research fields for decades as an effective analytical technique to determine the chemical composition and elucidate the molecular structure of an analyte (Van Bramer, 1998; Mowry et al., 2020; Siuzdak, 2016; Thomas, 2019). In this study, a Pfeiffer Vacuum Mass Spectrometer (GSD 350 Omnistar) equipped with PrismaPro as the gas analysis unit was employed. To reduce the possibility of ion-molecule collisions leading to ion reaction, neutralization, scattering or fragmentation during the mass analysis and ion detection, the mass spectrometer was equipped with a vacuum system to provide low pressure in the order of $\leq 10^{-9}$ mbar. Also, the electron energy of the MS was lowered to 65 eV to minimize molecule fragmentation during the ionization process (Bondue & Koper, 2020).

As output, the mass spectrometer generated a mass spectrum depicting the relative intensities or signals of the detected ions as ordinates and the atomic mass unit (Takai et al.) as abscises. The mass range of 1 to 50 amu (atomic mass unit) was utilized in this study since the heaviest component in the experiment was CO_2 (44 amu). The continuous acquisition of mass spectra was repeated during a preset time interval (5 seconds in this case), and then the peak intensities of determined components were collected and plotted as a signal versus time chart (Figure 2.1). The relative abundance or fraction of a specific

component in the gas sample could be derived through division of its total signal by the aggregate of all detected signals. To achieve this, the signal value for each component prior to measurement was used as a baseline and subtracted from the following signals.

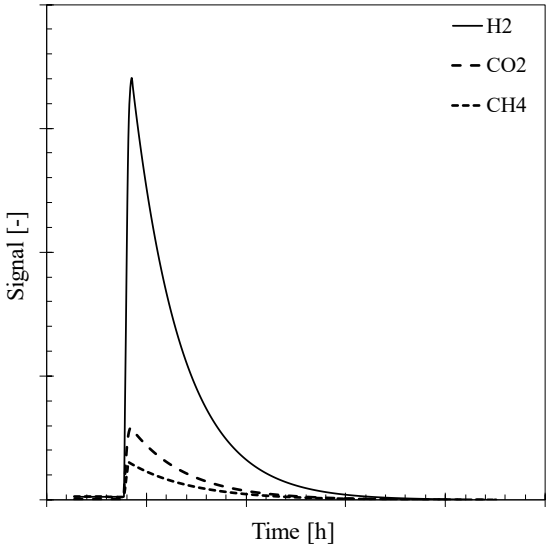

Figure 2.1. Schematic plot of extracted signals from mass spectra versus time for hydrogen, methane and carbon dioxide.

2.4.2. Pore volume measurement

Determination of the pore volume for dry cylindrical plugs under unconfined conditions were carried out using the He-pycnometry apparatus under isothermal conditions. In this method, the skeletal volume of a sample is measured through the expansion of helium from a reference container into a sample container with predetermined volumes (V_{ref} and V_{sc}). A description of apparatus and methodology has been previously provided in Gaus et al. (2019) in detail.

2.4.3. Specific surface area determination (BET technique)

Measurement of specific surface area was performed by running nitrogen physisorption experiments at 77 K in a liquid nitrogen bath on 1.5 to 2 g of dried and crushed bulk rock (T_{dry} = 105°C for 24h; particle size 250 to 600 µm). Isotherms were measured on a Gemini VII 2390t between 0.001 and 0.995 p/p^0 in ad- and desorption mode applying an equilibrium criterion of < 20 Pa/min. The saturation pressure was recorded separately for each pressure point. Specific surface areas were obtained by Brunauer-Emmett-Teller theory employing the Rouquerol criterion (Brunauer et al., 1938; Rouquerol et al., 2007).

2.4.4. Mineral composition (XRD measurement)

The mineral composition was analyzed using X-ray powder diffraction (XRD). A sample of particle size larger than 400 µm was crushed and mixed with Baikowski α-Al_2O_3 (0.2 g/g) as an internal standard. The mixture was ground (15 min) using ethanol as a coolant to avoid heat damage or dissolution of minerals. The powder was air-dried, homogenized, and prepared as a powder bed via the top-fill method. The XRD patterns were analyzed using a Bruker D8 with Cu Kα radiation (40 kV, 40 mA). The mineral components were identified and quantified using Rietveld refinement and the Profex software (Doebelin & Kleeberg, 2015). The mineral structures were identified based on their specific peak positions and symmetry. Additionally, custom-made clay models (Ufer et al., 2015; Ufer et al., 2008) were employed to quantify present clay minerals. A thorough explanation of the method can be found in Gaus et al. (2022).

2.4.5. Microbial activity measurements

Hydrogen-loss induced by methanogenesis was quantified in a setup consisting of 6 leak-tight glass bottles (Duran pressure bottles, 287.5 mL), each associated with a pressure transducer, a valve for connection to either a vacuum pump or gas bottle and a capillary connected to an automatic valve (Figure 2.2). A sampling loop was integrated into each automatic valve to collect gas samples periodically (every four hours) and then direct the samples to a mass spectrometer through a multi-positioning valve for subsequent gas analysis. The bottles and their caps were designed to endure pressures of up to 0.2 MPa and the self-sealing capability of the caps enabled injections of microorganisms with syringes without compromising their sealing integrity. Before running the experiments, a leak test with helium was performed in all bottles at a pressure of 0.2 MPa. All experiments were performed at 50°C with fresh overnight cultures grown in the skinny medium 141. Generally, cell densities were in the order of 10^8 cells/mL. The setup was used to evaluate the hydrogen-loss caused by *M. thermolithotrophicus* in solution (MTS) as well as MTS in porous media. It is worth noting that all pressure values measured and reported in this study are absolute.

First, an experiment was conducted to assess the validity of the gas compositions derived from pressure data (see Chapter 2.3). A bottle was first evacuated and then filled with 20 mL MTS. Then the bottle was pressurized by opening the corresponding valve to the gas

bottle (80% H_2/ 20% CO_2) up to 0.2 MPa and the pressure was subsequently measured. In addition, the changes in gas compositions were also monitored by mass spectrometer.

Afterwards, two repeatability tests were carried out on (1) three MTS samples and (2) three Bentheim rock specimens with different dimensions (bulk volumes: 20.43, 40.70 and 63.17 cm^3) saturated with MTS. For (1) a similar procedure to that described in the first test was employed to prepare three MTS samples with exactly the same boundary conditions. Next, pressure changes within the bottles were recorded in order to determine the microbial activity. For (2), three dry Bentheim specimens were installed in three bottles and, after evacuation of the bottles, 100 mL of the MTS was injected into the bottles, covering the entire rock specimens. Then the bottles were pressurized up to 0.2 MPa with gas mixture (80% H_2/ 20% CO_2) at room temperature to saturate the rock specimens. As the microbes are almost inactive at room temperature, their concentration presumably remained unchanged during saturation process. After 24 hours, excess MTS was withdrawn, all bottles were pressurized by opening the corresponding valves to the gas bottle (80% H_2/ 20% CO_2) up to 0.2 MPa and the pressures were subsequently monitored.

The effect of pore space on hydrogen consumption rate has been examined by running an experiment utilizing 6 bottles containing three rock specimens (Bentheim, Grey Weser, and Red Weser) as well as three MTS samples equivalent to the pore volumes of each rock specimen. The same procedure as mentioned above was employed to prepare the experimental setup and pressure changes inside the bottles were then recorded to monitor the activity of microorganisms within MTS as well as in MTS saturated porous media.

The effect of different rocks on microbial activity were examined in two additional experiments. The first attempt utilized five rock specimens of the same bulk volume derived from various rocks (see Table 2.1), while for the second experiment, the same rocks were employed with varying bulk volume but similar pore volume. During both tests, the rock specimens were placed in bottles (287.5 mL) and saturated with the MTS according to the above procedure. The bottles were then pressurized to 0.2 MPa and the gas pressure within the bottles was measured.

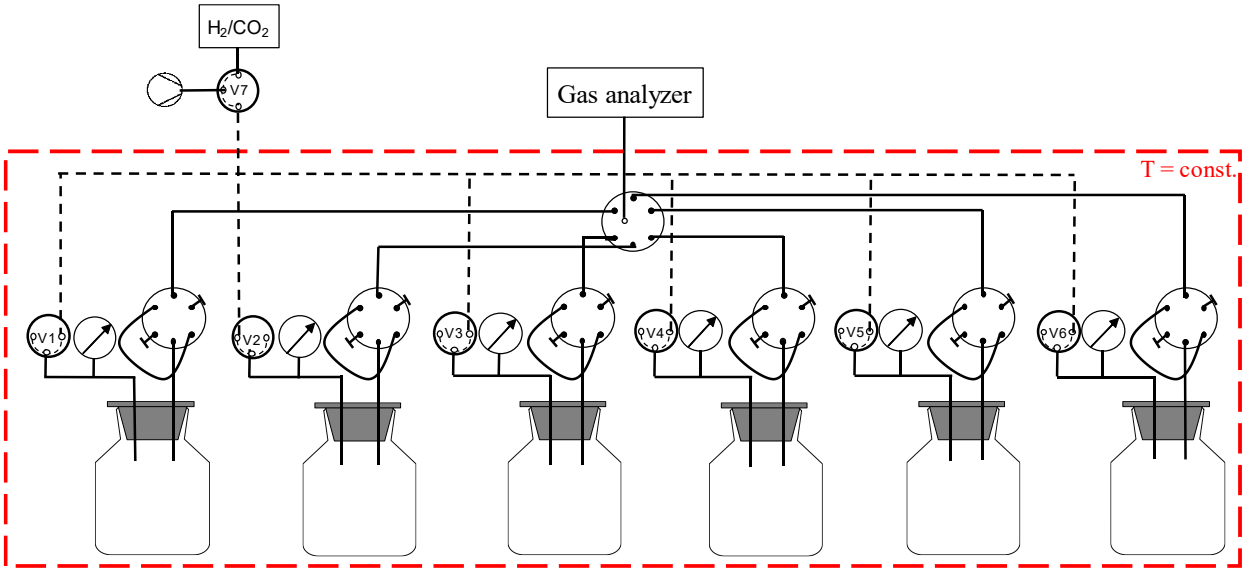

Figure 2.2. Sketch of the experimental setup used to quantify the hydrogen consumption by methanogens in pure MTS as bulk solution and within the MTS saturated porous media of rock specimens under unstressed conditions at 50 °C.

Prior to conducting experiments to investigate the effect of pore space in the setup described above, two preliminary tests were performed with a simpler setup to examine the influence of grain size on the rate of methane generation. Test one used serum bottles with approximately 287.5 mL volume (Figure 2.3). The bottles contained 10 g of differently sized particles of pulverized Bentheim sandstone of 0.25-0.5 mm, 0.5 - 1 mm, or 1 - 1.5 mm or zirconia beads of 1 millimeter size (#N038.1, Carl Roth GmbH, Karlsruhe, Germany). Triplicates were used and bottle without any particles served as references. 20 mL of medium 141 were injected into each bottle and subsequently inoculated with 6 mL of a fresh overnight culture of *M. thermolithotrophicus*. Additionally, one sterile control was prepared for each particle type. All particles were completely immersed in solution. All bottles were pressurized (80% H_2/ 20% CO_2) up to 0.2 MPa and incubated at 60°C. To determine the amount of methane generation during the experiment, 0.2 mL gas samples were taken using a syringe at the beginning of the experiment, after 2, 3, 4, 5, and 25 hours, and then analyzed using gas chromatography (Dohrmann & Krüger, 2023). As the amount of gas sample was negligible relative to the volume of the gas cap, sampling did not result in significant changes in gas pressure.

Test two used 50 mL infusion bottles (#13005, Zscheile & Klinger GmbH, Hamburg, Germany) which have a wider opening in order to put pieces of rock into them. Either semicircular rock pieces of 30 mm diameter and 15 mm height (each ~7.9 g) were placed in the bottles or 7.9 g of either zirconia beads of 1 mm size or 0.5 - 1 mm pulverized Bentheim sandstone. Triplicates were used and bottle without any particles served as

references. At the start of the experiment 4 mL of a fresh overnight culture of *M. thermolithotrophicus* grown in the skinny medium 141 were added. Bottles were pressurized (80% H_2/ 20% CO_2) up to 0.2 MPa and incubated at 60°C. Activity was measured manually as previously described.

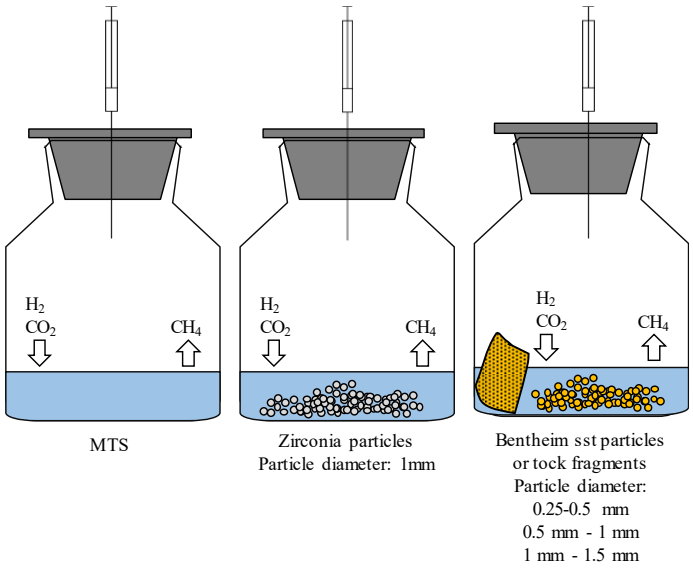

Figure 2.3. Scheme of the setup to quantify the generated methane by methanogens within bulk solution and bulk solution containing either zirconia particles with diameter of 1 mm or one type of Bentheim pulverized particles sized of i) between 0.25 and 0.5 mm, ii) between 0.5 and 1 mm or iii) between 1 and 1.5 mm.

2.5. Results

2.5.1. Comparison of gas composition from pressure profiles and mass spectrometry

Figure 2.4 exemplarily shows changes in pressure and gas composition in the head space of an assay containing medium inoculated with *M. thermolithotrophicus* (MTS) and a head space pressure of 0.2 MPa (80% H_2 / 20% CO_2) as a function of experimental time at 50°C (see Figure 2.2 for experimental setup). Evidently, after a characteristic threshold time (approximately 10 hours), the pressure declined at a nearly constant rate before reaching equilibrium at 0.05 MPa in accordance with the stoichiometry of equation (2.1) (Figure 2.4a). Pressures were translated to compositional fractions as described in Chapter 2.3 to compare with mass spectrometry measured composition (Fig 2.4b). Calculated gas fractions of H_2, CO_2 and CH_4 from pressures agree well with those measured by mass spectrometry. The accuracy was demonstrated by utilization of the correlation coefficient R^2 between compositional fractions for H_2 and CH_4 from pressure decay and mass

spectrometry (0.96 for H_2 and 0.95 for CH_4). Nevertheless, the initial fraction of CO_2, measuring less than 0.2, may be attributed to its dissolution into MTS, as CO_2 has a higher solubility compared to H_2. This discrepancy between the pressure converted and mass spectrometry fractions resulted in a relatively low R^2 value of 0.35 in their comparison. O_2 and N_2 fractions were monitored as well and were always <0.06. These measured fractions were considered as the baseline, representing the limit of quantification determined by MS and remained constant throughout the experiment. It means there was no measurable amount of O_2 and N_2 during the experiment. Pressure reduction (Figure 2.4a) is therefore solely attributable to methanogenesis (equation (2.1)). It should be noted that methane gas fractions when determined by mass spectrometry scattered within 0.8 – 0.95 as the reactants were fully consumed (Figure 2.4b, from approximately 125 h experimental time onwards). The reason for this is that as the pressure decreased, the amount of substance transferred from the sample loop to the mass spectrometer decreased and consequently the signal-to-noise ratio increased. This effect could have been minimized by using a larger sample loop, but this would have resulted in the pressure being reduced at each gas sampling step, thus falsifying the reaction rates. For this reason, the mass spectrometer was not used after verifying the determination of the gas composition by the pressure profile, and all reaction rates and concentrations shown in the following chapters are based on calculations from pressure profiles. Since rock specimens had different bulk volumes as compared to the corresponding pore filling media and bottles with the same volume (287.5 mL) were used for all experiments, the recorded pressures are given as gas cap-normalized pressures (equation (2.5)).

2.5.2. Data repeatability

A prerequisite for the study of microbial activities in different specimens was to ensure the repeatability of the experiments. Repeatability in this study meant that experiments with the same boundary conditions started at the same time yielded similar results. If the experiments were not started at the same time (e.g., successive experiments performed on the same sample and otherwise supposedly identical boundary conditions), repeatability could not be achieved. The reason is that in successive experiments smallest changes in microbial or nutrient concentration, pH, gas content, impurities, etc. can cause strongly different results.

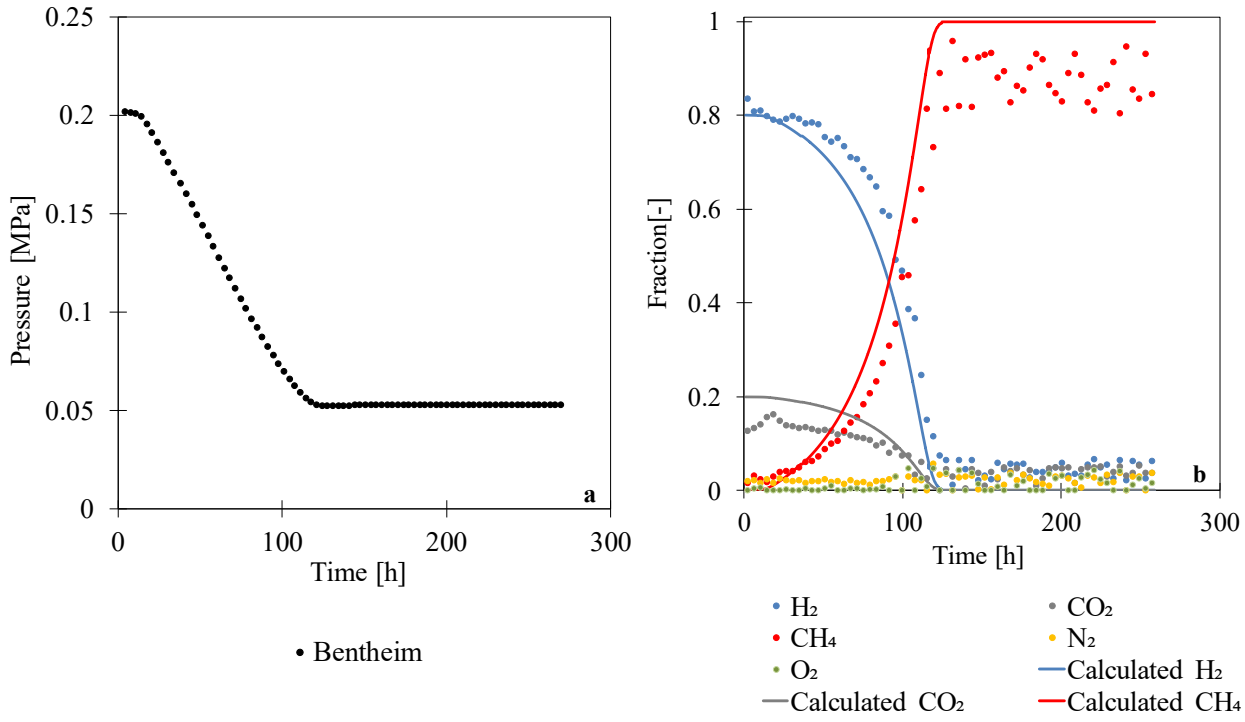

Figure 2.4. Results of head space pressure reduction (a), and head space gas compositional change (b) as a function of experimental time. The pressure profile in (a) was used to approximate H_2, CO_2 and CH_4 fractions (see Chapter 2.3) and compared to gas fractions measured directly by mass spectrometry as it is shown in (b).

Two repeatability experiments are exemplarily shown in Figure 2.5: (1) three independent activity measurements of 20 mL MTS, and (2) three independent measurements on Bentheim sandstone specimens of different bulk volumes that were saturated with the same MTS. Experiment 2 was, in addition to a repeatability measurement, also an experiment aimed at investigating whether normalization of the calculated rates to varying substance amount (different amount of MTS in pore volume due to different bulk volumes) under otherwise identical conditions also yields similar activities. Results for both experiments were expressed as gas cap normalized pressures (Figure 2.5a, b) or concentration profiles (Figure 2.5c, d). Gas cap normalized pressures and gas concentration profiles for the three MTS samples showed a similar time dependence. Pressure equilibration, indicating the complete consumption of hydrogen and carbon dioxide, was reached between 17 to 19 hours. Corresponding fluid volume normalized hydrogen consumption rates (Figure 2.5e) ranged between 0.13 and 0.14 H_2 mM/(h·cm^3) with a standard deviation of 0.006 H_2 mM/(h·cm^3). Gas cap normalized pressures for the three Bentheim specimens with different bulk volumes on the other hand showed strongly different equilibration times. These increased in accordance to decreasing substance amount with decreasing bulk volume from approximately 10 hours (Bentheim specimen with 63.17 cm³ bulk volume) to approximately 33 hours (20.43 cm³ bulk volume). Figure 2.5f depicts hydrogen and carbon

dioxide consumption as well as methane generation rates normalized to substance amount (equivalent to pore volume) from the same experiments. Pore volume normalized hydrogen consumption rates ranged between 0.39 and 0.45 H_2 mM/(h·cm^3) with a standard deviation of 0.025 H_2 mM/(h·cm³). The coefficients of variance were 4.3% and 6.1%, respectively, and were used in the following chapters as limits with which potential effects are interpreted. Details of these calculations along with specimen information including bulk volume (V_b), porosity (ϕ) and pore volume (V_p) were summarized in Table 2.2.

Table 2.2. Summary of the consumed concentration of H_2 and CH_4, their corresponding rates and equilibration time (T_{eq}) derived from the repeatability tests conducted on pure MTS or MTS saturated Bentheim samples. Sample information including bulk volume (V_b), porosity (ϕ) and pore volume (V_p) are as well presented. Mean and standard deviations for H_2 consumption rates were calculated for each test.

	V_b	V_p	ϕ	C_{H2}	C_{CH4}	T_{eq}	H_2 rate	CH_4 rate	Consumed Medium/Pore volume normalized H_2 rate	Consumed Normalized $\bar{H}_2$ rate	σ
	[cm^3]		[%]	Consumed /generated [mM]		[h]	Consumed /generated [mM/h]		[mM/(h·cm³)]	[mM/(h·cm³)]	
MTS_1	20.0	-	-	53.87	13.47	18.99	2.84	0.71	0.14	0.13	0.006
MTS_2	20.0	-	-	52.86	13.22	20.71	2.55	0.64	0.13		
MTS_3	20.0	-	-	52.49	13.12	19.48	2.69	0.67	0.13		
Bentheim	20.43	4.60	22.7	55.83	13.96	27.23	2.05	0.51	0.45	0.41	0.025
	40.70	9.20	22.7	57.80	14.45	15.89	3.64	0.91	0.40		
	63.17	14.30	22.7	56.96	14.24	10.20	5.59	1.40	0.39		

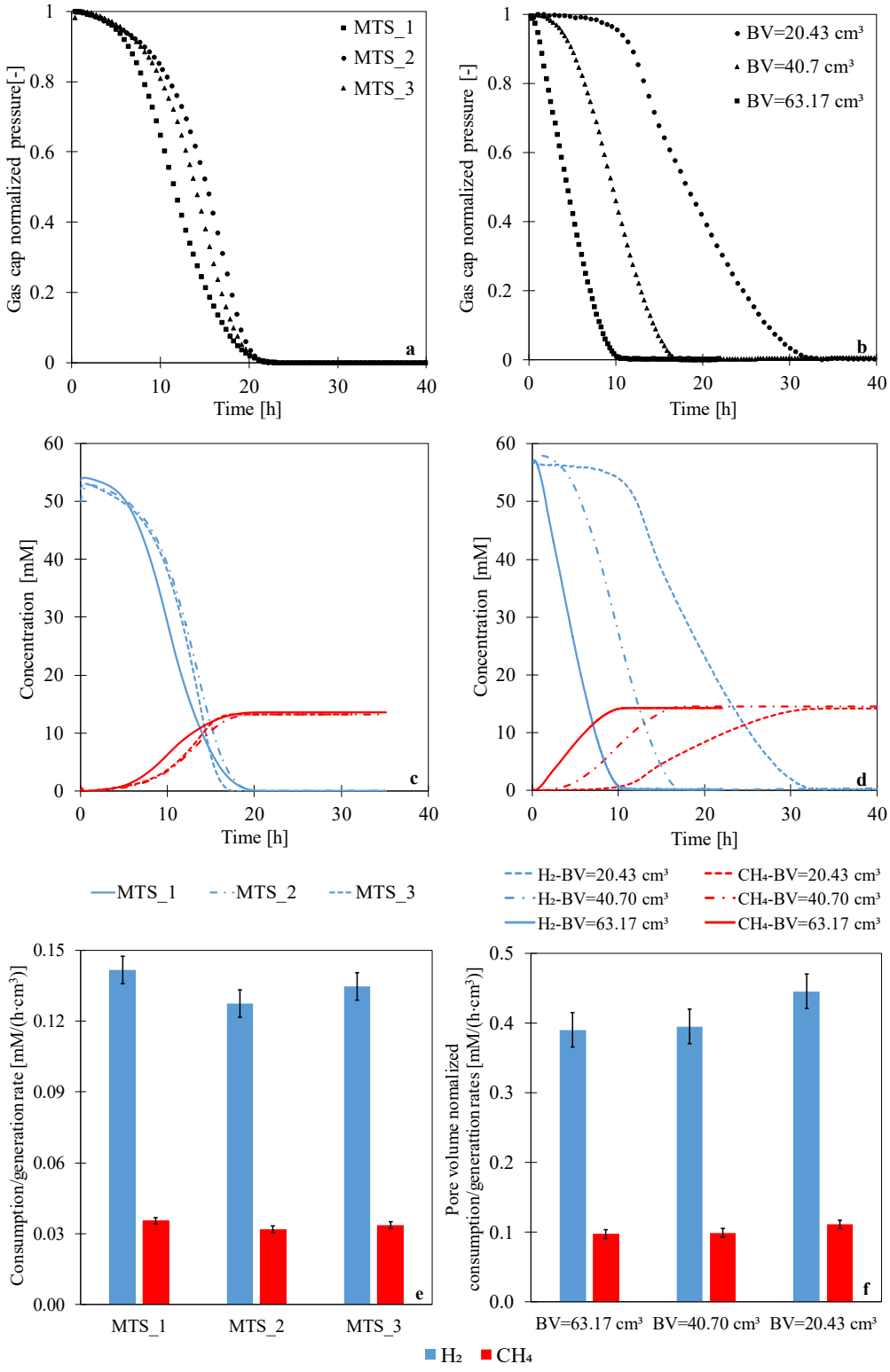

Figure 2.5. Results of gas cap normalized pressure reduction collected in three repeatability tests on MTS (a), and MTS saturated Bentheim samples (b) versus experimental time. Concentration profiles of H_2 and CH_4 were calculated from recorded pressure for MTS (c), and MTS saturated Bentheim samples (d). consumption/generation rates of H_2 and CH_4 for MTS (e) as well as pore volume normalized rates for MTS saturated Bentheim samples (f) were obtained from corresponding concentration profiles.

2.5.3. Particles and rock fragments introduced into solution

As described in Chapter 2.4.5, Bentheim sandstone particles with different particle sizes (0.25-0.5 mm, 0.5 – 1 mm and 1 – 1.5 mm), zirconia beads (1 mm diameter) and Bentheim sandstone fragments (30 mm diameter and 15 mm length) were introduced into MTS to investigate whether introduction of surface area causes a change in microbial activity. Microbial activity here was measured by monitoring of the CH_4 concentration in the head space. One experiment (Exp. 1, Table 2.3) focused on the comparison of different particle sizes and pure MTS (Figure 2.6a), whereas the other experiment (Exp. 2, Table 2.3) was designed to compare one particle size, rock fragments and pure MTS (Figure 2.6c). While activities within one experiment can be compared with each other, activities of the two successive experiments should not be compared because slightly different initial conditions might have prevailed. In general, activities between 0.11 and 0.97 CH_4 mM/h with the standard deviation of 0.004-0.07 CH_4 mM/h were measured in both experiments. Lowest activities were repeatedly measured in the MTS controls without particles. The experiment comparing different particle sizes (Figure 2.6a, b) further displayed an increase in activity in the order of pure MTS (0.11 CH_4 mM/h) < Zirconia beads < Bentheim 1-1.5 mm ≤ Bentheim 0.5-1 mm ≤ Bentheim < 0.5 mm (0.75 CH_4 mM/h). Activities in MTS with Bentheim particles were thereby larger by a factor of up to 3 and 7 when compared with activities of zirconia beads and pure MTS, respectively. Similarly, for the second experiment (Figure 2.6c, d) activities for Bentheim rock fragments and the Bentheim particle size fraction 0.5 – 1 mm were larger by a factor of ≈4 when compared to pure MTS. However, no significant differences were observed for activities of the rock fragments, zirconia beads and 0.5 – 1 mm Bentheim particle size fraction. A summary of these calculations as well as fluid volumes and masses of particles and rock fragments used in the experiments is shown in Table 2.3.

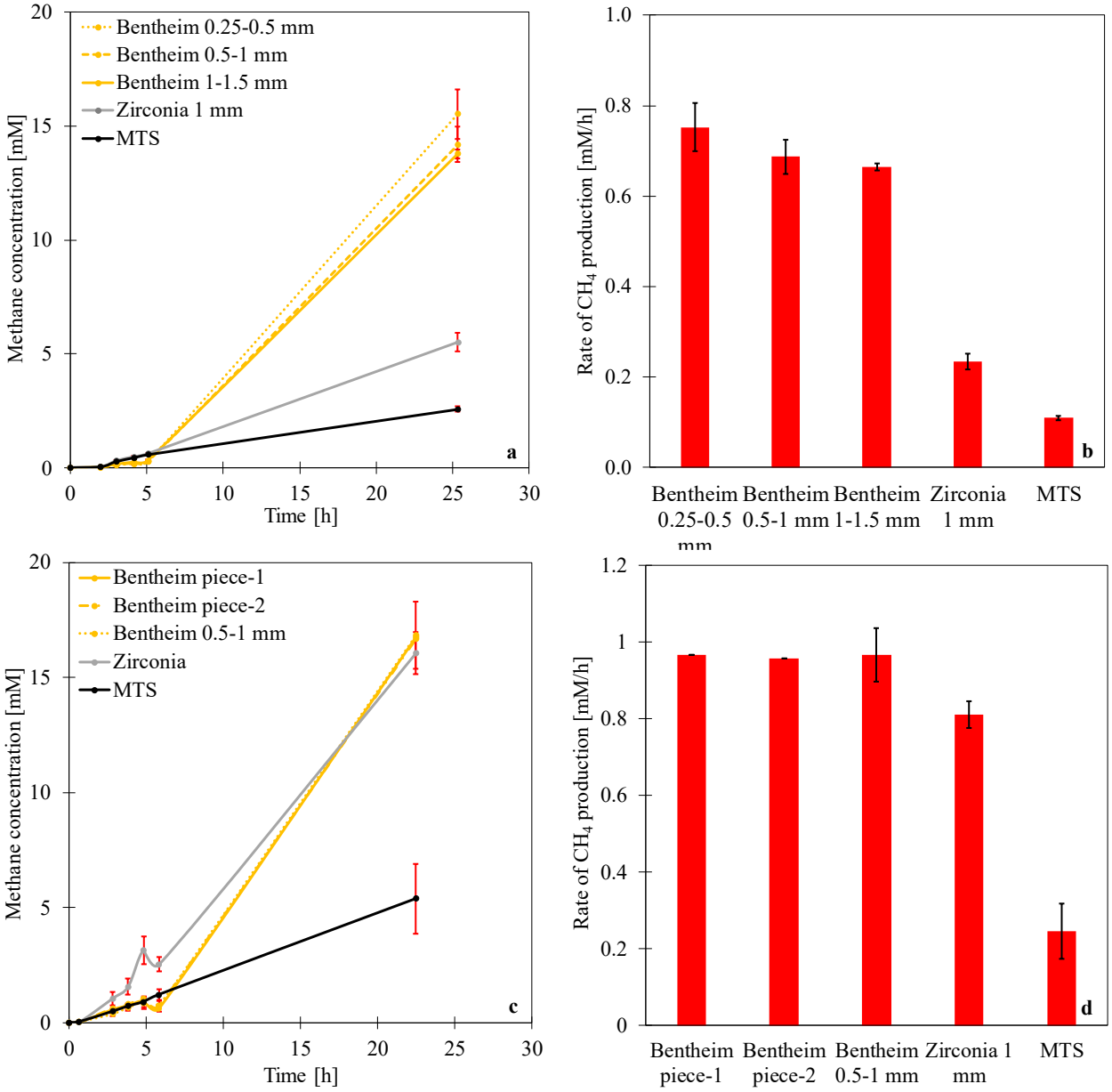

*Figure 2.6. Generated CH_4 concentration in the head space derived from microbial activity experiments performed on Bentheim particles with variable particle sizes (0.25-0.5 mm, 0.5 – 1 mm and 1 – 1.5 mm), zirconia beads (1 mm diameter) and Bentheim sandstone fragments (30 mm*15 mm) introduced into MTS as well as MTS without particles (a, c) versus experimental time. Rates of CH_4 generation (b, d) for all tests were obtained from the corresponding concentration profiles.*

*Table 2.3. Summary of methane amount and generation rate obtained from the activity experiments conducted on Bentheim specimens with variable particle sizes (0.25-0.5 mm, 0.5 – 1 mm and 1 – 1.5 mm), zirconia beads (1 mm diameter) and Bentheim sandstone fragments (30 mm*15 mm) introduced into MTS as well as MTS without particles. Standard deviations were determined using the data obtained from three measurements per sampling interval.*

Exp.	Sample	Volume of MTS	Mass of particles/rock fragments	Generated C_{CH4}	T_{eq}	$\overline{CH_4}$ rate	σ
		[mL]	[g]	[mM]	[h]	Generated [mM/h]	
1	Bentheim 0.25-0.5 mm	26	10	15.24	20.25	0.75	0.05
	Bentheim 0.5-1 mm	26		13.91	20.25	0.69	0.04
	Bentheim 1-1.5 mm	26		13.47	20.25	0.66	0.01
	Zirconia 1 mm	26		5.48	23.33	0.23	0.02
	MTS	26		2.5	23.33	0.11	0.00
2	Bentheim piece-1	4	7.9	16.13	16.67	0.97	-
	Bentheim 0.5-1 mm	4		16.12	16.67	0.97	0.07
	Bentheim piece-2	4		15.95	16.67	0.96	-
	Zirconia 1mm	4		13.53	16.67	0.81	0.04
	MTS	4	-	5.36	21.83	0.25	0.07

2.5.4. Microbial activities in intact rocks and bulk solutions

Microbial activities were commonly determined on inoculated media in bulk solution tests (Karadagli & Rittmann, 2005; Robinson & Tiedje, 1984; Smatlak et al., 1996). However, such activities might not represent those that will prevail in the pore space of saturated rocks. For this reason, activities for intact Bentheim, GWS, and RWS specimens saturated with MTS were compared to MTS as bulk solutions with the equivalent volumes of the respective rock pore volumes (Figure 2.7). In order to compare the data, pressures were normalized to the respective head spaces (Figure 2.7a). As in the previous chapters, pressures were also translated to hydrogen concentrations as a function of experimental time (Figure 2.7b). In total, hydrogen consumption rates ranged between 0.003 and 1.28 H_2 mM/h. Since bulk volumes of the intact rock specimens were similar and porosities were different (Table 2.4), MTS volumes were different for the respective three rock and bulk solution couples. Having the largest porosity, hydrogen consumption in the Bentheim rock specimen (≈ 23.7% porosity) was fastest (≈1.28 H_2 mM/h), followed by RWS (16.0% porosity, ≈ 0.82 H_2 mM/h) and GWS (8.0% porosity, 0.15 H_2 mM/h) specimens (Figure 2.7c). The same trend was observed for the equivalent volumes of MTS tested as bulk solutions. Clearly, the amount of MTS had a significant influence on consumption rates. However, when comparing the saturated rocks with the equivalent bulk solutions, it was evident that the conversion rates in the rocks were always higher than those in the equivalent bulk solutions. Complete hydrogen consumption occurred after 50, 72 and 343

hours for intact Bentheim, RWS and GWS specimens, respectively (Figure 2.7b). For comparison, complete hydrogen consumption for the Bentheim and RWS equivalent bulk solutions occurred after 347 and 677 hours. Note that hydrogen consumption for the GWS equivalent bulk solution could not be completed at laboratory timescales (≈5200 hours). Measured activities for Bentheim and RWS specimens were thus larger by a factor of 8 and 10 as compared to their corresponding bulk solutions.

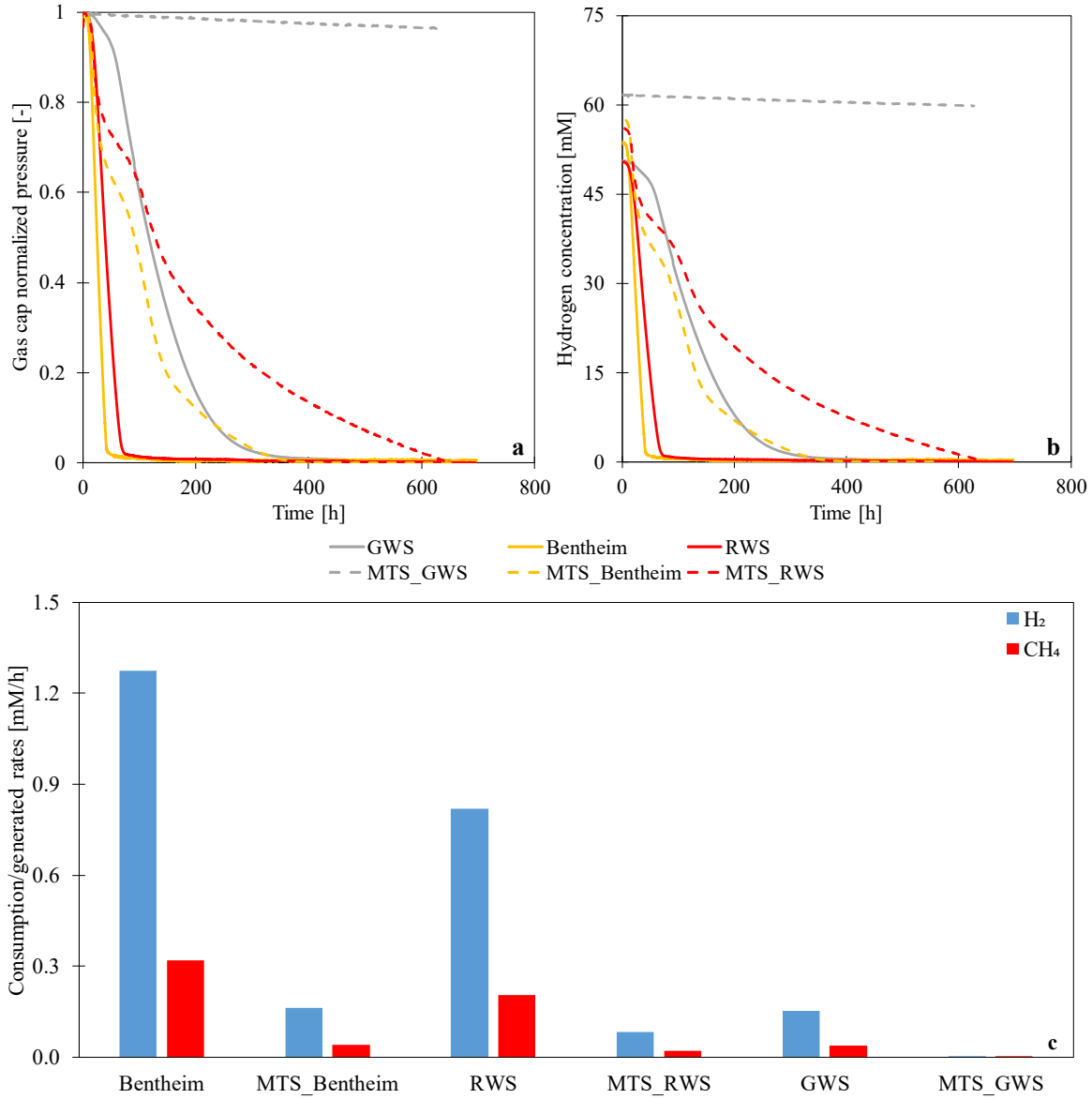

Figure 2.7. Gas cap normalized pressure as a function of experimental time collected during incubation of Bentheim, RWS, and GWS rock specimens saturated with MTS and samples of the same MTS as bulk solutions with the equivalent amounts of the corresponding rock pore volumes (a), Hydrogen concentrations profiles obtained from recorded pressure data (b), and H_2 consumption and CH_4 generation rates in each sample (c) were acquired from the corresponding concentration profiles.

Table 2.4. Summary of the consumed/generated concentrations of H_2 and CH_4, their corresponding rates, and equilibrium times derived from the microbial activity experiments carried out on three MTS saturated rock specimens (Bentheim, GWS, RWS) of similar bulk volume and pure MTS with equivalent amounts of their respective pore volumes along with sample information including bulk volume (V_b), porosity (ϕ) and pore volume (V_p) of samples.

Sample	V_b	V_p	ϕ	C_{H2}	C_{CH4}	T_{eq}	H_2 rate	C_{CH4} rate
	[cm^3]		[%]	Consumed/generated [mM]		[h]	Consumed/generated [mM/h]	
Bentheim	23.09	5.47	23.7	52.28	13.07	41.00	1.28	0.32
MTS_Bentheim		5.50		56.52	14.13	347.12	0.16	0.04
RWS	22.71	3.62	16.0	48.98	12.24	59.83	0.82	0.20
MTS_RWS		3.60		55.44	13.86	677.36	0.08	0.02
GWS	22.56	1.80	8.0	49.60	12.40	326.27	0.15	0.04
MTS_GWS		1.80		1.94	0.49	625.67	0.003	0.001

2.5.5. Comparison of activities in different reservoir analogues

In the previous chapter, results of activities for three different reservoir analogues (GWS, RWS, Bentheim) were displayed. Having the same bulk volume but different porosities a clear dependence of activity on MTS volume was apparent. In this chapter this experiment was repeated but extended with two further reservoir analogues (Obernkirchen sandstone and Anröchter Grün limestone). This chapter focused on the comparison of different reservoir analogues rather than the comparison of intact rocks with bulk solutions. Pure MTS as bulk solution was included as a blank. Additionally, another set of specimens from the same formations was prepared as such that bulk volumes were adjusted so that all specimens had approximately the same pore volume. The goal here was to investigate whether controlling parameters other than substance amount can be detected. Microbial activities were again displayed as gas cap normalized pressures and gas concentrations as a function of time for both experiments (Figure 2.8, 2.9).

Complete hydrogen consumption for the five rock specimens with constant bulk volume (V_b) occurred between 56 and 345 hours (Figure 2.8a, Table 2.5). Measured activities in the specimens derived from hydrogen concentration profiles (Figure 2.8c) varied between 1.22 and 0.17 H_2 mM/h and decreased in the order of Bentheim (23.7% porosity) > Anröchter Grün (12.4% porosity) > OBK (18.5% porosity) > RWS (16.0% porosity) > GWS (8.0% porosity). The activity of pure MTS (0.21 H_2 mM/h) was lower than for all specimens, except for the GWS specimen. Progressions of normalized gas cap pressures and hydrogen concentrations as a function of experimental time were shown for the constant pore volume (V_p) specimens in Figure 2.9a, b. Since the experiment did not continue until the hydrogen was depleted in all sample containers, the data were partially extrapolated (dashed lines in Figure 2.9a, b). Hydrogen consumption rates ranged from 0.2 to 1.2 H_2 mM/h and were completed in the order OBK < RWS < GWS < Bentheim <

Anröchter Grün (Table 2.5). Activity in the equivalent amount of pure MTS was completed after > 600 h (Figure 2.9a) which was significantly longer than measured for all specimens.

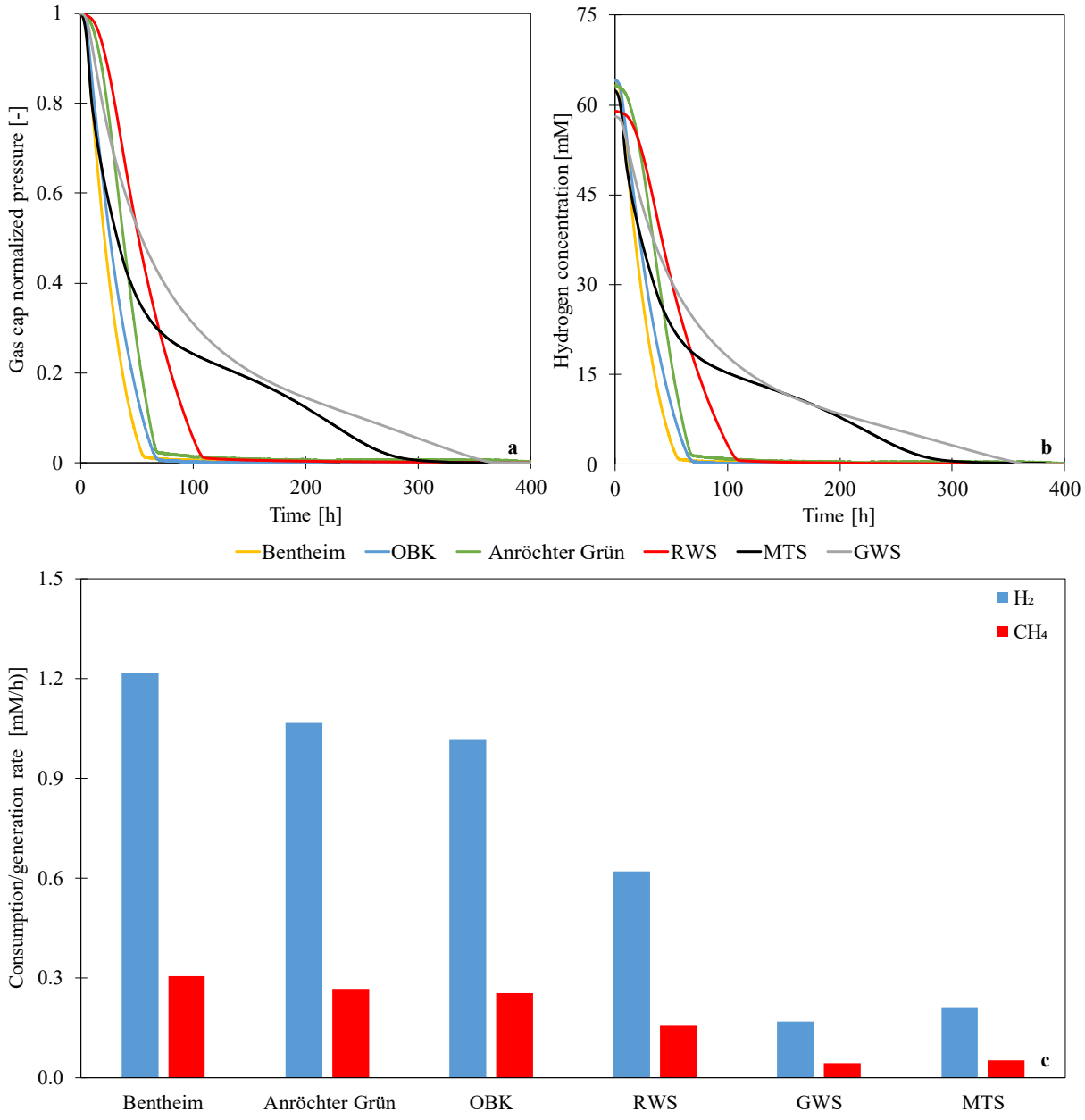

Figure 2.8. Gas cap normalized pressure profiles acquired during the incubation of MTS saturated rock specimens of Bentheim, GWS, RWS, OBK and Anröchter Grün of similar bulk volume as well as MTS as bulk solution with equivalent amount of Bentheim pore volume (BS) (a), hydrogen concentration profiles for each sample calculated from corresponding pressure data (b), and rates of H_2 consumption and CH_4 generation in each sample (c) obtained from the corresponding concentration profiles.

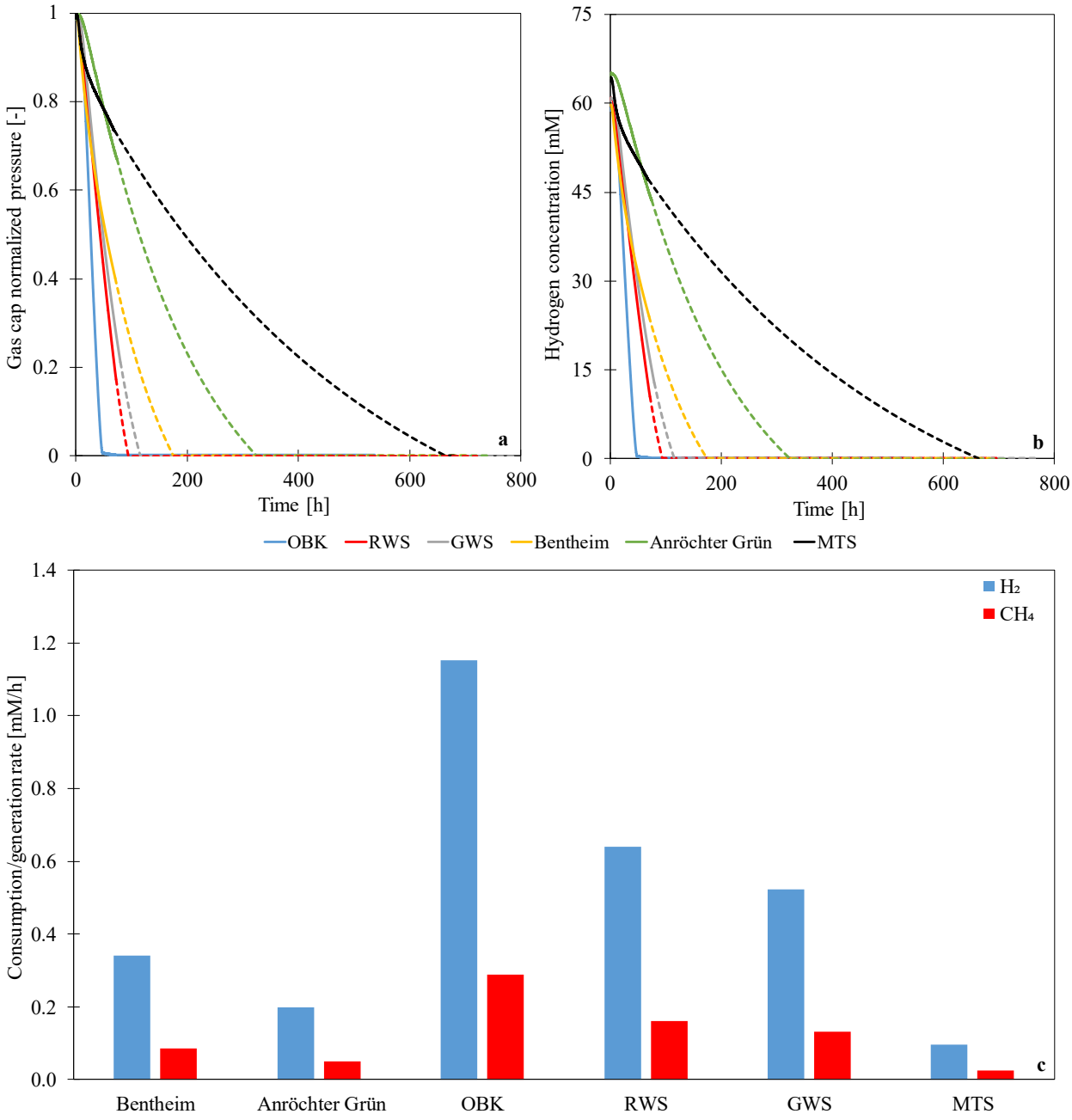

Figure 2.9. Gas cap normalized pressure versus experimental time derived from experiment carried out on MTS saturated rock specimens of Bentheim, GWS, RWS, OBK and Anröchter Grün of similar pore volume as well as pure MTS as bulk solution (BS) with equivalent amount of the rock specimens pore volume (a), hydrogen concentration profiles for each samples calculated from corresponding pressure data (b), and rates of H_2 consumption and CH_4 generation in each sample (c) obtained from the corresponding concentration profiles. The experiment was not continued until the hydrogen was consumed completely, thus the pressure and concentration profiles were partially extrapolated.

Table 2.5. Summary of the consumed/generated concentration of H_2 and CH_4 and their corresponding rates and equilibrium times derived from two microbial activity tests conducted on five rock specimens (Bentheim, GWS, RWS, OBK and Anröchter Grün) of similar bulk volume (1) and similar pore volume (2). Samples information including bulk volume (V_b), porosity (ϕ) and pore volume (V_p) of rock specimens used in each experiment are given as well.

Exp.	Sample	V_b	V_p	ϕ	C_{H2}	C_{CH4}	T_{eq}	H_2 rate	CH_4 rate
		[cm^3]		[%]	Consumed/generated [mM]		[h]	Consumed/generated [mM/h]	
Constant V_b	Bentheim	23.09	5.47	23.7	62.65	15.66	51.50	1.22	0.3
	Anröchter Grün	23.07	2.86	12.4	60.91	15.23	57.00	1.07	0.27
	OBK	23.00	4.25	18.5	63.12	15.78	62.00	1.02	0.25
	RWS	22.71	3.62	16.0	57.37	14.34	92.50	0.62	0.16
	GWS	22.56	1.80	8.0	57.51	14.38	339.00	0.17	0.04
	BS	6.00	-	-	61.04	15.26	291.00	0.21	0.05
Constant V_p	Bentheim	11.34	2.57	22.7	59.64	14.91	174.82	0.34	0.09
	Anröchter Grün	24.78	2.59	10.5	64.32	16.08	324.74	0.20	0.05
	OBK	16.44	2.60	15.8	58.56	14.64	50.80	1.15	0.29
	RWS	17.71	2.57	14.5	60.53	15.13	94.47	0.64	0.16
	GWS	42.33	2.61	6.2	60.42	15.10	115.57	0.52	0.13
	BS	2.6			63.66	15.91	663.46	0.10	0.02

2.6. Discussion

Prior research involving quantitative assessment of hydrogen loss induced by the activity of methanogens has primarily been carried out in bulk solutions (Robinson & Tiedje, 1984; Smatlak et al., 1996; Karadagli & Rittmann, 2005). The hydrogen consumption rates determined in this study from bulk solutions (0.004-0.21 mM/h) fall within the range of rates reported (0.0008-0.58 mM/h) in the literature ((Heinemann et al., 2021) and references therein). However, it is important to note that the previously reported rates were obtained under boundary conditions of 0.1-0.25 MPa and 30-40°C, whereas the experiments in this study were conducted under pressure and temperature ranges of 0.2 MPa and 50-60 °C. Additionally, the strain cultivated in this study (*M. thermolithotrophicus*) differs from the strains utilized in previous research.

Microbial activities in bulk solutions could be correlated with MTS amounts (Figure 2.10a). Notably, this correlation was also consistent across all sandstones studied (see Chapters 2.5.4 and 2.5.5) as shown in Figure 2.10a, b by plotting the rates of hydrogen consumption against pore volume (which is equivalent to MTS amount). The linear trends for hydrogen consumption rates in bulk solutions and also in sandstones emphasized the strong dependence of these rates on MTS amount. However, a linear correlation between the measured activities and substance amounts in sandstones was not expected. As mentioned in Chapter 2.3.2, the nominal size of *M. thermolithotrophicus* is approximately 1.5 µm, meaning that they require pore and pore throat sizes larger than this value to traverse and colonize the respective pores. Rocks typically have a wide range of pore sizes, thus the

abundance of microorganisms that are actively growing is closely related to the proportion of pore sizes that are large enough for cells to inhabit (Park & Santamarina, 2020; Phadnis & Santamarina, 2011). The occurrence of pores larger than 1.5 µm varies among rock specimens, leading to varying accessible pore volumes to the *Archaea* (Fitzner, 1988) which affects the quantity of substance that contribute to methanogenic reaction. Thus, considering the accessible pore volume instead of the total pore volume may result in a non-linear trend between hydrogen consumption rates and substance amounts. A similar series of experiments was conducted on rock specimens of lower Miocene "Haller" sandstones to investigate the activity of microorganisms within intact rock specimens (RAG Austria AG, 2020, 2021). While the activities of methanogens within the pore space were verified by monitoring changes in substrate concentration, a quantitative assessment of conversion rates is lacking. Therefore, the data could not be used for comparison with the results of this study. Furthermore, no experiments were carried out using pure MTS to gain insight into the effect of porous media on microbial activities.

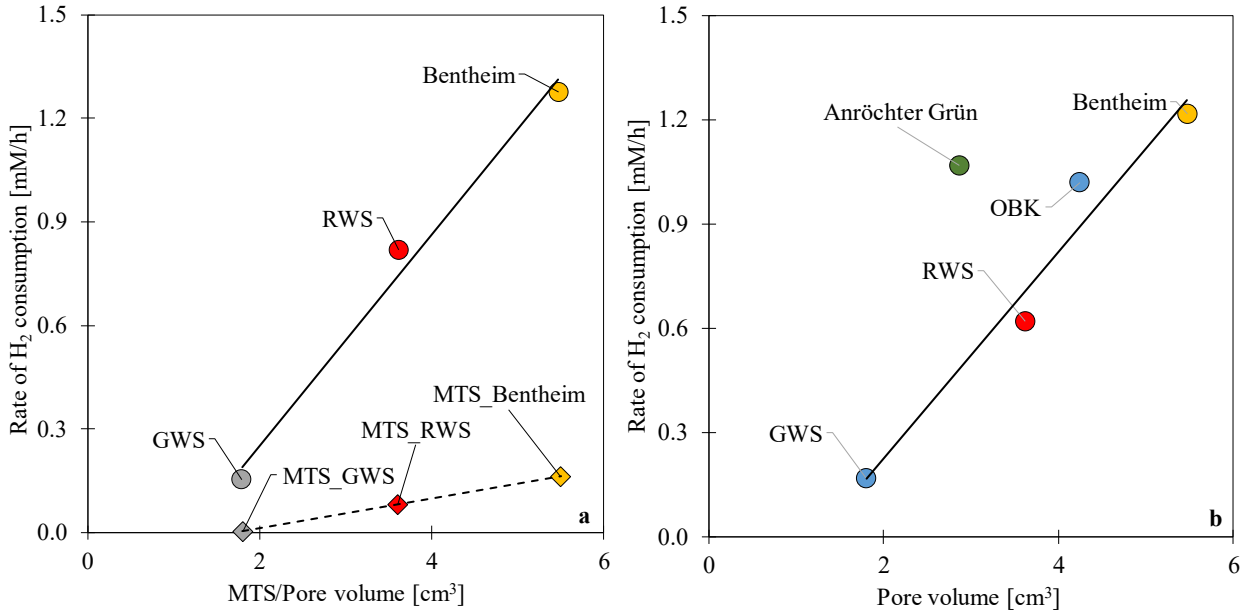

Figure 2.10. Relationship between hydrogen consumption rates and pore volume derived from microbial activity experiments performed on Bentheim, RWS, and GWS rock specimens saturated with MTS and samples of MTS as bulk solution with equivalent amounts of their corresponding pore volumes (a), and five rock specimens (Bentheim, RWS, GWS, OBK and Anröchter Grün) of similar bulk volume which were saturated with MTS (b).

Examination of sandstones data suggests that pore-filling volumes of MTS largely controlled hydrogen consumption. Nonetheless, when comparing hydrogen consumption rates in bulk solutions and intact rocks, it becomes evident that additional factors beyond volume of MTS also contributed to the increase in activity. The corresponding slopes for intact rock specimens and bulk solutions (Figure 2.10a) revealed that increasing volumes

of MTS in the pore space of intact rock specimens yielded larger increases in hydrogen consumption rates as compared to bulk solutions. As a result, the measured activities for the Bentheim and RWS specimens were larger by a factor of 8 and 10 as compared to their corresponding bulk solutions. It is crucial to emphasize that this disparity in activities between intact rocks and bulk solutions will be amplified if the accessibility of pores to microorganisms is taken into consideration. A potential explanation for this effect could be the strong tendency of microorganisms to adhere to particles or surfaces, thereby colonizing these environments (Mills, 2003). It is generally understood that surfaces promote microbial growth by providing a larger area for adsorbing nutrients, thus creating a more favorable environment for growth. As a result, cells are able to proliferate at higher concentrations of nutrients (Tuson & Weibel, 2013). Furthermore, Ahmerkamp et al. (2020) demonstrated that microbial cell population and consumption rates were linearly correlated with the surface area available for the colonization of microorganisms in sandy sediments. Therefore, the higher activities measured in MTS with the Bentheim particles and the zirconia beads compared to pure MTS without particles (same amount of MTS and same initial microbial concentration, see Chapter 2.5.3) could presumably be attributed to the role of surface area in stimulating bioactivity (Figure 2.6). As shown in Figure 2.11a, there appears to be a correlation between the methane generation rates in MTS containing the Bentheim particles and the specific surface area (i.e. the smaller the particle, the higher the activities). However, due to the inherent uncertainties in estimating specific surface area on rock particles and measuring methane generation rates, the validity of this correlation should be treated with caution. The specific surface areas of the Bentheim particles and the zirconia beads were determined geometrically using their average diameters. Then, the uncertainty values were computed by considering the range of diameters for the Bentheim particles, specifically the minimum and maximum diameters. Furthermore, the microbial activities in MTS with zirconia beads in Exp. 1&2 were lower than the activities measured in MTS containing the Bentheim particles, even when the particles were larger in size than the zirconia beads (Figure 2.11a). This could be related to the presence of pores within the Bentheim particles, which provided additional surface area for microbial colonization.

Once the influence of substance amounts has been eliminated by normalizing activities, the variations in measured activities among MTS saturated rock specimens could be attributed to the role of surface area. The surface area plays a role in promoting microbial activity, provided that the pores are accessible to microorganisms (Ahmerkamp et al., 2020).

Therefore, measuring bulk specific surface areas without considering the size of the pores, as is done in bulk BET measurements, may provide an approximation of the surface area available to microorganisms, particularly in rock specimens with a high proportion of large pores. In the absence of pore size distribution data, higher porosity can be reasonably inferred to indicate a greater abundance of larger pores, resulting in a larger fraction of pore volume available for microorganisms. The presence of clay minerals in the rock can further restrict inhabitable pore spaces and traversable pore throats, leading to a reduction in the surface area accessible to microorganisms. Consequently, clay content can be used as another rough criterion to compare the available surface areas of different rock specimens; the higher the clay content, the lower the available surface area. It is important to note that the specific surface area of rocks is not solely influenced by the clay content, but also by the other rock characteristics such as overall mineral composition, clay types, diagenesis, and burial history. These factors interact and work together to ultimately control and determine the specific surface area of a rock (Zhu et al., 2015). As a result, the higher normalized activity in the OBK rock specimen compared to Bentheim rock specimen collected from the study of microbial activities in five rock specimens with identical pore volumes, could be attributed to the effect of surface area on microbial activity (Figure 2.11b). Given the high porosities of Bentheim and OBK rock specimens (22.65%-23.7% and 15.82%-18.46%, respectively) and their relatively low clay contents (1.22% and 8.23%, respectively), it can be assumed that the BET surface area is likely a reliable approximation of the available surface area for *M. thermolithotrophicus*. On the contrary, the higher clay content found in RWS and GWS specimens (14.8% and 11.1%, respectively), is believed to have led to the observed increase in specific surface areas in these specimens. As most of the measured surface area is assumed to occur in micropores, the available surface areas for microorganisms in these specimens is limited. This leads to lower pore volume normalized hydrogen consumption rates for RWS and GWS, deviating from the trend observed between OBK and Bentheim rock specimens (Figure 2.11b, constant V_p-5 rock specimens). Furthermore, the higher porosity of the RWS specimen (14.5%) compared to the GWS specimen (6.2%) suggested that RWS may have a higher proportion of large pores and traversable pore throats making it more conducive to microbial colonization, and providing a greater available surface area for microorganism. This could explain the higher activity determined in the RWS specimen as compared to the GWS specimen. Furthermore, the results of constant V_b experiments reveal that the hydrogen consumption rates of OBK, RWS and GWS rock specimens, normalized by pore

volume (Figure 2.11b), are similar or even lower than those observed in Bentheim rock specimens, despite their surface areas being larger. This discrepancy can also be attributed to the presence of inaccessible pores or clays, which restrict the availability of surface area for microorganisms to colonize. The microbial activity observed in the Anröchter Grün sample was higher and did not conform to the linear regression obtained from the sandstones examined in this study (Figure 2.10b). Additionally, constant pore volume measurements suggested a much lower level of activity in the Anröchter Grün (Table 2.5). These results implied that the impact of this formation on the activity of *M. thermolithotrophicus* was not comparable to that of sandstones. This discrepancy may be attributed to its mineralogy (38.5% calcite, 4.9% apatite). However, as we currently have no evidence of the effect of these parameters, further investigations are necessary to fully understand the effect of this formation on the activity of *M. thermolithotrophicus*.

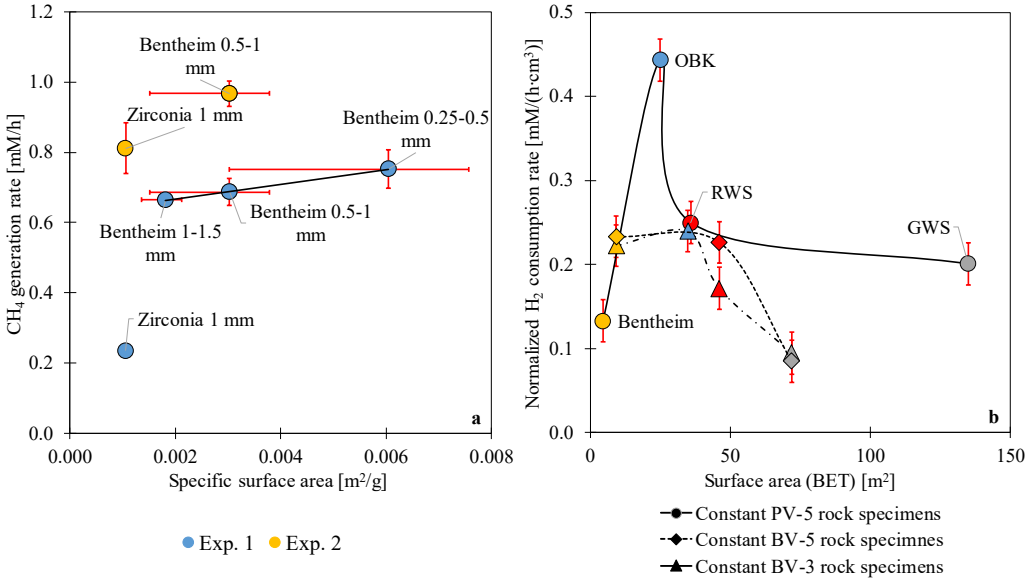

Figure 2.11. Correlation of CH_4 generation rates with specific surface area collected from microbial activity tests conducted on Bentheim specimens with variable particle sizes (0.25-0.5 mm, 0.5 – 1 mm and 1 – 1.5 mm) and zirconia beads (1 mm diameter) introduced into MTS (a), and relation of pore volume normalized H_2 consumption rates with surface area derived for microbial activity experiments performed on five MTS saturated rock specimens (constant V_b & V_p) as well as test to compare the microbial activities within three MTS saturated intact rocks with pure MTS as bulk solutions with the equivalent volumes of the respective rock pore volumes (b). In (b), each color represents a labeled formation with [yellow]: Bentheim, [blue]: Obernkirchen sandstone (OBK), [red]: Red Weser sandstone (RWS), [grey]: Grey Weser sandstone (GWS).

As depicted in Figure 2.11b, the results of tests conducted on rock samples with similar bulk volume did not conform to the trend observed in the experiment on samples with identical pore volume. The variations in measured activities for Bentheim, OBK, and RWS fell within the range of uncertainty. This apparent inconsistency in the results of tests on samples with identical bulk volume and pore volume may stem from the heterogeneity of the samples. The heterogeneity of the rock specimens may have resulted in a failure to fully

achieve a constant pore volume. The pore volume or the substance amount was much more significant than surface area, and small differences in pore volume could have a substantial impact on the correlation. Additionally, not all pores will have contributed to the microbial activity due to their size. Furthermore, the discrepancy in the results between these experiments could also be attributed to variations in the size of rock specimens and cell abundance of MTS as well as unknown effects of potential stress on the cells of *M. thermolithotrophicus* during the transfer process onto the rock specimens. The rock specimens' length in these two tests differed in order to achieve similar bulk volume and pore volume, which resulted in variations in circumference area. This area probably controlled the availability of substrate (H_2 and CO_2) concentration in the aqueous phase, which may influence the methanogenic reaction rate. Additionally, as the cell concentrations of MTS were not determined, this parameter represents an additional uncertainty that should be taken into consideration when comparing the results of different tests.

Previous numerical and modeling studies that aimed to quantitatively evaluate hydrogen loss during underground hydrogen storage (UHS) have largely relied on the growth kinetic of methanogens determined on bulk solutions as a proxy for methanogenic activity within porous media (Ebigbo et al., 2013; Hagemann, 2017; Jahanbani Veshareh et al., 2022). However, this experimental study has shown that the activities of methanogens determined in bulk solutions, may not accurately reflect the activities within intact rocks since not only pore volume but other pore characteristics influenced the microbial activities. As such, it is crucial to re-evaluate the current method of determining hydrogen loss in reservoirs, and conduct individual assessments of each potential reservoir to fully understand its unique characteristics. Additionally, it is important to acknowledge that microbial growth does not necessarily reflect microbial activity. Studies (Dohrmann & Krüger, 2023; Picard & Daniel, 2013) have revealed that microorganisms can carry out metabolism and consume hydrogen without showing any growth. This further emphasizes the need to determine the microbial activity independently from growth rates when assessing the extent of hydrogen loss during UHS in modeling studies.

2.7. Conclusions

The aim of this study was to examine the impact of pore space on methanogenic reactions during underground hydrogen storage. A series of experiments were conducted on five reservoir analogs from Bentheim, Obernkirchen, Anröchter Grün, Red and Grey Weser formations, with varying porosities between 8% and 24%. and microbial activity was tracked by monitoring pressure and gas compositions.

This study has found that the substance amount of MTS is the primary factor in controlling hydrogen loss caused by methanogens under consistent boundary conditions such as pressure, temperature, cell density, and gas volume. However, the comparison of measured activities in MTS containing sand particles and zirconia beads with pure MTS as bulk solutions as well as the varying trends observed in the measured activities of rock specimens and their corresponding bulk solutions, and the results of experiments conducted on rocks with similar pore volume suggested that other pore characteristics also played a role in the methanogenic reaction. The surface area of the pores has been found to have an impact on stimulating microbial activity when the substance amounts are held constant. However, it is important to note that the nominal size of *M. thermolithotrophicus* is approximately 1.5 μm, meaning that only the surface areas of pores larger than this value are available for the microorganisms to colonize and promote the microbial activity.

The measurement of the specific surface area of pores accessible to microorganisms, taking into account the distribution of pore sizes in future studies, is indispensable for in-depth investigation into the influence of surface area on microbial activity. Additionally, the examination of the physiochemical properties of water after microbial activity experiments, such as pH, can provide valuable insights into changes in the boundary conditions, which consequently affect growth and reaction rates. Furthermore, the experiments conducted on Anröchter Grün rock specimens reveal distinct behaviors in comparison to sandstone specimens, likely attributed to variations in mineralogy. To examine the role of carbonate minerals as a carbon source in methanogenic reactions, experiments with negligible or very low CO_2 concentrations can be conducted.

It is crucial to acknowledge that the current practice of determining hydrogen loss in reservoirs in modeling and numerical studies which is based on measured activity of methanogens in bulk solution, rather than within intact rocks, may need to be reevaluated. Furthermore, the variations in activity observed in different rocks are primarily but not

solely attributed to the quantity of substances, thus indicating that each reservoir should be evaluated separately.

Chapter 3

3.Methanogenic activity in water-saturated reservoir analogues for underground hydrogen storage: The role of surface area

Keywords: Specific surface area, microbial activity, underground hydrogen storage, pore size distributions

This chapter is a modified version of the publication: Khajooie, S., Gaus, G., Seemann, T., Klaver, J., Claes, H., Nehler, M., Ahrens, B., & Littke, R. (2024). Methanogenic Activity in Water-Saturated Reservoir Analogues for Underground Hydrogen Storage: The Role of Surface Area. International Journal of Hydrogen Energy, 90, 171-190. https://doi.org/10.1016/j.ijhydene.2024.09.395

Abstract

The activity of methanogenic *Archaea* in porous formations is influenced by various pore characteristics, including porosity, surface area, and the gas-liquid interfacial area. This study explores the impact of surface area on methanogenic activity using techniques such as MICP, NMR, SEM, and µCT. The cells of *Methanothermococcus thermolithotrophicus*, ranging from 1 to 2 µm, indicate that pores smaller than this threshold are not accessible for microbial traversal and colonization. Upon normalization of microbial activities based on pore volume and interfacial area, the findings exhibit strong correlations with specific surface areas of accessible pores in the examined rocks, as determined by MICP, NMR, and SEM. These areas ranged from 0.001 to 0.017 m^2/g, 0.003 to 0.024 m^2/g, and 0.012 to 0.02 m^2/g, respectively. The normalized activities increase from 0.19 to 0.44 $mM/(h \cdot cm^3 \cdot cm^2)$ with an increase in the specific surface area, varying by method. Furthermore, an empirical model has been established to quantitatively evaluate hydrogen loss during underground hydrogen storage or the efficiency of bio-methanation, incorporating pore volume, specific surface area, and interfacial area.

3.1. Introduction:

Underground hydrogen storage (UHS) has gained considerable attention as a promising solution to address the primary challenge in renewable energy: the imbalance between energy production and consumption caused by seasonal fluctuations. The envisaged approach involves converting surplus electricity gained from solar and/or wind power into hydrogen (H_2) by electrolysis (Halder et al., 2024) followed by subsurface storage in geological formations, such as salt caverns, depleted hydrocarbon reservoirs, or deep saline aquifers (Muhammed et al., 2022; Osman et al., 2022; Tarkowski, 2019; Zivar et al., 2021). Subsurface storage offers the essential capacity for large-scale hydrogen storage, facilitating grid stabilization and meeting the seasonal energy demand over prolonged periods (Liebscher et al., 2016). However, insights from storage projects involving hydrogen mixed with other gases (up to 60% H_2) in deep saline aquifers and depleted hydrocarbon reservoirs (Dopffel et al., 2021; Muhammed et al., 2022; Vítězová et al., 2023) have shown that the presence of hydrogen in geological formations can stimulate microbial activity (Pérez et al., 2016; RAG Austria AG, 2020, 2021; Šmigáň et al., 1990; Strobel et al., 2020; Vítězová et al., 2023). Microbial metabolism in the subsurface occurs through

several biotic processes, including iron (III) reduction, sulfate reduction, methanogenesis, and acetogenesis. (Dopffel et al., 2021; Gregory et al., 2019; Navaid et al., 2023; Thaysen et al., 2021). Such microbial processes give rise to various adverse effects such as H_2 loss, H_2 contamination with H_2S or CH_4, and generation of acidic byproducts. The produced H_2S and acetic acid (CH_3COOH) also raises concerns regarding health, safety and equipment corrosion during operation. These consequences influence the feasibility of UHS, underscoring the need for in-depth investigations to quantify the microbial reaction rates and their controlling parameters (Bade et al., 2024; Dopffel et al., 2021; Reitenbach et al., 2015).

Microbiologists have long acknowledged the influence of surface area in stimulating microbial growth (Mills, 2003; Zobell, 1947; Zobell, 1943). This is attributed to the availability of more surface area for nutrients to adsorb, creating a proliferative environment. Consequently, microorganisms exhibit a strong tendency to adhere to these surfaces or particles and colonize these environments, enabling them to flourish at higher concentrations of nutrients (Stark et al., 1938; Zobell & Anderson, 1936; Zobell, 1943). However, the role of surface area on the activity of hydrogen-consuming microorganisms within porous rocks or sediments remains an area of limited research. This gap exists because experimental studies aiming to quantify hydrogen consumption rates induced by biotic processes have predominantly been conducted in bulk solutions (Breznak et al., 1988; Ivanova et al., 2007; Smatlak et al., 1996).

In a recent study, Khajooie et al. (2024a) conducted a comprehensive series of experiments to investigate the influence of rock properties such as porosity and surface area on the activity of *Methanothermococcus thermolithotrophicus Archaea*. Microbial activity was quantified by measuring H_2 consumption rates throughout the experiments. The experiments involved utilizing *M. thermolithotrophicus* in solutions (MTS) containing sand particles, zirconia beads, or rock fragments, with a free-inoculated solution serving as a reference. Furthermore, a set of experiments was carried out on four sandstones and one carbonate rock with porosities ranging from 0.08 to 0.24, all saturated with MTS. For comparison, three MTS samples, each with an equivalent amount of respective pore volumes of three of these sandstones, were employed. The results demonstrate a substantial increase in microbial activity upon the introduction of sand particles of different sizes, zirconia beads, or rock fragments compared to MTS. Furthermore, a comparison of microbial activities in saturated rock specimens with their corresponding MTS samples

revealed a remarkable 8 to 10-fold increase in H_2 consumption rates. This observation was likely associated with the increased surface area available for microbial colonization provided by either the particles or the pore space of the rock specimens, although conclusive evidence was lacking. Considering that *M. thermolithotrophicus* typically measures between 1 and 2 µm in size (Huber et al., 1982; Whitman, 2015), only pores exceeding this threshold become accessible to this specific *Archaea.* Consequently, expecting a correlation between the measured microbial activities and the specific surface areas (SSA) determined via N_2 physisorption is unrealistic. This is attributed to the method's unsuitability for sandstones, as it can only assess length scales up to a maximum pore size of 0.36 µm (Bertier et al., 2016; Fu et al., 2017; Seemann et al., 2017). Moreover, the SSAs determined by N_2 physisorption are not representative for the actual internal SSA. Crushing the materials to particles ranging from 250 to 600 µm in size (Khajooie et al., 2024a), destroys the internal microstructure of the rocks under consideration, giving rise to the creation of artificial surface areas. As a result, the SSA values are dominated by the surfaces and roughness of individual grains rather than internal pore structure (Lowell et al., 2012).

The impact of surface area on bacterial growth has been extensively studied in various domains, including marine sediments, groundwater treatment, and biogas generation. Ahmerkamp et al. (2020) examined microbial colonization on North Sea sediments of different grain sizes (227 to 882 µm), revealing a correlation between cell abundance, oxygen consumption rates, and surface area available for colonization. Similarly, research on rapid sand filters for groundwater treatment demonstrated that mineral coating formed on grains surfaces significantly enhance microbial colonization and activity (Gülay et al., 2014). These coatings increase the internal porosity and the biologically available surface area of the filter material, creating more niches for microbial communities. A positive correlation was observed between the extent of mineral coating and the abundance and activity of nitrifying prokaryotes. Furthermore, the use of various carrier materials in biogas production through anaerobic digestion, such as polypropylene and glass rings, ceramsite, and biochar, emphasizes the crucial importance of surface area. These materials, with their larger SSA, significantly promote microbial growth and enhance methane production rates. (Burkhardt et al., 2015; Li et al., 2018; Porté et al., 2019; Yuan et al., 2012).

In this study, we extend prior research of Khajooie et al. (2024a) to enhance the understanding of the key factors influencing microbial activities in porous media.

Therefore, we employed several widely-used methods for characterizing porous media to determine porosity and SSA, including Mercury Injection Capillary Pressure (MICP), Nuclear Magnetic Resonance (NMR), Scanning Electron Microscopy (SEM), and X-ray micro-Computed Tomography (μCT). These methods complement each other by using diverse approaches to assess pore properties, thereby providing insights into SSA across different scales (Anovitz & Cole, 2015; Lai et al., 2018; Zhang et al., 2018). By means of these techniques, we aim to precisely assess SSAs for various pore sizes to evaluate their impacts on microbial activity within the rock specimens measured by Khajooie et al. (2024a).

3.2. Materials

3.2.1. Samples

This study focused on four sandstone formations, each characterized by distinct pore characteristics. These formations encompass the Lower Cretaceous Bentheim sandstone from the westernmost Lower Saxony Basin in Germany, the Triassic Gray and Red Weser (GWS & RWS) sandstone situated within the Lower Solling Formation (Buntsandstein) of the Reinhardswald Basin in Germany, and the Lower Cretaceous Obernkirchen (OBK) sandstone, also from the Lower Saxony Basin in Germany. These sandstones were investigated as analogues for hydrogen reservoirs ranging from tight to permeable. Detailed descriptions of these rock specimens have been provided in Khajooie et al. (2024a).

3.2.2. Microorganisms

Methanothermococcus thermolithotrophicus (DSM 2095) is a strain, cultured in an anaerobic, pressurized environment consisting of 80% H_2 and 20% CO_2. The cell morphology is slightly irregular but uniform in size, between 1 and 2 μm in diameter, typically found as solitary form or as pairs (Huber et al., 1982; Whitman, 2015). *M. thermolithotrophicus* proves conducive to biochemical experiments under laboratory timescales, owing to its exceptional growth rate. It doubles approximately every 55 minutes at optimal temperature of around 65 ºC. This particular strain was procured from the German Collection of Microorganisms and Cell Cultures GmbH in Braunschweig, Germany. A more comprehensive description of this microorganism can be accessed in Khajooie et al. (2024a).

3.3. Methodology:

3.3.1. Determination of Specific Surface Area

The subsequent subchapters briefly summarize the techniques and instruments employed in this study to determine SSA values. A comprehensive explanation of the theoretical background, including analyses and software used to derive SSAs from each method, is provided in Appendix A.

3.3.1.1 Mercury injection capillary pressure

A Micromeritics Autopore IV instruments was utilized to perform MICP analysis on vacuum-dried (105 °C) miniplugs (~25 mm length; ~15 mm diameter). This measurement comprised two phases: a low pressure phase (up to 0.2 MPa) followed by a high pressure phase (0.1 to 207 MPa) (Soete et al., 2022). Pore throat diameter distributions were derived by applying the Young-Laplace equation, ranging from 0.006 to 400 µm.

3.3.1.2 Nuclear magnetic resonance

The NMR transverse relaxation time of the studied rock specimens, each approximately 35 mm in length and around 14.5 mm in diameter was measured on an in-house constructed fixed-field (0.196 T; 8.33 MHz) Halbach-based rock core analyzer at the Sakellariou NMR lab of the KU Leuven. The calibration procedure involved employing an in-house correlation between pore volume and NMR amplitude. This correlation has been established based on NMR measurements conducted on known quantities of water and brine ($CuSO_4$), as well as various rock plugs. The NMR T_2 distributions were retrieved through the Carr-Purcell-Meiboom-Gill (CPMG) measurement method.

3.3.1.3 Scanning electron microscopy

Sub-samples of approximately 15 x 15 mm² were scanned by a Zeiss - Supra 55 field emission Scanning Electron Microscope. The SEM is equipped with SE detectors (Inlens or Everhart-Thornley = SE2), a Backscattered Electron (BSE) detector and Energy-Dispersive X-ray Spectroscopy (EDS) using Aztec software (Oxford Instruments). Large overviews were mapped with magnifications of 133-334x, pixel size corresponding to 852-2139 nm at an acceleration voltage of 15 kV using all three detectors simultaneously with a working distance of approximately 8 mm. Imaging was conducted at random locations (n > 10) with a magnification corresponding to 548.8 nm. Prior to the SEM imaging, samples

were impregnated with epoxy, cut, manually pre-polished using SiC paper and subsequently polished by low angle broad ion beam polishing for at least 3 hours using the TIC3X (Leica). The quality of the impregnated porous surface was sufficient to segment the macropores (> 2 µm) by systematic thresholding in *ImageJ* (Schneider et al., 2012).

It is noteworthy that the perimeter is a scale-dependent property, necessitating correction through the computation of surface area derived from multiscale images. However, as the images of the analyzed rock specimens possess identical resolutions, the values of SSA in relation to each other remain unaffected by this artifact.

3.3.1.4 X-ray micro-computed tomography

The three-dimensional datasets of the samples were captured using a ProCon X-ray system equipped with a multifocal X-ray tube operating up to 225 kV (for more details see Schepp et al. (2020)). Scanning resolution is dictated by the sample's positioning between the X-ray tube and detector, and consequently, by its size. To ensure precision, small cylindrical sample cores measuring 5 mm in diameter and 10 mm in length were drilled. Geometrical magnification in the µCT system is determined by the ratio of the source-detector distance to the source-object distance (Voland et al., 2010). All samples underwent scanning under uniform settings, resulting in voxel sizes of 4.036 µm. For each sandstone, five sub-volume datasets comprising 400 x 400 x 400 voxels were selected to ensure statistical robustness. Each sub-volume was tested to represent a representative elementary volume (REV) by calculating the porosity of multiple subdomains (Bachmat & Bear, 1987).

3.3.2. Pore volume measurement

The assessment of pore volume in unconfined dry and water-saturated cylindrical plugs was carried out using He-pycnometry and water immersion porosimetry, respectively. These methods have been extensively discussed in literature, offering detailed descriptions of the equipment and methodology employed (Gaus et al., 2019; Hu et al., 2021).

3.4. Results

3.4.1. Determination of surface area by mercury injection capillary pressure

MICP measurements were conducted on Bentheim, OBK, RWS, and GWS rock specimens to determine SSA corresponding to each pore size. The intrusion curves, depicting the normalized cumulative intrusion volumes relative to the dry sample weights versus

pressure, are illustrated in Figure 3.1a. Maximum cumulative intrusion values, indicative of SPVs, ranged from 0.031 to 0.113 cm³/g (Table 3.1).

Subsequently, PTD curves were derived from the mercury intrusion data for each rock specimen, as elaborated in Chapter A.2.1 (Figure 3.1b). The Bentheim rock specimen exhibited an average pore throat diameter of approximately 12.03 µm, two orders of magnitude larger than the mean pore throat diameter of OBK, RWS, and GWS rock specimens measuring 0.60, 0.31, and 0.11 µm, respectively. The SSA, equivalent to various pore sizes, was determined using equation (A.7) (Chapter A.2.1). Figure 3.1c illustrates the cumulative SSA plotted against pore throat diameter for each rock specimen, with maximum values varying from 0.04 to 1.07 m^2/g (Table 3.1).

As previously mentioned, the total normalized intrusion volume relative to the dry sample weight corresponds to the SPV, allowing to determine porosity, pore volume, and bulk density for the rock specimens using sample weight and bulk volume. An overview of these measurements along with the SSA values are provided in Table 3.1. The porosities, SPVs, and bulk densities obtained through MICP varied between 0.08 and 0.23, 0.041 and 0.113 cm³/g, and from 2.01 to 2.43 g/cm³, respectively.

Table 3.1. Summary of sample mass (m), pore volume (PV), porosity (Φ), specific surface area (SSA), specific pore volume (SPV) and bulk density (ρ_{bulk}) values determined from MICP measurements for Bentheim, OBK, RWS, and GWS rock specimens. Pore volume is determined as the total intrusion volume multiplied by the dry sample weight whereas bulk volume is obtained from subtracting the volume of mercury injected to fill the assembly (stem and penetrometer) containing the rock sample from the volume of the entire assembly.

Sample	*m*	*PV*	*BV*	*Φ*	*SSA*	*SPV*	ρ_{bulk}
	[g]	[cm^3]		[%]	[m^2/g]	[cm^3/g]	[g/cm^3]
Bentheim	5.94	0.67	2.95	22.9	0.04	0.113	2.01
OBK	6.92	0.50	3.14	15.8	0.48	0.072	2.20
RWS	7.81	0.54	3.50	15.5	0.90	0.069	2.23
GWS	7.68	0.24	3.18	7.60	1.07	0.031	2.41

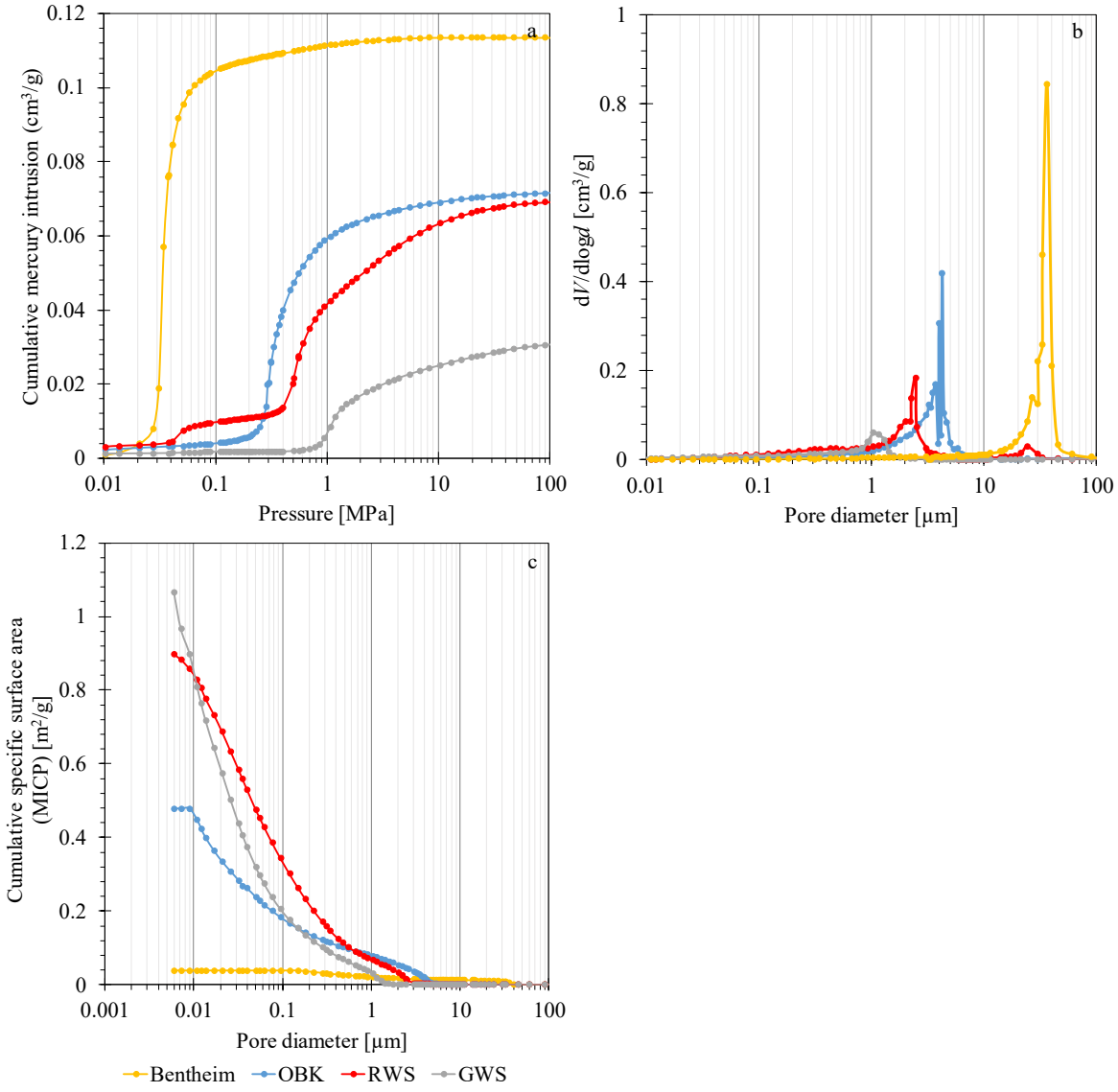

Figure 3.1. Cumulative mercury intrusion curve of Bentheim, OBK, RWS and GWS rock specimens plotted against applied pressure (a), along with the PTD derived from MICP data (b), and cumulative SSA versus pore diameter obtained from mercury intrusion data (c).

3.4.2. Determination of surface area by nuclear magnetic resonance

NMR T_2 measurements were performed on the examined rock specimens fully saturated with deionized water (Figure 3.2a). The Bentheim and RWS rock specimens display trimodal distributions, with peaks occurring at approximately 11, 56, and 631 ms for Bentheim, and 10, 63, and 178 ms for RWS, respectively. Conversely, the OBK and GWS specimens exhibit left-skewed bimodal and right-skewed trimodal distributions, respectively, revealing distinct tails or minor peaks associated with smaller or larger pores. Specifically, OBK's T_2 distribution is characterized by a dominant peak at around 89 ms, showing negative skewness with its left tail spanning from 6.3 to 25.1 ms. This portion of

pores reveals a second minor population, constituting around 20% of the total pore volume. Similarly, the GWS T_2 distribution demonstrates two prominent peaks at around 2.5 and 22 ms, including a weak right tail due to the presence of a few large pores, contributing to less than 5% of the total pore volume. These T_2 distributions can be transformed into PSD using a linear correlation between time and pore size as expressed in equation (A.9) (Figure 3.2b). This relationship relies on the surface relaxivity coefficient, which has been determined for the examined rock specimens as discussed in Chapter A.2.2. Specifically, for Bentheim, OBK, RWS, and GWS, these values are 14.28, 8.09, 13.49, and 8.96 µm/s, respectively. The observed values fall within the range of sandstones typical surface relaxivities (1.89-160 µm/s) documented in the literature (Keating & Knight, 2012; Kimura et al., 2021; Lucas-Oliveira et al., 2020). The direct proportionality between relaxation time and pore radius implies that longer T_2 times correspond to larger pores. Consequently, the patterns observed in PSD closely resemble those in the T_2 distribution, as clearly demonstrated in Figure 3.2a, b. Subsequently, the SSAs for various pore sizes were determined using NMR T_2 relaxation time data, employing a procedure similar to that applied to MICP data. The cumulative SSAs, plotted against pore diameter for the examined rock specimens (Figure 3.2c), exhibit maximum values ranging from 0.03 to 0.77 m^2/g (Table 3.2).

In addition, Table 3.2 provides a summary of the characteristics of the investigated rock specimens, including porosities, pore volumes, SPVs and bulk densities, ranging from 0.068 to 0.224, 0.41 to 1.30 cm^3, 0.028 to 0.110 cm^3/g and 2.04 to 2.41 g/cm^3, respectively.

Table 3.2. Overview of mass (m), porosity (Φ), specific surface area (SSA), and specific pore volume (SPV) obtained through NMR analysis for Bentheim, OBK, RWS, and GWS rock samples. Bulk density (ρ_{bulk}) measurements were conducted using the buoyancy method, relying on Archimedes' principle.

Sample	m	*PV*	*BV*	*Φ*	*SSA*	*SPV*	ρ_{bulk}
	[g]	[cm^3]		[%]	[m^2/g]	[cm^3/g]	[g/cm^3]
Bentheim	11.86	1.3	5.80	22.4	0.03	0.110	2.04
OBK	13.07	1.02	5.96	17.1	0.22	0.078	2.19
RWS	13.32	0.96	5.87	16.4	0.70	0.072	2.27
GWS	14.70	0.41	6.1	6.80	0.77	0.028	2.41

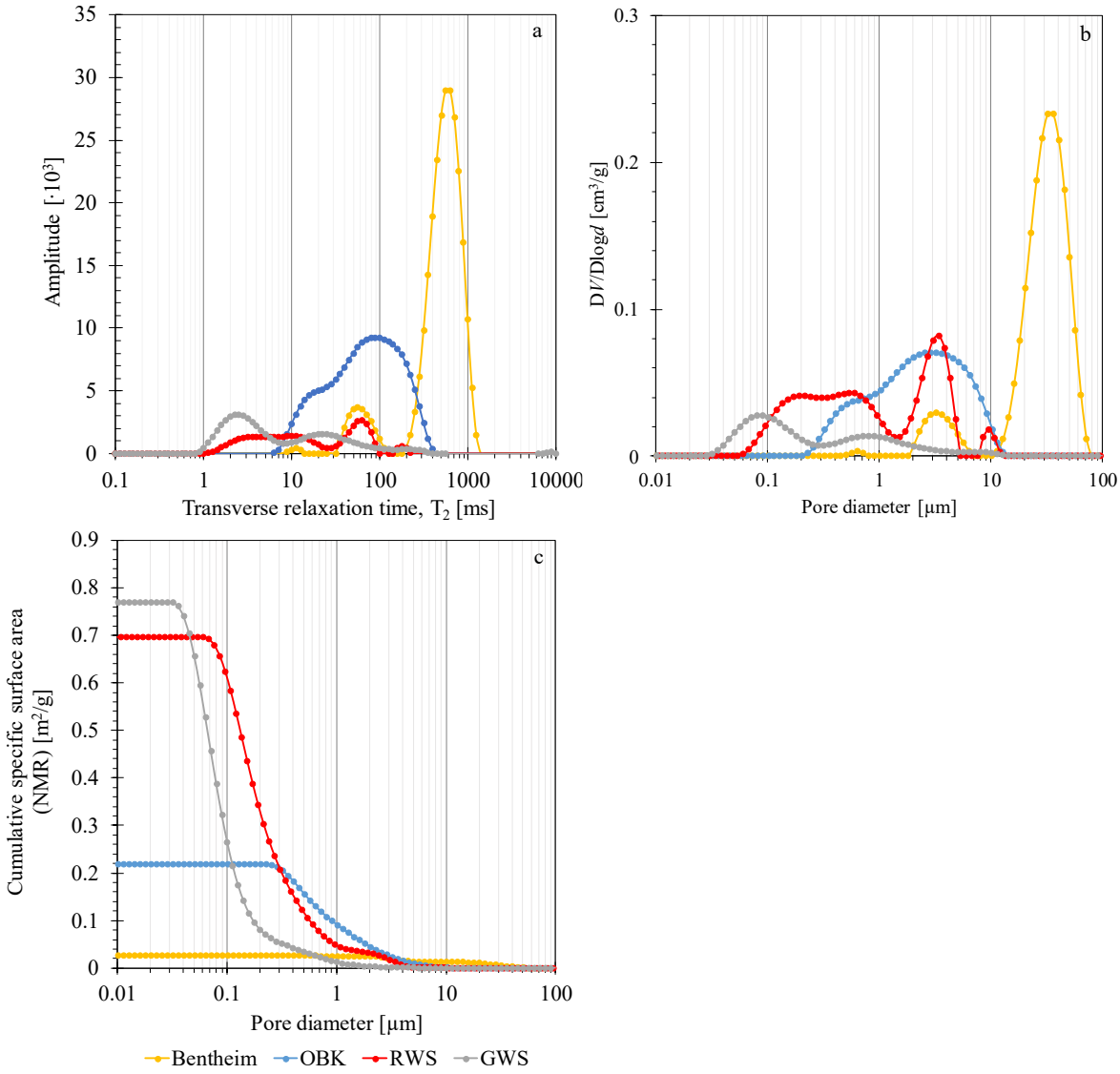

Figure 3.2. NMR T_2 spectrum distribution of Bentheim, OBK, RWS, and GWS rock specimens (a), along with the PSD derived from NMR data (b), and cumulative SSA versus pore diameter obtained from NMR data (c).

3.4.3. Determination of surface area by scanning electron microscopy

The polished epoxy impregnated rock samples were analyzed using SEM imaging to explore the pore equivalent diameter distribution. High-magnification images were captured from specific regions within each rock specimen, ranging from $2.61 \cdot 10^6$ to $11.61 \cdot 10^6$ µm^2 depending on the number of images acquired. A selection of SEM images for all samples at measured resolution (548.8 nm) is presented in Figure 3.3 (a, c, e, and g). To analyze these SEM images, the algorithm outlined in Chapter A.2.3 was implemented, resulting in the generation of segmented images (Figure 3.3b, d, f, and h), allowing for the determination of pore sizes and SSA. The pore equivalent diameters were derived from pore areas, assuming a circular pore geometry. Afterwards, the PSDs for the analyzed rock specimens were plotted, showing frequency against pore equivalent diameter (Figure 3.4a).

Considering that the applied morphological processes utilized a 3x3 pixels structuring element, it resulted in the minimum pore size in these images of 1.86 µm.

The cumulative SSA for each sample was determined by averaging the SSAs obtained from multiple images, which were in turn derived by aggregating the SSAs acquired from individual pores within each image. The resulting data was then plotted against pore equivalent diameter, as depicted in Figure 3.4b. The highest SSA values vary between 0.013 and 0.024 m^2/g (Table 3.3). Furthermore, the pore areas of individual images were compared against the total image areas to evaluate the 2D porosity. Subsequently, the mean porosity and SPV values for each rock specimen were derived from multiple images, ranging from 0.076 to 0.212, and 0.031 to 0.105 cm^3/g, respectively, as detailed in Table 3.3.

The SEM images of OBK rock specimens exhibit low quality, potentially attributed to either unfilled pore spaces with epoxy or breakout, suggesting ineffective surface impregnation. Consequently, ensuring the quality of segmentation becomes uncertain. Nevertheless, effective pore segmentation and separation of pores were achieved by employing the Isodata thresholding method, followed by applying erosion and dilation binary processes. This image processing algorithm is presumed to have yielded reliable outcomes, as the results of image analysis demonstrated consistency with findings obtained from other techniques - a point that will be thoroughly discussed in the subsequent chapter.

Table 3.3. Overview of the results of SEM image analysis including porosity (Φ) and specific surface area (SSA) with their corresponding standard deviations (STD) as well as specific pore volume (SPV) of the investigated rock specimens.

Sample	*Φ*		*SSA*		*SPV*
	[%]	STD [%]	[m^2/g]	STD [m^2/g]	[cm^3/g]
Bentheim	21.2	1.70	0.024	0.0036	0.105
OBK	17.0	1.20	0.038	0.0071	0.079
RWS	13.7	2.0	0.021	0.0020	0.061
GWS	7.60	0.20	0.013	0.0004	0.031

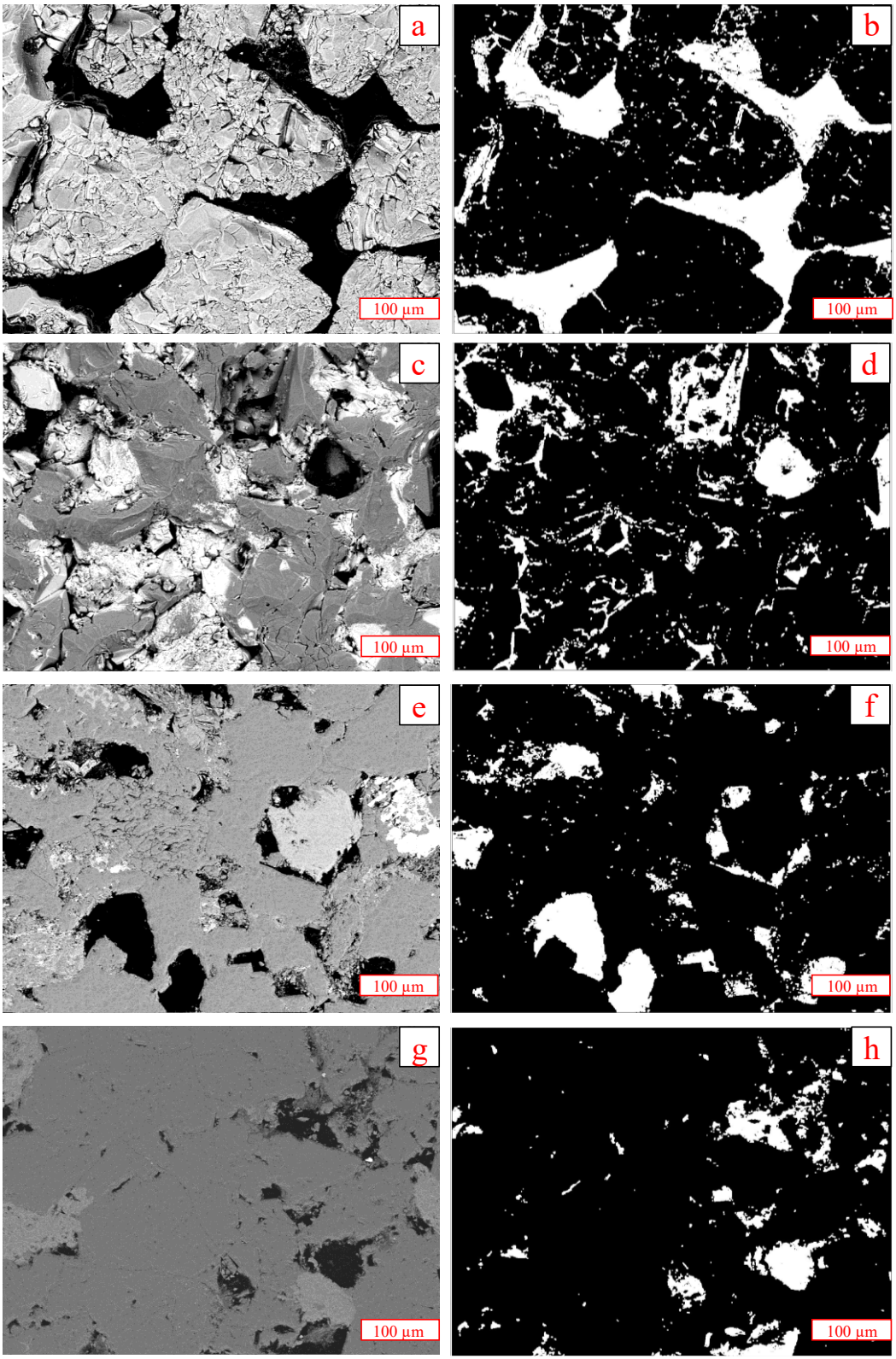

Figure 3.3. SEM images of Bentheim (a), OBK (c), RWS (e), and GWS (g). The segmented images were obtained using the Isodata thresholding technique, followed by erosion and dilation binary processes for Bentheim (b), OBK (d), RWS (f), and GWS (h). Pores are represented in white, while grains appear in black. The images dimensions are 562 × 421 µm. The image resolution for all samples is 548.8 nm.

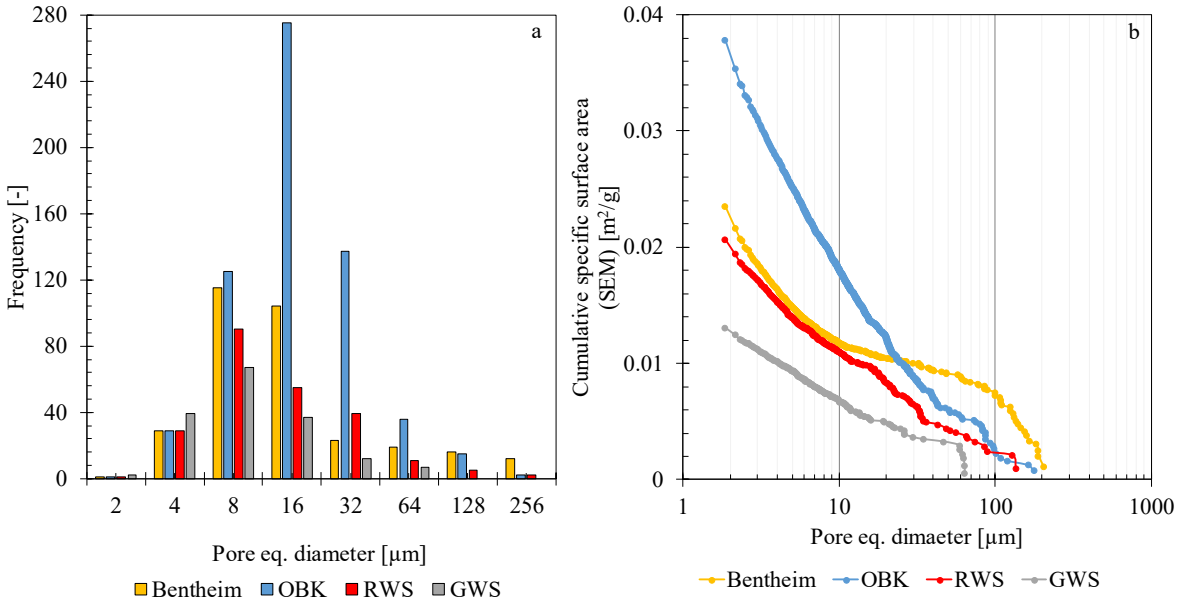

Figure 3.4. PSD derived from SEM images of Bentheim, OBK, RWS, and GWS rock specimens (a), alongside the cumulative SSA plotted against pore equivalent diameter for the analyzed rock specimens (b). The pore equivalent diameters were calculated from pore areas obtained through image analysis, assuming a circular pore shape.

3.4.4. Determination of surface area by X-ray micro-computed tomography

The rock specimens under investigations were examined utilizing µCT technique to ascertain pore characteristics, including porosity, surface area, and pore size distribution. Images were captured at a resolution of 4.036 µm and exemplary representations of these images for all rock specimens, alongside their respective binarized versions, are depicted in Figure 3.5 (a-h). The 3D visualizations of examined rock specimens, which provide intuitive information on porosity, are presented in Fig. A2. Subsequently, a detailed analysis was conducted following the workflow outlined in Chapter A.2.4, resulting in the determination of pore volume, pore equivalent diameters, as well as the SSA values corresponding to each pore size. The PSDs of the examined rock specimens were derived using logarithmic differential pore volume distribution (as detailed in Chapter A.2.1), alongside their respective pore size frequency distributions (Figure 3.6a, b). The pore size range of the Bentheim rock specimen extends from 12.11 to 395 µm, whereas the OBK, RWS, and GWS specimens exhibit nearly identical pore size spectra, ranging from 12.11 to 235 µm, 12.11 to 205 µm, and 12.11 to 185 µm, respectively. The SSA and porosity values for each sample were determined by averaging corresponding results obtained from multiple images. Subsequently, the cumulative SSAs were plotted against equivalent pore diameter for the examined rock specimens (Figure 3.6c), with the highest values measured between 0.0018 to 0.0063 m²/g. Moreover, the porosity and SPV values of the analyzed

rock specimens ranged from 0.026 to 0.17 and from 0.011 to 0.085 cm^3/g, respectively. The standard deviations associated with porosity values varied between 0.006 and 0.021. A comprehensive overview of the results obtained from this method, including porosity, SSA, and SPV, is listed in Table 3.4.

Table 3.4. Summary of μCT image analysis results, encompassing porosity (Φ) and specific surface area (SSA) alongside their respective standard deviations (STD), in addition to the specific pore volumes (SPV) of the examined rock specimens.

Sample	ϕ		*SSA*		*SPV*
	[%]	STD [%]	[m^2/g]	STD [m^2/g]	[cm^3/g]
Bentheim	17.0	2.10	0.0063	0.00010	0.085
OBK	7.40	1.10	0.0047	0.00011	0.034
RWS	4.30	0.80	0.0032	0.00003	0.019
GWS	2.60	0.60	0.0018	0.00008	0.011

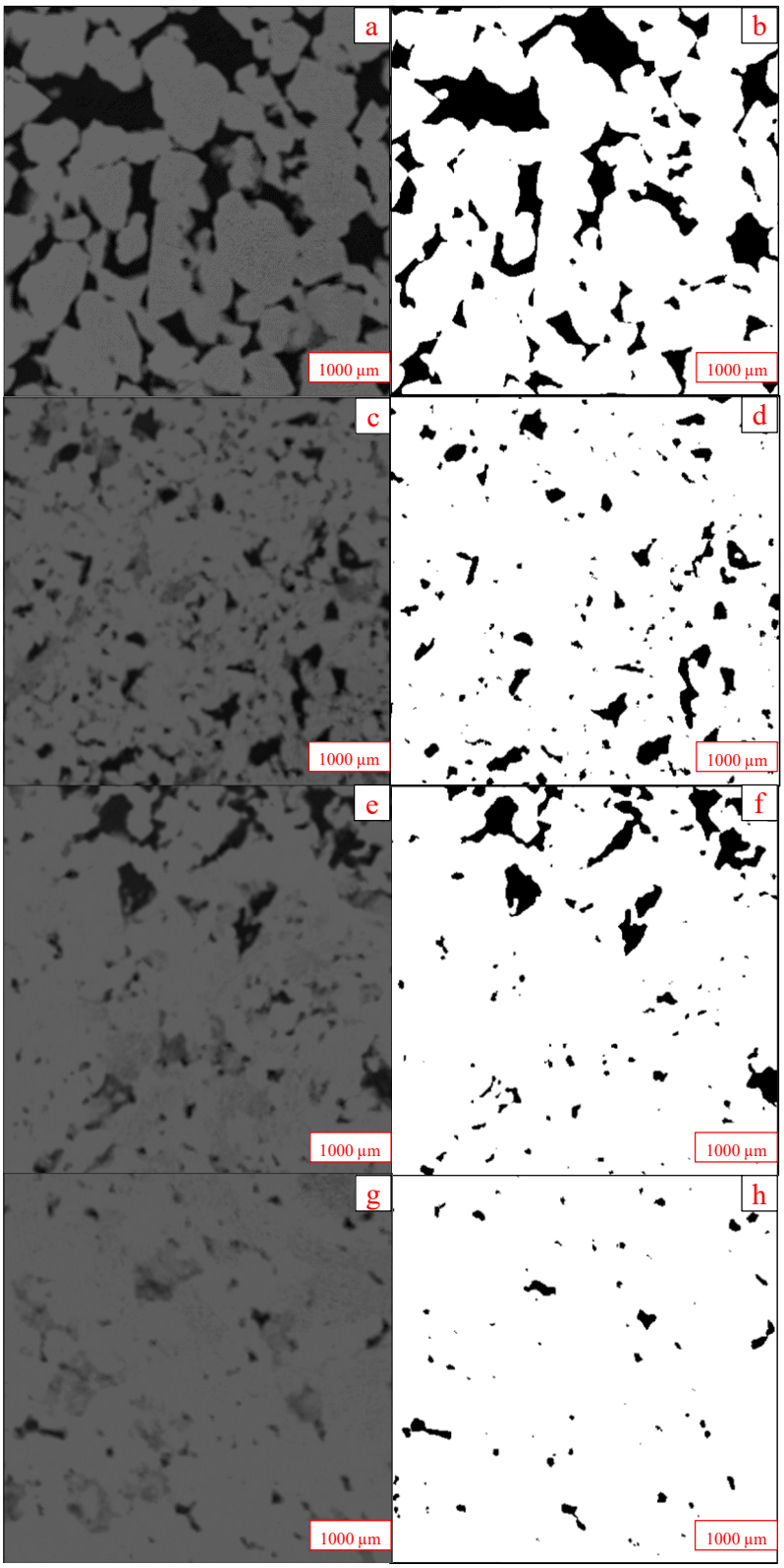

Figure 3.5. µCT images of Bentheim (a), OBK (c), RWS (e), and GWS (g) alongside their respective segmented images depicted in (b, d, f, h), respectively. Pores are represented as black, while grains appear in white. The images have dimensions of 4758.4x 4758.4 µm.

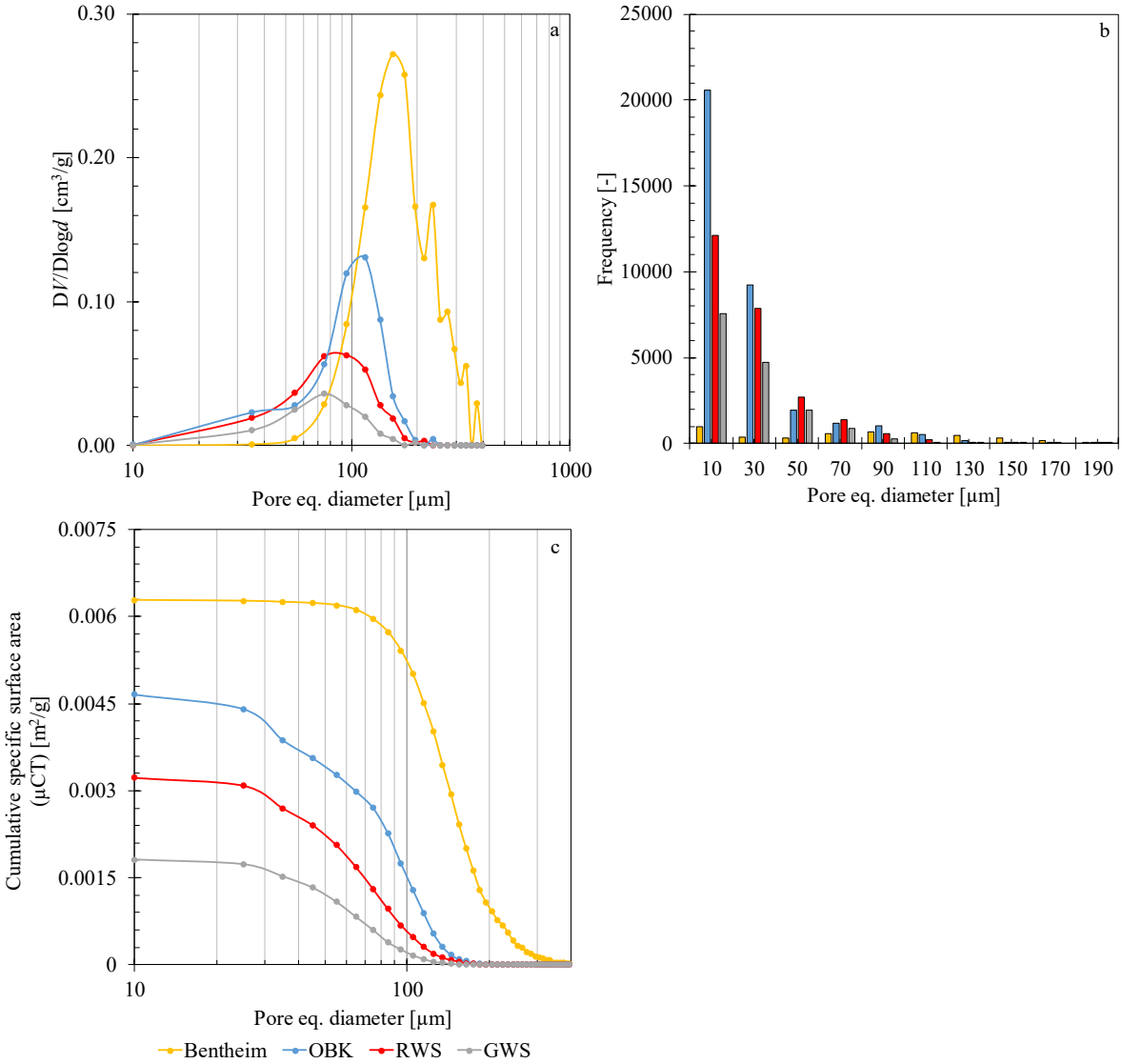

Figure 3.6. PSDs obtained from µCT images of Bentheim, OBK, RWS, and GWS specimens illustrating logarithmic differential pore volume distribution curve (a), accompanied by their respective pore size frequency distributions (b). The cumulative SSA was plotted against pore equivalent diameter for the analyzed rock specimens (c).

3.5. Discussion

Prior research led by Khajooie et al. (2024a) has provided insights into the constitutive relationship between the activity of *M. thermolithotrophicus Archaea* within porous media and the respective SSA. This study is a follow-up, aiming to further explore the correlation between the activities measured in previous investigations and the SSAs of similar rock specimens obtained through designated techniques. Microbial activities were quantified through two experiments conducted on rock specimens with (1) similar bulk volumes and (2) similar pore volumes, resulting in rates ranging from 0.17 to 1.22 mM/h and 0.34 to 1.15 mM/h, respectively. Furthermore, SSAs and Gurvich volumes were determined employing N_2 physisorption technique and are reported within the range of 0.2 to 1.3 m^2/g

and 0.001 to 0.01 cm^3/g, respectively (Khajooie et al., 2024a). The comprehensive results of microbial activity tests, along with the characteristics of the rock specimens are presented in Table 3.5. Furthermore, the normalized hydrogen consumption rates, based on pore volume and interfacial area, have been calculated and will be discussed in the subsequent chapters. An overview of the results from the N_2 physisorption measurements is also provided in Table 3.6.

Table 3.5. Overview of hydrogen consumption rates obtained from two microbial activity experiments carried out on four rock specimens (Bentheim, GWS, RWS, OBK) with identical bulk volume (1) and identical pore volume (2). Additionally, the characteristics of rock specimens including bulk volume (V_b), porosity (Φ), pore volume (V_p), and interfacial area, used in both experiments are provided (Khajooie et al., 2024a). The normalized hydrogen consumption rate by pore volume and interfacial area for all rock specimens obtained from two experiments are also provided.

Exp.	Sample	V_b	V_p	Φ	$A_{interfacial}$	R_{H_2}	$R_{H_2(normalized)}$
		[cm^3]		[%]	[cm^2]	[mM/h]	[mM/(h·cm^3·cm^2)]
Identical V_b (1)	Bentheim	23.09	5.47	23.7	44.59	1.22	0.005
	OBK	23.00	4.25	18.5	44.24	1.02	0.005
	RWS	22.71	3.62	16	44.44	0.62	0.004
	GWS	22.56	1.80	8	44.82	0.17	0.002
	MTS	6.00	-	-	20.73	0.21	0.002
Identical V_p (2)	Bentheim	11.34	2.57	22.7	28.57	0.34	0.005
	OBK	16.44	2.60	15.8	70.81	1.15	0.012
	RWS	17.71	2.57	14.5	37.71	0.64	0.007
	GWS	42.33	2.61	6.2	36.02	0.52	0.003
	MTS	-	2.6	-	20.73	0.1	0.002

Table 3.6. Summary of N_2 physisorption results acquired from dried and crushed rock samples of Bentheim, OBK, RWS, and GWS including Gurvich volumes and SSAs (Khajooie et al., 2024a).

Sample	Gurvich volume	*SSA*
	[cm^3/g]	[m^2/g]
Bentheim	0.001	0.2
OBK	0.005	0.7
RWS	0.01	0.9
GWS	0.008	1.3

Most bacteria proliferate through binary fission, while a minority employ non-binary fission patterns like budding, hyphal growth, the generation of daughter cells, and the formation of multicellular baeocytes. During binary fission, cells double in mass and replicate their genome before dividing in the middle, resulting in equivalently sized daughter cells (Chien et al., 2012; Pląskowska et al., 2023). This implies that the cell size of 1 to 2 µm for *M. thermolithotrophicus* likely represents the minimum threshold, indicating that pores larger than 2 µm are accessible for microbial traversal and colonization by this specific *Archaea*. Chapter 5.1 provides a comparative analysis of porosity and SSA values obtained through various techniques. Additionally, Chapters 5.2 and 5.3 investigate the correlation between microbial activity and the SSA of the analyzed rock specimens, before and after the cutting of inaccessible pores SSA.

3.5.1. Comparison of specific surface area

The comparative analysis of the SSAs for the analyzed rock specimens, across various techniques is illustrated in Figure 3.8a, b. N_2 physisorption yielded the highest values, followed by MICP and NMR, for all rock specimens. Specifically, the SSAs determined through these techniques indicate a progressive increase among all rock specimens. SSAs derived from SEM and µCT consistently showed values one to two orders of magnitude lower than those obtained from alternative methods, illustrating a distinct ranking of rock specimens in terms of SSAs (Figure 3.8b). These disparities arise from the unique pore size ranges that each method can analyze, attributable to their specific technical and methodological limitations (Figure 3.7). The inverse relationship between SSA and pore size (equation (A.7)) highlights the stronger influence of smaller pores on SSA compared to larger ones. As illustrated in Figure 3.7, MICP analysis captured a wider spectrum of smaller pores compared to the relatively limited coverage provided by NMR, SEM, and µCT. Consequently, the MICP technique yields higher SSAs for all rock specimens, followed by NMR, SEM, and µCT methods. SSAs, as determined through N_2 physisorption, consistently demonstrate highest values compared to those obtained through alternative techniques across all rock specimens. This observation is likely attributed to artificially generated surfaces (particle size distribution) (Lowell et al., 2012)(cf. Chapter 1).

MICP is applicable to detect and quantify pores across a considerably broad spectrum, from 0.003 to 350 µm (Anovitz & Cole, 2015; Fu et al., 2017). During MICP measurements of the analyzed rock specimens, mercury intrusion data is acquired in a pressure range between 0.003 and 207 MPa, allowing for the characterization of pore structures within a size range of 0.006 to 178.9 µm. Capillary pressures in a pore network are primarily influenced by narrow pores (throats) rather than pore bodies (equation (A.3)). Consequently, MICP overestimates the frequency of pore throats at the expense of the pore bodies, causing a shift in the pore size distribution towards smaller pores (Schmitt et al., 2015). This inherent limitation in the methodology, coupled with its ability to characterize nano-scale pores, ultimately yields higher SSA compared to those derived from other techniques (Figure 3.8a). In addition, the observed variations in SSAs can be attributed to the unique pore size spectra of each rock specimens. The MICP PTDs indicate that GWS has the smallest pore size range, resulting in the highest SSA (Figure 3.1b). Following this,

RWS, OBK, and Bentheim exhibit progressively larger pore size ranges, leading to a corresponding decrease in SSAs (Figure 3.8a).

NMR analysis revealed pore sizes ranging from 0.03 to 71.89 µm, resulting in lower SSAs compared to MICP (Figure 3.8a). The SSA variations among rock specimens can be clarified through a comparative PSD analysis (Figure 3.2b). This analysis reveals that GWS exhibits the smallest pore size range, followed by RWS, OKB, and Bentheim, consequently leading to a proportional reduction in SSAs. Additionally, the pore size spectrum measured though SEM spanning from 1.86 to 205 µm across the examined rock specimens. The minimum pore diameter detected by SEM is larger than that identified by MICP and NMR by two orders of magnitude. This discrepancy suggests that SEM fails to capture smaller pores, which significantly contribute to SSAs, resulting in a notable decrease in SSA values across all specimens except for Bentheim (Figure 3.8a). While the minimum pore size of Bentheim, as detected by MICP and NMR, appears to be smaller than that measured by SEM, a closer examination of MICP PTD and NMR PSD of Bentheim revealed that pores with considerable frequencies are larger than the resolution of SEM. Thus, SSAs derived from MICP, NMR, and SEM demonstrate consistent values, unaffected by the limited resolution of SEM (Figure 3.8a). The ranking of rock specimens concerning SSA can be clarified by analyzing the SEM-derived PSD (Figure 3.4a). It is apparent that while the minimum pore size remains consistent across all rock specimens, the frequency of pores, particularly those smaller than 16 µm, is highest for OBK, followed by Bentheim, RWS, and GWS. Consequently, this sequence mirrors the order of variations in SSA among the specimens (Figure 3.8b). Similarly, the limited resolution of the µCT method resulted in the oversight of substantial portions of small pores, resulting in the lowest SSAs compared to alternative techniques. This method identified pores ranging from 12.11 to 395 µm, thereby excluding the majority of pores that significantly govern SSA. As a result, the differences among SSAs are negligible (approximately 0.0015 m^2/g) (Figure 3.8b).

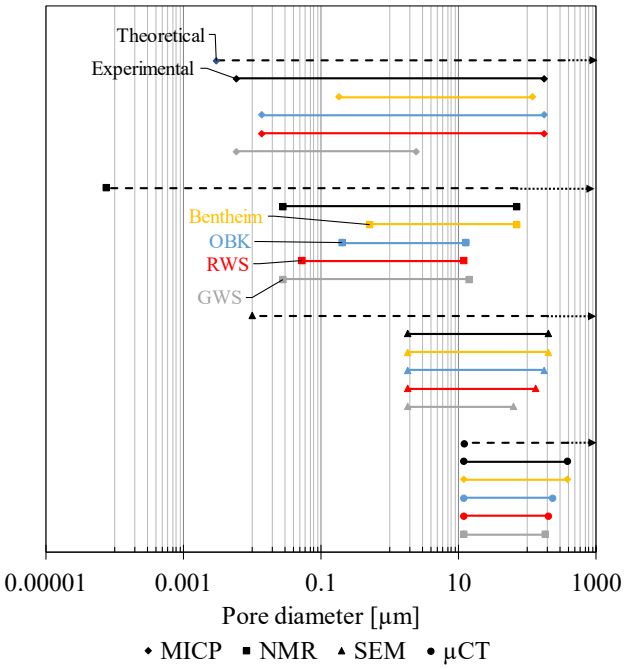

Figure 3.7. Comparison between theoretical and experimental pore size ranges determined using MICP, NMR, SEM, and µCT techniques, with respective ranges depicted for each rock specimen. Theoretical pore size ranges are illustrated with dashed lines and experimental ranges with solid lines. The minimum detectable values by NMR, SEM, and µCT techniques were established according to the capabilities and configurations of the devices employed in this investigation. There are no uppermost boundaries for theoretical range of pore size. The idea of this illustration has been taken from Busch et al. (2016).

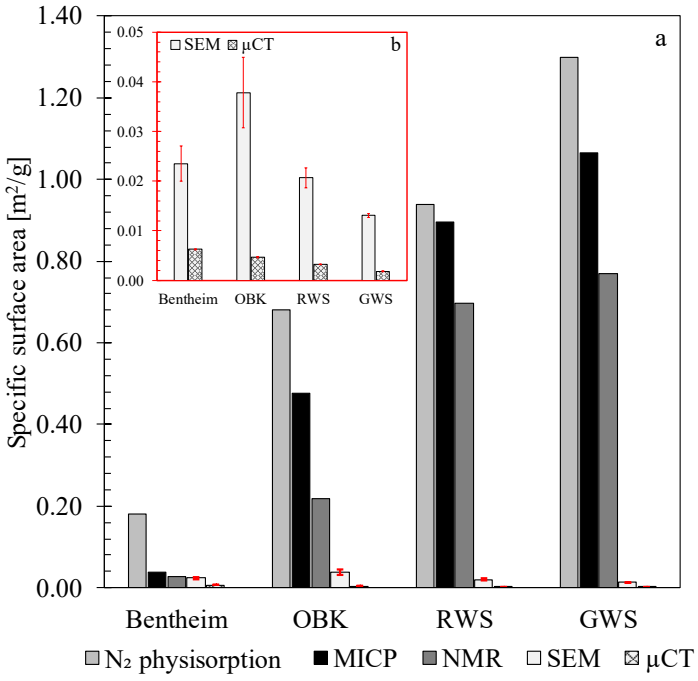

Figure 3.8. Comparative assessment of the SSAs for Bentheim, GWS, OBK, and RWS rock specimens employing various techniques, including N_2 physisorption, MICP, NMR, SEM, and µCT (a). A detailed view focusing on the SSAs obtained through SEM and µCT (b).

3.5.2. Correlation of normalized H_2 consumption rates with specific surface area

Prior research conducted by Khajooie et al. (2024a) shows a strong correlation between the activity of methanogens, whether within porous media or the bulk solution, with the quantity of MTS - a factor tightly linked to the porosity in geological formations. Furthermore, research has highlighted that the mass transfer of hydrogen to water plays a crucial role in restricting the methanogenic reaction (Dupnock & Deshusses, 2019; Jensen et al., 2018). This limitation arises because methanogenic *Archaea* exclusively convert dissolved hydrogen and carbon dioxide (Osman et al., 2022). The mass transfer flux is dependent not only on the transfer coefficient and concentration gradient but also on the interfacial area between gas and liquid phases (Jensen et al., 2021). Therefore, to investigate the influence of surface area on microbial activities, it is imperative to normalize for the effect of MTS amounts and interfacial area between gas and liquid phases, according to the following equation:

$$R_{H_2}(\text{normalized}) = R_{H_2}/(V_p \cdot A_{\text{interfacial}}) \quad (3.1)$$

where R_{H_2} is the rate of hydrogen consumption [mM/h], V_p pore volume [cm^3], reflecting the MTS amount, and $A_{\text{interfacial}}$ interfacial area between gas and liquid phases [cm^2]. Given the presence of a water film covering the bulk surface of rock specimens, which contributes to mass transfer from gas to liquid phases, it becomes essential to utilize the total interfacial area.

As illustrated in Figure 3.9a, b, the normalized hydrogen consumption rates correlate with SSAs determined by the SEM, whereas no correlation was observed with those determined by other methods. A comparison of MICP- and NMR-derived cumulative SSA versus pore diameter plots (Figures 3.1c & 3.2c), with respect to the *M. thermolithotrophicus* cell size threshold, demonstrates that a substantial proportion of pores contributing to the SSAs of all rock specimens, except Bentheim, fall below the specified cutoff. This suggests their inaccessibility for microbial activity, thereby resulting in no correlation with microbial activity. In contrast, the correlation between normalized hydrogen consumption rates and SSAs acquired from SEM (Figure 3.9b) can be elucidated by implementing the cell size threshold on SEM-derived cumulative SSA plot (Figure 3.4b). The minimal pore sizes analyzed by this technique is 1.86 µm, indicating that a majority of the pores assessed for determining SSAs are accessible for *M. thermolithotrophicus*. While it was acknowledged earlier that SSAs obtained from N_2 physisorption do not precisely reflect the pore surfaces

of rock specimens, they were nonetheless utilized in these plots to facilitate comparison with findings from alternative techniques. Notably, the analysis demonstrates a lack of correlation between microbial activity and these SSAs. Additionally, upon investigating the relationship between microbial activity and µCT-derived SSAs (Figure 3.9c), it was apparent that there is no discernible correlation between them. This lack of correlation can be attributed to the nearly identical values of SSAs.

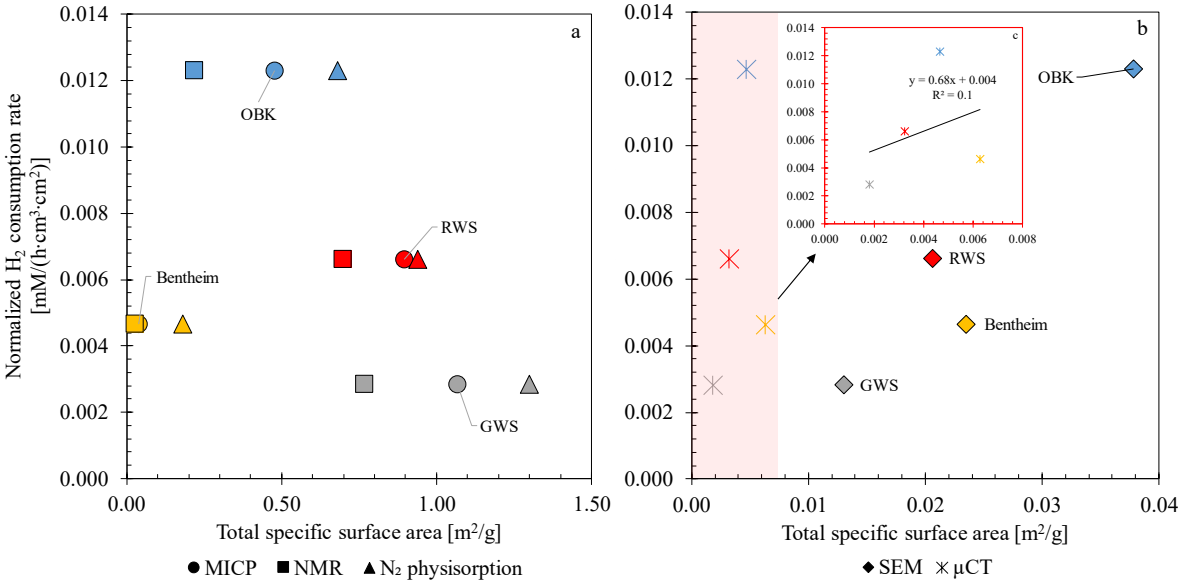

Figure 3.9. Comparison of correlations between normalized H_2 consumption rates by pore volume and interfacial area and SSA determined by MICP, NMR, and N_2 physisorption (a) as well as SEM and µCT (b). Detailed visualization of microbial activity in relation to SSA, derived from µCT data, indicates a lack of correlation between them (c). The H_2 consumption rates were derived from two microbial activity experiments conducted on four MTS-saturated rock specimens with identical bulk volumes and pore volumes (Khajooie et al., 2024a). Each color represents specific geological formations: [Yellow]-Bentheim, [Blue]-OBK, [Red]-RWS, and [Gray]-GWS. The horizontal axis ranges vary across these plots: plot (a) spans from 0 to 1.5 m^2/g, while plot (b) ranges from 0 to 0.04 m^2/g.

3.5.3. Correlation of normalized H_2 consumption rates with accessible specific surface area

The influence of surface area on the activity of *M. thermolithotrophicus Archaea* in pore spaces can be explored by assessing the SSAs of pores accessible to these *Archaea*. This involves establishing a cutoff line at 2 µm pore throat/body diameter on the cumulative SSA versus pore diameter plots, obtained through various techniques (Figures 3.1c, 3.2c, & 3.4b). The analysis of SSAs for the microbe-available pores in each rock specimen illustrates a consistent pattern across all methods employed (Figure 3.10). Comparing Figure 3.10 and Figure 3.8a indicates a significant reduction in SSA as determined by both MICP and NMR methods. Upon implementing a 2 µm cutoff line on the pore size range (Figure 3.7), it becomes apparent that a substantial portion of pores detected by MICP and

NMR falls below this threshold. As a result, these pores are excluded from the determination of SSA for accessible pores.

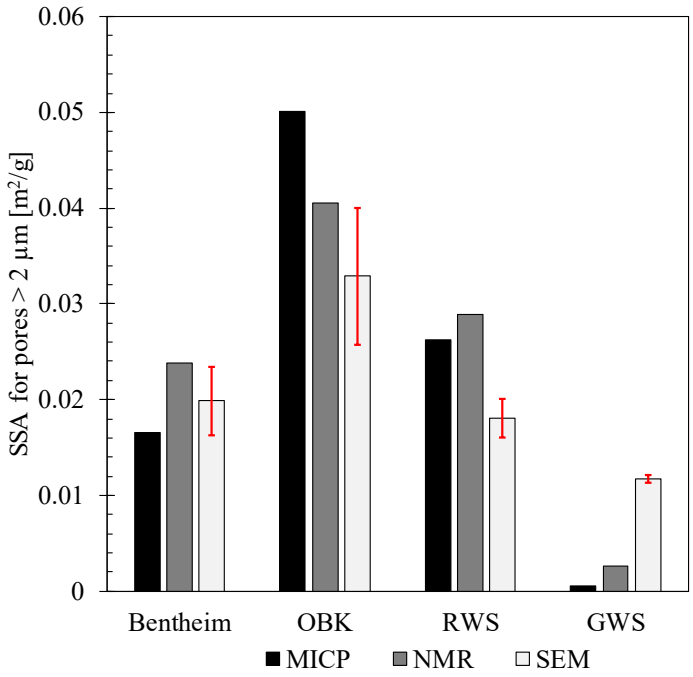

Figure 3.10. Comparative analysis of the SSAs of accessible pores for M. thermolithotrophicus Archaea, as determined by MICP, NMR, and SEM techniques. The SSAs of accessible pores in Bentheim, OBK, RWS, and GWS were assessed by applying the cell size of M. thermolithotrophicus Archaea as the designated threshold (diameter > 2 µm) on cumulative SSA plots obtained through MICP, NMR, and SEM methods.

The normalized hydrogen consumption rates acquired from experiments conducted on rock specimens possessing identical pore volumes and bulk volumes were correlated with the SSAs of accessible pores (Figure 3.11 a-c). These correlations highlight the profound impact of surface area on microbial activity within porous media. The normalized microbial activities observed in rock specimens with similar pore volumes exhibit enhancements between 0.19 to 0.44 mM/(h·cm^3·cm^2) as the SSA increases, depending on the methodology. Furthermore, when considering specimens of similar bulk volumes, these activities demonstrate a modest increase from 0.05 to 0.14 mM/(h·cm^3·cm^2) as the SSA rises. Nevertheless, the role of surface area as a crucial parameter influencing hydrogen-consuming microbes within porous media has been largely overlooked in the literature. However, research unrelated to UHS, conducted on North Sea sediments, found a strong correlation between cell abundance, oxygen consumption rates, and grain surface area for microbial colonization (Ahmerkamp et al., 2020). Another study investigated the effects of mineral coatings formed on grain surfaces during treatment of groundwater with rapid sand filtration on microbial activity. The findings revealed a positive correlation between the extent of the mineral coatings, which increases the available surface area for

microorganisms, and the activity of nitrifying prokaryotes (Gülay et al., 2014). Unlike these studies conducted on sediments or sandy filters, our tests were carried out on intact rock with varying pore sizes, partially inaccessible to microorganisms. This highlights the importance of considering cell size when correlating microbial activity with SSA. Moreover, Khajooie et al. (2024a) observed increased activity in the presence of sand particles, zirconia beads, and rock fragments, as well as within porous rocks compared to corresponding bulk solutions. This underscores the stimulating impact of surface area on microbial activity.

The discrepancy in the correlation slopes is primarily driven by the variances in SSAs of accessible pores for GWS and OBK specimens (Figure 3.10). The substantial differences in SSAs observed in the GWS specimen can be attributed to variations in pore size spectra determined by MICP, NMR, and SEM, ranging from 0.006 to 2.45 µm, 0.03 to 14.27 µm, and 1.86 to 63.86 µm, respectively (Figure 3.7). It is evident that a substantial fraction of pores identified via MICP falls below the cell size threshold, thereby yielding the minimum SSA value. Conversely, this proportion progressively rises for NMR and SEM analyses. Additionally, the ink-bottle effect (Chapter A.2.1) observed during MICP measurements resulted in higher frequencies of smaller pores for the OBK specimen, consequently contributing to a higher SSA compared to those derived from alternative methods. Furthermore, the intercepts of these correlations signify the microbial activity in the absence of the SSA effect, which reflects the bulk solution activity. The intercepts derived from MICP and NMR range between 0.001 to 0.003 mM/(h·cm^3·cm^2), closely aligning with the measured values for MTS samples (0.002 mM/(h·cm^3·cm^2)) (Table 3.5). The observed disparity in correlations between normalized hydrogen consumption rates and SSAs of accessible pores in rock specimens with identical pore volumes and bulk volumes can be ascribed to an additional factor—presumably, variations in the cell abundance of MTS. The MTS employed to saturate the rock specimens in these experiments were prepared independently, potentially leading to different cell abundances.

Based on the findings of the presented study, microbial activities of *M. thermolithotrophicus Archaea* within porous media can be determined by considering the impact of MTS quantity, interfacial area, and surface area:

$$R_{H_2} = (a \cdot SSA + b) \cdot V_p \cdot A_{interfacial} \quad (3.2)$$

The variables a and b correspond to the slope and intercept of the correlations, respectively, and are dependent on the method employed for determining the SSA. Additionally, another influential factor impacting the correlation coefficients (a, b) is the cell concentration, as previously explained. To accurately assess the SSA of available pores in a specific rock specimen, it is recommended to integrate MICP with either NMR or SEM techniques. Microorganisms must traverse through pore throats to access pore bodies, making the MICP technique indispensable for providing valuable insights into pore body accessibility. Once it is established that microorganisms can traverse pore throats, determining the SSA of accessible pore bodies can be achieved through NMR or SEM methods. The determined SSA of accessible pores using the MICP method tends to be overestimated due to the method's limitations in accurately measuring pore bodies. To obtain more precise coefficients for the proposed equation, further research should be conducted, encompassing the integration of various methods within a pore network model.

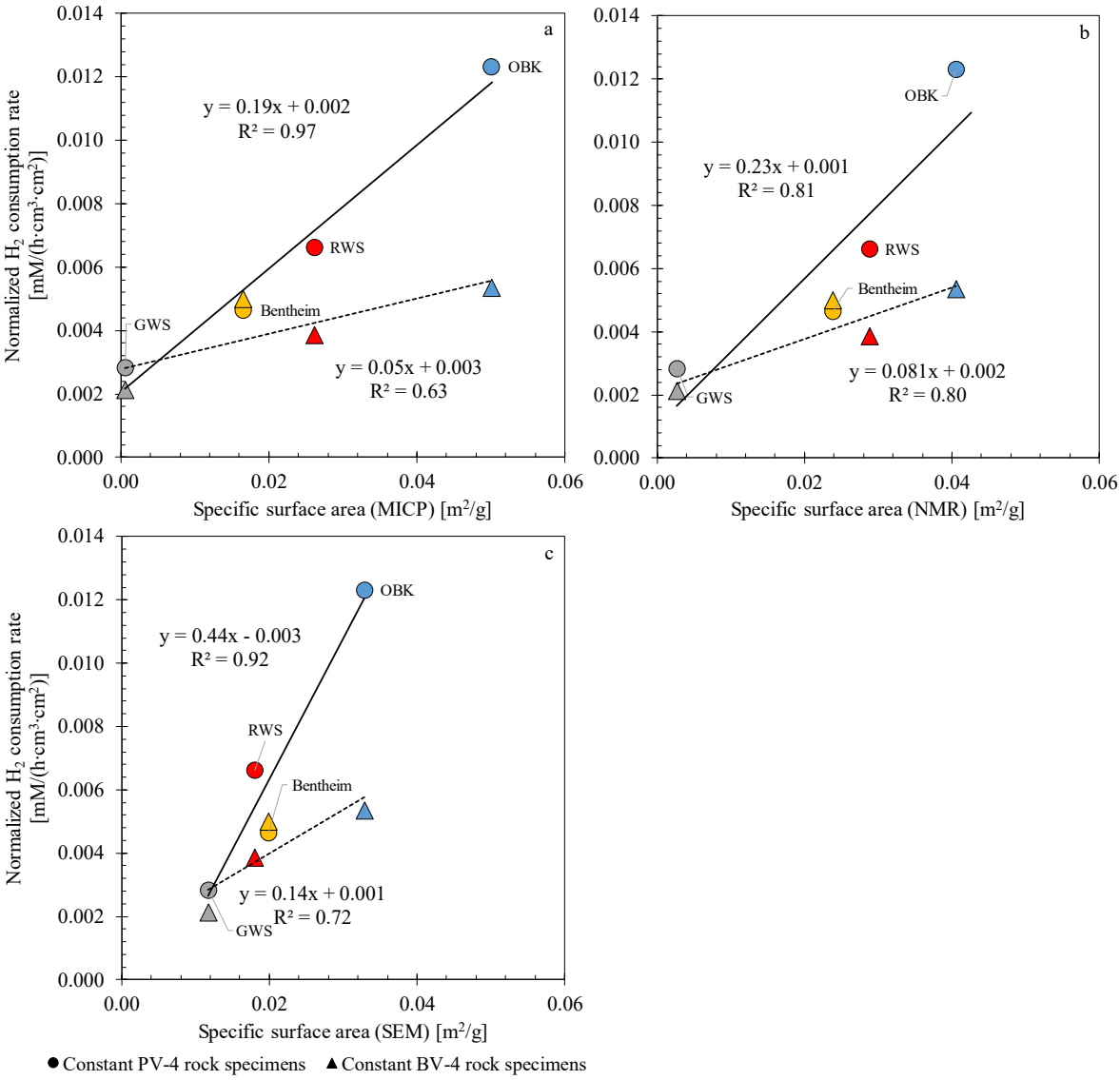

Figure 3.11. Correlation between the normalized H_2 consumption rates by pore volume and interfacial area, and the SSA of accessible pores, determined using MICP (a), SEM (b), and NMR (c). The H_2 consumption rates were derived from microbial activity experiments conducted on four MTS-saturated rock specimens with identical bulk volumes and pore volumes (Khajooie et al., 2024a). Each color corresponds to a specific geological formation: [Yellow]-Bentheim, [Blue]-OBK, [Red]-RWS, and [Gray]-GWS.

3.5.4. Critical considerations and implications

This research revealed the considerable influence of SSA on stimulating microbial activities within porous media. The findings suggest that SSA should be considered as an additional parameter influencing microbial growth rates, indicating that hydrogen may be converted into other products at rates higher than previously anticipated (Dohrmann & Krüger, 2023; Heinemann et al., 2021; Thaysen et al., 2021). In the context of UHS projects, the impact of SSA could potentially compromise storage objectives, as hydrogen is converted into undesirable byproducts (Dopffel et al., 2021). Conversely, a higher SSA would prove beneficial for underground bio-methanation, enhancing the efficiency of

hydrogen conversion into methane. The empirical model proposed in this study offers a tool for estimating hydrogen conversion rates within porous media. However, before its application to real reservoirs, several important considerations should be taken into account. Because the rate coefficients of the model depend on the chosen methodology, achieving accurate estimations requires integrating multiple approaches. Therefore, to obtain more precise rate coefficients, further research should be conducted to incorporate MICP, NMR, and SEM methods within a pore network model. Moreover, it is essential to acknowledge that this model was developed based on limited data. Consequently, extrapolating the model beyond the investigated range of SSAs should be approached with caution.

Further considerations arise from implementing simplified conditions in experiments, as opposed to the complex conditions found in porous formations, with the aim of obtaining meaningful results within the laboratory time-scale. The microbial activity tests carried out in the previous research utilized a microbial solution with a cell abundance of approximately 10^8 cells/mL (Khajooie et al., 2024a), whereas microbial cell abundance within porous geological formations varied in different conditions, ranging from 10^3 to 10^7 cells/mL (Dohrmann & Krüger, 2023; Šmigáň et al., 1990; Zink et al., 2008). In addition, the nutrient composition in the solution was specifically tailored for *M. thermolithotrophicus Archaea.* However, essential nutrients may not naturally be present in the formation water or may be insufficient over prolonged periods. Furthermore, in the microbial activity tests, the substrates necessary for the methanogenic reaction were supplied in accordance with stoichiometric coefficients (80% H_2, 20% CO_2). However, during UHS, only hydrogen will be injected, indicating a scarcity of the carbon source compared to experimental conditions. All these discrepancies imply that hydrogen conversions may occur at slower rates within the reservoirs. The literature on how limited cell abundance, nutrient availability, and carbon sources impact microbial activity is scarce (RAG Austria AG, 2020, 2021; Thaysen et al., 2021). Conducting additional research is therefore imperative to comprehensively understand and quantify these potential influences. The interfacial area between liquid and gas phases is notably higher within the reservoirs compared to experimental conditions in Khajooie et al. (2024a). In previous laboratory experiments, microbial activities were assessed under conditions where the pore space was completely water saturated, leading to interfacial areas that are confined to the external surfaces of rock specimens. However, these conditions may not represent those in

actual reservoirs, where pores are often only partially saturated. In such environments, a thin layer of water forms around the grains, greatly enlarging the interfacial area. Consequently, the mass transfer flux and substrate supply for microorganisms are significantly enhanced, potentially resulting in higher microbial activities (Kimmel et al., 1991; Liu et al., 2023). Furthermore, the mass transfer coefficient is dependent upon both gas solubility and gas diffusivity within partially or fully water-saturated rocks, requiring further investigation (Ale Enriquez & Ahring, 2023; Jensen et al., 2021).

This study primarily focused on examining *M. thermolithotrophicus*; however, its findings extend beyond this specific microorganism and can be applied to various others. Notably, the typical cell size for most species ranges around 2 µm, with certain exceptions extending up to 750 µm (Volland et al., 2022). In addition, ultra-small microorganisms, with a cell volume of < 0.1 cm^3, frequently occur in aqueous environments (Lauro et al., 2009). Understanding the diversity of microbial cell sizes, the comprehensive investigation outlined in this research offers a systematic approach to assess the impact of SSA on microbial activity across different scales. Another aspect to consider is that the strain utilized in this research was not representative of those typically found within porous formations. Instead, it was sourced from sandy sea sediments close to Naples, Italy (Huber et al., 1982). Hence, conducting additional research using cultures isolated from the respective reservoirs would yield more precise insights into their behavior within porous media. Furthermore, the presence of competing microorganisms (Ebigbo et al., 2013) in the pore space could potentially influence microbial activity which requires to be investigated in the future work.

This study revealed a potential limitation in current methodologies for evaluating hydrogen loss during UHS. Previous numerical and modeling research have predominately quantified hydrogen loss by relying on the activities of methanogens in bulk solutions as a proxy for their behavior within porous media (Ebigbo et al., 2013; Hagemann, 2017; Jahanbani Veshareh et al., 2022). However, our study underscores the pivotal role of pore characteristics in influencing microbial activity. Overlooking these factors results in inaccurate estimations, underlining the critical necessity for a re-evaluation of such methodologies. Future investigations could explore the integration of rock properties into the current models to achieve a more representative depiction of microbial consumption within reservoirs. Furthermore, the specific attributes of each potential reservoir emphasize the need for individual assessments. These evaluations are necessary to thoroughly

comprehend the impact of pore characteristics on microbial activities. Therefore, a better understanding of these features is imperative to enhance the accuracy and reliability of assessments related to hydrogen conversion in UHS.

3.6. Conclusions

The present study has explored the relationship between the activity of *M. thermolithotrophicus Archaea* within Bentheim, Obernkirchen, Red, and Grey Weser sandstones and the surface area available for microbial colonization., Consequently, a variety of techniques including MICP, NMR, SEM, and μCT have been employed to assess SSAs of pores accessible to this *Archaea*.

Upon factoring in the influence of substance amount and interfacial area, strong correlations have been identified between the normalized microbial activity and the SSAs of the analyzed rocks acquired from MICP, NMR and SEM techniques. This highlights the pivotal role of surface area in stimulating activity of microorganisms within porous media. Moreover, an empirical model has been established based on these correlations, incorporating pore characteristics such as pore volume, SSA, and the gas-liquid interfacial area to estimate the rate of hydrogen consumption within porous media.

Future research could enhance the accuracy of the proposed model by integrating these techniques. The methods employed are complementary: MICP provides information on pore throats, which regulate the accessibility of pores for microorganisms, while NMR/SEM characterizes SSA of pore bodies, influencing microbial activity. Another promising research area is incorporating SSA into existing kinetic models, such as the Monod equation, to improve their predictions of microbial behavior within porous media. Additionally, implementing boundary conditions that closely mimic the complex environments of UHS could lead to a more precise determination of microbial activities and their controlling factors. This includes using native microorganisms, formation brine, and of injected gas compositions similar to those in UHS. Furthermore, investigating microbial activity in partially saturated rock specimens could enhance our understanding of the role of interfacial area in microbial reactions.

Chapter 4

4.Exploring effective diffusion coefficients in water-saturated reservoir rocks via pressure decay technique: Implications for Underground Hydrogen Storage

Keywords: Diffusion coefficient, pressure decay, tortuosity, effective diffusivity, underground hydrogen storage

This chapter is a modified version of the publication: Khajooie, S., Gaus, G., Seemann, T., Ahrens, B., Tian, H., & Littke, R. (2025). Exploring effective diffusion coefficients in water-saturated reservoir rocks via pressure decay technique: Implications for Underground Hydrogen Storage. Transport in Porous Media, 152(2), 12. https://doi.org/10.1007/s11242-024-02148-y

Abstract

The assessment of gas diffusion in water-saturated rocks is essential for quantifying gas loss and determining the amount of gas that could trigger abiotic and biotic processes, potentially altering fluid and rock properties. Additionally, estimating diffusion coefficients is critical for evaluating the balance between hydrogen generation and dissipation in radioactive waste repositories. This investigation involved experimental determination of diffusion coefficients for various gases both in water and in water-saturated Bentheim, Obernkirchen, Grey Weser and Red Weser sandstones. Experimental conditions included pressures ranging from 0.2 to 1.0 MPa, consistently maintained at a temperature of 35°C. The diffusion coefficients of hydrogen, helium, and methane in water were determined to be $6.7 \cdot 10^{-9}$, $9.6 \cdot 10^{-9}$, and $2.8 \cdot 10^{-9}$ m^2/s, respectively, consistent with literature values obtained through gas concentration measurements without pressure gradients. However, the diffusivity of carbon dioxide and argon in water were measured at $10.9 \cdot 10^{-9}$ and $44.6 \cdot 10^{-9}$ m^2/s, significantly exceeding their corresponding literature values by an order of magnitude. This discrepancy is attributed to the significant solubility of these gases in water, resulting in density-driven convection as the primary transport mechanism. Furthermore, the effective diffusion coefficients for hydrogen within the analyzed rock specimens varied from $0.8 \cdot 10^{-9}$ to $2.9 \cdot 10^{-9}$ m^2/s, which are higher than for methane and carbon dioxide, both ranging from $0.3 \cdot 10^{-9}$ to $0.9 \cdot 10^{-9}$ m^2/s. This yielded diffusive tortuosity values ranging from 2.6 to 8.2. The observed effective diffusivity values were positively correlated with porosity, permeability, and mean pore size, while exhibiting a negative correlation with tortuosity. Given that the gas-liquid mass transfer coefficient is directly proportional to the effective gas diffusivity in water, the determined values for H_2 are essential for studying the impact of pore characteristics on microbial activity.

4.1. Introduction:

Molecular diffusion plays a crucial role in assessing the potential risks or benefits associated with solute transfer through caprocks, reservoir rocks and wellbore cements during underground storage of natural gas, CO_2, and H_2 in water-saturated porous formations (Charlet et al., 2017; Hanson et al., 2022; Hubao et al., 2024). Moreover, evaluating the diffusion process is essential for ensuring the safe disposal of radioactive waste in geological host rocks (clay formations) or engineered barriers (Jacops et al., 2020).

During the gas storage phase, once the injected gas reaches pressure equilibrium within the reservoir, diffusion is the primary mode of gas transport within reservoirs, highlighting its critical role in ensuring effective gas storage (Jacops et al., 2020; Song & Zhang, 2013). Gas molecules are recognized to diffuse through the water-filled pore space of cap rocks, but the rates of this process remain controversial (Krooss et al., 1988; Wollenweber et al., 2009). Investigating the diffusive loss through caprock is essential for assessing its integrity during prolonged subsurface gas storage (Michelsen et al., 2022). In addition, gas dissolution and diffusion in the underlying aquifers may pose challenges for the storage of natural gas and H_2, resulting in a gas loss and a reduction in deliverability (Reitenbach et al., 2015). Notably, the higher diffusivity of H_2 compared to CH_4 can increase gas loss into the formation water of the cap rock or adjacent aquifer (Carden & Paterson, 1979; Krooss, 2008).

However, the primary impact of gas diffusion through pore fluids in caprock, reservoir rock, or wellbore cement- particularly in the context of H_2 and CO_2 storage- is the initiation of biochemical and geochemical reactions with substantial consequences. Specifically, mineral dissolution within caprock and wellbore cement can create migration pathways, potentially compromising the integrity of the storage system (Aftab et al., 2023; Fleury et al., 2009; Wigand et al., 2009; Zivar et al., 2021). The primary concern with wellbore cement is that fluid-rock interactions may lead to leakage along the rock-cement and casing-cement interfaces (Gherardi et al., 2012; Labus & Wertz, 2017). In reservoir rocks, mineral dissolution or precipitation can alter transport and storage as well as mechanical properties (Dabbaghi et al., 2024; Muller et al., 2024). In the case of CO_2 storage, water-rock interactions primarily result from chemical changes in the brine, such as a reduction in pH due to CO_2 dissolution (Jun et al., 2013). For underground hydrogen storage (UHS), abiotic reactions occur as hydrogen interacts with dissolved ions, such as sulfate in formation water, or with minerals in the rock matrix, including iron-, sulfur-, and carbonate-bearing minerals (M. Berta et al., 2018; Hassanpouryouzband et al., 2022b; Reitenbach et al., 2015). Furthermore, biotic reactions can lead to the permanent conversion of hydrogen into other products, including methane, hydrogen sulfide, and acetic acid (Dopffel et al., 2021; Heinemann et al., 2021). Biotic processes are particularly likely within reservoir rocks, as most microorganisms have cell sizes around 2 µm (Volland et al., 2022). Furthermore, small microorganisms with cell volumes below 0.1 μm^3 (corresponding to a cell size of approximately 0.6 µm, assuming a spherical shape) are often present in aqueous

environments (Lauro et al., 2009), indicating that microbial activity could also drive reactions within caprocks, with the majority of pores smaller than 2 µm.

Moreover, hydrogen is generated near radioactive waste repositories through corrosion and radiolysis mechanisms. It partially dissolves in the formation water and dissipates from the repositories by diffusion (Harrington et al., 2012; Ortiz et al., 2002). However, if the gas generation rate exceeds the diffusive flux, a gas pressure buildup and subsequent capillary breakthrough could ultimately compromise the host rock's barrier function (Amann-Hildenbrand et al., 2015; Jacops, 2018). Numerous studies have extensively examined diffusion coefficients of various gases, including CH_4, CO_2, and hydrocarbons in liquid or liquid-saturated rocks (Krooss & Schaefer, 1987; Pomeroy et al., 1933; Riazi, 1996; Upreti & Mehrotra, 2000; Zarghami et al., 2017). These investigations have primarily been conducted in the context of underground natural gas storage, CO_2 sequestration, or enhanced oil recovery. Research on effective H_2 diffusivity is still limited, with only a few experimental attempts carried out on liquid-saturated rocks. For instance, the effective H_2 diffusivity was assessed in water-saturated samples of Bentheim sandstone, Werra rock salt, and Opalinus Clay, yielding values in the order of 10^{-9} m^2/s (Strauch et al., 2023). Jacops et al. (2015) performed a study to evaluate the H_2 diffusivity in water-saturated Boom Clay, with the aim of achieving a comprehensive understanding of the balance between gas generation and gas dissipation during the disposal of radioactive waste. The measured values for samples aligned parallel to the bedding were higher than those perpendicular to the bedding, both quantified in the order of 10^{-10} m^2/s. In another experimental study, Michelsen et al. (2022) quantified H_2 diffusivity in water-saturated rock specimens to assess the potential for H_2 loss through cap rocks during UHS. The determined effective diffusivities were in the order of 10^{-11} m^2/s. Despite these efforts, systematic studies on diffusion coefficients of different gases in liquid or through various rocks with varying petrophysical properties are still limited. Jacops et al. (2017) determined diffusion coefficients of dissolved gases of differently sized molecules (He, Ne, H_2, Ar, CH_4, C_2H_6, and Xe) in water and water-saturated clayey and silty Boom Clay. The study investigated the influence of the molecular size of the diffusing species, anisotropy, and pore network geometry on diffusive transport. The diffusion coefficients, in both water and Boom Clay, were found to be inversely related to the kinetic diameter of gases. Furthermore, the study observed that variations in grain size, which significantly affect hydraulic conductivity, resulted in only minor changes in the diffusion coefficients.

In the experimental studies addressing gas diffusivity, the amount of gas that diffuses into liquid is determined either by direct or indirect techniques. Direct methods measure the diffusion coefficient by analyzing changes in the composition of the diffusing species along the length of the sample over time, providing a spatial gradient of concentration (Ratnakar & Dindoruk, 2015; Schmidt, 1989). Direct diffusion experiments can be performed in various ways. One approach involves gas transport through a water-saturated rock, with gas concentrations measured in the aqueous phase (Hanebeck, 1995; Jacops et al., 2013; Schlömer & Krooss, 1997). In another approach, gas reservoirs are in direct contact with the water-saturated rock, and concentrations are measured directly from the gas phase using gas chromatography (GC), mass spectrometry (MS) (Hogeweg et al., 2024; Michelsen et al., 2023) or a hydrogen sensor (Strauch et al., 2023). These different approaches may lead to discrepancies in the measured diffusion coefficients. Strauch et al. (2023) determined the hydrogen diffusivity in Opalinus Clay under in-situ saturation using the latter approach, finding value 1-2 orders of magnitude higher than those obtained by (Krooss, 2008) and (Jacops et al., 2017) through the former approach. This discrepancy can be attributed to the use of gaseous hydrogen instead of dissolved hydrogen, potentially leading to partial drying of the pore system. However, these techniques tend to be expensive and time-consuming as they require compositional analysis using techniques such as mass spectrometry or chromatography. In contrast, indirect techniques measure changes in physical properties of the gas-liquid system rather than gas concentration (Riazi, 1996). Indirect techniques typically rely on measuring various physical properties such as gas pressure (Ratnakar & Dindoruk, 2015; Schmidt, 1989; Upreti & Mehrotra, 2002), volume of dissolved gas (Jamialahmadi et al., 2006; Renner, 1988), interface velocity (Das & Butler, 1996; Grogan et al., 1988), or magnetic field strength (Wen & Kantzas, 2005). The most popular indirect technique is measuring pressure decay within a constant volume cell at a constant temperature. This technique provides a temporal evolution of gas pressure as gas dissolves in a liquid in a closed system. This evolution is then converted to the amount of diffused species using the equation of state for real gas and subsequently a suitable diffusion model is applied to determine the gas diffusion coefficient.

Several researchers have employed the pressure decay method to investigate gas diffusion in liquid-saturated porous media (Gao et al., 2019; Li et al., 2016; Li et al., 2006; Lv et al., 2019). In the experiments carried out by Gao et al. (2019), the diffusivity of CO_2 in oil-saturated pore space was determined in the direction parallel to the symmetry axis of the

cylindrical test samples (i.e., axial direction). They developed a mathematical model that incorporates both porosity and tortuosity to evaluate CO_2 diffusivity based on pressure recording. The study investigated four different types of artificial rocks with varying permeability values under pressure and temperature conditions ranging from 15 to 30 MPa and 20 to 80 °C, respectively. The results indicated that the model could accurately predict the pressure data and CO_2 diffusivity. Furthermore, it has been shown that the measured effective diffusivities correlate positively with permeability and inversely with tortuosity. Li et al. (2006) suggested an experimental method and derived a mathematical model to measure the diffusion coefficient of CO_2 in brine-saturated Berea and Bentheim rock specimens within a pressure range of 2.4 to 7.3 MPa. Their experimental approach involved sealing the two end faces of the core and allowing gas to diffuse solely in radial direction. This design increases the diffusion area and enables a larger volume of gas to transfer per time interval, resulting in more representative measurements. The mathematical model predicted the experimentally recorded pressure drop over time with good agreement. However, no correlation has been found for effective diffusivities and other petrophysical properties.

This study aims to address the knowledge gap concerning the diffusion coefficients of various gases, particularly hydrogen, in water-saturated rocks using the pressure decay technique. Experiments were conducted on four porous sandstones from Lower Cretaceous (Bentheim and Obernkirchen) and Triassic (Grey and Red Weser) formations, which are reservoir analogues for underground gas storage. Furthermore, the study demonstrates the effectiveness of the pressure decay technique in determining the diffusion coefficients of various gases in both water and water-saturated rocks.

4.2. Theoretical background

4.2.1. Mathematical model to determine the diffusion coefficient in water

The analytical model for determining the gas diffusion coefficient in water, as proposed by Ratnakar and Dindoruk (2015), is as follows:

$$\rho_g(t) - \rho_{g\infty} = \beta\exp(\gamma t), \quad \beta = \frac{2\rho_{g0}}{\left(1+\alpha H_{cc}+\frac{\lambda_1^2}{\alpha H_{cc}}\right)}, \quad \text{and} \quad \gamma = \frac{-\lambda_1^2 D}{h_L^2} \tag{4.1}$$

Here, subscripts ∞ and 0 denote the equilibrium and initial conditions for gas density [kg/m^3], respectively, β is the rate coefficient of pressure decay representing the driving

force behind the dissolution process [kg/m^3], γ refers to the exponent factor indicating the rate of pressure decay at late times [1/s]. The other parameters include H_{cc}, representing Henry's constant at a constant temperature [-], α, the volume ratio of the liquid phase to gas phase, h_L, the height of water in the diffusion cell [m], and D, the gas diffusion coefficient [m^2/s], and λ_1, can be approximated by the following equation:

$$\lambda_1 \to \frac{\pi}{2} + \frac{2}{\pi}\alpha H_{cc} \text{ with } \alpha H_{cc} \ll 1 \tag{4.2}$$

The assumptions and derivation process are explained in detail in Appendix B.1

4.2.2. Mathematical model to determine the effective diffusion coefficient in water-saturated rock

According to Li et al. (2006), the effective gas diffusion coefficient in water-saturated rocks during radial gas diffusion can be calculated using the following equation:

$$\Delta P_g = \frac{ZRTN_\infty}{V_g}\left(1 - \sum_{n=1}^{\infty} \frac{4}{r_0^2 \alpha_n^2} exp(-D_{eff}\alpha_n^2 t)\right) \tag{4.3}$$

where, ΔP_g refers to the pressure drop [Pa] at time t [s], V_g denotes the gas phase volume (i.e., the sum of the reference cell and the diffusion volumes, excluding the bulk volume of the rock specimen) [m^3], Z is the gas compressibility, R is the universal gas constant [8.314 J/(mol·K)], and T is temperature [K], N_∞ is the maximum amount of gas that will eventually diffuse into water [mol], D_{eff} is the effective diffusion coefficient [m^2/s], and α_n are the positive roots of the first kind of Bessel function of zero order as follows:

$$J_0(r\alpha_n) = 0 \tag{4.4}$$

Li et al. (2006) approximated equation (4.3) as a linear relationship between ΔP_g and $\sqrt{t}$, with the slope of k_1, providing an initial estimate for D_{eff}

$$\Delta P_g = k_1\sqrt{t} \tag{4.5}$$

With

$$k_1 = \frac{4ZRTN_\infty}{r_0 V_g}\sqrt{\frac{D_{eff}}{\pi}} \tag{4.6}$$

Appendix B.2 provides a detailed explanation of the assumptions and derivation process.

The effective gas diffusion coefficient in a water-saturated rock is a function of the corresponding gas diffusivity in water and the restrictive effects of the microstructure. These effects are attributed to porosity ($\emptyset$), tortuosity (τ) and constrictivity (δ). Porosity represents the reduction in available surface area for diffusion, tortuosity describes the deviation of diffusion pathways from a straight pathway, and constrictivity introduces transport resistance that inversely relates to the width of bottlenecks. Constrictivity depends on the ratio of the diffusing molecular diameter to the pore diameter. Thus, the relationship between the effective diffusivity and its corresponding value in water is expressed as follows (Grathwohl, 1998):

$$D_{eff} = D\emptyset\delta/\tau \tag{4.7}$$

Constrictivity becomes relevant when the size of the species approaches that of the pore (Shen & Chen, 2007), however, for pores larger than 1 nm, its value is approximately 1 (Grathwohl, 1998). In addition, in most experimental studies, its effect was implicitly included in tortuosity due to the lack of a suitable measurement techniques (Holzer et al., 2013). Furthermore, the diffusive flux in porous media is expressed in two ways in the literature (Bear, 1972; Cussler, 1997; Krooss et al., 1992; Liu et al., 2012). It can be determined by measuring gas concentration gradients either within the bulk volume (C_r) or within the pore volume (C). The diffusion coefficients obtained from these approaches are related as follow (Li et al., 2006):

$$D^r_{eff} = \emptyset D^p_{eff} \tag{4.8}$$

where, D^r_{eff} represents the diffusion coefficient determined based on C_r, while D^p_{eff} corresponds to the diffusion coefficient derived from C. Since porosity is already accounted for in the definition of D^r_{eff}, equation (4.7) is simplifies as follows, assuming a constrictivity factor 1 (Li et al., 2006):

$$D^r_{eff} = D/\tau \tag{4.9}$$

4.3. Materials and methods:

4.3.1. Samples

This study investigated core samples obtained from four distinct sandstone formations, chosen as analogs for underground gas storage reservoirs, characterized by a wide range of permeabilities from 10^{-12} to 10^{-17} m^2 (Arekhov et al., 2023; Nolte et al., 2021a; Peksa et al.,

2015). Cylindrical plugs (diameter ≈ 14.85 mm; length ≈ 34.8 mm) were drilled from outcrop blocks. The sandstone formations investigated include the Lower Cretaceous (Valanginian) Bentheim sandstone from the westernmost Lower Saxony Basin, Germany, the Triassic (Olenekian) Grey (GWS) and Red Weser sandstone (RWS) from the Lower Solling Formation of the Reinhardswald Basin, Germany, and the Lower Cretaceous (Berriasian) Obernkirchen (OBK) sandstone from the Lower Saxony Basin, Germany. Comprehensive descriptions of these rock specimens are documented in Khajooie et al. (2024a).

4.3.2. Experimental setup and procedure

4.3.2.1 Setup

Gas diffusion coefficients in water and water-saturated rocks were determined in two similar setups: one with three high-pressure diffusion cells (Figure 4.1) and another with a single cell. Each cylindrical diffusion cell (V_{sc} = 19.5 to 27.7 mL), was equipped with a welded Keller pressure transducer with a precision of ±0.1 kPa (±0.01% of the full scale range: 1.0 MPa) and a capillary connected to a multi-positioning selector valve (Valco). The diffusion cells were sealed with stainless steel porous filters (*FITOK Snubber gasket with silver coating for additional sealing*) and intermittently linked to the selector valve ports, with a port in between for a closed position. The selector valve was also connected to a reference cell (V_{ref} = 83.9 mL), which ensured that the pressurized gas reached the equilibrium temperature before expansion to the diffusion cells. Valves 1 & 2 were installed before the reference cell to connect the system to different gas bottles (He, H_2, Ar, CO_2, and CH_4) for pressurizing, or a vacuum pump for evacuation. In our setup, O-rings were deliberately excluded to prevent any interaction between gas molecules and rubber or FKM (Viton) seals, which could cause swelling. The entire system was placed in an oven, and the temperature was maintained at 35 ± 0.1 °C (Figure 4.1). The temperatures of the diffusion cells and the reference cell were measured using their corresponding transducers directly connected to them. Prior to diffusion measurements, a leak test with helium was performed on all reference and diffusion cells at a pressure of 1.0 MPa with recorded leak rates ranging from 0.001 to 0.01 kPa/h. The pressure stability of the system revealed that temperature fluctuations had a negligible effect on the pressure within ±0.1 kPa for a period of 10 h. Furthermore, the volume calibration of reference and diffusion cells as well as their corresponding pressure transducers and capillaries was performed by the expansion of

helium into the system from a known volume. The maximum pressure applied for calibration was 1.0 MPa, and the coefficient of variations of the measured volumes ranged from 0.08 to 0.46 %. The blank experiments (detailed in Appendix B.3) were conducted on all cells with helium to establish the baseline for pressure transducer recordings.

4.3.2.2 Deionized degassed water

The water used in the diffusion experiments was deionized and degassed. Degassing was achieved by evacuating the water samples in a desiccator for 24 hours.

4.3.2.3 Gas diffusion experiments in bulk water

To measure the diffusion coefficient of gases in water, approximately 10 mL of water was added to each cell. Then, the reference cell and a diffusion cell, along with their respective capillaries and pressure transducers, were evacuated. Subsequently, the reference cell was pressurized with either H_2, He, CH_4, Ar, or CO_2 to a desired pressure and allowed to temperature-equilibrate for 2 hours. The respective gas was then expanded into the diffusion cell, after which the cell was closed. Next, the pressure decay within the cell was continuously monitored. Similar procedures were repeated to conduct diffusion experiments in other cells. The diffusivities of all aforementioned gases in water were measured at 1.0 MPa.

4.3.2.4 Setup validation

The validation of the setup was assessed by conducting repeatability tests with H_2 and CH_4 in water, each in a separate diffusion cell at 0.5 and 0.2 MPa, respectively. Furthermore, setup-independency was tested by parallel measurements in different cells using the same gas and maintaining consistent boundary conditions. Hereby, CH_4 diffusivities in water were determined simultaneously in four cells at a pressure of 1.0 MPa. These finding were compared with corresponding values reported in the literature under similar boundary conditions. Furthermore, a repeatability test was conducted on the water saturated Bentheim rock specimen to determine the effective diffusivity of H_2 at a pressure of 1.0 MPa. The procedures for these experiments are detailed in Chapter 3.2.5.

4.3.2.5 Gas diffusion experiments in water-saturated rock specimens

The rock specimens were prepared for experiments by sealing their two end faces using epoxy resin *(Araldite XW396),* allowing it to solidify over a 24-hour period. The dry rock specimens were weighed and immersed in water within an evacuated desiccator to achieve

full saturation. To verify full saturation, the weight difference before and after saturation was compared to the pore volumes measured using He-pycnometry and water immersion porosimetry techniques. Upon completion of the preparation process, the saturated rock specimens were positioned within the cells, and the diffusion experiments were carried out following the procedures detailed in Chapter 3.2.3. These experiments were conducted under a pressure of 1.0 MPa to ascertain the diffusivity of H_2, CH_4, and CO_2 within individual water-saturated rock specimens.

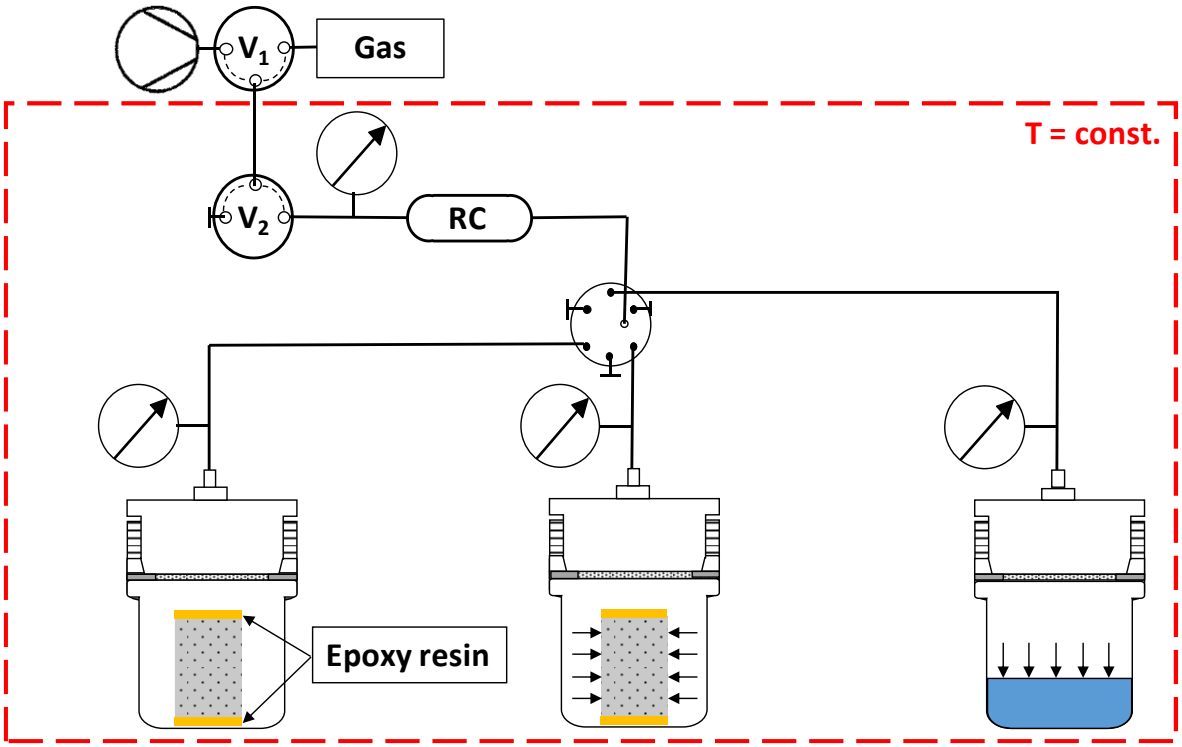

Figure 4.1. Experimental setup for measuring gas diffusion in water and water-saturated rock specimens using the pressure decay method. The top and bottom end faces of the rock specimens were sealed with epoxy resin (yellow color) to enable gas diffusion exclusively in the radial direction (as denoted by the horizontal arrows) through the porous column. Gas diffusion tests in water were conducted vertically (as indicated by the vertical arrows), from top to bottom.

4.3.3. Pore volume measurement

The pore volume of cylindrical rock specimens was determined through He-pycnometry and water immersion porosimetry methods. These techniques are well-documented in the literature, offering comprehensive explanations of the equipment and methodology employed (Gaus et al., 2019; Hu et al., 2021).

4.4. Results and discussion

4.4.1. Determination of gas diffusion coefficients in water

The measured pressures during a CH_4 diffusion test in water (P = 1.0 MPa; T = 35°C) were evaluated with the mathematical model outlined in Chapter 2.1 to determine the diffusion coefficient. Gas densities were calculated from the recorded pressures and temperatures using the GERG-2008 equation of state (Kunz & Wagner, 2012) and subsequently plotted against time (Figure 4.2a). As the experiment continued until pressure equilibrium was reached, the final equilibrated density ($\rho_{g\infty}$) was obtained by averaging the density readings at this phase (after 200 h), resulting in a value of 6.084 kg/m^3. To linearize the data, $\ln(\rho_g(t) - \rho_{g\infty})$ was plotted against time, facilitating the preliminary determination of γ and β, which were found to be 0.022 1/h and 0.192 (exp(-1.65)) kg/m^3, respectively, as derived from the slope and intercept (Figure 4.2b). These parameters were subsequently fine-tuned employing an optimization algorithm to align the model with experimental observations. The optimized values for γ and β were determined to be 0.021 1/h and 0.188 kg/m^3, respectively. Ultimately, the gas diffusion coefficient was determined using equation (4.1), by with γ, λ_1 (1.6) and h_L (0.033 m) known, resulting in a value of 2.59·10^{-9} m^2/s.

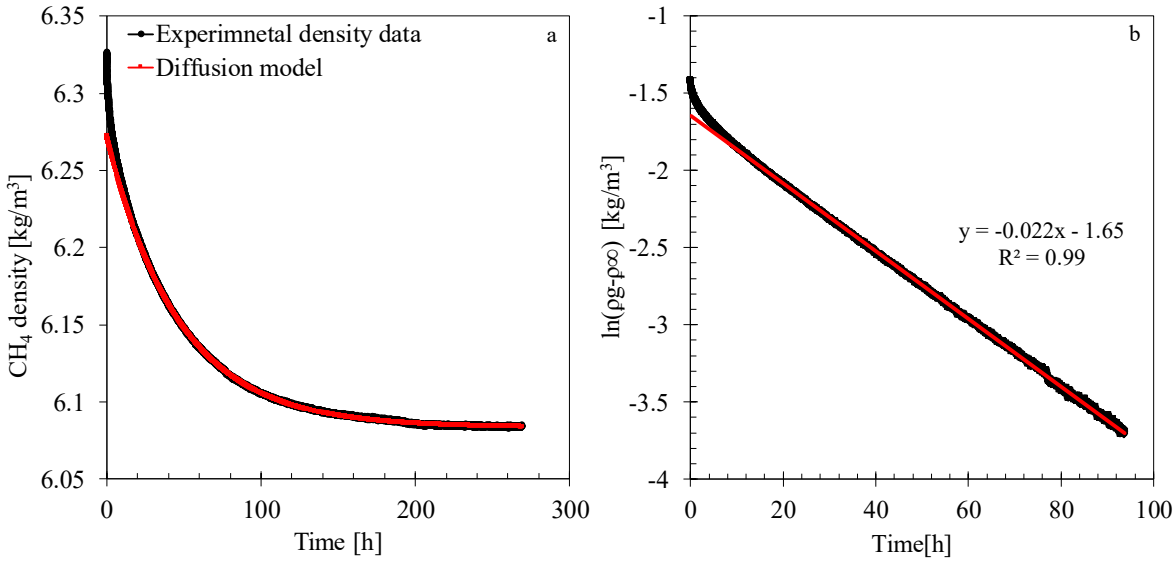

Figure 4.2. Comparison of the density derived from pressure decay measured during CH_4 diffusion in water with the model after regression (a), semi-log plot of $(\rho_g(t) - \rho_{g\infty})$ against time, representing the driving force for gas dissolution, to derive the γ and β values as the slope and intercept of the plots, respectively (b).

4.4.2. Determination of gas diffusion coefficients in water-saturated rock specimens

The pressure decay recorded during the CH_4 diffusion experiment on water-saturated OBK (Figure 4.3a) was analyzed by the mathematical model presented in Chapter 2.2. This evaluation was performed after subtracting the pressure drop observed during the blank experiments, in order to eliminate the impact of this artifact (see Appendix B.3). The experiment was carried out at a pressure of 1.14 MPa and a temperature of 35 °C. The pressure drop (ΔP) was calculated and plotted against the square root of time, revealing four distinct zones characterized by their slopes (Figure 4.3b). In the initial stage, marked in blue, pressure decline occurs more rapidly than in the subsequent linear phase (Figure 4.3b). This deviation, similarly observed in other diffusion studies, was dismissed, as the subsequent linear portion holds greater relevance in determining the diffusion coefficient (Caskey et al., 1973; Reamer et al., 1956; Renner, 1988; Tan & Thorpe, 1992). The observed positive intercept primarily arises from the dissolution of gas into the water film surrounding the outer surface of the rock specimen, thereby establishing a stable gas concentration at the gas-water interface. Consequently, this period is commonly referred to as the "incubation region" (Renner, 1988). While fluctuations in temperature and pressure resulting from gas expansion into the diffusion cell may play a role during this phase, their influence is minor in comparison to gas dissolution (Li et al., 2016; Li et al., 2006). The linear phase (yellow zone), known as the steady-state diffusion stage (Caskey et al., 1973; Reamer et al., 1956; Renner, 1988; Tan & Thorpe, 1992), represents transfer of gas molecules from the gas-liquid interface toward the center of rock specimens. Subsequently, the plot of ΔP versus $\sqrt{t}$ begins to deviate from linearity, leading to a transition (green zone), which indicates that gas molecules have reached the center of the rock specimens. This suggests that the assumption of the semi-infinite diffusion pathway is no longer applicable (Renner, 1988). However, this assumption remains valid and introduces minimal uncertainties in interpreting the data, provided that the liquid phase contains less than half the gas necessary for full saturation (Pomeroy et al., 1933). Finally, when the gas concentration within the water-saturated rock specimen becomes equal to that on the outer surface, thereby eliminating concentration gradients, the stabilized phase (orange zone) occurs.

An initial approximation of the diffusivity was derived by applying equation (4.6), yielding a value of $2.32 \cdot 10^{-9}$ m^2/s. This was obtained from the slope of the linear relationship

between ΔP and $\sqrt{t}$ during the steady-state diffusion phase. Subsequently, the initial mathematical model was developed, allowing for the quantification of the additional ΔP during the incubation stage by calculating the average deviation between the model and experimental data. This enabled correction of the experimental dataset. The effective gas diffusivity was then accurately determined by fitting the mathematical model to the corrected experimental data in this phase (Figure 4.3b), resulting in an adjusted value of $3.7 \cdot 10^{-9}$ m^2/s. As depicted in the plot, the theoretical ΔP intersects the origin, whereas extrapolating the straight part of experimental data to $\sqrt{t} = 0$ yields a positive intercept, indicative of a deviation in the incubation phase.

The analysis of steady-state diffusion stage across all measurements indicates that this phase maintains linearity until the total quantity of diffused gas reaches between 50 and 75% of the saturation limit. Therefore, when the recorded gas uptakes achieve 50% of full saturation, assuming the setup is leak-tight, the experimental results can be confidently evaluated. This is because only the linear portion of the plot is relevant for determining the diffusion coefficient. The influence of leak rate on experimental outcomes has been examined, revealing that the measurements remain unaffected by leak rates on the order of 10^{-2} kPa/h.

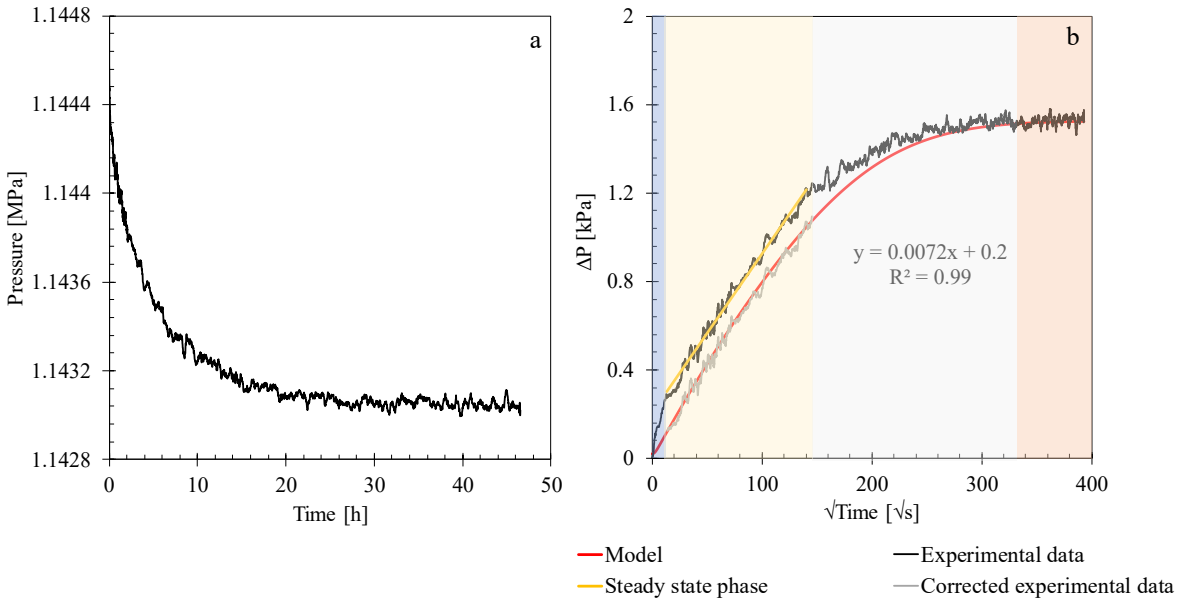

Figure 4.3. Pressure decay observed during the CH_4 diffusion experiment on water-saturated OBK over time (a), and comparison between the corrected experimental ΔP plotted against the square root of time (√t) with the ΔP derived from the mathematical model (b). The experimental ΔP plot delineates four distinct zones: the incubation (blue shading), the steady-state diffusion (yellow shading), the transition (green shading), and stabilized stages (orange shading).

4.4.3. Data validity and accuracy

A series of experiments were conducted to thoroughly evaluate the reliability and accuracy of the setup. This involved reproducing the diffusion coefficients of H_2 and CH_4 in water as reported by Jähne et al. (1987), which were $6.2 \cdot 10^{-9}$ and $2.4 \cdot 10^{-9}$ m^2/s, respectively. These values were determined by measuring the gas concentration at a pressure of 0.1 MPa and a temperature of 35 °C without applying any pressure gradient. Jähne et al. (1987) reported a maximum systematic error of 5% or less. To validate our findings, five repeatability tests of H_2 and CH_4 diffusivities in water have been conducted using a specific cell for each gas, under pressure of 0.5 and 0.2 MPa (T = 35 °C), respectively. The results of these experiments are illustrated in Figure 4.4a. The observed diffusion coefficients of H_2 and CH_4 in water ranged from $6.3 \cdot 10^{-9}$ *to* $7.0 \cdot 10^{-9}$ m^2/s and $2.3 \cdot 10^{-9}$ *to* $2.9 \cdot 10^{-9}$ m^2/s, respectively, with corresponding standard deviations of $0.3 \cdot 10^{-9}$ and $0.3 \cdot 10^{-9}$ m^2/s, indicative of the reproducibility of our measurements. Furthermore, the average measured diffusivities for H_2 and CH_4 were $6.7 \cdot 10^{-9}$ and $2.7 \cdot 10^{-9}$ m^2/s, respectively, showing a minor deviation of 5.1% and 6.8% from literature values, emphasizing good agreement. Furthermore, a comparability assessment was conducted to evaluate the findings derived from four diffusion cells within the experimental setup. This entailed measuring the diffusivity of CH_4 in water across four cells, under consistent boundary conditions of 1.0 MPa pressure and 35 °C temperature. As depicted in Figure 4.4a, the measured diffusion coefficients ranged from $2.6 \cdot 10^{-9}$ to $3.1 \cdot 10^{-9}$ m^2/s, with the standard deviation of $0.2 \cdot 10^{-9}$ m^2/s, indicating consistent experimental findings regardless of the specific diffusion cell used. It is worth noting that the experiments were conducted at higher pressures than those reported in the literature to enhance the accuracy of measurements. It was observed that experiments performed at lower pressures experienced significant pressure fluctuations, likely due to minor temperature variations, which impeded the accurate determination of diffusivity. Additionally, the effect of pressure on the diffusion coefficient is negligible, as discussed in detail in Chapter 4.4.

Moreover, to evaluate the accuracy and reliability of gas diffusivity measurements in water-saturated rocks, five experiments were conducted to reproduce the diffusion of H_2 in water-saturated Bentheim. A comparative analysis was then performed against existing literature (Figure 4.4b). Diffusivity values for H_2 measured in this study ranged between $1.9 \cdot 10^{-9}$ and $3.4 \cdot 10^{-9}$ m^2/s, with an average of $2.9 \cdot 10^{-9}$ m^2/s and a standard deviation of $0.6 \cdot 10^{-9}$ m^2/s. The consistently low standard deviations indicate a sufficient reproducibility of diffusion

measurements within water-saturated rocks. Furthermore, H_2 diffusivity in water-saturated Bentheim utilizing a direct method (Strauch et al., 2023) was similar at $1.6 \cdot 10^{-9}$ m^2/s.

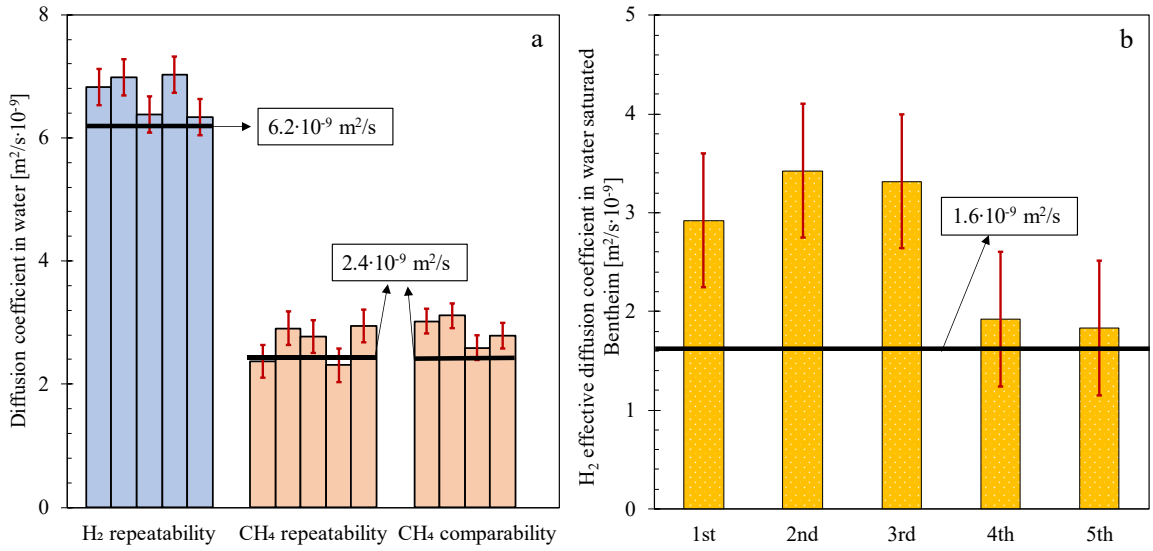

Figure 4.4. The diffusion coefficients of H_2 and CH_4 in water, as determined in repeatability and comparability tests, were compared with corresponding literature data (Jähne et al., 1987) (a). The repeatability tests for H_2 and CH_4 were conducted at pressures of 0.02 MPa and 0.05 MPa, respectively. The comparability tests involved comparing results obtained from different diffusion cell. These experiments, whichmeasured CH_4 diffusivity in water across four cells, were performed at a pressure of 1.0 MPa. All tests were conducted at a temperature of 35 °C. Comparison of five measurements of the H_2 effective diffusion coefficient in water-saturated Bentheim sandstone (P = 1.0 MPa; T = 35 °C) against literature value (Strauch et al., 2023) (b).

4.4.4. Diffusion of gases in water

The diffusion coefficients of H_2, He, CH_4, Ar, and CO_2, were precisely determined under consistent boundary conditions of 1.0 MPa and 35 °C. The findings from these experiments, as well as those from reproducibility and comparability assessments detailed in Chapter 4.3, are presented in Table 4.1 and depicted in Figure 4.5. The mean diffusivities for H_2 and CH_4 are $6.7 \cdot 10^{-9}$ and $2.8 \cdot 10^{-9}$ m^2/s, respectively, with standard deviations of $0.3 \cdot 10^{-9}$ for both gases. The observed diffusivity values for He, Ar and CO_2 in water are $9.6 \cdot 10^{-9}$, $10.9 \cdot 10^{-9}$ and $44.56 \cdot 10^{-9}$ m^2/s, respectively.

The diffusion coefficients of the gases under examination in water were already determined through a range of direct methods including Raman spectroscopy (Chen et al., 2018; Guo et al., 2013), capillary cell (Sahores & Witherspoon, 1970; Witherspoon & Saraf, 1965) , diaphragm cell (Gubbins et al., 1966; Vivian & King, 1964), and modified Barrer (Jähne et al., 1987), Taylor dispersion (Cadogan et al., 2014; Frank et al., 1996) across various pressures and temperatures, often differing from those employed in our research.

Table 4.1. Overview of the measured diffusion coefficients of H_2, H_2, CH_4, Ar, and CO_2 in water under indicated pressures and 35 °C.

Gas	Pressure [MPa]	Temperature [°C]	Diffusion coefficient [$\cdot 10^{-9}$ m^2/s]
H_2	0.5	35.0	6.8
	0.5	35.0	7.0
	0.5	35.0	6.4
	0.5	35.0	7.0
	0.5	34.9	6.3
CH_4	0.2	36.6	2.4
	0.2	36.6	2.9
	0.2	36.6	2.8
	0.2	36.6	2.3
	0.2	36.6	2.9
	1.0	36.6	3.0
	1.0	34.9	3.1
	1.0	36.2	2.6
	1.0	34.8	2.8
He	0.9	36.6	9.6
Ar	1.0	36.6	10.9
CO_2	1.0	34.9	44.6

All these techniques determine the diffusion coefficient by analyzing the gas concentration in the liquid phase. At a given pressure, increasing the temperature leads to higher diffusion coefficients. This behavior likely arises from the increased kinetic energy of gas and water molecules, as well as a reduction in water viscosity, which facilitates diffusive mass transport (Upreti & Mehrotra, 2002). The Stokes-Einstein relation describes this temperature dependence, indicating that the product of the diffusion coefficient and viscosity is directly proportional to temperature (Guo et al., 2013):

$$D = \frac{k_B(T+273.15)}{6\pi\mu r_s} \tag{4.10}$$

here, k_B is the Boltzmann constant [$1.38 \cdot 10^{-23}$, J/K], T is temperature [°C], μ represents viscosity of water, and r_s [nm] is the radius of the diffusing solute molecule. Assuming r_s remains constant with temperature, the diffusion coefficient at desired temperature (T_2=35 °C) can be determined from its corresponding value at T_1 using known water viscosities at these temperatures (Li, 2006):

$$D_{T_2} = \frac{D_{T_1}\mu_{T_1}(T_2+273.15)}{(T_1+273.15)\mu_{T_2}} \tag{4.11}$$

Conversely, several researchers have reported that the impact of pressure on gas diffusivities in water is negligible. Guo et al. (2013) conducted an investigation into the diffusion coefficients of CH_4 in water across a range of pressures from 5 to 40 MPa. Their investigation revealed a minor discrepancy of only 3 % between the lowest and highest

measured values (Table 4.2). In another study, Sachs (1998) examined CH_4 diffusivities in water within a pressure range of 7.6 to 32.5 MPa, maintaining a constant temperature of 50 °C. While this study suggested the potential impact of pressure on diffusion coefficients, it is found that within the specified pressure range, CH_4 diffusivities varied from $3.6 \cdot 10^{-9}$ to $3.2 \cdot 10^{-9}$ m^2/s. Furthermore, two experimental studies were carried out to explore the diffusion behavior of CO_2 in water across a pressure range of 10 MPa to 45 MPa. Similarly, these investigations inferred that the impact of pressure on CO_2 diffusion coefficients in water remained minimal within the examined ranges (Cadogan et al., 2014; W. Lu et al., 2013). However, research conducted by Renner (1988) on CO_2 diffusivity in 0.25M NaCl brine at a temperature of 38°C, across a pressure range of 1.5 to 5.8 MPa, revealed an upward trend in diffusivity with increasing pressure. The latter investigation has been performed through the monitoring of volume changes over time under constant pressure. The observed diffusivities ranged from $3.0 \cdot 10^{-9}$ to $7.3 \cdot 10^{-9}$ m^2/s across the examined pressure range, surpassing those previously documented in the literature (Table 4.2).

Diffusion coefficients for H_2, He, CH_4, Ar, and CO_2 derived from literature (Table 4.2) were averaged, resulting in values of $6.2 \cdot 10^{-9}$, $8.3 \cdot 10^{-9}$, $2.1 \cdot 10^{-9}$, $2.5 \cdot 10^{-9}$, and $2.4 \cdot 10^{-9}$ m^2/s, respectively, with corresponding standard deviations of $1.1 \cdot 10^{-9}$, $1.7 \cdot 10^{-9}$, $0.1 \cdot 10^{-9}$, $0.7 \cdot 10^{-9}$, and $0.2 \cdot 10^{-9}$ m^2/s. These values are in good agreement with our experimentally obtained diffusion coefficients, particularly for H_2, CH_4, and He (Figure 4.5). However, the observed diffusivity values for Ar and CO_2 in water demonstrate significant discrepancies compared to the literature data. Measured diffusion coefficients for Ar and CO_2 amount to $10.9 \cdot 10^{-9}$ and $44.6 \cdot 10^{-9}$ m^2/s, respectively, representing one order of magnitude higher than their corresponding literature values. This significant discrepancy can be attributed to the formation of a denser layer at the gas-liquid interface, caused by dissolution of the CO_2 and Ar molecules. The change in water density is governed by the concentration of gas in water and the molar mass-to-molar volume ratio of the dissolved gas molecules. Previous experimental and modeling studies have shown that CO_2 and Ar dissolution increases water density, while CH_4 dissolution leads to a decrease (Duan & Mao, 2006; Watanabe & Iizuka, 1985). This occurs because the molar volume of any gas dissolved in water is greater than that of pure water; thus, the dissolution of CH_4, with a molar mass of 16 g/mol-lower than that of water (18 g/mol)-results in a reduction in density. Consequently, the measured CH_4 diffusivity in water remains unaffected by density-driven convection, despite its solubility being similar to that of Ar (Sander, 2015).

Table 4.2. Compilation of experimental and calculated diffusion coefficients for H_2, H_2, CH_4, Ar, and CO_2 in water, derived from various methodologies under different pressures and temperatures. To ensure consistency, diffusion coefficients were adjusted to 35 °C using the Dμ/T constant, considering the differing temperature conditions of the original measurements.

Gas	Pressure [MPa]	Diffusion coefficient [$\cdot 10^{-9}$ m^2/s]	Method (reference)	Gas	Pressure [MPa]	Diffusion coefficient [$\cdot 10^{-9}$ m^2/s]	Method (reference)
CH_4	5	2.1	Raman spectroscopic (Guo et al., 2013)	H_2	0.1	5.1	Diaphragm cell (Gubbins et al., 1966)
	10	2.1			0.1	5.5	Laminar dispersion (Ferrell & Himmelblau, 1967)
	20	2.1			0.1	7.6	Bubble collapse (Wise & Houghton, 1966)
	30	2.1			0.1	6.1	Diaphragm cell (Vivian & King, 1964)
	40	2.1			0.1	6.3	Dissolution of bubbles Hughton (Houghton et al., 1962)
	0.1	2.2	Capillary cell (Sahores & Witherspoon, 1970)		0.1	6.8	Wetted sphere (Baird & Davidson, 1962)
	0.1	2.1	Capillary cell (Witherspoon & Saraf, 1965)		0.1	8.9	Wetted sphere (Davidson, 1957)
	0.1	2.3	Diaphragm cell (Gubbins et al., 1966)		0.1	5.2	Rising bubble (Gertz, 1954)
	8.0	2.3	Pressure decay (Sachs, 1998)		0.1	5.7	Polarography (Aikazyan & Fedorova, 1952)
	0.1	2.0	Moving boundary (Maharajh & Walkley, 1973)		0.1	5.1	Gel (Tammann, 1929)
	0.1	2.4	Modified Barrer (Jähne et al., 1987)		0.1	6.2	Modified Barrer (Jähne et al., 1987)
	10.3	2.0	Raman spectroscopic (Chen et al., 2018)	CO_2	14	2.6	Taylor dispersion (Cadogan et al., 2014)
	0.1	2.1	Theoretical study (Oelkers, 1991)		31.6	2.7	Taylor dispersion (Cadogan et al., 2014)
He	0.1	7.6	Laminar dispersion (Ferrell & Himmelblau, 1967)		47.7	2.9	Taylor dispersion (Cadogan et al., 2014)
	0.1	7.9	Bubble collapse (Wise & Houghton, 1966)		0.1	2.5	Moving boundary (Maharajh & Walkley, 1973)
	0.1	8.1	Diaphragm cell (Vivian & King, 1964)		0.1	2.4	Modified Barrer (Jähne et al., 1987)
	0.1	8.1	Dissolution of bubbles (Houghton et al., 1962)		0.1	2.5	Taylor-Aris dispersion (Frank et al., 1996)
	0.1	12.1	Wetted sphere (Baird & Davidson, 1962)		10	2.1	Raman spectroscopic (W. Lu et al., 2013)
	0.1	6.1	Rising bubble (Gertz, 1954)		20	2.4	
	0.1	8.5	Modified Barrer (Jähne et al., 1987)		30	2.2	
Ar	0.1	1.8	Moving boundary (Maharajh & Walkley, 1973)		40	2.0	
	0.1	3.2	Bubble collapse (Wise & Houghton, 1966)		1.54	3.1	volume of dissolved gas (Renner, 1988)
					2.92	3.6	
					4.46	4.9	
					5.67	6.7	

The denser water layer formed by CO_2 and Ar establishes a distinct density gradient within the water column, thereby triggering convective transport phenomena. With convective transport exerting a dominant influence, the evaluation of pressure decay results in a non-representative diffusivity coefficient (Blair & Quinn, 1969; Gholami et al., 2015; Gill et al., 1997). Other researchers, employing the change in gas volume over time at constant pressure to ascertain the diffusivity of Ar in Benzene, have likewise documented this issue. (Bennett et al., 1968).

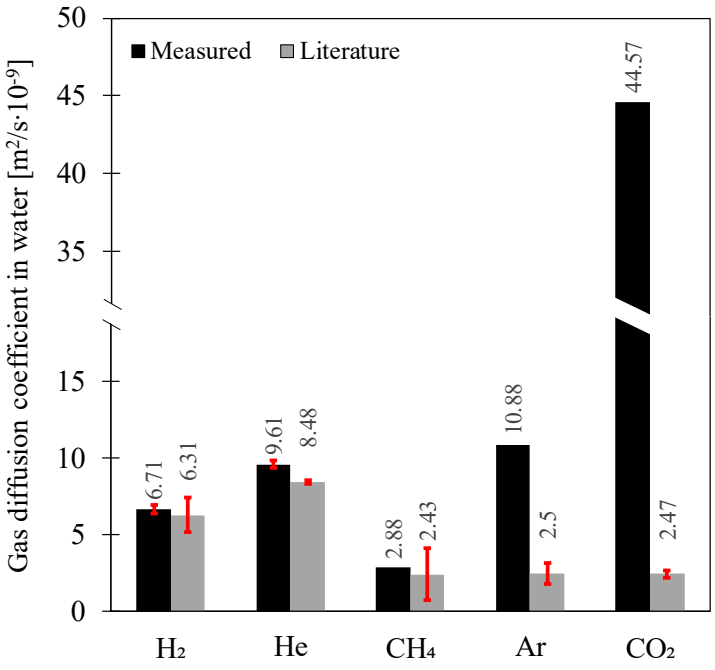

Figure 4.5. Comparison of measured diffusivities of H_2, He, CH_4, Ar, and CO_2 with their respective average values from the literature compiled in Table 4.2. The H_2 and CH_4 diffusivities were determined by averaging the results presented Chapter 4.3. While the diffusion coefficients of H_2, He, and CH_4 closely align with their published values, significant disparities are evident for Ar and CO_2 when compared to their corresponding literature data. Red bars indicate standard deviations.

4.4.5. Diffusion of gases into water-saturated rock specimens

Effective diffusion coefficients of H_2, CH_4, and CO_2 in water-saturated rock specimens from Bentheim, OBK, RWS, and GWS formations were determined and compared with the corresponding diffusion coefficients in water (Figure 4.6). The effective H_2 diffusivity ranges from $0.8 \cdot 10^{-9}$ to $2.9 \cdot 10^{-9}$ m^2/s, while the CH_4 and CO_2 effective diffusion coefficients vary from $0.3 \cdot 10^{-9}$ to $0.8 \cdot 10^{-9}$ m^2/s and from $0.2 \cdot 10^{-9}$ to $0.9 \cdot 10^{-9}$ m^2/s, respectively (Table 4.3). The effective diffusivity of H_2, CH_4, and CO_2 within water-saturated rock specimens investigated in this study has not been previously documented under identical pressure and temperature conditions. Nevertheless, two experimental studies have measured the effective diffusivities of H_2 and CO_2 in the water-saturated Bentheim sandstone, yielding

diffusivities of the same order of magnitude: $1.6 \cdot 10^{-9}$ m^2/s for H_2 (Strauch et al., 2023) and $0.5 \cdot 10^{-9}$ m^2/s for CO_2 (Li et al., 2006). The H_2 diffusivity was determined under ambient pressure and temperature by measuring the gas concentration gradient, while the CO_2 diffusivity was determined using the pressure decay method under conditions of 4.4 MPa pressure and 59 °C temperature.

To further characterize the rock specimens, the diffusive tortuosity was calculated using equation (4.9). The majority of pore throat diameters in the examined rock specimens were found to exceed 0.1 µm, while the molecular diameters of H_2, CH_4, and CO_2 are 0.29, 0.38, and 0.33 nm (Gnanasekaran & Reddy, 2013), respectively. Given that the ratio of molecular diameter to pore diameter is significantly less than 1, the constrictivity factor for these gases can thus be reasonably approximated as 1 (Grathwohl, 1998; Renkin, 1954). Furthermore, the diffusion model for water-saturated rocks used in this study has been developed in analogy to diffusion in bulk liquids (Li et al., 2006), indicating that porosity is incorporated into the diffusion coefficient. Therefore, equation (4.9) is appropriate for relating effective diffusivity to the value measured in water. The obtained values ranged from 2.2 to 3.0 for Bentheim, 4.2 to 6.3 for OBK, 4.4 to 6.5 for RWS, and 7.7 to 8.5 for GWS rock specimens depending on the gas type. As tortuosity increased from 2.6 to 8.1, the effective diffusivities of investigated gases decreased, with reductions ranging between 60% and 80% (Table 4.3). This suggests that the complex pore network and tortuous pathways substantially interfere with the diffusion process. The diffusive tortuosity for Bentheim sandstone has been previously determined through the measurement of CH_4 effective diffusivities in oil-saturated rock samples (pressure decay method) ranging from 2.7 to 4.1 (Li & Dong, 2010). As previously discussed, determining the CO_2 diffusion coefficient in water posed challenges possibly due to the interference of density-induced natural convection. Nevertheless, the similarity observed in the tortuosity derived from CO_2 measurements compared to those of H_2 and CH_4 measurements, suggests that the convective transport occurring during CO_2 diffusion in water was effectively impeded. This can be attributed to the presence of the porous medium acting as obstacle, resulting in diffusive transport dominating the process (Gholami et al., 2015). The comparable tortuosity values derived from different gas measurements suggest that CO_2 diffusion coefficients in water can be estimated indirectly. This approach involves measuring the effective CO_2 diffusivity in a rock specimen and utilizing the tortuosity obtained from other gas diffusivity measurements, such as CH_4 or H_2 which are not influenced by density-driven convection

(Li & Dong, 2010; Li et al., 2006). Thus, employing equation (4.9) allows for the computation of the CO_2 diffusion coefficient in water, resulting in values spanning from $2.3 \cdot 10^{-9}$ to $2.5 \cdot 10^{-9}$ m^2/s, which align well with those documented in the literature (Table 4.2). Likewise, Li & Dong (2010) conducted calculations of CO_2 diffusion coefficients in water, utilizing tortuosity values acquired from effective diffusion measurements of CH_4 within Berea and Bentheim sandstones. The outcomes revealed values within the range of $1.9 \cdot 10^{-9}$ to $2.7 \cdot 10^{-9}$ m^2/s, consistent with previously reported values (Table 4.2).

Table 4.3. Overview of the effective diffusion coefficients (D_{eff}) measured and tortuosities calculated for H_2, CH_4, and CO_2 within water-saturated specimens of Bentheim, OBK, RWS, and GWS. Additionally, the experimental average pressure, ΔP, gas cap volume (V), gas solubility (C_0), and gas compressibility (Z) are provided.

Sample	Gas	Average pressure (MPa)	ΔP (kPa)	V (cm^3)	C_0 (10^{-3}mol/cm^3)	Z	D_{eff} (10^{-9} m^2/s)	Tortuosity
Bentheim	H_2	1.016	1.70	15.12	7.39	1.006	2.90	2.2
	CH_4	0.964	15.23	19.28	11.02	0.986	0.80	3.0
	CO_2	1.075	38.43	21.54	291.75	0.950	0.90	2.7
OBK	H_2	1.092	1.35	14.28	7.97	1.006	1.49	4.2
	CH_4	1.144	1.52	21.38	13.49	0.983	0.39	6.3
	CO_2	1.075	29.75	21.38	291.95	0.950	0.43	5.7
RWS	H_2	1.038	1.25	14.02	7.59	0.985	0.96	6.5
	CH_4	1.059	1.93	14.02	12.12	0.984	0.55	4.4
	CO_2	1.086	19.66	21.46	294.94	0.950	0.47	5.3
GWS	H_2	1.037	0.63	13.80	7.59	1.006	0.80	7.7
	CH_4	1.047	0.93	13.80	11.98	0.984	0.29	8.4
	CO_2	1.061	13.89	21.24	288.44	0.951	0.28	8.5

The variation in effective diffusivities of each gas across the studied rock specimens can be attributed to differences in pore structure, which impact the effective area available for gas transport and lead to deviation in diffusion paths from a straight pathway, known as tortuosity (Bear, 1972; Grathwohl, 1998). This effective area is influenced by the matrix structure and is largely governed by porosity. Furthermore, tortuosity is inversely related to porosity, as supported by numerous studies in the literature (da Silva et al., 2022; Ghanbarian et al., 2013; Holzer et al., 2023). Thus, porosity influences the diffusion mechanism by affecting both the available area at the gas-liquid interface for molecular transport and the complexity of the diffusion pathway. Additionally, as permeability and mean pore diameter are directly related to porosity in sandstones (Chilingar, 1964; Nelson, 1994; Tiab & Donaldson, 2016), their values also offer insights into these diffusion constraints.

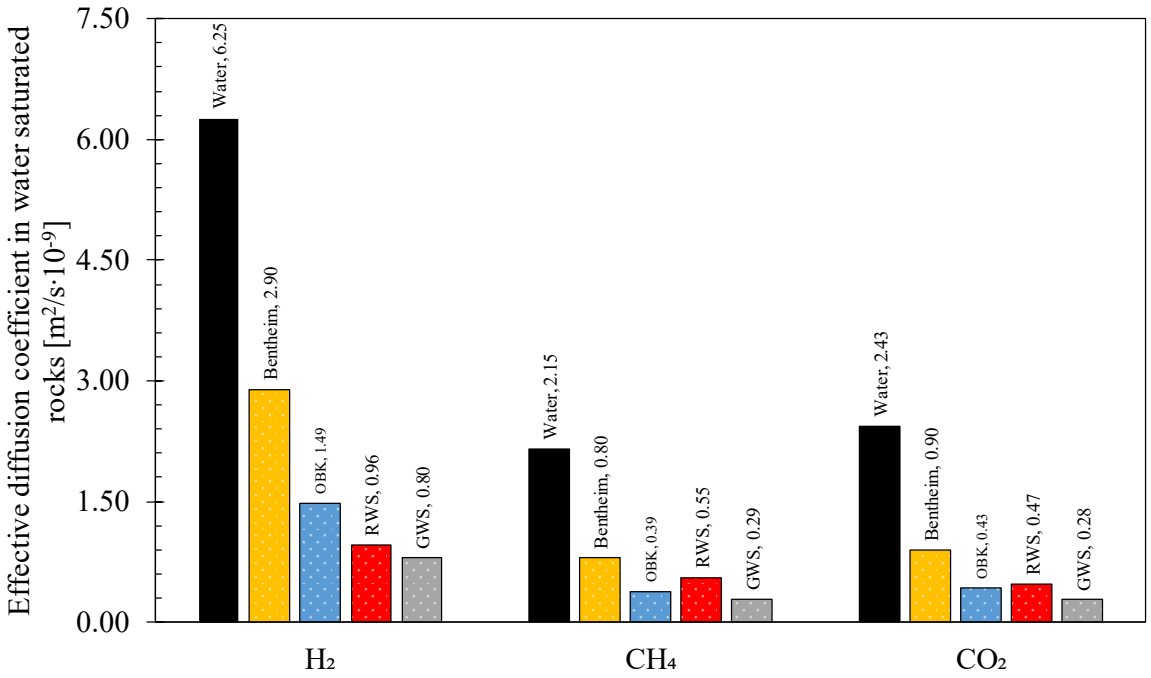

Figure 4.6. Comparison of effective diffusivity for H_2, CH_4, and CO_2 within water-saturated specimens of Bentheim, OBK, RWS, and GWS rocks, alongside the corresponding gas diffusion coefficients in water.

The measured effective diffusion coefficients were plotted against porosity, permeability, and mean pore diameter properties, demonstrating positive correlations in Figure 4.7 (a-c). Permeability values of examined rocks were sourced from literature (Arekhov et al., 2023; Nolte et al., 2021a; Peksa et al., 2015), while mean pore diameters were determined from pore throat size distribution obtained through mercury injection capillary pressure measurements, previously published (Khajooie et al., 2024b). RWS was not included for permeability correlation since no permeability measurements for RWS were found in the literature. These correlations (Figure 4.7 (a-c)) suggest that the increase in effective gas diffusivity from GWS, RWS, OBK, to Bentheim correspond to an expanded area for gas transport and a reduction in tortuous pathways. Additionally, Figure 4.7a reveals a steeper increasing trend for porosity above 15% compared to values below 15%. This observation aligns with the semi-logarithmic relationship of effective diffusion coefficients with permeability and mean pore diameter. Thus, the influence of pore structure in reducing available area for diffusion and imposing tortuous pathways is more pronounced in tight rocks compared to highly porous, permeable rocks. Overall, these findings indicate that the influence of pore structure on reducing available diffusion area and creating tortuous pathways is more pronounced in low porosity and low-permeability rocks compared to rocks with porosity and permeability higher than approximately 15% and $0.1 \cdot 10^{-12}$ m^2, respectively. Furthermore, the inverse relationship between effective diffusivity and

tortuosity, illustrated in Figure 4.7d, confirms that gas molecules move more freely through a porous medium with lower tortuosity (Li et al., 2016; Li et al., 2006; Lou et al., 2021; Lv et al., 2019). Similar observations were reported by Gao et al. (2019) regarding the diffusivity of CO_2 within oil-saturated porous media, with permeabilities ranging from $1.97 \cdot 10^{-14}$ to $2.24 \cdot 10^{-12}$ m^2. Their findings showed a significant initial increase in diffusivity, followed by stabilization for permeabilities greater than $9.87 \cdot 10^{-14}$ m^2. Additionally, consistent correlations with porosity, permeability, and tortuosity have been observed in similar studies exploring CO_2, CH_4, or He diffusion coefficients in water- or oil-saturated rocks of lithologies (Li et al., 2016; Lou et al., 2021; Lv et al., 2019; Pandey, 1974). However, some experimental studies have reported a lack of correlation between their observed diffusivities and either porosity or permeability (Li et al., 2006).

While the observed effective gas diffusivities in water-saturated rocks correlate with porosity, permeability, and mean pore size, these relationships have been established using a limited dataset. Hence, it is imperative to conduct further research on various rock types with a wide range of porosity, permeability, and pore size to enhance the reliability of these correlations. Otherwise, individual assessments of any potential reservoir involving gas diffusion are necessary to attain a comprehensive understanding of its unique characteristics.

Potential errors in measuring effective diffusivity can likely be attributed to deviations from the assumptions used in developing the mathematical model. Both gas solubility and the gas compressibility factor are pressure-dependent, causing variations in gas concentration at the outer surface of the rock specimen and in the diffusion coefficients, which were assumed to be constant. The pressure drops for H_2 and CH_4 diffusivity tests were negligible ($< 0.2\%$) whereas the CO_2 experiment experienced a 3.5% pressure drop, leading to a proportional reduction in gas concentration. Meanwhile, although the gas compressibility factors increased as the pressure decreased, these changes were considered negligible (even for CO_2). Assuming a direct relationship between gas concentration and effective diffusivity (Li et al., 2006), this suggests that the maximum error due to pressure reduction would be 3.5%. The greater pressure drop observed in CO_2 experiments is primarily due to its higher solubility in water compared to H_2 and CH_4 (Sander, 2015). Furthermore, gas adsorption resulting from gas-rock interactions may occur for all tested gases, albeit to varying extents (Al-Yaseri & Fatah, 2024; Ding et al., 2022). However, given the low clay

content of the rock specimens (Khajooie et al., 2024a) and their fully water-saturated condition (Grekov et al., 2023), this effect is anticipated to be minimal.

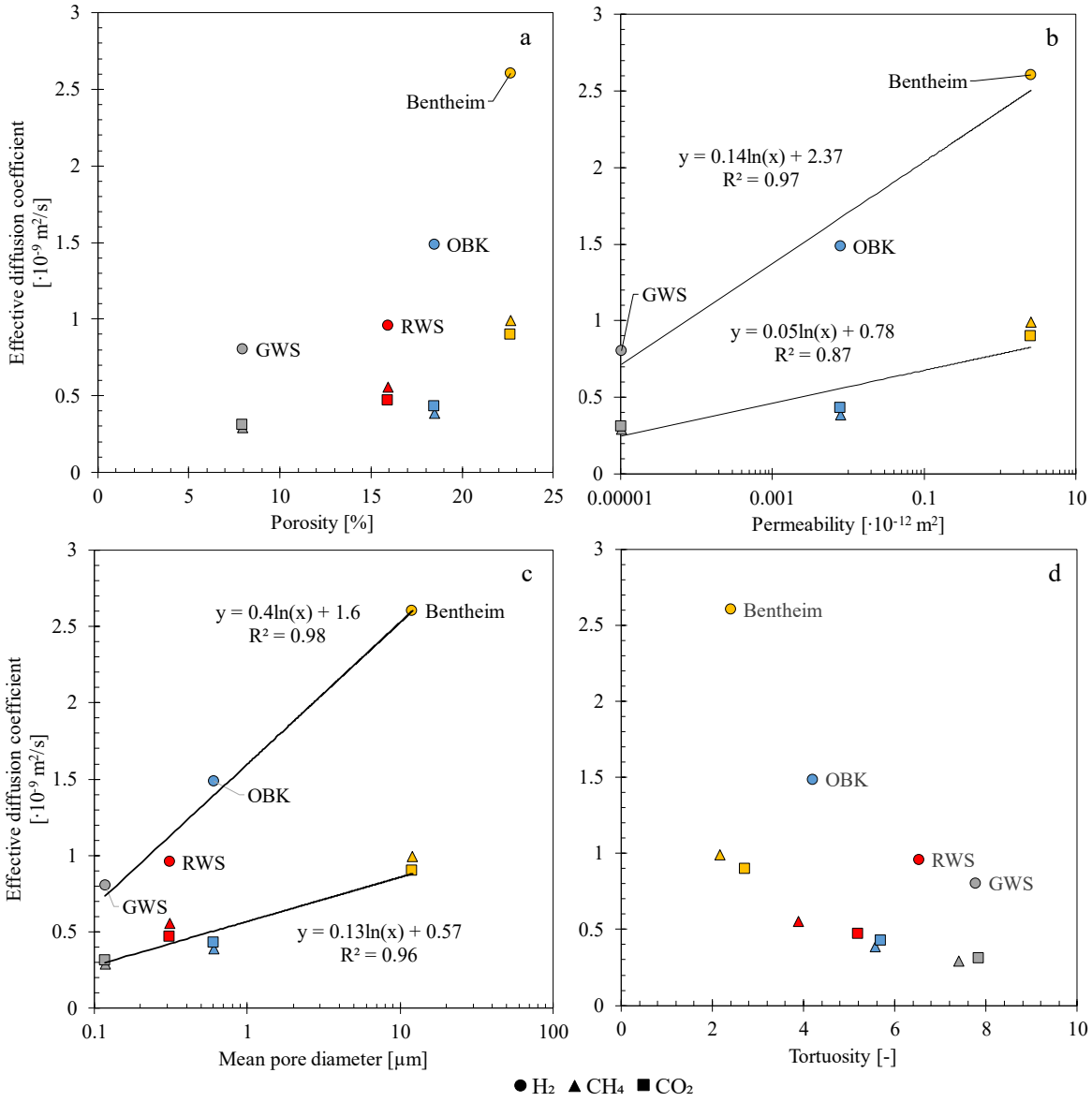

Figure 4.7. Correlation of measured effective diffusion coefficients for H_2, CH_4, and CO_2 in the examined rock specimens (fully water-saturated) with porosity (a), permeability (Arekhov et al., 2023; Nolte et al., 2021a; Peksa et al., 2015) (b), mean pore size (Khajooie et al., 2024b) (c), and diffusive tortuosity (d).

4.4.6. Implications of diffusion coefficient to Underground Hydrogen Storage

This investigation demonstrated that the pressure decay technique is effective in assessing the diffusivity of various gases, from relatively low to highly soluble, in both water and water-saturated rocks. The analyzed rock specimens, collected from four sandstone formations, serve as analogues for hydrogen reservoirs with varying permeability, exhibiting porosities from 8% to 24%. While the effective diffusion coefficients measured offer significant insights, they may not fully represent subsurface conditions due to the

absence of in-situ stresses and potential alterations from weathering processes as the rock specimens were retrieved from surface mines. Differences between the saturating fluid used in the experiments and in-situ formation fluids may also affect the transport characteristics. Nonetheless, the effective diffusivities obtained here provide valuable information for estimating potential gas loss during underground storage and enhance our understanding of the impact of gas diffusion on abiotic and biotic reactions.

The loss of hydrogen is directly related to the square root of the effective diffusion coefficient (Ghaedi et al., 2023). In addition, the relatively smaller molecular size and higher diffusivity of H_2 compared to other gases, such as CH_4 and CO_2, under similar thermophysical conditions, enhance its ability to diffuse through water saturated rocks (Perera, 2023; Zivar et al., 2021). However, a modeling study investigating hydrogen storage in a dormant aquifer with a porosity of 20% and 7 m height within Australia's Cooper Basin indicated a 1% loss from the reservoir during 15 years (Carden & Paterson, 1979). The diffusion-driven mass transfer enhances hydrogen saturation within the pore fluid, resulting in a decreased concentration gradient and gradually mitigating diffusive losses over time. Therefore, this effect is particularly significant in the early life of the reservoir or during the initial cycles of cyclic storage (Carden & Paterson, 1979; Hassannayebi, 2019). Furthermore, in an underground He storage project, it was found that the diffusive loss remained negligible, despite He exhibiting a higher diffusivity compared to H_2 (Hart, 1997).

During UHS or biological methanation, the occurrence of microbial metabolism depends on the availability of H_2 molecules as electron donors in the aqueous phase. Thus, the process of mass transfer from the gas to the liquid phase constrains the substrate supply, thereby influencing microbial reactions and, subsequently, the rate of H_2 conversion (Dupnock & Deshusses, 2019). Gas transport into the liquid phase is governed by the principles of the two-film theory, a conceptual framework describing this physical processes (Lewis & Whitman, 1924). According to this model, the rate of gas-liquid mass transfer depends on the concentration gradient, the mass transfer coefficient, and the gas-liquid interfacial area. The mass transfer coefficient represents the cumulative resistance for transporting gas molecules through the gas and liquid film layers surrounding the gas-liquid interface. Nonetheless, studies have shown that diffusional resistance within the stagnant gas film is negligible, with the mass transfer coefficient primarily controlled by the liquid side (Jensen et al., 2021). This parameter, in turn, is closely linked to both the

gas diffusion coefficients in the liquid and the film thickness (Charpentier, 1981; Villadsen et al., 2011b). Therefore, measuring effective gas diffusivities provides valuable insight into understanding and quantifying gas supply required for microbial metabolisms. However, microbial activity influences the concentration gradient, another parameter controlling the transfer process. The conversion of hydrogen by microorganisms results in higher or at least sustained concentration gradients compared to those observed in the pure diffusion process (Jensen et al., 2021). This highlights a consistent and indirect effect of H_2 diffusivity on the rate of biological hydrogen conversion. The loss of hydrogen due to biological processes significantly contributes to the total loss during storage in subsurface formations (Liu et al., 2023; Perera, 2023). This emphasizes the subtle yet critical importance of accurately determining H_2 diffusivity. It is worth mentioning that the selection of gases for experiments conducted on water-saturated rock specimens in this study was tailored to those implicated in methanogenic reactions during underground hydrogen storage or biological methanation.

4.5. Conclusions

This research systematically investigated the diffusion coefficients of various gases in both water and water-saturated rocks using the pressure decay technique. The measured diffusivities in water for H_2, CH_4, and He at pressures above ambient conditions (0.2 to 1.0 MPa) were consistent with literature values obtained through direct methods, where diffusion coefficients are determined through gas concentration analysis. Additionally, the employed method demonstrated good reproducibility, delivering consistent results across different cells and thereby confirming its reliability for diffusivity assessments. However, the discrepancy observed between the diffusion coefficients of CO_2 and Ar in water and those reported in the literature is likely due to the effect of density-driven convection. This phenomenon occurs as CO_2 and Ar gas molecules dissolve, forming a denser layer at the gas-liquid interface due to their higher density in the aqueous phase relative to water.

The effective diffusivities showed positive correlations with porosity, permeability, and pore diameter, supporting the increased effective area for diffusion and the reduced tortuosity of transport pathways as these parameters increase. This relationship is further evidenced by the inverse correlation between effective diffusion coefficients and tortuosity. The CO_2 diffusion coefficient in water can calculated using the effective diffusivities measured in the analyzed rock samples, together with tortuosity values derived from H_2 or

CH_4 measurements. The results agree with published data, indicating that the presence of porous media or the horizontal diffusive flow direction impedes density-driven convection.

The diffusion process plays a significant role in supporting substrate supply for biotic reactions during UHS. Therefore, integrating diffusion models with kinetic microbial growth models can provide a comprehensive understanding of the interplay between diffusion and biotic processes. Furthermore, there is a scarcity of experimental data on H_2 diffusivity across various rock types, such as sandstone, mudstone, and claystone, under different conditions of pressure, temperature, water salinity, and presence of hydrocarbon. The methodology and experimental setup employed in this study provide a straightforward and reliable approach for future studies intended to bridge this knowledge gap in data within this area of research. Further research on H_2 diffusivity in claystone and mudstone, could provide critical insights into the H_2 loss through caprocks (Michelsen et al., 2023; Salina Borello et al., 2024). Additionally, these measurements are essential for estimating the H_2 diffusive flux from potential host formations intended for radioactive waste storage (Bardelli et al., 2014; Jacops et al., 2015; Rebour et al., 1997).

Chapter 5

5. Concluding remarks and outlook

In this thesis, the impacts of porosity and surface area on the activity of methanogenic *Archaea* within the pore spaces of four sandstones as reservoir analogues for UHS have been experimentally investigated. The results demonstrated that both porosity and SSA of accessible pores positively influence microbial activity (Figure 2.10 and 3.11). The impact of porosity can be attributed to its role in supporting larger microbial cell populations, leading to higher conversion rates of H_2 to CH_4. Meanwhile, the effect of surface area is primarily associated with enhanced nutrient adsorption, creating a more favorable environment for microbial proliferation. Additionally, this study highlights the importance of gas-liquid mass transfer processes, which are regulated by the mass transfer coefficient, gas-liquid interfacial area, and concentration gradient. These factors collectively govern substrate availability for microorganisms and, consequently, biotic reaction rates. A key parameter affecting mass transfer is gas diffusivity in water-saturated rocks, which was measured for H_2 and CO_2 in the latter stage of this research. These findings were thoroughly discussed and documented in Chapters 2, 3, and 4.

Among all factors analyzed, porosity was identified as the primary determinant of microbial activity in porous media, as evidenced by the strong linear correlation between H_2 consumption rate and pore volume (Figure 2.10b). Microbial activity is significantly enhanced in sandstones characterized by higher porosity. Although variations in SSA and gas diffusivities (Figures 3.10 and 4.6) were observed across the rock specimens, the impact of porosity remained unequivocal. The second most influential parameter was the gas-liquid interfacial area, which controls gas-liquid mass transfer flux. This conclusion is supported by the higher H_2 consumption rates observed in GWS compared to Bentheim, despite their similar pore volumes. While Bentheim exhibits higher SSA and H_2 diffusivity,

the greater microbial activity in GWS is attributed to its larger gas-liquid interfacial area (Figure 3.10, Table 3.5 and 4.3). Upon normalizing microbial activity to pore volume and gas-liquid interfacial area, a linear correlation with SSA of accessible pores was observed, indicating that SSA plays a third-order role in governing the kinetics of biotic reactions within porous media.

5.1. Implications for Underground Hydrogen Storage efficiency

The findings of this research provide critical insights into the pore-scale factors influencing hydrogen loss and storage efficiency in sandstone formations intended for UHS. Key parameters such as porosity, surface area, and gas-liquid mass transfer characteristics govern microbial hydrogen consumption and should be considered when selecting and operating a storage reservoir.

From a practical standpoint, the primary concern for a UHS project is minimizing hydrogen loss due to microbial activity and enhancing gas recovery. The role of porosity is pivotal, as increased water containing nutrients and microbial cells leads to a higher hydrogen conversion rate. This suggests that controlling the water saturation in the reservoir is a key parameter governing microbial activity within the porous media. In a reservoir setting, formations with large pore sizes should be prioritized, as they offer high storage and deliverability capacities while maintaining low capillary pressure. This reduces the remained water saturation after drainage process (displacement of brine with gas) (Zivar et al., 2021), thereby reducing available microbial habitats. However, large pore sizes alone are not sufficient; but the spatial distribution of pore sizes and heterogeneity of transport properties must also be considered, as they affect sweep efficiency, potentially leading to uneven displacement of brine and inefficient storage (Heinemann et al., 2021; Muhammed et al., 2022). To mitigate microbial hydrogen loss, it is crucial to achieve a piston-like displacement of brine with hydrogen during injection, minimizing residual water saturation. This reduces microbial colonization and limits the biotic conversion of hydrogen. Reservoirs with large, well-connected pores and homogeneous distribution would facilitate such displacement, enhancing storage efficiency. Additionally, the use of a cushion gas (e.g., nitrogen or methane) could be beneficial to create a buffer zone, preventing direct hydrogen contact with underlying aquifer, which causes microbial activity.

The impact of gas-liquid interfacial area and surface area on microbial activity has been shown to be significant, assuming a constant microbial solution volume. Therefore,

hydrogen loss due to biotic reactions in reservoirs is generally higher than in bulk solutions with similar volumes. However, the contributions of second and third-order factors are limited at irreducible water saturation, where nutrient availability and cell populations are constrained. Moreover, the surface area of rocks in reservoirs with larger pores is smaller compared to those with smaller pores, further restricting the impact of pore structure on hydrogen conversion. This scenario represents an optimal condition for UHS, with minimal hydrogen loss. Conversely, reservoirs with smaller pore sizes and heterogeneous pore distributions may experience higher water saturation levels and increased SSA, which could enhance microbial activity and accelerate hydrogen conversion into methane. While clay minerals contribute to higher irreducible water saturation (Sun et al., 2021) and SSA (Woodruff & Revil, 2011), their impact on enhancing hydrogen loss is significant only when their pores are larger than microbial cell size, making them accessible for microbial traverse and colonization.

In practice, most reservoirs exhibit some degree of pore structure heterogeneity, which complicates the assessment of the factors influencing hydrogen loss. This complexity necessitates numerical modeling efforts, and the incorporation of experimental data will be essential for upscaling results and predicting long-term hydrogen storage behavior.

While the laboratory-scale experiments conducted in this study offer valuable qualitative insights, there are still uncertainties when translating these findings to real-world reservoir conditions. The experiments were conducted under optimal conditions for a specific strain of methanogenic *Archaea*. To apply these findings quantitatively, further research is needed under environmental conditions representative of UHS, considering factors such as pressure, temperature, salinity, native microbial consortia, and in-situ nutrient availability. The correlations observed in these experiments between pore characteristics and microbial activities can then be integrated into existing microbial growth models such as the Monod, Contois, Moser, and Panfilov (Muloiwa et al., 2020; Murphy & Ginn, 2000; Moser, 2012; Panfilov, 2010), which have predominantly been developed based on bulk-phase kinetics. This would improve the predictive accuracy of these models and provide a more reliable framework for assessing hydrogen storage efficiency in real-world conditions. Additionally, alternative experimental approaches, such as using porous ceramics with controlled SSA and advanced imaging techniques, could provide further insights into microorganism-rock interactions. This approach could help refine our understanding of the role of pore-scale characteristics in microbial activity, further enhancing our ability to predict and optimize UHS systems.

5.2. Outlook

5.2.1. Influence of environmental variables on microbial activity

M. thermolithotrophicus Archaea, in this thesis, was used with an estimated concentration of 10^8 cells/mL. It was incubated in a specifically formulated methanogenic medium designed to promote its growth. During the experiments, a gas mixture reflecting the stoichiometric ratios of the methanogenic reaction (80 % H_2, 20 % CO_2) was introduced into the reactors. These optimal conditions facilitated the highest growth rate for the *Archaea*, allowing for the collection of meaningful results within the laboratory time frame. However, environmental variables in an underground hydrogen reservoir, such as nutrient availability, pH, salinity, pressure, and temperature may deviate from the optimal conditions for microorganisms, leading to reduced growth rates (Thaysen et al., 2021). Additionally, the cell density of native microorganisms is lower than that used in this study, typically ranging from 10^3-10^7 cells/mL (Dohrmann & Krüger, 2023). The composition of the injected gas can also vary depending on the goals of the storage projects. Furthermore, the indigenous microbial communities include a variety of organisms, and competition among them for nutrients and substrates could significantly affect their activity (Dopffel et al., 2023; Hellerschmied et al., 2024; Thaysen et al., 2021). While some research has examined native microbial communities and varying gas concentrations (RAG Austria AG, 2020, 2021), further studies are necessary to quantify the influence of each environmental variable on biotic processes. Such studies will offer in-depth understanding of the actual behavior of microorganisms within porous media.

5.2.2. Integrating pore characteristics into microbial growth models

The investigation of microbial activity within porous media in this thesis has demonstrated the impact of various pore characteristics-including porosity, surface area, and interfacial area between gas and liquid phases-on the rate of biotic processes. In addition, the effective diffusivities of H_2 and CO_2 in water-saturated rocks have been determined. These diffusivities, along with the interfacial area, are key factors controlling the gas-liquid mass transfer flux (Jensen et al., 2021). However, existing microbial growth models in the literature, such as the Monod (Monod, 1949), Moser (Moser, 2012), and Panfilov (Panfilov, 2010) models, primarily focus on substrate availability when reproducing the rate of microbial processes during UHS (Hagemann, 2017). Furthermore, some studies have been attempted to couple mass transfer coefficients with the Monod model to describe microbial

metabolism in batch reactors (Mazzeo et al., 2021; Strobel et al., 2023). Despite these efforts, existing models currently lack the capability to accurately predict hydrogen conversion rates, a critical factor for assessing the feasibility of UHS and the efficiency of bio-methanation projects. Therefore, further research is imperative to incorporate the impact of pore characteristics into these models, thereby enhancing their predictive accuracy. The established correlations between microbial activity, surface area, and pore volume provide valuable insights for advancing these studies.

5.2.3. Investigating surface area and interfacial area on porous ceramics

In this thesis, the impact of surface area on microbial activity was investigated on four sandstones with varying mineralogy, pore sizes and porosities ranging from 8 % to 24 %. During the microbial activity tests, either the gas-liquid interfacial area (for experiment involving rock specimens with equivalent pore volumes) or the pore volume (for experiment involving rock specimens with similar bulk volumes) also varied alongside the surface area. This superposition necessitates normalizing the measured activities based on both pore volume and interfacial area to isolate surface area as the sole influencing factor. However, this method is subject to the inherent uncertainties in measuring these pore characteristics. An effective strategy to reduce the number of influencing parameters involves using artificial samples, such as porous ceramics, with consistent porosity and dimensions but varying pore sizes, thereby making surface area the sole variable. A similar approach was employed in a study exploring fluid-dynamic effects at higher pressures by using artificial micro- to nanoporous materials. The high rigidity of these samples effectively avoided the interference of poro-mechanical effects (Nolte et al., 2021b). Furthermore, the hydrogen conversion rates measured in this study may vary from those observed in gas storage reservoirs due to variations in water saturation. In hydrogen-containing porous rocks, a thin film of water remains around the grains after water displacement, creating a substantial interfacial area. This increased interfacial area can significantly enhance substrate supply, potentially leading to higher reaction rates, as mass transfer flux is directly related to the interfacial area between the gas and liquid phases (Jensen et al., 2021). Future research can utilize water-wet porous ceramics with partial saturation to determine the rates of biotic reactions under these conditions.

5.2.4. Imaging of microbial colonization within porous media

The methodology outlined in Chapter 2 for monitoring microbial activity includes tracking changes in pressure and gas composition throughout the experiments. Detailed assessments, discussed in Chapters 2 and 3, demonstrated the impact of pore volume, surface area, and gas-liquid interfacial area on the recorded activities. The variation in pore sizes within geological formations may result in a heterogeneous distribution of *M. thermolithotrophicus Archaea* within porous media, as these organisms can only traverse pores larger than 2 µm. This heterogeneity was similarly noted in the USC project, where the gas composition in one area remained unchanged from the injected gas, while another area exhibited significant variations (RAG Austria AG, 2021). Moreover, the higher concentration of substrate gas near the outer surface of rock specimens may lead to increased hydrogen conversion rates compared to deeper positions. Observations from the USC project also indicated that reaction rates were higher near the wellbore than in deeper reservoir regions (RAG Austria AG, 2021). A potential solution for addressing these uncertainties involves using advanced imaging techniques such as Scanning Electron Microscopy (SEM), micro-Computed Tomography (µCT), and fluorescence microscopy to visualize the distribution of microorganisms within porous media. This approach allows for the investigation of microorganism attachment to surfaces, providing further validation of the results presented in this thesis. Additionally, the role of specific minerals in adsorbing nutrients and microbes can be explored. These methods also enable the quantification of cell abundance and the evaluation of changes in the storage and transport properties of the media (Gaol et al., 2021; Hassannayebi et al., 2021). Despite these benefits, the application of the SEM technique has largely been limited to microfluidic samples, and its applicability to rock specimens remains to be explored. To preserve the in-situ distribution of microorganisms within the pore space, rock samples must undergo the Cryo-BIB preparation process before SEM imaging (Hrubanova et al., 2016; Schmatz et al., 2017). However, the effectiveness of this preparation process still needs to be verified. In addition, coupling µCT with flow cell measurements allows for real-time monitoring of microbial growth and distribution within porous rock samples without destroying core integrity. An experimental study employed a similar approach to investigate microbial populations and mobility during bioremediation of a soil column (Hata et al., 2006). However, X-ray exposure can result in the death or decay of microbes, significantly impacting the microbial communities (Fischer et al., 2013). Therefore, it is crucial to carefully design factors such

as core volume, radiation duration, and energy to minimize alterations to microbial communities. Additionally, using microorganisms that are unaffected by X-ray radiation is essential for maintaining the integrity of the study (Ewton et al., 2021).

5.2.5. Effect of biofilm accumulation on storage and transport properties

The findings of this study have demonstrated that surface area significantly enhances the rate of methanogenic reactions. These observations have been attributed to the adsorption of nutrients and the colonization of microbes on surfaces, which potentially facilitates microbial growth and biofilm formation. This, in turn, may lead to pore-clogging and consequently, a substantial decrease in permeability (Eddaoui et al., 2021; Hassannayebi et al., 2021; Hommel et al., 2018). The effects of bio-clogging on hydraulic conductivity have been investigated extensively in both experimental and theoretical studies in a wide variety of fields including aquifer storage and recovery, geothermal applications, CO_2 sequestration, and microbial enhanced oil recovery (Banerjee & Samanta, 2022; Baveye et al., 1998; Gao et al., 2020; Rinck-Pfeiffer et al., 2000; Zettlitzer et al., 2010). According to the published results of the experimental studies which were conducted on various porous media such as sand- or glass-filled columns, micromodels, and sand packs, the permeability values have generally decreased by up to three orders of magnitude, although even higher reductions have been observed in a few cases (Gaol et al., 2021; Gerlach & Cunningham, 2010; Halim et al., 2014; Thullner, 2010). Furthermore, biomass growth has been found to have a greater impact on hydraulic conductivity reduction in tight formations (Vandevivere, 1995). Bio-clogging has an adverse impact on the primary objective of underground hydrogen storage since the gas mobility reduction hinders the energy deliverability with a high flow rate especially when energy is urgently needed. While modeling studies (Ebigbo et al., 2013; Eddaoui et al., 2021) have explored bio-clogging during UHS, experimental research on the impact of biomass accumulation on hydraulic conductivity has primarily been conducted on artificial samples, often overlooking the inherent heterogeneity present in actual rock specimens. Therefore, the insights gained from the microbial reactors (Chapter 2) can be applied to future research on flow cells to integrate microbial activity measurements with two-phase flow, thereby determining the potential impacts of bio-clogging on storage and transport properties.

5.2.6. Diffusion coefficients in water saturated caprocks and radioactive waste repositories

The effectiveness of the pressure decay method in determining the effective diffusivity of various gases in water-saturated reservoir rocks was demonstrated in Chapter 4. In addition, it was discussed that pure diffusion process may be of little relevance in terms of H_2 loss even though for a long term (Carden & Paterson, 1979; Hassannayebi, 2019). However, this mechanism can control the biological processes, occurring within the formation water of reservoir rocks, resulting in H_2 consumption (Jensen et al., 2021; Perera, 2023). Similarly, the diffusive gas transport into and through low-permeability rocks such as shale, claystone, and mudstone, which act as caprocks for gas storage, has been reported to be negligible. Nevertheless, the rate of molecular diffusion of H_2 or CO_2 governs geochemical reactions, resulting in diagenetic alterations such as dissolution and precipitation. The adverse effect of mineral dissolution creates secondary porosity and gas breakthrough pathways, alongside alterations in mechanical properties, thereby posing risks to sealing integrity (Bertier et al., 2016; Dabbaghi et al., 2024; Hassanpouryouzband et al., 2022a). Furthermore, hydrogen is generated within the repositories of radioactive waste by corrosion and radiolysis mechanisms that is partially dissolved in the formation water and dissipates from repositories by diffusion (Harrington et al., 2012; Ortiz et al., 2002). However, if the rate of gas generation exceeds the diffusive flux, it can create a free gas phase resulting in a gas pressure build up that poses a potential risk of creating a transport pathway and compromising the barrier function of the host rock (Amann-Hildenbrand et al., 2015; Jacops, 2018). The pressure decay is a straightforward technique having the potential to be employed in future research to address the knowledge gas related to diffusion coefficients in water-saturated cap rocks and potential host rocks for radioactive waste repositories.

Chapter 6

6. References

Aftab, A., Hassanpouryouzband, A., Martin, A., Kendrick, J. E., Thaysen, E. M., Heinemann, N., Utley, J., Wilkinson, M., Haszeldine, R. S., & Edlmann, K. (2023). Geochemical Integrity of Wellbore Cements during Geological Hydrogen Storage. *Environmental Science & Technology Letters*, *10*(7), 551-556. https://doi.org/10.1021/acs.estlett.3c00303

Ahmerkamp, S., Marchant, H. K., Peng, C., Probandt, D., Littmann, S., Kuypers, M. M. M., & Holtappels, M. (2020). The effect of sediment grain properties and porewater flow on microbial abundance and respiration in permeable sediments. *Scientific Reports*, *10*(1), 3573. https://doi.org/10.1038/s41598-020-60557-7

Aikazyan, E. A., & Fedorova, I. A. (1952). Determination of the diffusion coefficient of H2 by electrochemical method. *Doklady Akademii Nauk (Russian)*, *86*, 1137-1140.

Aimikhe, V. J., & Eyankware, O. E. (2023). Recent Advances in White Hydrogen Exploration and Production: A Mini Review. *Journal of Energy Research and Reviews*, *13*(4), 64-79. https://doi.org/10.9734/jenrr/2023/v13i4272

Ajanovic, A., Sayer, M., & Haas, R. (2022). The economics and the environmental benignity of different colors of hydrogen. *International Journal of Hydrogen Energy*, *47*(57), 24136-24154. https://doi.org/10.1016/j.ijhydene.2022.02.094

Al-Yaseri, A., & Fatah, A. (2024). Impact of H2-CH4 mixture on pore structure of sandstone and limestone formations relevant to subsurface hydrogen storage. *Fuel*, *358*, 130192. https://doi.org/10.1016/j.fuel.2023.130192

Albes, D., Ball, M., Becker, A., Bünger, U., Capito, S., Correas, L., Evans, R., Ferriz, A., Iordache, I., & Kruck, O. (2014). HyUnder–Hydrogen Underground Storage at large scale, Part I: General project results (European Level)". The 20th World Hydrogen Energy Conference (WHEC 2014), Gwangju, South Korea,

Ale Enriquez, F., & Ahring, B. K. (2023). Strategies to overcome mass transfer limitations of hydrogen during anaerobic gaseous fermentations: A comprehensive review. *Bioresource Technology*, *377*, 128948. https://doi.org/10.1016/j.biortech.2023.128948

Amann-Hildenbrand, A., Krooss, B. M., Harrington, J., Cuss, R., Davy, C., Skoczylas, F., Jacops, E., & Maes, N. (2015). Chapter 7 - Gas Transfer Through Clay Barriers. In C. Tournassat, C. I. Steefel, I. C. Bourg, & F. Bergaya (Eds.), *Developments in Clay*

Science (Vol. 6, pp. 227-267). Elsevier. https://doi.org/10.1016/B978-0-08-100027-4.00007-3

Amez, I., Gonzalez, S., Sanchez-Martin, L., Ortega, M. F., & Llamas, B. (2021). 5 - Underground methanation, a natural way to transform carbon dioxide into methane. In D. S. K. Ting & J. A. Stagner (Eds.), *Climate Change Science* (pp. 81-106). Elsevier. https://doi.org/10.1016/B978-0-12-823767-0.00005-7

Amin M. A., Eric C., William E. (2011). Review of methane catalytic cracking for hydrogen production. *International Journal of Hydrogen Energy*, *36*(4), 2904-2935. https://doi.org/10.1016/j.ijhydene.2010.11.035

Andrä, H., Combaret, N., Dvorkin, J., Glatt, E., Han, J., Kabel, M., Keehm, Y., Krzikalla, F., Lee, M., Madonna, C., Marsh, M., Mukerji, T., Saenger, E. H., Sain, R., Saxena, N., Ricker, S., Wiegmann, A., & Zhan, X. (2013). Digital rock physics benchmarks—Part I: Imaging and segmentation. *Computers & Geosciences*, *50*, 25-32. https://doi.org/10.1016/j.cageo.2012.09.005

Anovitz, L. M., & Cole, D. R. (2015). Characterization and Analysis of Porosity and Pore Structures. *Reviews in Mineralogy and Geochemistry*, *80*(1), 61-164. https://doi.org/10.2138/rmg.2015.80.04

Antoine, C. (1891). Annales de Physique et de Chimie 281; ibid, Annales de Physique et de Chimie (1892) 26: 426; . *Comptes Rendus Acad Sci (Paris) (1888) 107: 1143*. ISBN:

Arekhov, V., Zhainakov, T., Clemens, T., & Wegner, J. (2023). Measurement of Effective Hydrogen-Methane Gas Diffusion Coefficients in Reservoir Rocks. *SPE Reservoir Evaluation & Engineering*, *26*(04), 1242-1257. https://doi.org/10.2118/214451-PA

Bachaud, P., Meiller, C., Brosse, E., Durand, I., & Beaumont, V. (2017). Modeling of Hydrogen Genesis in Ophiolite Massif. *Procedia Earth and Planetary Science*, *17*, 265-268. https://doi.org/10.1016/j.proeps.2016.12.051

Bachmat, Y., & Bear, J. (1987). On the Concept and Size of a Representative Elementary Volume (Rev). In J. Bear & M. Y. Corapcioglu (Eds.), *Advances in Transport Phenomena in Porous Media* (pp. 3-20). Springer Netherlands. https://doi.org/10.1007/978-94-009-3625-6_1

Bade, S. O., Taiwo, K., Ndulue, U. F., Tomomewo, O. S., & Aisosa Oni, B. (2024). A review of underground hydrogen storage systems: Current status, modeling approaches, challenges, and future prospective. *International Journal of Hydrogen Energy*, *80*, 449-474. https://doi.org/10.1016/j.ijhydene.2024.07.187

Baek, G., Kim, K.-Y., & Logan, B. E. (2021). Impact of surface area and current generation of microbial electrolysis cell electrodes inserted into anaerobic digesters. *Chemical Engineering Journal*. (Lausanne, Switzerland: 1996) 426, 131281

Baird, M. H. I., & Davidson, J. F. (1962). Annular jets—II: Gas absorption. *Chemical Engineering Science*, *17*(6), 473-480. https://doi.org/10.1016/0009-2509(62)85016-7

Balat, M. (2008). Possible Methods for Hydrogen Production. *Energy Sources, Part A: Recovery, Utilization, and Environmental Effects*, *31*(1), 39-50. https://doi.org/10.1080/15567030701468068

Banerjee, T., & Samanta, A. (2022). Chapter 23 - Bioclogging and microbial enhanced oil recovery. In J. A. Malik (Ed.), *Microbes and Microbial Biotechnology for Green Remediation* (pp. 443-462). Elsevier. https://doi.org/10.1016/B978-0-323-90452-0.00042-6

Bardelli, F., Mondelli, C., Didier, M., Vitillo, J. G., Cavicchia, D. R., Robinet, J.-C., Leone, L., & Charlet, L. (2014). Hydrogen uptake and diffusion in Callovo-Oxfordian clay rock for nuclear waste disposal technology. *Applied Geochemistry*, *49*, 168-177. https://doi.org/10.1016/j.apgeochem.2014.06.019

Baveye, P., Vandevivere, P., Hoyle, B. L., DeLeo, P. C., & de Lozada, D. S. (1998). Environmental Impact and Mechanisms of the Biological Clogging of Saturated Soils and Aquifer Materials. *Critical Reviews in Environmental Science and Technology*, *28*(2), 123-191. https://doi.org/10.1080/10643389891254197

Baykara, S. Z. (2018). Hydrogen: A brief overview on its sources, production and environmental impact. *International Journal of Hydrogen Energy*, *43*(23), 10605-10614. https://doi.org/10.1016/j.ijhydene.2018.02.022

Bear, J. (1972). Dynamics of Fluids in Porous Media. *Elsevier, New York, Chap. 4*. ISBN: 0486131807

Bennett, L., Ng, W. Y., & Walkley, J. (1968). Diffusion of gases in nonpolar liquids. Open-tube method. *The Journal of Physical Chemistry*, *72*(13), 4699-4700.

Berg, S., & Ott, H. (2012). Stability of CO2–brine immiscible displacement. *International Journal of Greenhouse Gas Control*, *11*, 188-203. https://doi.org/10.1016/j.ijggc.2012.07.001

Bernardez, L. A., de Andrade Lima, L. R. P., de Jesus, E. B., Ramos, C. L. S., & Almeida, P. F. (2013). A kinetic study on bacterial sulfate reduction. *Bioprocess and Biosystems Engineering*, *36*(12), 1861-1869. https://doi.org/10.1007/s00449-013-0960-0

Bernhardt, G., Distèche, A., Jaenicke, R., Koch, B., Lüdemann, H.-D., & Stetter, K.-O. (1988a). Effect of carbon dioxide and hydrostatic pressure on the pH of culture media and the growth of methanogens at elevated temperature. *Applied Microbiology and Biotechnology*, *28*(2), 176-181. https://doi.org/10.1007/BF00694308

Bernhardt, G., Jaenicke, R., Lüdemann, H. D., König, H., & Stetter, K. O. (1988b). High Pressure Enhances the Growth Rate of the Thermophilic Archaebacterium Methanococcus thermolithotrophicus without Extending Its Temperature Range. *Applied and Environmental Microbiology*, *54*(5), 1258-1261. https://doi.org/10.1128/aem.54.5.1258-1261.1988

Berta, M., Dethlefsen, F., Ebert, M., Schafer, D., & Dahmke, A. (2018). Geochemical Effects of Millimolar Hydrogen Concentrations in Groundwater: An Experimental Study in the Context of Subsurface Hydrogen Storage. *Environ Sci Technol*, *52*(8), 4937-4949. https://doi.org/10.1021/acs.est.7b05467

Berta, M., Dethlefsen, F., Ebert, M., Schäfer, D., & Dahmke, A. (2018). Geochemical Effects of Millimolar Hydrogen Concentrations in Groundwater: An Experimental Study in the Context of Subsurface Hydrogen Storage. *Environmental Science & Technology*, *52*(8), 4937-4949. https://doi.org/10.1021/acs.est.7b05467

Bertier, P., Schweinar, K., Stanjek, H., Ghanizadeh, A., Clarkson, C. R., Busch, A., Kampman, N., Prinz, D., Amann-Hildenbrand, A., Krooss, B. M., & Pipich, V. (2016). On the Use and Abuse of N2 Physisorption for the Characterization of the Pore Structure of Shales. In T. Schäfer, R. Dohrmann, & H. C. Greenwell (Eds.), *Filling the Gaps – from Microscopic Pore Structures to Transport Properties in Shales* (Vol. 21, pp. 0). Clay Minerals Society. https://doi.org/10.1346/CMS-WLS-21-12

Blair, L. M., & Quinn, J. A. (1969). The onset of cellular convection in a fluid layer with time-dependent density gradients. *Journal of Fluid Mechanics*, *36*(2), 385-400. https://doi.org/10.1017/S0022112069001716

Blay-Roger, R., Bach, W., Bobadilla, L. F., Reina, T. R., Odriozola, J. A., Amils, R., & Blay, V. (2024). Natural hydrogen in the energy transition: Fundamentals, promise, and enigmas. *Renewable and Sustainable Energy Reviews*, *189*, 113888. https://doi.org/10.1016/j.rser.2023.113888

Bo, Z., Zeng, L., Chen, Y., & Xie, Q. (2021). Geochemical reactions-induced hydrogen loss during underground hydrogen storage in sandstone reservoirs. *46*(38), 19998-20009. https://doi.org/10.1016/j.ijhydene.2021.03.116

Bondue, C. J., & Koper, M. T. M. (2020). A DEMS approach for the direct detection of CO formed during electrochemical CO2 reduction. *Journal of Electroanalytical Chemistry*, *875*, 113842. https://doi.org/10.1016/j.jelechem.2020.113842

Boon, M., & Benson, S. M. (2021). A physics-based model to predict the impact of horizontal lamination on CO2 plume migration. *Advances in Water Resources*, *150*, 103881. https://doi.org/10.1016/j.advwatres.2021.103881

Boon, M., & Hajibeygi, H. (2022). Experimental characterization of H2/water multiphase flow in heterogeneous sandstone rock at the core scale relevant for underground hydrogen storage (UHS). *Scientific Reports*, *12*(1), 14604. https://doi.org/10.1038/s41598-022-18759-8

Bovik, A. C. (2009). Chapter 4 - Basic Binary Image Processing. In A. Bovik (Ed.), *The Essential Guide to Image Processing* (pp. 69-96). Academic Press. https://doi.org/10.1016/B978-0-12-374457-9.00004-4

Breznak, J. A., Switzer, J. M., & Seitz, H. J. (1988). Sporomusa termitida sp. nov., an H2/CO2-utilizing acetogen isolated from termites. *Archives of Microbiology*, *150*(3), 282-288. https://doi.org/10.1007/BF00407793

Brunauer, S., Emmett, P. H., & Teller, E. (1938). Adsorption of Gases in Multimolecular Layers. *Journal of the American Chemical Society*, *60*(2), 309-319. https://doi.org/10.1021/ja01269a023

Buades, A., Coll, B., & Morel, J. M. (2005). A non-local algorithm for image denoising. IEEE Computer Society Conference on Computer Vision and Pattern Recognition (CVPR'05), 20-25 June 2005

Bünger, U., Michalski, J., Crotogino, F., & Kruck, O. (2016). 7 - Large-scale underground storage of hydrogen for the grid integration of renewable energy and other applications. In M. Ball, A. Basile, & T. N. Veziroğlu (Eds.), *Compendium of Hydrogen Energy* (pp. 133-163). Woodhead Publishing. https://doi.org/10.1016/B978-1-78242-364-5.00007-5

Burkhardt, M., Koschack, T., & Busch, G. (2015). Biocatalytic methanation of hydrogen and carbon dioxide in an anaerobic three-phase system. *Bioresource Technology*, *178*, 330-333. https://doi.org/10.1016/j.biortech.2014.08.023

Busch, A., Schweinar, K., Kampman, N., Coorn, A., Pipich, V., Feoktystov, A., Leu, L., Amann-Hildenbrand, A., & Bertier, P. (2016). Shale Porosity - What Can We Learn from Different Methods? In *Fifth EAGE Shale Workshop* (Vol. 2016, No. 1, pp. 1-5). European Association of Geoscientists & Engineers. https://doi.org/10.3997/2214-4609.201600391

Bustin, R. M., Bustin, A. M. M., Cui, X., Ross, D. J. K., & Pathi, V. S. M. (2008). Impact of Shale Properties on Pore Structure and Storage Characteristics *SPE Shale Gas Production Conference*, https://doi.org/10.2118/119892-MS

Cadogan, S. P., Maitland, G. C., & Trusler, J. P. M. (2014). Diffusion Coefficients of CO2 and N2 in Water at Temperatures between 298.15 K and 423.15 K at Pressures up to 45 MPa. *Journal of Chemical & Engineering Data*, *59*(2), 519-525. https://doi.org/10.1021/je401008s

Carden, P. O., & Paterson, L. (1979). Physical, chemical and energy aspects of underground hydrogen storage. *International Journal of Hydrogen Energy*, *4*(6), 559-569. https://doi.org/10.1016/0360-3199(79)90083-1

Caskey, J. A., Michelsen, D. L., & To, Y. P. (1973). The effect of surfactant hydrophilic group on gas absorption rates. *Journal of Colloid and Interface Science*, *42*(1), 62-69. https://doi.org/10.1016/0021-9797(73)90007-6

Cathles, L., & Prinzhofer, A. (2020). What Pulsating H2 Emissions Suggest about the H2 Resource in the Sao Francisco Basin of Brazil. *Geosciences*, *10*(4).

Charlet, L., Alt-Epping, P., Wersin, P., & Gilbert, B. (2017). Diffusive transport and reaction in clay rocks: A storage (nuclear waste, CO2, H2), energy (shale gas) and water quality issue. *Advances in Water Resources*, *106*, 39-59. https://doi.org/10.1016/j.advwatres.2017.03.019

Charpentier, J.-C. (1981). Mass-Transfer Rates in Gas-Liquid Absorbers and Reactors. In T. B. Drew, G. R. Cokelet, J. W. Hoopes, & T. Vermeulen (Eds.), *Advances in Chemical Engineering* (Vol. 11, pp. 1-133). Academic Press. https://doi.org/10.1016/S0065-2377(08)60025-3

Chauhan, S., Rühaak, W., Khan, F., Enzmann, F., Mielke, P., Kersten, M., & Sass, I. (2016). Processing of rock core microtomography images: Using seven different machine learning algorithms. *Computers & Geosciences*, *86*, 120-128. https://doi.org/10.1016/j.cageo.2015.10.013

Chen, Y. A., Chu, C. K., Chen, Y. P., Chu, L. S., Lin, S. T., & Chen, L.-J. (2018). Measurements of diffusion coefficient of methane in water/brine under high pressure. *Terrestrial, Atmospheric and Oceanic sciences journal*, *29*(5). https://doi.org/10.3319/TAO.2018.02.23.02

Chien, A.-C., Hill, Norbert S., & Levin, Petra A. (2012). Cell Size Control in Bacteria. *Current Biology*, *22*(9), R340-R349. https://doi.org/10.1016/j.cub.2012.02.032

Chilingar, G. V. (1964). Relationship Between Porosity, Permeability, and Grain-Size Distribution of Sands and Sandstones. In L. M. J. U. van Straaten (Ed.), *Developments in Sedimentology* (Vol. 1, pp. 71-75). Elsevier. https://doi.org/10.1016/S0070-4571(08)70469-2

Cnudde, V., & Boone, M. N. (2013). High-resolution X-ray computed tomography in geosciences: A review of the current technology and applications. *Earth-Science Reviews*, *123*, 1-17. https://doi.org/10.1016/j.earscirev.2013.04.003

Coates, G. R., Xiao, L., & Prammer, M. G. (1999). NMR logging : principles and applications. *Halliburton Energy Services*. ISBN: 0967902606 https://cir.nii.ac.jp/crid/1130282271026258560

Collins, R. E. (1976). Flow of fluids through porous materials. *Petroleum Publishing Co.,Tulsa, OK*. ISBN: https://www.osti.gov/biblio/7099752

Crank, J. (1979). The mathematics of diffusion. *Oxford university press*. ISBN: 0198534116

Cussler, E. L. (1997). Diffusion: Mass Transfer in Fluid Systems. *Cambridge University Press*. ISBN: 0521564778

da Silva, M. T. Q. S., do Rocio Cardoso, M., Veronese, C. M. P., & Mazer, W. (2022). Tortuosity: A brief review. *Materials Today: Proceedings*, *58*, 1344-1349. https://doi.org/10.1016/j.matpr.2022.02.228

Dabbaghi, E., Ng, K., Brown, T. C., & Yu, Y. (2024). Experimental study on the effect of hydrogen on the mechanical properties of hulett sandstone. *International Journal of Hydrogen Energy*, *60*, 468-478. https://doi.org/10.1016/j.ijhydene.2024.02.210

Dang, H., & Lovell Charles, R. (2015). Microbial Surface Colonization and Biofilm Development in Marine Environments. *Microbiology and Molecular Biology Reviews*, *80*(1), 91-138. https://doi.org/10.1128/MMBR.00037-15

Das, D., & Veziroğlu, T. N. (2001). Hydrogen production by biological processes: a survey of literature. *International Journal of Hydrogen Energy*, *26*(1), 13-28. https://doi.org/10.1016/S0360-3199(00)00058-6

Das, S. K., & Butler, R. M. (1996). Diffusion coefficients of propane and butane in peace river bitumen. *The Canadian Journal of Chemical Engineering*, *74*(6), 985-992. https://doi.org/10.1002/cjce.5450740623

Dash, S. K., Chakraborty, S., & Elangovan, D. (2023). A Brief Review of Hydrogen Production Methods and Their Challenges. *Energies*, *16*(3).

Dautriat, J., Gland, N., Dimanov, A., & Raphanel, J. (2011). Hydromechanical behavior of heterogeneous carbonate rock under proportional triaxial loadings. *Journal of Geophysical Research: Solid Earth*, *116*(B1). https://doi.org/10.1029/2009JB000830

Davidson, J. F. (1957). The determination of diffusion coefficient for sparingly soluble gases in liquids. *Trans. Inst. Chem. Engrs.*, *35*, 51-60.

Dawood, F., Anda, M., & Shafiullah, G. M. (2020). Hydrogen production for energy: An overview. *International Journal of Hydrogen Energy*, *45*(7), 3847-3869. https://doi.org/10.1016/j.ijhydene.2019.12.059

Díaz-Abad, S., Millán, M., Rodrigo, M. A., & Lobato, J. (2019). Review of Anodic Catalysts for SO2 Depolarized Electrolysis for "Green Hydrogen" Production. *9*(1), 63. https://www.mdpi.com/2073-4344/9/1/63

Ding, J., Yan, C., Wang, G., He, Y., & Zhao, R. (2022). Competitive adsorption between CO2 and CH4 in tight sandstone and its influence on CO2-injection enhanced gas recovery (EGR). *International Journal of Greenhouse Gas Control*, *113*, 103530. https://doi.org/10.1016/j.ijggc.2021.103530

Dodgshun, J. *Hydrogen: Clearing Up the Colours*. https://www.enapter.com/blog/hydrogen-clearing-up-the-colours/

Doebelin, N., & Kleeberg, R. (2015). Profex: a graphical user interface for the Rietveld refinement program BGMN. *Journal of Applied Crystallography*, *48*(5), 1573-1580. https://doi.org/doi:10.1107/S1600576715014685

Dohrmann, A. B., & Krüger, M. (2023). Microbial H2 Consumption by a Formation Fluid from a Natural Gas Field at High-Pressure Conditions Relevant for Underground H2 Storage. *Environmental Science & Technology*, *57*(2), 1092-1102. https://doi.org/10.1021/acs.est.2c07303

Dopffel, N., Jansen, S., & Gerritse, J. (2021). Microbial side effects of underground hydrogen storage – Knowledge gaps, risks and opportunities for successful implementation. *International Journal of Hydrogen Energy*, *46*(12), 8594-8606. https://doi.org/10.1016/j.ijhydene.2020.12.058

Dopffel, N., Mayers, K., Kedir, A., Alagic, E., An-Stepec, B. A., Djurhuus, K., Boldt, D., Beeder, J., & Hoth, S. (2023). Microbial hydrogen consumption leads to a significant pH increase under high-saline-conditions: implications for hydrogen storage in salt caverns. *Scientific Reports*, *13*(1), 10564. https://doi.org/10.1038/s41598-023-37630-y

Duan, Z., & Mao, S. (2006). A thermodynamic model for calculating methane solubility, density and gas phase composition of methane-bearing aqueous fluids from 273 to 523K and from 1 to 2000bar. *Geochimica et Cosmochimica Acta*, *70*(13), 3369-3386. https://doi.org/10.1016/j.gca.2006.03.018

Dullien, F. A. L. (1992). 1 - Pore Structure. In F. A. L. Dullien (Ed.), *Porous Media (Second Edition)* (pp. 5-115). Academic Press. https://doi.org/10.1016/B978-0-12-223651-8.50007-9

Dupnock, T. L., & Deshusses, M. A. (2019). Detailed investigations of dissolved hydrogen and hydrogen mass transfer in a biotrickling filter for upgrading biogas. *Bioresource Technology*, *290*, 121780. https://doi.org/10.1016/j.biortech.2019.121780

Dutta, A., Dutta Gupta, S., Gupta, A., Sarkar, J., Roy, S., Mukherjee, A., & Sar, P. (2018). Exploration of deep terrestrial subsurface microbiome in Late Cretaceous Deccan traps and underlying Archean basement, India. *Scientific Reports*, *8*(1), 17459. https://doi.org/10.1038/s41598-018-35940-0

Ebigbo, A., Golfier, F., & Quintard, M. (2013). A coupled, pore-scale model for methanogenic microbial activity in underground hydrogen storage. *Advances in Water Resources*, *61*, 74-85. https://doi.org/10.1016/j.advwatres.2013.09.004

Eddaoui, N., Panfilov, M., Ganzer, L., & Hagemann, B. (2021). Impact of Pore Clogging by Bacteria on Underground Hydrogen Storage. *Transport in Porous Media*, *139*(1), 89-108. https://doi.org/10.1007/s11242-021-01647-6

Edlmann, K., Haszeldine, S., Heinemann, N., Hassanpouryouzband, A., & Thaysen, E. J. H. B. (2021). HyStorPor: unlocking the UK's hydrogen storage. *HyStorPor Brief*.

ElHadidy, A. M., Peldszus, S., & Van Dyke, M. I. (2013). Development of a pore construction data analysis technique for investigating pore size distribution of ultrafiltration membranes by atomic force microscopy. *Journal of Membrane Science*, *429*, 373-383. https://doi.org/10.1016/j.memsci.2012.11.054

Energiewende, A. (2021). Making renewable hydrogen cost-competitive: Policy instruments for supporting green H_2. Conclusions drawn. *Agora Energiewende*.

Erdmann, E. (1910). Über heliumhaltige Gase der deutschen Kalilager. *Berichte der deutschen chemischen Gesellschaft*, *43*(1), 777-782. https://doi.org/10.1002/cber.191004301134

Ewton, E., Klasek, S., Peck, E., Wiest, J., & Colwell, F. (2021). Microbial Community Characteristics Largely Unaffected by X-Ray Computed Tomography of Sediment Cores. *Frontiers in Microbiology.12:584676*. https://doi.org/10.3389/fmicb.2021.584676

Fang, T., Zhang, L., Liu, N., Zhang, L., Wang, W., Yu, L., Li, C., & Lei, Y. (2018). Quantitative characterization of pore structure of the Carboniferous–Permian tight sandstone gas reservoirs in eastern Linqing depression by using NMR technique. *Petroleum Research*, *3*(2), 110-123. https://doi.org/10.1016/j.ptlrs.2018.06.003

Ferrell, R. T., & Himmelblau, D. M. (1967). Diffusion coefficients of hydrogen and helium in water. *AIChE Journal*, *13*(4), 702-708. https://doi.org/10.1002/aic.690130421

Fick, A. (1855). Ueber Diffusion. *Annalen der Physik*, *170*(1), 59-86. https://doi.org/10.1002/andp.18551700105

Fischer, D., Pagenkemper, S., Nellesen, J., Peth, S., Horn, R., & Schloter, M. (2013). Influence of non-invasive X-ray computed tomography (XRCT) on the microbial community structure and function in soil. *Journal of Microbiological Methods*, *93*(2), 121-123. https://doi.org/10.1016/j.mimet.2013.02.009

Fitzner, B. (1988). Untersuchung der Zusammenhänge zwischen dem Hohlraumgefüge von Natursteinen und physikalischen Verwitterungsvorgängen. *Mitteilungen zur Ingenieurgeologie und Hydrogeologie*. ISBN:

Fleury, M., Berne, P., & Bachaud, P. (2009). Diffusion of dissolved CO2 in caprock. *Energy Procedia*, *1*(1), 3461-3468. https://doi.org/10.1016/j.egypro.2009.02.137

Foh, S., Novil, M., Rockar, E., & Randolph, P. (1979). *Underground hydrogen storage. Final report. [Salt caverns, excavated caverns, aquifers and depleted fields]*. https://www.osti.gov/biblio/6536941

Frank, M. J. W., Kuipers, J. A. M., & van Swaaij, W. P. M. (1996). Diffusion Coefficients and Viscosities of CO2 + H2O, CO2 + CH3OH, NH3 + H2O, and NH3 + CH3OH Liquid Mixtures. *Journal of Chemical & Engineering Data*, *41*(2), 297-302. https://doi.org/10.1021/je950157k

Fu, F., Lin, L., & Xu, E. (2017). 4 - Functional pretreatments of natural raw materials. In M. Fan & F. Fu (Eds.), *Advanced High Strength Natural Fibre Composites in Construction* (pp. 87-114). Woodhead Publishing. https://doi.org/10.1016/B978-0-08-100411-1.00004-2

Gahleitner, G. (2013). Hydrogen from renewable electricity: An international review of power-to-gas pilot plants for stationary applications. *International Journal of Hydrogen Energy*, *38*(5), 2039-2061. https://doi.org/10.1016/j.ijhydene.2012.12.010

Gao, H., Zhang, B., Fan, L., Zhang, H., Chen, G., Tontiwachwuthikul, P., & Liang, Z. (2019). Study on Diffusivity of CO2 in Oil-Saturated Porous Media under High Pressure and Temperature. *Energy & Fuels*, *33*(11), 11364-11372. https://doi.org/10.1021/acs.energyfuels.9b01947

Gao, Z., Xu, H., Zhang, P., Ji, D., Xia, L., Wang, X., Li, B., Dou, M., & Xu, Y. (2020). Variations in bacterial community structures during geothermal water recharge-induced bioclogging. *Journal of Environmental Science and Health, Part A*, *55*(5), 629-637. https://doi.org/10.1080/10934529.2020.1724744

Gaol, C. L., Ganzer, L., Mukherjee, S., & Alkan, H. (2021). Investigation of clogging in porous media induced by microorganisms using a microfluidic application [10.1039/D0EW00766H]. *Environmental Science: Water Research & Technology*, *7*(2), 441-454. https://doi.org/10.1039/D0EW00766H

Gaus, G., Amann-Hildenbrand, A., Krooss, B. M., & Fink, R. (2019). Gas permeability tests on core plugs from unconventional reservoir rocks under controlled stress: A comparison of different transient methods. *Journal of Natural Gas Science and Engineering*, *65*, 224-236. https://doi.org/10.1016/j.jngse.2019.03.003

Gaus, G., Hoyer, E.-M., Seemann, T., Fink, R., Amann, F., & Littke, R. (2022). Laboratory investigation of permeability, pore space and unconfined compressive strength of uplifted Jurassic mudstones: The role of burial depth and thermal maturation. *Zeitschrift der Deutschen Gesellschaft für Geowissenschaften : ZDGG*, *173*(3), 469-489. https://doi.org/DOI:10.1127/zdgg/2022/0329

Ge, X., Myers, M. T., Liu, J., Fan, Y., Zahid, M. A., Zhao, J., & Hathon, L. (2021). Determining the transverse surface relaxivity of reservoir rocks: A critical review and perspective. *Marine and Petroleum Geology*, *126*, 104934. https://doi.org/10.1016/j.marpetgeo.2021.104934

Gerlach, R., & Cunningham, A. (2010). Influence of Biofilms on Porous Media Hydrodynamics. In: Porous Media: Applications in Biological Systems and Biotechnology, ed. Vafai K, *CRC Press Taylor Francis Group*, pp 173-230.. https://scholarworks.montana.edu/handle/1/13116

Gertz, K. H., & Loeschcke, H. H. (1954). Bestimmung der Diffusions-Koeffizienten von H2, O2, N2, und He in Wasser und Blutserum bei konstant gehaltener Konvektion. *Zeitschrift für Naturforschung B*, *9*(1), 1-9.

Ghaedi, M., Andersen, P. Ø., & Gholami, R. (2023). Hydrogen diffusion into caprock: A semi-analytical solution and a hydrogen loss criterion. *Journal of Energy Storage*, *64*, 107134. https://doi.org/10.1016/j.est.2023.107134

Ghanbarian, B., Hunt, A. G., Ewing, R. P., & Sahimi, M. (2013). Tortuosity in Porous Media: A Critical Review. *Soil Science Society of America Journal*, *77*(5), 1461-1477. https://doi.org/10.2136/sssaj2012.0435

Gherardi, F., Audigane, P., & Gaucher, E. C. (2012). Predicting long-term geochemical alteration of wellbore cement in a generic geological CO2 confinement site: Tackling a difficult reactive transport modeling challenge. *Journal of Hydrology*, *420-421*, 340-359. https://doi.org/10.1016/j.jhydrol.2011.12.026

Gholami, Y., Azin, R., Fatehi, R., Osfouri, S., & Bahadori, A. (2015). Prediction of carbon dioxide dissolution in bulk water under isothermal pressure decay at different boundary conditions. *Journal of Molecular Liquids*, *202*, 23-33. https://doi.org/10.1016/j.molliq.2014.11.031

Gill, W. N., Sankarasubramanian, R., & Taylor, G. I. (1997). Exact analysis of unsteady convective diffusion. *Proceedings of the Royal Society of London. A. Mathematical and Physical Sciences*, *316*(1526), 341-350. https://doi.org/10.1098/rspa.1970.0083

Gnanasekaran, D., & Reddy, B. S. R. (2013). Cost effective poly(urethane-imide)-POSS membranes for environmental and energy-related processes. *Clean Technologies and Environmental Policy*, *15*(2), 383-389. https://doi.org/10.1007/s10098-012-0500-7

Gonzalez, R., & Woods, R. (2008). Digital image processing. In: Pearson Education Ltd.

Grathwohl, P. (1998). Diffusion in Natural Porous Media: Contaminant Transport, Sorption/Desorption and Dissolution Kinetics (1 ed.). *Springer New York, NY*. ISBN: https://doi.org/10.1007/978-1-4615-5683-1

Gregg, S. J., Sing, K. S. W. & Salzberg, H. W. (1967). Adsorption surface area and porosity. *Journal of The Electrochemical Society, 114*(11), 279Ca. https://doi.org/10.1149/1.2426447

Gregory, S. P., Barnett, M. J., Field, L. P., & Milodowski, A. E. (2019). Subsurface Microbial Hydrogen Cycling: Natural Occurrence and Implications for Industry. *Microorganisms*, *7*(2). https://doi.org/10.3390/microorganisms7020053

Grekov, D. I., Robinet, J.-C., & Grambow, B. (2023). Adsorption of methane and carbon dioxide by water-saturated clay minerals and clay rocks. *Applied Clay Science*, *232*, 106806. https://doi.org/10.1016/j.clay.2022.106806

Grogan, A. T., Pinczewski, V. W., Ruskauff, G. J., & Orr, F. M., Jr. (1988). Diffusion of CO2 at Reservoir Conditions: Models and Measurements. *SPE Reservoir Engineering*, *3*(01), 93-102. https://doi.org/10.2118/14897-PA

Grunewald, E., & Knight, R. (2009). A laboratory study of NMR relaxation times and pore coupling in heterogeneous media. *Geophysics*, *74*(6), E215-E221. https://doi.org/10.1190/1.3223712

Gubbins, K. E., Bhatia, K. K., & Walker, R. D. (1966). Diffusion of gases in electrolytic solutions. *AIChE Journal*, *12*(3), 548-552. https://doi.org/10.1002/aic.690120328

Guélard, J., Beaumont, V., Rouchon, V., Guyot, F., Pillot, D., Jézéquel, D., Ader, M., Newell, K. D., & Deville, E. (2017). Natural H2 in Kansas: Deep or shallow origin? *Geochemistry, Geophysics, Geosystems*, *18*(5), 1841-1865. https://doi.org/10.1002/2016GC006544

Gülay, A., Tatari, K., Musovic, S., Mateiu Ramona, V., Albrechtsen, H.-J., & Smets Barth, F. (2014). Internal Porosity of Mineral Coating Supports Microbial Activity in Rapid Sand Filters for Groundwater Treatment. *Applied and Environmental Microbiology*, *80*(22), 7010-7020. https://doi.org/10.1128/AEM.01959-14

Guo, H., Chen, Y., Lu, W., Li, L., & Wang, M. (2013). In situ Raman spectroscopic study of diffusion coefficients of methane in liquid water under high pressure and wide

temperatures. *Fluid Phase Equilibria*, *360*, 274-278. https://doi.org/10.1016/j.fluid.2013.09.051

Hage, R.; Kombargi, R.; Elborai, S.; & Anouti, Y. (2020). The dawn of green hydrogen: Maintaining the GCC's edge in a decarbonized world. *Strategy & PwC: New York*

Hagemann, B. (2017). Numerical and Analytical Modeling of Gas Mixing and Bio-Reactive Transport during Underground Hydrogen Storage , 1. edition edn. Schriftenreihe Des Energie-ForschungszentrumsNiedersachsen, vol. Band 50. Cuvillier Verlag, Göttingen. https://doi.org/10.21268/20180116-085820

Hagemann, B., Rasoulzadeh, M., Panfilov, M., Ganzer, L., & Reitenbach, V. (2014). Hydrogenization of Underground Storage of Natural Gas - Impact of Hydrogen on Bio-chemical Transformations of Stored Gas *ECMOR XIV - 14th European Conference on the Mathematics of Oil Recovery*,

Hagemann, B., Rasoulzadeh, M., Panfilov, M., Ganzer, L., & Reitenbach, V. (2015). Mathematical modeling of unstable transport in underground hydrogen storage. *Environmental Earth Sciences*, *73*(11), 6891-6898. https://doi.org/10.1007/s12665-015-4414-7

Hagemann, B., Rasoulzadeh, M., Panfilov, M., Ganzer, L., & Reitenbach, V. (2016). Hydrogenization of underground storage of natural gas. *Computational Geosciences*, *20*(3), 595-606. https://doi.org/10.1007/s10596-015-9515-6

Halder, P., Babaie, M., Salek, F., Haque, N., Savage, R., Stevanovic, S., Bodisco, T. A., & Zare, A. (2024). Advancements in hydrogen production, storage, distribution and refuelling for a sustainable transport sector: Hydrogen fuel cell vehicles. *International Journal of Hydrogen Energy*, *52*, 973-1004. https://doi.org/10.1016/j.ijhydene.2023.07.204

Halim, A., Shapiro, A., Lantz, A. E., & Nielsen, S. M. (2014). Experimental Study of Bacterial Penetration into Chalk Rock: Mechanisms and Effect on Permeability. *Transport in Porous Media*, *101*(1), 1-15. https://doi.org/10.1007/s11242-013-0227-x

Hanebeck, D. (1995). Experimentelle Simulation und Untersuchung der Genese und Expulsion von Erdölen aus Muttergesteinen. *Forschungszentrum, Zentralbibliothek*. ISBN: http://hdl.handle.net/2128/21296

Hanson, A. G., Kutchko, B., Lackey, G., Gulliver, D., Strazisar, B. R., Tinker, K. A., Haeri, F., Wright, R., Huerta, N., Baek, S., Bagwell, C., Toledo Camargo, J. d., Freeman, G., Kuang, W., Torgeson, J., White, J., Buscheck, T., Castelletto, N., & Smith, M. (2022). *Subsurface Hydrogen and Natural Gas Storage: State of Knowledge and Research Recommendations Report*. https://www.osti.gov/biblio/1846632

Harrington, J. F., Milodowski, A. E., Graham, C. C., Rushton, J. C., & Cuss, R. J. (2012). Evidence for gas-induced pathways in clay using a nanoparticle injection technique. *Mineralogical Magazine*, *76*(8), 3327-3336. https://doi.org/10.1180/minmag.2012.076.8.45

Hart, D. (1997). Hydrogen power : the commerical future of 'the ultimate fuel'. *Financial Times Energy Pub, a division of Pearson Professional Limited*. ISBN: 1853347604 https://cir.nii.ac.jp/crid/1130000794060174848

Hashemi, L., Blunt, M., & Hajibeygi, H. (2021). Pore-scale modelling and sensitivity analyses of hydrogen-brine multiphase flow in geological porous media. *Scientific Reports*, *11*(1), 8348. https://doi.org/10.1038/s41598-021-87490-7

Hassannayebi, N. (2019). An assessment of underground hydrogen storage: Transport, geochemistry, and bioactivity. *Doctoral Thesis, Montanuniversitaet Leoben*.

Hassannayebi, N., Jammernegg, B., Schritter, J., Arnold, P., Enzmann, F., Kersten, M., Loibner, A. P., Fernø, M., & Ott, H. (2021). Relationship Between Microbial

Growth and Hydraulic Properties at the Sub-Pore Scale. *Transport in Porous Media*, *139*(3), 579-593. https://doi.org/10.1007/s11242-021-01680-5

Hassanpouryouzband, A., Adie, K., Cowen, T., Thaysen, E. M., Heinemann, N., Butler, I. B., Wilkinson, M., & Edlmann, K. (2022a). Geological Hydrogen Storage: Geochemical Reactivity of Hydrogen with Sandstone Reservoirs. *ACS energy letters*, *vol. 7 (7)*(2203–2210). https://doi.org/doi:10.1021/acsenergylett.2c01024

Hassanpouryouzband, A., Adie, K., Cowen, T., Thaysen, E. M., Heinemann, N., Butler, I. B., Wilkinson, M., & Edlmann, K. (2022b). Geological Hydrogen Storage: Geochemical Reactivity of Hydrogen with Sandstone Reservoirs. *ACS Energy Letters*, *7*(7), 2203-2210. https://doi.org/10.1021/acsenergylett.2c01024

Hata, T., Kuwano, R., & Kikuchi, Y. (2006). Characterization of the Micro Organism Mobility in In-Situ Bioremediation: Visualization using micro-focus X-ray CT Scanner. In *Advances in X-ray Tomography for Geomaterials* (pp. 333-339). https://doi.org/10.1002/9780470612187.ch34

Heinemann, N., Alcalde, J., Miocic, J. M., Hangx, S. J. T., Kallmeyer, J., Ostertag-Henning, C., Hassanpouryouzband, A., Thaysen, E. M., Strobel, G. J., Schmidt-Hattenberger, C., Edlmann, K., Wilkinson, M., Bentham, M., Stuart Haszeldine, R., Carbonell, R., & Rudloff, A. (2021). Enabling large-scale hydrogen storage in porous media – the scientific challenges. *Energy & Environmental Science*, *14*(2), 853-864. https://doi.org/10.1039/d0ee03536j

Heinemann, N., Booth, M. G., Haszeldine, R. S., Wilkinson, M., Scafidi, J., & Edlmann, K. (2018). Hydrogen storage in porous geological formations – onshore play opportunities in the midland valley (Scotland, UK). *International Journal of Hydrogen Energy*, *43*(45), 20861-20874. https://doi.org/10.1016/j.ijhydene.2018.09.149

Hellerschmied, C., Schritter, J., Waldmann, N., Zaduryan, A. B., Rachbauer, L., Scherr, K. E., Andiappan, A., Bauer, S., Pichler, M., & Loibner, A. P. (2024). Hydrogen storage and geo-methanation in a depleted underground hydrocarbon reservoir. *Nature Energy*, *9*(3), 333-344. https://doi.org/10.1038/s41560-024-01458-1

Hemme, C., & van Berk, W. (2017). Potential risk of H2S generation and release in salt cavern gas storage. *Journal of Natural Gas Science and Engineering*, *47*, 114-123. https://doi.org/10.1016/j.jngse.2017.09.007

Hemme, C., & van Berk, W. (2018). Hydrogeochemical Modeling to Identify Potential Risks of Underground Hydrogen Storage in Depleted Gas Fields. *Applied Sciences*, *8*(11). https://doi.org/10.3390/app8112282

Hoehler, T. M., & Jørgensen, B. B. (2013). Microbial life under extreme energy limitation. *Nature Reviews Microbiology*, *11*(2), 83-94. https://doi.org/10.1038/nrmicro2939

Hogeweg, S., Michelsen, J., Hagemann, B., & Ganzer, L. (2024). Empirical and Numerical Modelling of Gas–Gas Diffusion for Binary Hydrogen–Methane Systems at Underground Gas Storage Conditions. *Transport in Porous Media*, *151*(1), 213-232. https://doi.org/10.1007/s11242-023-02039-8

Hojat, N., Gentile, P., Ferreira, A. M., & Šiller, L. (2023). Automatic pore size measurements from scanning electron microscopy images of porous scaffolds. *Journal of Porous Materials*, *30*(1), 93-101. https://doi.org/10.1007/s10934-022-01309-y

Holzer, L., Marmet, P., Fingerle, M., Wiegmann, A., Neumann, M., & Schmidt, V. (2023). Tortuosity-Porosity Relationships: Review of Empirical Data from Literature. In L. Holzer, P. Marmet, M. Fingerle, A. Wiegmann, M. Neumann, & V. Schmidt (Eds.), *Tortuosity and Microstructure Effects in Porous Media: Classical Theories,*

Empirical Data and Modern Methods (pp. 51-89). Springer International Publishing. https://doi.org/10.1007/978-3-031-30477-4_3

Holzer, L., Wiedenmann, D., Münch, B., Keller, L., Prestat, M., Gasser, P., Robertson, I., & Grobéty, B. (2013). The influence of constrictivity on the effective transport properties of porous layers in electrolysis and fuel cells. *Journal of Materials Science*, *48*(7), 2934-2952. https://doi.org/10.1007/s10853-012-6968-z

Hommel, J., Coltman, E., & Class, H. (2018). Porosity–Permeability Relations for Evolving Pore Space: A Review with a Focus on (Bio-)geochemically Altered Porous Media. *Transport in Porous Media*, *124*(2), 589-629. https://doi.org/10.1007/s11242-018-1086-2

Horsfield, B., Mahlstedt, N., Weniger, P., Misch, D., Vranjes-Wessely, S., Han, S., & Wang, C. (2022). Molecular hydrogen from organic sources in the deep Songliao Basin, P.R. China. *International Journal of Hydrogen Energy*, *47*(38), 16750-16774. https://doi.org/10.1016/j.ijhydene.2022.02.208

Houghton, G., Ritchie, P. D., & Thomson, J. A. (1962). The rate of solution of small stationary bubbles and the diffusion coefficients of gases in liquids. *Chemical Engineering Science*, *17*(4), 221-227. https://doi.org/10.1016/0009-2509(62)85001-5

Hrubanova, K., Skoupy, R., Nebesarova, J., Ruzicka, F., & Krzyzanek, V. (2016). The sample preparation for cryo-SEM: the real ultrastructure of microbial biofilm or just artifacts? In *European Microscopy Congress 2016: Proceedings* (pp. 203-204). https://doi.org/10.1002/9783527808465.EMC2016.6907

Hu, Z., Gaus, G., Seemann, T., Zhang, Q., Littke, R., & Fink, R. (2021). Pore structure and sorption capacity investigations of Ediacaran and Lower Silurian gas shales from the Upper Yangtze platform, China. *Geomechanics and Geophysics for Geo-Energy and Geo-Resources*, *7*(3), 71. https://doi.org/10.1007/s40948-021-00262-5

Hubao, Zhibing Yang, Yongqiang Chen, Ran Hu, Colin D. Wood, Qinjun Kang, & Yi-Feng Chen. (2024). H2 diffusion in cement nanopores and its implication for underground hydrogen storage. *Journal of Energy Storage*, *102*, 113926. https://doi.org/https://doi.org/10.1016/j.est.2024.113926

Huber, H., Thomm, M., König, H., Thies, G., & Stetter, K. O. (1982). Methanococcus thermolithotrophicus, a novel thermophilic lithotrophic methanogen. *Archives of Mikrobiology.*, *132*, 47-50. https://epub.uni-regensburg.de/11162/

Hutchinson Ian, P., Jackson, O., Stocks Andrew, E., Barnicoat Andrew, C., & Lawrence Stephen, R. (2024). Greenstones as a source of hydrogen in cratonic sedimentary basins. *Geological Society, London, Special Publications*, *547*(1), SP547-2023-2039. https://doi.org/10.1144/SP547-2023-39

Iassonov, P., Gebrenegus, T., & Tuller, M. (2009). Segmentation of X-ray computed tomography images of porous materials: A crucial step for characterization and quantitative analysis of pore structures. *Water Resources Research*, *45*(9). https://doi.org/10.1029/2009WR008087

IEA. (2023). World Energy Outlook 2023, IEA, Paris https://www.iea.org/reports/world-energy-outlook-2023, Licence: CC BY 4.0 (report); CC BY NC SA 4.0 (Annex A)

Incer-Valverde, J., Korayem, A., Tsatsaronis, G., & Morosuk, T. (2023). "Colors" of hydrogen: Definitions and carbon intensity. *Energy Conversion and Management*, *291*, 117294. https://doi.org/10.1016/j.enconman.2023.117294

Ivanova, A. E., Borzenkov, I. A., Tarasov, A. L., Milekhina, E. I., & Belyaev, S. S. (2007). A microbiological study of an underground gas storage in the process of gas

extraction. *Microbiology*, *76*(4), 461-468. https://doi.org/10.1134/S0026261707040121

Jackson, O., Lawrence, S. R., Hutchinson, I. P., Stocks, A. E., Barnicoat, A. C., & Powney, M. (2024). Natural hydrogen: sources, systems and exploration plays. *Geoenergy*, *2*(1), geoenergy2024-2002. https://doi.org/10.1144/geoenergy2024-002

Jacops, E. (2018). Development and application of an innovative method for studying the diffusion of dissolved gases in porous saturated media. *Doctoral Thesis, RWTH Aachen University*. http://publications.rwth-aachen.de/record/748491

Jacops, E., Aertsens, M., Maes, N., Bruggeman, C., Krooss, B. M., Amann-Hildenbrand, A., Swennen, R., & Littke, R. (2017). Interplay of molecular size and pore network geometry on the diffusion of dissolved gases and HTO in Boom Clay. *Applied Geochemistry*, *76*, 182-195. https://doi.org/10.1016/j.apgeochem.2016.11.022

Jacops, E., Rogiers, B., Frederickx, L., Swennen, R., Littke, R., Krooss, B. M., Amann-Hildenbrand, A., & Bruggeman, C. (2020). The relation between petrophysical and transport properties of the Boom Clay and Eigenbilzen Sands. *Applied Geochemistry*, *114*, 104527. https://doi.org/10.1016/j.apgeochem.2020.104527

Jacops, E., Volckaert, G., Maes, N., Weetjens, E., & Govaerts, J. (2013). Determination of gas diffusion coefficients in saturated porous media: He and CH4 diffusion in Boom Clay. *Applied Clay Science*, *83-84*, 217-223. https://doi.org/10.1016/j.clay.2013.08.047

Jacops, E., Wouters, K., Volckaert, G., Moors, H., Maes, N., Bruggeman, C., Swennen, R., & Littke, R. (2015). Measuring the effective diffusion coefficient of dissolved hydrogen in saturated Boom Clay. *Applied Geochemistry*, *61*, 175-184. https://doi.org/10.1016/j.apgeochem.2015.05.022

Jahanbani Veshareh, M., Thaysen, E. M., & Nick, H. M. (2022). Feasibility of hydrogen storage in depleted hydrocarbon chalk reservoirs: Assessment of biochemical and chemical effects. *Applied Energy*, *323*, 119575. https://doi.org/https://doi.org/10.1016/j.apenergy.2022.119575

Jähne, B., Heinz, G., & Dietrich, W. (1987a). Measurement of the diffusion coefficients of sparingly soluble gases in water. *Journal of Geophysical Research: Oceans*, *92*(C10), 10767-10776. https://doi.org/10.1029/JC092iC10p10767

Jamialahmadi, M., Emadi, M., & Müller-Steinhagen, H. (2006). Diffusion coefficients of methane in liquid hydrocarbons at high pressure and temperature. *Journal of Petroleum Science and Engineering*, *53*(1), 47-60. https://doi.org/10.1016/j.petrol.2006.01.011

Jensen, M. B., Kofoed, M. V. W., Fischer, K., Voigt, N. V., Agneessens, L. M., Batstone, D. J., & Ottosen, L. D. M. (2018). Venturi-type injection system as a potential H2 mass transfer technology for full-scale in situ biomethanation. *Applied Energy*, *222*, 840-846. https://doi.org/10.1016/j.apenergy.2018.04.034

Jensen, M. B., Ottosen, L. D. M., & Kofoed, M. V. W. (2021). H2 gas-liquid mass transfer: A key element in biological Power-to-Gas methanation. *Renewable and Sustainable Energy Reviews*, *147*, 111209. https://doi.org/10.1016/j.rser.2021.111209

Jørgensen, B. B., Isaksen, M. F., & Jannasch, H. W. (1992). Bacterial Sulfate Reduction Above 100°C in Deep-Sea Hydrothermal Vent Sediments. *Science*, *258*(5089), 1756-1757. https://doi.org/10.1126/science.258.5089.1756

Jun, Y.-S., Giammar, D. E., & Werth, C. J. (2013). Impacts of Geochemical Reactions on Geologic Carbon Sequestration. *Environmental Science & Technology*, *47*(1), 3-8. https://doi.org/10.1021/es3027133

Kapellos, G. E., Alexiou, T. S., & Pavlou, S. (2015). Chapter 8 - Fluid-Biofilm Interactions in Porous Media. In S. M. Becker & A. V. Kuznetsov (Eds.), *Heat Transfer and*

Fluid Flow in Biological Processes (pp. 207-238). Academic Press. https://doi.org/10.1016/B978-0-12-408077-5.00008-0

Karadagli, F., & Rittmann, B. E. (2005). Kinetic Characterization of Methanobacterium bryantii M.o.H. *Environmental Science & Technology*, *39*(13), 4900-4905. https://doi.org/10.1021/es047993b

Kashefi, K., & Lovley Derek, R. (2000). Reduction of Fe(III), Mn(IV), and Toxic Metals at 100°C by Pyrobaculum islandicum. *Applied and Environmental Microbiology*, *66*(3), 1050-1056. https://doi.org/10.1128/AEM.66.3.1050-1056.2000

Kaye, G. W. C., & Laby, T. H. (1928). Tables of physical and chemical constants and some mathematical functions. *Longmans, Green and Company Limited*. ISBN:

Keating, K., & Knight, R. (2012). The effect of spatial variation in surface relaxivity on nuclear magnetic resonance relaxation rates. *GEOPHYSICS*, *77*(5), E365-E377. https://doi.org/10.1190/geo2011-0462.1

Kenyon, W. E. (1997). Petrophysical Principles of Applications of NMR Logging. *The Log Analyst*, *38*(02).

Khajooie, S., Gaus, G., Dohrmann, A. B., Krüger, M., & Littke, R. (2024a). Methanogenic conversion of hydrogen to methane in reservoir rocks: An experimental study of microbial activity in water-filled pore space. *International Journal of Hydrogen Energy*, *50*, 272-290. https://doi.org/10.1016/j.ijhydene.2023.07.065

Khajooie, S., Gaus, G., Seemann, T., Klaver, J., Claes, H., Nehler, M., Ahrens, B., & Littke, R. (2024b). Methanogenic activity in water-saturated reservoir analogues for underground hydrogen storage: The role of surface area. *International Journal of Hydrogen Energy*, *90*, 171-190. https://doi.org/10.1016/j.ijhydene.2024.09.395

Kim, H. Y., Maruta, R. H., Huanca, D. R., & Salcedo, W. J. (2013). Correlation-based multi-shape granulometry with application in porous silicon nanomaterial characterization. *Journal of Porous Materials*, *20*(2), 375-385. https://doi.org/10.1007/s10934-012-9607-9

Kimmel, D. E., Klasson, K. T., Clausen, E. C., & Gaddy, J. L. (1991). Performance of trickle-bed bioreactors for converting synthesis gas to methane. *Applied Biochemistry and Biotechnology*, *28*(1), 457-469. https://doi.org/10.1007/BF02922625

Kimura, S., Noda, S., & Minagawa, H. (2021). Experimental investigation of effects of mica content, Fe and pressure on the pore size distribution and permeability of sandy sediment using proton nuclear magnetic resonance. *Engineering Geology*, *295*, 106408. https://doi.org/10.1016/j.enggeo.2021.106408

Klaver, J., Desbois, G., Littke, R., & Urai, J. L. (2015a). BIB-SEM characterization of pore space morphology and distribution in postmature to overmature samples from the Haynesville and Bossier Shales. *Marine and Petroleum Geology*, *59*, 451-466. https://doi.org/10.1016/j.marpetgeo.2014.09.020

Klaver, J., Hemes, S., Houben, M., Desbois, G., Radi, Z., & Urai, J. L. (2015b). The connectivity of pore space in mudstones: insights from high-pressure Wood's metal injection, BIB-SEM imaging, and mercury intrusion porosimetry. *Geofluids*, *15*(4), 577-591. https://doi.org/10.1111/gfl.12128

Krevor, S. C. M., Pini, R., Zuo, L., & Benson, S. M. (2012). Relative permeability and trapping of CO2 and water in sandstone rocks at reservoir conditions. *Water Resources Research*, *48*(2). https://doi.org/10.1029/2011WR010859

Krooss, B. (2008). Evaluation of Database on Gas Migration through Clayey Host Rocks. *Report for NIRAS-ONDRAF, RWTH Aachen University*.

Krooss, B., & Schaefer, R. (1987). Experimental measurements of the diffusion parameters of light hydrocarbons in water-saturated sedimentary rocks—I. A new experimental procedure. *Organic Geochemistry*, *11*(3), 193-199.

Krooss, B. M., Leythaeuser, D., & Schaefer, R. G. (1988). Light hydrocarbon diffusion in a caprock. *Chemical Geology*, *71*(1), 65-76. https://doi.org/10.1016/0009-2541(88)90106-4

Krooss, B. M., Leythaeuser, D., & Schaefer, R. G. (1992). The Quantification of Diffusive Hydrocarbon Losses Through Cap Rocks of Natural Gas Reservoirs—A Reevaluation: Reply1. *AAPG Bulletin*, *76*(11), 1842-1846. https://doi.org/10.1306/BDFF8AF6-1718-11D7-8645000102C1865D

Krumholz Lee, R., Harris Steve, H., Tay Stephen, T., & Suflita Joseph, M. (1999). Characterization of Two Subsurface H2-Utilizing Bacteria, Desulfomicrobium hypogeium sp. nov. and Acetobacterium psammolithicumsp. nov., and Their Ecological Roles. *Applied and Environmental Microbiology*, *65*(6), 2300-2306. https://doi.org/10.1128/AEM.65.6.2300-2306.1999

Kuila, U., & Prasad, M. J. G. P. (2013). Specific surface area and pore-size distribution in clays and shales. *61*(2-Rock Physics for Reservoir Exploration, Characterisation and Monitoring), 341-362.

Kunz, O., & Wagner, W. (2012). The GERG-2008 Wide-Range Equation of State for Natural Gases and Other Mixtures: An Expansion of GERG-2004. *Journal of Chemical & Engineering Data*, *57*(11), 3032-3091. https://doi.org/10.1021/je300655b

Labus, M., & Wertz, F. (2017). Identifying geochemical reactions on wellbore cement/caprock interface under sequestration conditions. *Environmental Earth Sciences*, *76*(12), 443. https://doi.org/10.1007/s12665-017-6771-x

Lai, J., Wang, G., Wang, Z., Chen, J., Pang, X., Wang, S., Zhou, Z., He, Z., Qin, Z., & Fan, X. (2018). A review on pore structure characterization in tight sandstones. *Earth-Science Reviews*, *177*, 436-457. https://doi.org/10.1016/j.earscirev.2017.12.003

Lauro, F. M., McDougald, D., Thomas, T., Williams, T. J., Egan, S., Rice, S., DeMaere, M. Z., Ting, L., Ertan, H., Johnson, J., Ferriera, S., Lapidus, A., Anderson, I., Kyrpides, N., Munk, A. C., Detter, C., Han, C. S., Brown, M. V., Robb, F. T., . . . Cavicchioli, R. (2009). The genomic basis of trophic strategy in marine bacteria. *Proceedings of the National Academy of Sciences*, *106*(37), 15527-15533. https://doi.org/10.1073/pnas.0903507106

Leal-Egaña, A., Braumann, U.-D., Díaz-Cuenca, A., Nowicki, M., & Bader, A. (2011). Determination of pore size distribution at the cell-hydrogel interface. *Journal of Nanobiotechnology*, *9*(1), 24. https://doi.org/10.1186/1477-3155-9-24

Lewis, W. K., & Whitman, W. G. (1924). Principles of Gas Absorption. *Industrial & Engineering Chemistry*, *16*(12), 1215-1220. https://doi.org/10.1021/ie50180a002

Li, Q., Xu, M., Wang, G., Chen, R., Qiao, W., & Wang, X. (2018). Biochar assisted thermophilic co-digestion of food waste and waste activated sludge under high feedstock to seed sludge ratio in batch experiment. *Bioresource Technology*, *249*, 1009-1016. https://doi.org/10.1016/j.biortech.2017.11.002

Li, S., Li, Z., & Dong, Q. (2016). Diffusion coefficients of supercritical CO2 in oil-saturated cores under low permeability reservoir conditions. *Journal of CO2 Utilization*, *14*, 47-60. https://doi.org/10.1016/j.jcou.2016.02.002

Li, S., Tang, D., Xu, H., Pan, Z., Huang, W., & Zhu, X. (2015). Comparative analysis on water movability in pores of different reservoir rocks by nuclear magnetic resonance. *Energy Exploration & Exploitation*, *33*(5), 689-705. https://www.jstor.org/stable/90007147

Li, Z. (2006). Study of gas diffusion in liquid-saturated porous media for oil recovery and CO2 sequestration *Ph. D. Dissertation, University of Regina, Regina, SK*.

Li, Z., & Dong, M. (2010). Experimental Study of Diffusive Tortuosity of Liquid-Saturated Consolidated Porous Media. *Industrial & Engineering Chemistry Research*, *49*(13), 6231-6237. https://doi.org/10.1021/ie901765d

Li, Z., Dong, M., Li, S., & Dai, L. (2006). A New Method for Gas Effective Diffusion Coefficient Measurement in Water-Saturated Porous Rocks under High Pressures. *Journal of Porous Media*, *9*(5), 445-461. https://doi.org/10.1615/JPorMedia.v9.i5.50

Liao, P.-S., Chen, T.-S., & Chung, P.-C. (2001). A Fast Algorithm for Multilevel Thresholding. *J. Inf. Sci. 17*, 713-727.

Liebscher, A., Wackerl, J., & Streibel, M. (2016). Geologic Storage of Hydrogen – Fundamentals, Processing, and Projects. In *Hydrogen Science and Engineering : Materials, Processes, Systems and Technology* (pp. 629-658). https://doi.org/10.1002/9783527674268.ch26

Liponi, A., Pasini, G., Baccioli, A., & Ferrari, L. (2023). Hydrogen from renewables: Is it always green? The Italian scenario. *Energy Conversion and Management*, *276*, 116525. https://doi.org/10.1016/j.enconman.2022.116525

Liu, G., Zhao, Z., Sun, M., Li, J., Hu, G., & Wang, X. (2012). New insights into natural gas diffusion coefficient in rocks. *Petroleum Exploration and Development*, *39*(5), 597-604. https://doi.org/10.1016/S1876-3804(12)60081-0

Liu, K., & Ostadhassan, M. (2019). The impact of pore size distribution data presentation format on pore structure interpretation of shales. *Advances in Geo-Energy Research*, *3*(2), 187-197. https://doi.org/10.26804/ager.2019.02.08

Liu, N., Kovscek, A. R., Fernø, M. A., & Dopffel, N. (2023). Pore-scale study of microbial hydrogen consumption and wettability alteration during underground hydrogen storage. *Frontiers in Energy Research*, *11*. https://doi.org/10.3389/fenrg.2023.1124621

Lou, X., Chakraborty, N., Karpyn, Z. T., Ayala, L. F., Nagarajan, N., & Wijaya, Z. (2021). Experimental Study of Gas/Liquid Diffusion in Porous Rocks and Bulk Fluids To Investigate the Effect of Rock-Matrix Hindrance. *SPE Journal*, *26*(03), 1174-1188. https://doi.org/10.2118/195941-PA

Lovley, D. R., & Goodwin, S. (1988). Hydrogen concentrations as an indicator of the predominant terminal electron-accepting reactions in aquatic sediments. *Geochimica et Cosmochimica Acta*, *52*(12), 2993-3003. https://doi.org/10.1016/0016-7037(88)90163-9

Lowell, S., Shields, J. E., Thomas, M. A., & Thommes, M. (2012). Characterization of porous solids and powders: surface area, pore size and density (Vol. 16). *Springer Science & Business Media*. ISBN: 1402023030

Lu, M., Gu, L.-P., & Xu, W.-H. (2013). Treatment of petroleum refinery wastewater using a sequential anaerobic–aerobic moving-bed biofilm reactor system based on suspended ceramsite. *Water Science and Technology*, *67*(9), 1976-1983. https://doi.org/10.2166/wst.2013.077

Lu, W., Guo, H., Chou, I. M., Burruss, R. C., & Li, L. (2013). Determination of diffusion coefficients of carbon dioxide in water between 268 and 473K in a high-pressure capillary optical cell with in situ Raman spectroscopic measurements. *Geochimica et Cosmochimica Acta*, *115*, 183-204. https://doi.org/10.1016/j.gca.2013.04.010

Lubbe, F., Rongé, J., Bosserez, T., & Martens, J. A. (2023). Golden hydrogen. *Current Opinion in Green and Sustainable Chemistry*, *39*, 100732. https://doi.org/10.1016/j.cogsc.2022.100732

Lucas-Oliveira, E., Araujo-Ferreira, A. G., Trevizan, W. A., dos Santos, B. C. C., & Bonagamba, T. J. (2020). Sandstone surface relaxivity determined by NMR T2 distribution and digital rock simulation for permeability evaluation. *Journal of Petroleum Science and Engineering*, *193*, 107400. https://doi.org/10.1016/j.petrol.2020.107400

Lv, J., Chi, Y., Zhao, C., Zhang, Y., & Mu, H. (2019). Experimental study of the supercritical CO2 diffusion coefficient in porous media under reservoir conditions. *Royal Society Open Science*, *6*(6), 181902. https://doi.org/10.1098/rsos.181902

Lysyy, M., Ersland, G., & Fernø, M. (2022). Pore-scale dynamics for underground porous media hydrogen storage. *Advances in Water Resources*, *163*, 104167. https://doi.org/10.1016/j.advwatres.2022.104167

Machel, H. G. (2001). Bacterial and thermochemical sulfate reduction in diagenetic settings — old and new insights. *Sedimentary Geology*, *140*(1), 143-175. https://doi.org/10.1016/S0037-0738(00)00176-7

Magot, M., Ollivier, B., & Patel, B. K. C. (2000). Microbiology of petroleum reservoirs. *Antonie van Leeuwenhoek*, *77*(2), 103-116. https://doi.org/10.1023/A:1002434330514

Maharajh, D. M., & Walkley, J. (1973). The Temperature Dependence of the Diffusion Coefficients of Ar, CO2, CH4, CH3Cl, CH3Br, and CHCl2F in Water. *Canadian Journal of Chemistry*, *51*(6), 944-952. https://doi.org/10.1139/v73-140

Mahlstedt, N., Horsfield, B., Weniger, P., Misch, D., Shi, X., Noah, M., & Boreham, C. (2022). Molecular hydrogen from organic sources in geological systems. *Journal of Natural Gas Science and Engineering*, *105*, 104704. https://doi.org/10.1016/j.jngse.2022.104704

Maiga, O., Deville, E., Laval, J., Prinzhofer, A., & Diallo, A. B. (2024). Trapping processes of large volumes of natural hydrogen in the subsurface: The emblematic case of the Bourakebougou H2 field in Mali. *International Journal of Hydrogen Energy*, *50*, 640-647. https://doi.org/10.1016/j.ijhydene.2023.10.131

Marcogaz. (2017). Guidance: Injection of hydrogen/natural gas admixtures in underground gas storage (UGS). *In: Technical Association of the European Natural Gas Industry*, Brussels, Belgium.

Mazloomi, K., & Gomes, C. (2012). Hydrogen as an energy carrier: Prospects and challenges. *Renewable and Sustainable Energy Reviews*, *16*(5), 3024-3033. https://doi.org/10.1016/j.rser.2012.02.028

Mazzeo, L., Signorini, A., Lembo, G., Bavasso, I., Di Palma, L., & Piemonte, V. (2021). In Situ Bio-Methanation Modelling of a Randomly Packed Gas Stirred Tank Reactor (GSTR). *Processes*, *9*(5). https://doi.org/10.3390/pr9050846

McPhee, C., Reed, J., & Zubizarreta, I. (2015). Chapter 9 - Capillary Pressure. In C. McPhee, J. Reed, & I. Zubizarreta (Eds.), *Developments in Petroleum Science* (Vol. 64, pp. 449-517). Elsevier. https://doi.org/10.1016/B978-0-444-63533-4.00009-3

Mendoza-Lera, C., Frossard, A., Knie, M., Federlein, L. L., Gessner, M. O., & Mutz, M. (2017). Importance of advective mass transfer and sediment surface area for streambed microbial communities. *Freshwater Biology*, *62*(1), 133-145. https://doi.org/10.1111/fwb.12856

Mertineit, M., & Schramm, M. (2019). Lithium Occurrences in Brines from Two German Salt Deposits (Upper Permian) and First Results of Leaching Experiments. *Minerals*, *9*(12).

Metz, B., Davidson, O., Coninck, H. d., Loos, M., & Meyer, L. (2005). IPCC special report on carbon dioxide capture and storage. *Cambridge University Press, New York, NY (United States)*. ISBN: https://www.osti.gov/biblio/20740954

Michelsen, J., Hagemann, B., Ganzer, L., & Hujer, W. (2022). Measurement of Hydrogen Diffusion through Caprock Samples. *In: Sixth International Conference on Fault and Top Seals. pp. 1–5. European Association of Geoscientists & Engineers*, Vienna, Austria. https://doi.org/10.3997/2214-4609.202243061

Michelsen, J., Langanke, N., Hagemann, B., Hogeweg, S., & Ganzer, L. (2023). Diffusion measurements with hydrogen and methane through reservoir rock samples, in: Advanced SCAL for Carbon Storage & CO2 Utilization. *Presented at the 36th International Symposium of the Society of Core Analysts*, Abu Dhabi, UAE, October 12, 2023.

Milkov, A. V. (2022). Molecular hydrogen in surface and subsurface natural gases: Abundance, origins and ideas for deliberate exploration. *Earth-Science Reviews*, *230*, 104063. https://doi.org/10.1016/j.earscirev.2022.104063

Mills, A. L. (2003). Keeping in Touch: Microbial Life on Soil Particle Surfaces. In *Advances in Agronomy* (Vol. 78, pp. 1-43). Academic Press. https://doi.org/10.1016/S0065-2113(02)78001-2

Monge, A. M., & Vayssaire, A. (2022). A Review of Some Aspects of the Molecular Hydrogen Transport Behaviour in the Subsurface. In *83rd EAGE Annual Conference & Exhibition* (Vol. 2022, No. 1, pp. 1-5). European Association of Geoscientists & Engineers. https://doi.org/10.3997/2214-4609.202210914

Monod, J. (1949). The growth of bacterial cultures. *Annual Reviews in Microbiology*, *3 (1)*, 371-394. https://doi.org/10.1146/annurev.mi.03.100149.002103

Moreno-Brieva, F., Guimón, J., & Salazar-Elena, J. C. (2023). From grey to green and from west to east: The geography and innovation trajectories of hydrogen fuel technologies. *Energy Research & Social Science*, *101*, 103146. https://doi.org/10.1016/j.erss.2023.103146

Morrill, P. L., Kuenen, J. G., Johnson, O. J., Suzuki, S., Rietze, A., Sessions, A. L., Fogel, M. L., & Nealson, K. H. (2013). Geochemistry and geobiology of a present-day serpentinization site in California: The Cedars. *Geochimica et Cosmochimica Acta*, *109*, 222-240. https://doi.org/10.1016/j.gca.2013.01.043

Moser, A. (2012). Bioprocess technology: kinetics and reactors. *Springer Science & Business Media*. ISBN: 1461387485

Mouli-Castillo, J., Heinemann, N., & Edlmann, K. (2021). Mapping geological hydrogen storage capacity and regional heating demands: An applied UK case study. *Applied Energy*, *283*, 116348. https://doi.org/10.1016/j.apenergy.2020.116348

Mouser, P. J., Borton, M., Darrah, T. H., Hartsock, A., & Wrighton, K. C. (2016). Hydraulic fracturing offers view of microbial life in the deep terrestrial subsurface. *FEMS Microbiology Ecology*, *92*(11), fiw166. https://doi.org/10.1093/femsec/fiw166

Mowry, C. D., Jarek, R. L., Kustas, J., Telles, A. C., & Pimentel, A. S. (2020). Gas Analysis by Mass Spectrometry. *ASM International*. ISBN: https://www.osti.gov/biblio/1630394

Muhammed, N. S., Haq, B., Al Shehri, D., Al-Ahmed, A., Rahman, M. M., & Zaman, E. (2022). A review on underground hydrogen storage: Insight into geological sites, influencing factors and future outlook. *Energy Reports*, *8*, 461-499. https://doi.org/10.1016/j.egyr.2021.12.002

Muller, E., Guélard, J., Sissmann, O., Tafit, A., & Poirier, S. (2024). Evidencing the influence of temperature and mineralogy on microbial competition for hydrogen consumption: Implications for underground hydrogen storage (UHS). *International Journal of Hydrogen Energy*, *82*, 1101-1113. https://doi.org/10.1016/j.ijhydene.2024.08.024

Muloiwa, M., Nyende-Byakika, S., & Dinka, M. (2020). Comparison of unstructured kinetic bacterial growth models. *South African Journal of Chemical Engineering*, *33*, 141-150. https://doi.org/10.1016/j.sajce.2020.07.006

Murphy, E. M., & Ginn, T. R. (2000). Modeling microbial processes in porous media. *Hydrogeology Journal*, *8*(1), 142-158. https://doi.org/10.1007/s100409900043

Navaid, H. B., Emadi, H., & Watson, M. (2023). A comprehensive literature review on the challenges associated with underground hydrogen storage. *International Journal of Hydrogen Energy*, *48*(28), 10603-10635. https://doi.org/10.1016/j.ijhydene.2022.11.225

Neal, C., & Stanger, G. (1983). Hydrogen generation from mantle source rocks in Oman. *Earth and Planetary Science Letters*, *66*, 315-320. https://doi.org/10.1016/0012-821X(83)90144-9

Nelson, P. H. (1994). Permeability-porosity relationships in sedimentary rocks. *Log Analyst*, *35*(3), 38-62. https://pubs.usgs.gov/publication/70016961

Newborough, M., & Cooley, G. (2020). Developments in the global hydrogen market: The spectrum of hydrogen colours. *Fuel Cells Bulletin*, *2020*(11), 16-22. https://doi.org/10.1016/S1464-2859(20)30546-0

Nijjer, J. S., Hewitt, D. R., & Neufeld, J. A. (2019). Stable and unstable miscible displacements in layered porous media. *Journal of Fluid Mechanics*, *869*, 468-499. https://doi.org/10.1017/jfm.2019.190

Nijjer, J. S., Hewitt, D. R., & Neufeld, J. A. (2022). Horizontal miscible displacements through porous media: the interplay between viscous fingering and gravity segregation. *Journal of Fluid Mechanics*, *935*, A14, Article A14. https://doi.org/10.1017/jfm.2021.1067

Nock, W. J., Serna-Maza, A., Heaven, S., & Banks, C. J. (2019). Evaluation of microporous hollow fibre membranes for mass transfer of H2 into anaerobic digesters for biomethanization. *Journal of Chemical Technology & Biotechnology*, *94*(8), 2693-2701. https://doi.org/10.1002/jctb.6081

Nolte, S., Fink, R., Krooss, B. M., & Littke, R. (2021a). Simultaneous determination of the effective stress coefficients for permeability and volumetric strain on a tight sandstone. *Journal of Natural Gas Science and Engineering*, *95*. https://doi.org/10.1016/j.jngse.2021.104186

Nolte , S., Fink, R., Krooss, B.M., Amann-Hildenbrand, A., Wang, Y., Wang, M., Schmatz, J., Klaver, J. & Littke, R. (2021b). Experimental Investigation of Gas Dynamic Effects Using Nanoporous Synthetic Materials as Tight Rock Analogues. *Transport in Porous Media*, *137*(3), 519-553. https://doi.org/10.1007/s11242-021-01572-8

Oelkers, E. H. (1991). Calculation of diffusion coefficients for aqueous organic species at temperatures from 0 to 350 °C. *Geochimica et Cosmochimica Acta*, *55*(12), 3515-3529. https://doi.org/10.1016/0016-7037(91)90052-7

Oren, A. (2001). The bioenergetic basis for the decrease in metabolic diversity at increasing salt concentrations: Implications for the functioning of salt lake ecosystems [Article]. *Hydrobiologia*, *466*, 61-72. https://doi.org/10.1023/A:1014557116838

Oren, A. (2006). Life at High Salt Concentrations. In M. Dworkin, S. Falkow, E. Rosenberg, K.-H. Schleifer, & E. Stackebrandt (Eds.), *The Prokaryotes: Volume 2: Ecophysiology and Biochemistry* (pp. 263-282). Springer New York. https://doi.org/10.1007/0-387-30742-7_9

Ortiz, L., Volckaert, G., & Mallants, D. (2002). Gas generation and migration in Boom Clay, a potential host rock formation for nuclear waste storage. *Engineering Geology*, *64*(2), 287-296. https://doi.org/10.1016/S0013-7952(01)00107-7

Osman, A. I., Mehta, N., Elgarahy, A. M., Hefny, M., Al-Hinai, A., Al-Muhtaseb, A. a. H., & Rooney, D. W. (2022). Hydrogen production, storage, utilisation and environmental impacts: a review. *Environmental Chemistry Letters*, *20*(1), 153-188. https://doi.org/10.1007/s10311-021-01322-8

Ostermeier, R. M. (1995). Deepwater Gulf of Mexico Turbidites— Compaction Effects on Porosity and Permeability. *SPE Formation Evaluation*, *10*(02), 79-85. https://doi.org/10.2118/26468-PA

Otsu, N. (1979). A Threshold Selection Method from Gray-Level Histograms. *IEEE Transactions on Systems, Man, and Cybernetics*, *9*(1), 62-66. https://doi.org/10.1109/TSMC.1979.4310076

Pandey, G. N., Tek, M. R., & Katz, D. L. (1974). Diffusion of fluids through porous media with implications in petroleum geology. *AAPG Bulletin*, *58*(2), 291-303.

Panfilov, M. (2010). Underground Storage of Hydrogen: In Situ Self-Organisation and Methane Generation. *Transport in Porous Media*, *85*(3), 841-865. https://doi.org/10.1007/s11242-010-9595-7

Panfilov, M. (2016). Underground and pipeline hydrogen storage. In *Compendium of Hydrogen Energy* (pp. 91-115). https://doi.org/10.1016/b978-1-78242-362-1.00004-3

Park, J., & Santamarina, J. C. (2020). The critical role of pore size on depth-dependent microbial cell counts in sediments. *Scientific Reports*, *10*(1), 21692. https://doi.org/10.1038/s41598-020-78714-3

Paterson, L. (1983). The implications of fingering in underground hydrogen storage. *International Journal of Hydrogen Energy*, *8*(1), 53-59. https://doi.org/10.1016/0360-3199(83)90035-6

Peksa, A. E., Wolf, K.-H. A. A., & Zitha, P. L. J. (2015). Bentheimer sandstone revisited for experimental purposes. *Marine and Petroleum Geology*, *67*, 701-719. https://doi.org/10.1016/j.marpetgeo.2015.06.001

Peng, S., Zhang, T., Loucks, R. G., & Shultz, J. (2017). Application of mercury injection capillary pressure to mudrocks: Conformance and compression corrections. *Marine and Petroleum Geology*, *88*, 30-40. https://doi.org/10.1016/j.marpetgeo.2017.08.006

Perera, M. S. A. (2023). A review of underground hydrogen storage in depleted gas reservoirs: Insights into various rock-fluid interaction mechanisms and their impact on the process integrity. *Fuel*, *334*, 126677. https://doi.org/10.1016/j.fuel.2022.126677

Pérez, A., Pérez, E., Dupraz, S., & Bolcich, J. (2016). Patagonia wind-hydrogen project: Underground storage and methanation. In: *21st world hydrogen energy conference*

Phadnis, H. S., & Santamarina, J. C. (2011). Bacteria in sediments: pore size effects. *Géotechnique Letters*, *1*(4), 91-93. https://doi.org/10.1680/geolett.11.00008

Picard, A., & Daniel, I. (2013). Pressure as an environmental parameter for microbial life — A review. *Biophysical Chemistry*, *183*, 30-41. https://doi.org/10.1016/j.bpc.2013.06.019

Pichler, M. (2019). Underground Sun Storage Results and Outlook. *2019*(1), 1-4. https://doi.org/10.3997/2214-4609.201900257

Pini, R., Krevor, S. C. M., & Benson, S. M. (2012). Capillary pressure and heterogeneity for the CO2/water system in sandstone rocks at reservoir conditions. *Advances in Water Resources*, *38*, 48-59. https://doi.org/10.1016/j.advwatres.2011.12.007

Pląskowska, K., Makowski, Ł., Strzałka, A., & Zakrzewska-Czerwińska, J. (2023). Binary or Nonbinary Fission? Reproductive Mode of a Predatory Bacterium Depends on Prey Size. *mBio*, *14*(3), e00772-00723. https://doi.org/10.1128/mbio.00772-23

Pomeroy, R. D., Lacey, W. N., Scudder, N. F., & Stapp, F. P. (1933). Rate of Solution of Methane in Quiescent Liquid Hydrocarbons. *Industrial & Engineering Chemistry*, *25*(9), 1014-1019. https://doi.org/10.1021/ie50285a021

Porté, H., Kougias, P. G., Alfaro, N., Treu, L., Campanaro, S., & Angelidaki, I. (2019). Process performance and microbial community structure in thermophilic trickling biofilter reactors for biogas upgrading. *Science of The Total Environment*, *655*, 529-538. https://doi.org/10.1016/j.scitotenv.2018.11.289

Prinzhofer, A., Tahara Cissé, C. S., & Diallo, A. B. (2018). Discovery of a large accumulation of natural hydrogen in Bourakebougou (Mali). *International Journal of Hydrogen Energy*, *43*(42), 19315-19326. https://doi.org/10.1016/j.ijhydene.2018.08.193

Purcell, W. R. (1949). Capillary Pressures - Their Measurement Using Mercury and the Calculation of Permeability Therefrom. *Journal of Petroleum Technology*, *1*(02), 39-48. https://doi.org/10.2118/949039-G %J Journal of Petroleum Technology

Qu, Y., Sun, W., Tao, R., Luo, B., Chen, L., & Ren, D. (2020). Pore–throat structure and fractal characteristics of tight sandstones in Yanchang Formation, Ordos Basin. *Marine and Petroleum Geology*, *120*, 104573. https://doi.org/10.1016/j.marpetgeo.2020.104573

Rabbani, A., & Jamshidi, S. (2014). Specific surface and porosity relationship for sandstones for prediction of permeability. *International Journal of Rock Mechanics and Mining Sciences*, *71*, 25-32. https://doi.org/10.1016/j.ijrmms.2014.06.013

RAG Austria AG, R. (2020). Underground Sun Storage (USS): Final Report Public. Vienna. https://www.underground-sun-storage.at.

RAG Austria AG, R. (2021). Underground Sun Conversion (USC): Final Report. Vienna. https://www.underground-sun-conversion.at.

Ramesh Kumar, K., Honorio, H., Chandra, D., Lesueur, M., & Hajibeygi, H. (2023). Comprehensive review of geomechanics of underground hydrogen storage in depleted reservoirs and salt caverns. *Journal of Energy Storage*, *73*, 108912. https://doi.org/10.1016/j.est.2023.108912

Ratnakar, R. R., & Dindoruk, B. (2015). Measurement of Gas Diffusivity in Heavy Oils and Bitumens by Use of Pressure-Decay Test and Establishment of Minimum Time Criteria for Experiments. *SPE Journal*, *20*(05), 1167-1180. https://doi.org/10.2118/170931-PA

Reamer, H. H., Opfell, J. B., & Sage, B. H. (1956). Diffusion Coefficients in Hydrocarbon Systems Methane-Decane-Methane in Liquid Phase - Methane-Decane-Methane in Liquid Phase. *Industrial & Engineering Chemistry*, *48*(2), 275-282. https://doi.org/10.1021/ie50554a034

Rebour, V., Billiotte, J., Deveughele, M., Jambon, A., & le Guen, C. (1997). Molecular diffusion in water-saturated rocks: A new experimental method. *Journal of Contaminant Hydrology*, *28*(1), 71-93. https://doi.org/10.1016/S0169-7722(96)00051-4

Reitenbach, V., Ganzer, L., Albrecht, D., & Hagemann, B. (2015). Influence of added hydrogen on underground gas storage: a review of key issues. *Environmental Earth Sciences*, *73*(11), 6927-6937. https://doi.org/10.1007/s12665-015-4176-2

Renkin, E. M. (1954). Filtration, diffusion, and molecular sieving through porous cellulose membranes. *The Journal of general physiology*, *38*(2), 225-243. https://doi.org/D - CLML: 5527:23778:100 OTO - NLM

Renner, T. A. (1988). Measurement and Correlation of Diffusion Coefficients for CO2 and Rich-Gas Applications. *SPE Reservoir Engineering*, *3*(02), 517-523. https://doi.org/10.2118/15391-PA

Reza Etminan, S., Pooladi-Darvish, M., Maini, B. B., & Chen, Z. (2013). Modeling the interface resistance in low soluble gaseous solvents-heavy oil systems. *Fuel*, *105*, 672-687. https://doi.org/10.1016/j.fuel.2012.08.048

Riazi, M. R. (1996). A new method for experimental measurement of diffusion coefficients in reservoir fluids. *Journal of Petroleum Science and Engineering*, *14*(3), 235-250. https://doi.org/10.1016/0920-4105(95)00035-6

Rinck-Pfeiffer, S., Ragusa, S., Sztajnbok, P., & Vandevelde, T. (2000). Interrelationships between biological, chemical, and physical processes as an analog to clogging in aquifer storage and recovery (ASR) wells. *Water Research*, *34*(7), 2110-2118. https://doi.org/10.1016/S0043-1354(99)00356-5

Robinson, J. A., & Tiedje, J. M. (1984). Competition between sulfate-reducing and methanogenic bacteria for H2 under resting and growing conditions. *Archives of Microbiology*, *137*(1), 26-32. https://doi.org/10.1007/BF00425803

Rootare, H. M., & Prenzlow, C. F. (1967). Surface areas from mercury porosimeter measurements. *The Journal of Physical Chemistry*, *71*(8), 2733-2736. https://doi.org/10.1021/j100867a057

Ross, C. F. (2012). 2.02 - Headspace Analysis. In J. Pawliszyn (Ed.), *Comprehensive Sampling and Sample Preparation* (pp. 27-50). Academic Press. https://doi.org/10.1016/B978-0-12-381373-2.00036-3

Rouquerol, J., Llewellyn, P., & Rouquerol, F. (2007). Is the bet equation applicable to microporous adsorbents? In P. L. Llewellyn, F. Rodriquez-Reinoso, J. Rouqerol, & N. Seaton (Eds.), *Studies in Surface Science and Catalysis* (Vol. 160, pp. 49-56). Elsevier. https://doi.org/10.1016/S0167-2991(07)80008-5

Russ, J. C. (2006). The Image Processing Handbook (5th ed.). *CRC Press.* ISBN: 0429206925 https://doi.org/10.1201/9780203881095

Sachs, W. (1998). The diffusional transport of methane in liquid water: method and result of experimental investigation at elevated pressure. *Journal of Petroleum Science and Engineering*, *21*(3), 153-164. https://doi.org/10.1016/S0920-4105(98)00048-5

Safari, H., Balcom, B. J., & Afrough, A. (2021). Characterization of pore and grain size distributions in porous geological samples – An image processing workflow. *Computers & Geosciences*, *156*, 104895. https://doi.org/10.1016/j.cageo.2021.104895

Sahores, J. J., & Witherspoon, P. A. (1970). Diffusion of light paraffin hydrocarbons in water from 2°C to 80°C. In G. D. Hobson & G. C. Speers (Eds.), *Advances in Organic Geochemistry* (pp. 219-230). Pergamon. https://doi.org/10.1016/B978-0-08-012758-3.50018-9

Saidian, M., & Prasad, M. (2015). Effect of mineralogy on nuclear magnetic resonance surface relaxivity: A case study of Middle Bakken and Three Forks formations. *Fuel*, *161*, 197-206. https://doi.org/10.1016/j.fuel.2015.08.014

Salina Borello, E., Bocchini, S., Chiodoni, A., Coti, C., Fontana, M., Panini, F., Peter, C., Pirri, C. F., Tawil, M., Mantegazzi, A., Marzano, F., Pozzovivo, V., Verga, F., & Viberti, D. (2024). Underground Hydrogen Storage Safety: Experimental Study of Hydrogen Diffusion through Caprocks. *Energies*, *17(2):394.* https://doi.org/10.3390/en17020394

Sander, R. (2015). Compilation of Henry's law constants (version 4.0) for water as solvent. *Atmos. Chem. Phys.*, *15*(8), 4399-4981. https://doi.org/10.5194/acp-15-4399-2015

Schepp, L. L., Ahrens, B., Balcewicz, M., Duda, M., Nehler, M., Osorno, M., Uribe, D., Steeb, H., Nigon, B., Stöckhert, F., Swanson, D. A., Siegert, M., Gurris, M., & Saenger, E. H. (2020). Digital rock physics and laboratory considerations on a high-porosity volcanic rock. *Scientific Reports*, *10*(1), 5840. https://doi.org/10.1038/s41598-020-62741-1

Schimmel, M. T. W., Hangx, S. J. T., & Spiers, C. J. (2022). Effect of pore fluid chemistry on uniaxial compaction creep of Bentheim sandstone and implications for reservoir injection operations. *Geomechanics for Energy and the Environment*, *29*, 100272. https://doi.org/10.1016/j.gete.2021.100272

Schlömer, S., & Krooss, B. M. (1997). Experimental characterisation of the hydrocarbon sealing efficiency of cap rocks. *Marine and Petroleum Geology*, *14*(5), 565-580. https://doi.org/10.1016/S0264-8172(97)00022-6

Schmatz, J., Klaver, J., Jiang, M., & Urai, J. L. (2017). Nanoscale Morphology of Brine/Oil/Mineral Contacts in Connected Pores of Carbonate Reservoirs: Insights on Wettability From Cryo-BIB-SEM. *SPE Journal*, *22*(05), 1374-1384. https://doi.org/10.2118/180049-PA

Schmidt, T. (1989). Mass Transfer by Diffusion. AOSTRA Handbook on Oil Sands, Bitumens and Heavy Oils; Hepler, L. G.; Zhu, X (Eds). *Alberta Oil Sands Technology & Research Authority (AOSTRA)*. ISBN: 978-0-7732-0189-7

Schmitt, M., Fernandes, C. P., Wolf, F. G., Bellini da Cunha Neto, J. A., Rahner, C. P., & Santiago dos Santos, V. S. (2015). Characterization of Brazilian tight gas sandstones relating permeability and Angstrom-to micron-scale pore structures. *Journal of Natural Gas Science and Engineering*, *27*, 785-807. https://doi.org/10.1016/j.jngse.2015.09.027

Schneider, C. A., Rasband, W. S., & Eliceiri, K. W. (2012). NIH Image to ImageJ: 25 years of image analysis. *Nature Methods*, *9*(7), 671-675. https://doi.org/10.1038/nmeth.2089

Schneider, P. *The colours of hydrogen," Ewe,*. https://www.ewe.com/en/shaping-the-future/hydrogen/the-colours-of-hydrogen.

Sheikha, H., Pooladi-Darvish, M., & Mehrotra, A. K. (2005). Development of Graphical Methods for Estimating the Diffusivity Coefficient of Gases in Bitumen from Pressure-Decay Data. *Energy & Fuels*, *19*(5), 2041-2049. https://doi.org/10.1021/ef050057c

Shen, L., & Chen, Z. (2007). Critical review of the impact of tortuosity on diffusion. *Chemical Engineering Science*, *62*(14), 3748-3755. https://doi.org/10.1016/j.ces.2007.03.041

Sheppard, A. P., Sok, R. M., & Averdunk, H. (2004). Techniques for image enhancement and segmentation of tomographic images of porous materials. *Physica A: Statistical Mechanics and its Applications*, *339*(1), 145-151. https://doi.org/10.1016/j.physa.2004.03.057

Sherwood Lollar, B., Lacrampe-Couloume, G., Slater, G. F., Ward, J., Moser, D. P., Gihring, T. M., Lin, L. H., & Onstott, T. C. (2006). Unravelling abiogenic and biogenic sources of methane in the Earth's deep subsurface. *Chemical Geology*, *226*(3), 328-339. https://doi.org/10.1016/j.chemgeo.2005.09.027

Shiva Kumar, S., & Lim, H. (2022). An overview of water electrolysis technologies for green hydrogen production. *Energy Reports*, *8*, 13793-13813. https://doi.org/10.1016/j.egyr.2022.10.127

Siuzdak, G. (2016). An Introduction to Mass Spectrometry Ionization: An Excerpt from The Expanding Role of Mass Spectrometry in Biotechnology, 2nd ed.; MCC Press: San Diego, 2005. *JALA: Journal of the Association for Laboratory Automation*, *9*(2), 50-63. https://doi.org/10.1016/j.jala.2004.01.004

Smatlak, C. R., Gossett, J. M., & Zinder, S. H. (1996). Comparative Kinetics of Hydrogen Utilization for Reductive Dechlorination of Tetrachloroethene and Methanogenesis in an Anaerobic Enrichment Culture. *Environmental Science & Technology*, *30*(9), 2850-2858. https://doi.org/10.1021/es9602455

Šmigáň, P., Greksák, M., Kozánková, J., Buzek, F., Onderka, V., & Wolf, I. (1990). Methanogenic bacteria as a key factor involved in changes of town gas stored in an underground reservoir. *FEMS Microbiology Letters*, *73*(3), 221-224. https://doi.org/10.1016/0378-1097(90)90733-7

Soete, J., Claes, S., Claes, H., Erthal, M. M., Hamaekers, H., De Boever, E., Foubert, A., Klitzsch, N., & Swennen, R. (2022). Unravelling the pore network and its behaviour: An integrated NMR, MICP, XCT and petrographical study of continental spring carbonates from the Ballık area, SW Turkey. *The Depositional Record*, *8*(1), 292-316. https://doi.org/10.1002/dep2.135

Song, J., & Zhang, D. (2013). Comprehensive Review of Caprock-Sealing Mechanisms for Geologic Carbon Sequestration. *Environmental Science & Technology*, *47*(1), 9-22. https://doi.org/10.1021/es301610p

Stark, W., Stadler, J., & McCoy, E. (1938). Some factors affecting the bacterial population of freshwater lakes. *J. Bacteriol*, *36*, 653-654.

Stark, W., Stadler, J., McCoy, E. (1938). Some factors affecting the bacterial population of freshwater lakes. *J. Bacteriol 36*, 653-654.

Strauch, B., Pilz, P., Hierold, J., & Zimmer, M. (2023). Experimental simulations of hydrogen migration through potential storage rocks. *International Journal of Hydrogen Energy*, *48*(66), 25808-25820. https://doi.org/10.1016/j.ijhydene.2023.03.115

Strobel, G., Hagemann, B., Huppertz, T. M., & Ganzer, L. (2020). Underground bio-methanation: Concept and potential. *Renewable and Sustainable Energy Reviews*, *123*, 109747. https://doi.org/10.1016/j.rser.2020.109747

Strobel, G., Hagemann, B., Lüddeke, C. T., & Ganzer, L. (2023). Coupled model for microbial growth and phase mass transfer in pressurized batch reactors in the context of underground hydrogen storage. *Frontiers in Microbiology. 14:1150102.* https://doi.org/10.3389/fmicb.2023.1150102

Stull, D. R. (1947). Vapor Pressure of Pure Substances. Organic and Inorganic Compounds. *Industrial & Engineering Chemistry*, *39*(4), 517-540. https://doi.org/10.1021/ie50448a022

Suckale, J. (2009). Chapter 2 - Induced Seismicity in Hydrocarbon Fields. In *Advances in Geophysics* (Vol. 51, pp. 55-106). Elsevier. https://doi.org/10.1016/S0065-2687(09)05107-3

Suckale, J. (2010). Moderate-to-large seismicity induced by hydrocarbon production. *The Leading Edge*, *29*(3), 310-319. https://doi.org/10.1190/1.3353728

Sun, J., Xiao, X., Wei, Q., Cheng, P., & Tian, H. (2021). Occurrence of Irreducible Water and Its Influences on Gas-Bearing Property of Gas Shales From Shallow Longmaxi Formation in the Xishui Area, Guizhou, Southern China. *Frontiers in Earth Science*, *9*. https://doi.org/10.3389/feart.2021.654136

Szuhaj, M., Ács, N., Tengölics, R., Bodor, A., Rákhely, G., Kovács, K. L., & Bagi, Z. (2016). Conversion of H2 and CO2 to CH4 and acetate in fed-batch biogas reactors

by mixed biogas community: a novel route for the power-to-gas concept. *Biotechnology for Biofuels*, *9*(1), 102. https://doi.org/10.1186/s13068-016-0515-0

Takai, K., Nakamura, K., Toki, T., Tsunogai, U., Miyazaki, M., Miyazaki, J., Hirayama, H., Nakagawa, S., Nunoura, T., & Horikoshi, K. (2008). Cell proliferation at 122°C and isotopically heavy CH4 production by a hyperthermophilic methanogen under high-pressure cultivation. *Proceedings of the National Academy of Sciences*, *105*(31), 10949-10954. https://doi.org/10.1073/pnas.0712334105

Tammann, G., & Jessen, V. . (1929). Über die Diffusionskoeffizienten von Gasen in Wasser und ihre Temperaturabhängigkeit. *Zeitschrift für anorganische und allgemeine Chemie*, *179*(1), 125-144.

Tan, K. K., & Thorpe, R. B. (1992). Gas diffusion into viscous and non-Newtonian liquids. *Chemical Engineering Science*, *47*(13), 3565-3572. https://doi.org/10.1016/0009-2509(92)85071-I

Tarkowski, R. (2019). Underground hydrogen storage: Characteristics and prospects. *Renewable and Sustainable Energy Reviews*, *105*, 86-94. https://doi.org/10.1016/j.rser.2019.01.051

Teske, S., Fattal, A., Lins, C., Hullin, M., & Williamson, L. E. (2017). *Renewables Global Futures Report: Great debates towards 100% renewable energy* (978-3-9818107-4-5). http://inis.iaea.org/search/search.aspx?orig_q=RN:48058287

Thaysen, E. M., McMahon, S., Strobel, G. J., Butler, I. B., Ngwenya, B. T., Heinemann, N., Wilkinson, M., Hassanpouryouzband, A., McDermott, C. I., & Edlmann, K. (2021). Estimating microbial growth and hydrogen consumption in hydrogen storage in porous media. *Renewable and Sustainable Energy Reviews*, *151*. https://doi.org/10.1016/j.rser.2021.111481

Thiyagarajan, S. R., Emadi, H., Hussain, A., Patange, P., & Watson, M. (2022). A comprehensive review of the mechanisms and efficiency of underground hydrogen storage. *Journal of Energy Storage*, *51*, 104490. https://doi.org/10.1016/j.est.2022.104490

Thomas, S. N. (2019). Mass spectrometry. In *Contemporary Practice in Clinical Chemistry* (pp. 171-185). https://doi.org/10.1016/b978-0-12-815499-1.00010-7

Thullner, M. (2010). Comparison of bioclogging effects in saturated porous media within one- and two-dimensional flow systems. *Ecological Engineering*, *36*(2), 176-196. https://doi.org/10.1016/j.ecoleng.2008.12.037

Thüns, N., Krooss, B. M., Zhang, Q., & Stanjek, H. (2019). The effect of H2 pressure on the reduction kinetics of hematite at low temperatures. *International Journal of Hydrogen Energy*, *44*(50), 27615-27625. https://doi.org/10.1016/j.ijhydene.2019.08.178

Tiab, D., & Donaldson, E. C. (2016). Chapter 3 - Porosity and Permeability. In D. Tiab & E. C. Donaldson (Eds.), *Petrophysics (Fourth Edition)* (pp. 67-186). Gulf Professional Publishing. https://doi.org/10.1016/B978-0-12-803188-9.00003-6

Tissot, B. P., & Welte, D. H. (2013). Petroleum formation and occurrence. *Springer Science & Business Media*. ISBN: 364287813X

Truche, L., Berger, G., Destrigneville, C., Pages, A., Guillaume, D., Giffaut, E., & Jacquot, E. (2009). Experimental reduction of aqueous sulphate by hydrogen under hydrothermal conditions: Implication for the nuclear waste storage. *Geochimica et Cosmochimica Acta*, *73*(16), 4824-4835. https://doi.org/10.1016/j.gca.2009.05.043

Truche, L., Jodin-Caumon, M.-C., Lerouge, C., Berger, G., Mosser-Ruck, R., Giffaut, E., & Michau, N. (2013). Sulphide mineral reactions in clay-rich rock induced by high hydrogen pressure. Application to disturbed or natural settings up to 250°C and

30bar. *Chemical Geology*, *351*, 217-228. https://doi.org/10.1016/j.chemgeo.2013.05.025

Tuson, H. H., & Weibel, D. B. (2013). Bacteria-surface interactions. *Soft matter*, *9*(17), 4368-4438. https://doi.org/10.1039/c3sm27705d

Ufer, K., Kleeberg, R., & Monecke, T. (2015). Quantification of stacking disordered Si–Al layer silicates by the Rietveld method: application to exploration for high-sulphidation epithermal gold deposits. *Powder Diffraction*, *30*(S1), S111-S118. https://doi.org/10.1017/S0885715615000111

Ufer, K., Stanjek, H., Roth, G., Dohrmann, R., Kleeberg, R., & Kaufhold, S. (2008). Quantitative phase analysis of bentonites by the rietveld method. *Clays and Clay Minerals*, *56*(2), 272-282. https://doi.org/10.1346/CCMN.2008.0560210

Upreti, S. R., & Mehrotra, A. K. (2000). Experimental measurement of gas diffusivity in bitumen: results for carbon dioxide. *Industrial engineering chemistry research*, *39*(4), 1080-1087. https://doi.org/10.1021/ie990635a

Upreti, S. R., & Mehrotra, A. K. (2002). Diffusivity of CO2, CH4, C2H6 and N2 in Athabasca bitumen. *The Canadian Journal of Chemical Engineering*, *80*(1), 116-125. https://doi.org/10.1002/cjce.5450800112

Van Bramer, S. E. (1998). An introduction to mass spectrometry. *Widener University, Department of Chemistry, One University Place, Chester, PA*, *19013*.

Van de Riet, S., & Bais, N. *A hydrogen rainbow is emerging, but which colors lead to the pot of gold?* https://www2.deloitte.com/nl/nl/pages/energy-resources-industrials/articles/hydrogen-rainbow.html

van der Walt, S., Schönberger, J. L., Nunez-Iglesias, J., Boulogne, F., Warner, J. D., Yager, N., Gouillart, E., & Yu, T. (2014). scikit-image: image processing in Python. (2167-8359 (Print)).

van Renssen, S. (2020). The hydrogen solution? *Nature Climate Change*, *10*(9), 799-801. https://doi.org/10.1038/s41558-020-0891-0

Vandevivere, P. (1995). Bacterial clogging of porous media: A new modelling approach. *Biofouling*, *8*(4), 281-291. https://doi.org/10.1080/08927019509378281

Villadsen, J., Nielsen, J., & Lidén, G. (2011a). Gas–Liquid Mass Transfer. In J. Villadsen, J. Nielsen, & G. Lidén (Eds.), *Bioreaction Engineering Principles* (pp. 459-496). Springer US. https://doi.org/10.1007/978-1-4419-9688-6_10

Villadsen, J., Nielsen, J., & Lidén, G. (2011b). Bioreaction engineering principles. *Springer Science & Business Media*. ISBN: 1441996885

Vincent, B., Fleury, M., Santerre, Y., & Brigaud, B. (2011). NMR relaxation of neritic carbonates: An integrated petrophysical and petrographical approach. *Journal of Applied Geophysics*, *74*(1), 38-58. https://doi.org/10.1016/j.jappgeo.2011.03.002

Vincent, L., & Soille, P. (1991). Watersheds in digital spaces: an efficient algorithm based on immersion simulations. *IEEE Transactions on Pattern Analysis and Machine Intelligence*, *13*(6), 583-598. https://doi.org/10.1109/34.87344

Vítězová, M., Onderka, V., Urbanová, I., Molíková, A., Hanišáková, N., Buriánková, I., Vítěz, T., Novák, D., Lochman, J., Machálková, M., & Javůrek, J. (2023). In situ field experiment shows the potential of methanogenic archaea for biomethane production from underground gas storage in natural rock environment. *Environmental Technology & Innovation*, *32*, 103253. https://doi.org/10.1016/j.eti.2023.103253

Vivian, J. E., & King, C. J. (1964). Diffusivities of slightly soluble gases in water. *AIChE Journal*, *10*(2), 220-221. https://doi.org/10.1002/aic.690100217

Voland, V., Müller, A., Firsching, M., Gruber, R., Mohr, S., Habl, M., Schön, T., Oeckl, S., Schröpfer, S., & Hess, J. (2010). Computed tomography (CT) system for

automatic analysis of ice cores. European Conference on Non-Destructive Testing (ECNDT) 2010. https://publica.fraunhofer.de/entities/publication/f8138613-5466-47e1-a722-d192b2d212ba

Volland, J.-M., Gonzalez-Rizzo, S., Gros, O., Tyml, T., Ivanova, N., Schulz, F., Goudeau, D., Elisabeth, N. H., Nath, N., Udwary, D., Malmstrom, R. R., Guidi-Rontani, C., Bolte-Kluge, S., Davies, K. M., Jean, M. R., Mansot, J.-L., Mouncey, N. J., Angert, E. R., Woyke, T., & Date, S. V. (2022). A centimeter-long bacterium with DNA contained in metabolically active, membrane-bound organelles. *Science*, *376*(6600), 1453-1458. https://doi.org/10.1126/science.abb3634

Volokitin, Y., Looyestijn, W., Slijkerman, W., & Hofman, J. J. T. (1999). Constructing capillary pressure curves from NMR log data in the presence of hydrocarbons, In *SPWLA Annual Logging Symposium* (pp. SPWLA-1999). SPWLA.

Vreeland, R. H., Piselli Jr, A. F., McDonnough, S., & Meyers, S. S. (1998). Distribution and diversity of halophilic bacteria in a subsurface salt formation. *Extremophiles*, *2*(3), 321-331. https://doi.org/10.1007/s007920050075

Wait, A., & Wait, A. (2011). Novel aspects of the reactions of hydrogenases with small molecule inhibitors *Oxford University, UK*.

Waksman, S. A., & Carey, C. L. (1935a). Decomposition of Organic Matter in Sea Water by Bacteria: II. Influence of Addition of Organic Substances upon Bacterial Activities. *Journal of Bacteriology*, *29*(5), 545-561. https://doi.org/10.1128/jb.29.5.545-561.1935

Waksman S., A., & Carey C., L. (1935b). Decomposition of Organic Matter in Sea Water by Bacteria. *Journal of Bacteriology*, *29*(5), 531-543. https://doi.org/10.1128/jb.29.5.531-543.1935

Wang, D., Ai, J., Shen, F., Yang, G., Zhang, Y., Deng, S., Zhang, J., Zeng, Y., & Song, C. (2017). Improving anaerobic digestion of easy-acidification substrates by promoting buffering capacity using biochar derived from vermicompost. *Bioresource Technology*, *227*, 286-296. https://doi.org/10.1016/j.biortech.2016.12.060

Wang, L., Jin, Z., Chen, X., Su, Y., & Huang, X. (2023). The Origin and Occurrence of Natural Hydrogen. *Energies*, *16(5),* 2400. https://doi.org/10.3390/en16052400

Wardlaw, N. C., McKellar, M., & Yu, L. (1988). Pore and throat size distributions determined by mercury porosimetry and by direct observation. *Carbonates and Evaporites*, *3*(1), 1-16. https://doi.org/10.1007/BF03174408

Wardlaw, N. C., & Taylor, R. P. (1976). Mercury capillary pressure curves and the interpretation of pore structure and capillary behaviour in reservoir rocks. *Bulletin of Canadian Petroleum Geology*, *24*(2), 225-262. https://doi.org/10.35767/gscpgbull.24.2.225

Washburn, E. W. (1921). The Dynamics of Capillary Flow. *Physical Review*, *17*(3), 273-283. https://doi.org/10.1103/PhysRev.17.273

Watanabe, H., & Iizuka, K. (1985). The Influence of Dissolved Gases on the Density of Water. *Metrologia*, *21*(1), 19. https://doi.org/10.1088/0026-1394/21/1/005

Wen, Y. W., & Kantzas, A. (2005). Monitoring Bitumen−Solvent Interactions with Low-Field Nuclear Magnetic Resonance and X-ray Computer-Assisted Tomography. *Energy & Fuels*, *19*(4), 1319-1326. https://doi.org/10.1021/ef049764g

Whitman, W. (2015). Methanothermococcus gen. nov. In. https://doi.org/10.1002/9781118960608.gbm00503

Wigand, M., Kaszuba, J. P., Carey, J. W., & Hollis, W. K. (2009). Geochemical effects of CO2 sequestration on fractured wellbore cement at the cement/caprock interface.

Chemical Geology, *265*(1), 122-133. https://doi.org/https://doi.org/10.1016/j.chemgeo.2009.04.008

Williams, B. (2022). "Exploring the wonders of yellow hydrogen", Hydrogen Fuel News. https://www.hydrogenfuelnews.com/what-is-yellow-hydrogen/8552843/?utm_content=cmp-true

Willige, A. (2022). The colors of hydrogen: Expanding ways of decarbonization, Mitsubishi Heavy Industry Group. https://spectra.mhi.com/the-colors-of-hydrogen-expanding-ways-of-decarbonization

Wise, D. L., & Houghton, G. (1966). The diffusion coefficients of ten slightly soluble gases in water at 10–60 C. *Chemical Engineering Science*, *21*(11), 999-1010. https://doi.org/https://doi.org/10.1016/0009-2509(66)85096-0

Witherspoon, P. A., & Saraf, D. N. (1965). Diffusion of Methane, Ethane, Propane, and n-Butane in Water from 25 to 43°. *The Journal of Physical Chemistry*, *69*(11), 3752-3755. https://doi.org/10.1021/j100895a017

Wollenweber, J., Alles, S. a., Kronimus, A., Busch, A., Stanjek, H., & Krooss, B. M. (2009). Caprock and overburden processes in geological CO2 storage: An experimental study on sealing efficiency and mineral alterations. *Energy Procedia*, *1*(1), 3469-3476. https://doi.org/10.1016/j.egypro.2009.02.138

Woodruff, W. F., & Revil, A. (2011). CEC-normalized clay-water sorption isotherm. *Water Resources Research*, *47*(11). https://doi.org/https://doi.org/10.1029/2011WR010919

Yang, H.-J., Yang, Z.-M., Xu, X.-H., & Guo, R.-B. J. B. t. (2020). Increasing the methane production rate of hydrogenotrophic methanogens using biochar as a biocarrier. *Bioresource Technology, Volume 302, 122829.* https://doi.org/10.1016/j.biortech.2020.122829

Yao, Y., Liu, D., Che, Y., Tang, D., Tang, S., & Huang, W. (2010). Petrophysical characterization of coals by low-field nuclear magnetic resonance (NMR). *Fuel*, *89*(7), 1371-1380. https://doi.org/10.1016/j.fuel.2009.11.005

Yedinak, E. M. (2022). The Curious Case of Geologic Hydrogen: Assessing its Potential as a Near-Term Clean Energy Source. *Joule*, *6*(3), 503-508. https://doi.org/10.1016/j.joule.2022.01.005

Yekta, A. E., Manceau, J. C., Gaboreau, S., Pichavant, M., & Audigane, P. (2018). Determination of Hydrogen–Water Relative Permeability and Capillary Pressure in Sandstone: Application to Underground Hydrogen Injection in Sedimentary Formations. *Transport in Porous Media*, *122*(2), 333-356. https://doi.org/10.1007/s11242-018-1004-7

Yu, M., Wang, K., & Vredenburg, H. (2021). Insights into low-carbon hydrogen production methods: Green, blue and aqua hydrogen. *International Journal of Hydrogen Energy*, *46*(41), 21261-21273. https://doi.org/10.1016/j.ijhydene.2021.04.016

Yuan, S.-Z., Lu, H., Wang, J., Zhou, J.-T., Wang, Y., & Liu, G.-F. (2012). Enhanced bio-decolorization of azo dyes by quinone-functionalized ceramsites under saline conditions. *Process Biochemistry*, *47*(2), 312-318. https://doi.org/10.1016/j.procbio.2011.11.015

Zarghami, S., Boukadi, F., & Al-Wahaibi, Y. (2017). Diffusion of carbon dioxide in formation water as a result of CO2 enhanced oil recovery and CO2 sequestration. *Journal of Petroleum Exploration and Production Technology*, *7*(1), 161-168. https://doi.org/10.1007/s13202-016-0261-7

Zeng, L., Sarmadivaleh, M., Saeedi, A., Chen, Y., Zhong, Z., & Xie, Q. (2023). Storage integrity during underground hydrogen storage in depleted gas reservoirs. *Earth-Science Reviews*, *247*, 104625. https://doi.org/10.1016/j.earscirev.2023.104625

Zettlitzer, M., Moeller, F., Morozova, D., Lokay, P., & Würdemann, H. (2010). Re-establishment of the proper injectivity of the CO2-injection well Ktzi 201 in Ketzin, Germany. *International Journal of Greenhouse Gas Control*, *4*(6), 952-959. https://doi.org/10.1016/j.ijggc.2010.05.006

Zgonnik, V. (2020). The occurrence and geoscience of natural hydrogen: A comprehensive review. *Earth-Science Reviews*, *203*, 103140. https://doi.org/10.1016/j.earscirev.2020.103140

Zhang, Z., Kruschwitz, S., Weller, A., & Halisch, M. (2018). Enhanced pore space analysis by use of μ-CT, MIP, NMR, and SIP. *Solid Earth*, *9*(6), 1225-1238. https://doi.org/10.5194/se-9-1225-2018

Zhao, H., Jones, E. A., Singh, R. S., Ismail, H. H. B., & WahTan, S. (2023). The Hydrogen System in the Subsurface: Implications for Natural Hydrogen Exploration *ADIPEC*, https://doi.org/10.2118/216710-MS

Zhao, Z., Zhang, Y., Holmes, D. E., Dang, Y., Woodard, T. L., Nevin, K. P., & Lovley, D. R. (2016). Potential enhancement of direct interspecies electron transfer for syntrophic metabolism of propionate and butyrate with biochar in up-flow anaerobic sludge blanket reactors. *Bioresource Technology*, *209*, 148-156. https://doi.org/10.1016/j.biortech.2016.03.005

Zhu, X., Cai, J., Song, G., & Ji, J. (2015). Factors influencing the specific surface areas of argillaceous source rocks. *Applied Clay Science*, *109-110*, 83-94. https://doi.org/10.1016/j.clay.2015.02.016

Zink, K.-G., Mangelsdorf, K., Granina, L., & Horsfield, B. (2008). Estimation of bacterial biomass in subsurface sediments by quantifying intact membrane phospholipids. *Analytical and Bioanalytical Chemistry*, *390*(3), 885-896. https://doi.org/10.1007/s00216-007-1732-y

Zivar, D., Kumar, S., & Foroozesh, J. (2021). Underground hydrogen storage: A comprehensive review. *International Journal of Hydrogen Energy*, *46*(45), 23436-23462. https://doi.org/10.1016/j.ijhydene.2020.08.138

Zobell, C. E. (1947). Microbial Transformation of Molecular Hydrogen in Marine Sediments, with Particular Reference to Petroleum1. *AAPG Bulletin*, *31*(10), 1709-1751. https://doi.org/10.1306/3D933A4C-16B1-11D7-8645000102C1865D

Zobell, C. E., & Anderson, D. Q. (1936). Observations on the Multiplication of Bacteria in Different Volumes of Stored Sea Water and the Influence of Oxygen Tension and Solid Surfaces. *The Biological Bulletin*, *71*(2), 324-342. https://doi.org/10.2307/1537438

Zobell, C. E. (1943). The effect of solid surfaces upon bacterial activity. *Journal of bacteriology*, *46*(1), 39-56. https://doi.org/10.1128/jb.46.1.39-56.1943

Chapter 7

7.Appendices

7.1. Appendix A: Theoretical background (Chapter 3)

A.1 Methanogenic reaction

Hydrogen storage in subsurface geological formations initiates and catalyzes microbial metabolisms, as hydrogen provides energy for various biological processes. The principal hydrogen-consuming processes encompass methanogenesis, acetogenesis, sulfate-reduction, and iron-reduction and have been explored and detailed in the literature (Dopffel et al., 2021; Gregory et al., 2019; Muhammed et al., 2022). The presented study focuses, in particular, on methanogenesis, representing a process wherein hydrogen is oxidized in the presence of methanogenic *Archaea*. These *Archaea* employ hydrogen as electron donor and carbon dioxide as electron acceptor, ultimately yielding methane and water, according to:

$$CO_2+4H_2 \rightarrow CH_4+2H_2O \quad (A.1)$$

The methanogenic reaction rate is influenced by various environmental parameters, including pressure, temperature, nutrient availability, salinity, and pH (Thaysen et al., 2021). Laboratory and field data consistently demonstrated that the highest activity is achieved under optimal conditions, with a pressure of 9.0 MPa and a temperature range of 30 to 40 ºC (Heinemann et al., 2021; Panfilov, 2016). However, certain species exhibit resilience even at elevated temperatures up to 122 °C (Lovley & Goodwin, 1988; Magot et al., 2000; Takai et al., 2008). The recent study conducted by Khajooie et al. (2024a) utilized *Methanothermococcus thermolithotrophicus* as the chosen strain with optimal growth temperature at around 65 °C (Huber et al., 1982).

A.2 Determination of the Specific Surface Area

The surface characteristics of solids play a crucial role in diverse processes occurring within porous media, including adsorption, ion exchange reactions, fluid conductivity, and microbial attachment (Kapellos et al., 2015; Kuila & Prasad, 2013; Rabbani & Jamshidi, 2014). The SSA of rocks is typically measured as the interstitial area of pores per unit mass of the porous rock [m^2/g], expressed as (Collins, 1976; Dullien, 1992):

$$SSA = A/m \quad (A.2)$$

where A represents the total surface area of solids [m^2] and m is the mass of porous rock [g]. Various methods for determining SSA have been extensively reviewed in the literature

(Anovitz & Cole, 2015; Lowell et al., 2012; Tiab & Donaldson, 2016). In this study, a range of techniques, including MICP, NMR, SEM, and µCT were employed to ascertain this rock property.

A.2.1 Mercury injection capillary pressure

The characterization of pore sizes and their distribution at nano- to micrometer scale (0.003 to 350 µm) is commonly conducted through the application of MICP, a widely employed technique (Anovitz & Cole, 2015). Mercury is a non-wetting fluid, requiring external pressure to overcome the capillary forces of pores and invade pore networks (Purcell, 1949; Wardlaw et al., 1988; Wardlaw & Taylor, 1976). The required pressure for mercury intrusion is primarily governed by both pore size and the interfacial tension between air/mercury, according to the Young-Laplace equation. Assuming the pore network as a bundle of capillary tubes, Young-Laplace relationship reduces to the Washburn equation (Washburn, 1921):

$$P_c = \frac{4\gamma_{Hg}\cos\theta_{Hg}}{d} \tag{A.3}$$

where d is the pore diameter [µm], γ_{Hg} is the surface tension [N/m], θ_{Hg} is the contact angle of mercury in air [degree] and P_c is the pressure required to intrude mercury into the pore network, expressed as capillary pressure [MPa]. The air/mercury surface tension is 0.485 N/m and the contact angle measures at 130°. This method enables characterization of pores extended to the nanoscale; however, at high pressures, particularly in mudrocks, pore structure alteration may occur due to deformation and compression (Bustin et al., 2008; Klaver et al., 2015b; Peng et al., 2017). The other drawback of this technique is associated with the ink-bottle effect, which arises due to the pore network comprising large pores (bodies) connected by narrow pores (throats). Consequently, the capillary pressures are predominantly controlled by pore throats, leading to an overestimation of smaller pores at the expense of larger ones (Schmitt et al., 2015).

MICP measures the normalized volume of mercury relative to the dry sample weight (V/m, [mL/g]) as it infiltrates the pores under applied pressure. The intrusion volume reflects the pore volume and, when integrated with pressure data, facilitates the characterization of the pore network. The equivalent pore throat radius determined by equation (A.3), along with cumulative pore volumes enables the derivation of the pore throat distribution (PTD) by calculating the logarithmic differential pore volume (Liu & Ostadhassan, 2019; McPhee et al., 2015):

$$\mathrm{PTD} = \frac{\mathrm{dV}}{\mathrm{d[log(d)]}} = \frac{\mathrm{V_{i+1} - V_i}}{\mathrm{logd_{i+1} - logd_i}} \tag{A.4}$$

where V_i and V_{i+1} are the cumulative pore volumes [mL/g] corresponding to pore throat diameters of d_i and d_{i+1} [µm], respectively. Alternative presentations of pore size include incremental pore volume versus diameter ($\mathrm{d}V$) and differential pore volume versus diameter ($\mathrm{d}V/\mathrm{d}d$), which may be utilized by other researchers (Liu & Ostadhassan, 2019). Furthermore, the SSA determination for individual pore sizes involves evaluating the reversible work ($\mathrm{d}W = P\mathrm{d}V$) required to submerge a non-wetting surface area (dS) in mercury as (Gregg et al., 1967; Rootare & Prenzlow, 1967)

$$\gamma_{\mathrm{Hg}}\cos\theta_{\mathrm{Hg}}\mathrm{dS} = -\mathrm{PdV} \tag{A.5}$$

Assuming γ_{Hg} and θ_{Hg} remain independent of pressure, then equation (A.5) can be written as

$$\mathrm{SSA_i} = \Delta\mathrm{S} = \frac{1}{\gamma_{\mathrm{Hg}}\cos\theta_{\mathrm{Hg}}}\int_{\mathrm{v_i}}^{\mathrm{v_{i+1}}}\mathrm{PdV} \tag{A.6}$$

where v_{i} and $v_{\mathrm{i+1}}$ are the incremental pore volumes [mL/g]. By integrating equation (A.3) and equation (A.6), the following equation is derived

$$\mathrm{SSA_i} = \frac{4\mathrm{v_i}}{\mathrm{d}} \tag{A.7}$$

where $\mathrm{SSA_i}$ is the specific surface area at each pore size [$\mathrm{m^2/g}$], v_i the incremental pore volume corresponding to pore throat diameter of d_i, and d the average value of d_i and d_{i-1} [µm].

A.2.2 Nuclear magnetic resonance

NMR is a popular method for comprehensive analysis of various rock and fluid properties, including porosity, permeability and fluid viscosity as well as pore characteristics, particularly pore size distribution (PSD) (Coates et al., 1999; Grunewald & Knight, 2009; Kenyon, 1997; Vincent et al., 2011). One of the most common ways to extract these properties is by measuring the transverse relaxation time (T_2) of hydrogen nuclei within the fluid content of the pore space. T_2 is influenced by three independent processes: bulk fluid relaxation, diffusion-induced relaxation, and surface relaxation. The contribution of bulk fluid relaxation to T_2 is negligible, and in a homogeneous magnetic field, the diffusion-induced relaxation can be neglected (Coates et al., 1999; Kenyon, 1997). Instead, T_2 is

significantly influenced by surface relaxation, which is governed by fluid-pore surface interactions and thus T_2 can be approximated as follows (Volokitin et al., 1999):

$$\frac{1}{T_{2S}} = \rho \frac{S}{V} \tag{A.8}$$

where T_{2S} is the surface relaxation time [s], ρ is the transversal surface relaxivity [µm/s], S is the pore surface area [µm^2] and V is the pore volume [µm^3]. The S/V ratio is related to pore size and pore shape; thus the T_2 can be defined as follows (Volokitin et al., 1999):

$$\frac{1}{T_{2S}} = \rho \frac{F_S}{r} \tag{A.9}$$

where F_S is the shape factor of the pore with values of 2 and 3 for cylindrical and spherical pores, respectively (Li et al., 2015) and r is the pore radius [µm]. The surface relaxivity, acting as the proportionality coefficient, is a pore characteristic that measures the surface's capacity to induce relaxation, depending on the strength of interactions between the fluid and the matrix (Coates et al., 1999). Numerous studies have explored various approaches to determine surface relaxivity using data generated from techniques such as MICP, gas adsorption, and image-based methods like SEM and X-ray computed tomography (µCT), as well as NMR diffusion and centrifugal methods (Ge et al., 2021; Saidian & Prasad, 2015; Yao et al., 2010). An alternative approach involves the calibration of NMR equivalent pore diameter with those acquired through MICP, utilizing cumulative mercury intrusion fractions and cumulative NMR amplitude fractions. The NMR equivalent pore diameters were derived using equation (A.9), with F_S set at 2, and an arbitrary initial value assigned for the surface relaxivity (Figure A1a). Since the data spacing in MICP and NMR measurements differs, incremental linear interpolation was performed on each dataset to compute pore diameters and T_2 values corresponding to similar cumulative fractions (Figure A1b). Following this, an optimization program was executed to align the NMR-derived pore diameters with those obtained via MICP and ascertain the optimal value for the surface relaxivity (Figure A1c). A comprehensive explanation of this approach can be found in Fang et al. (2018) and Qu et al. (2020). Following this, the NMR pore size distributions (PSDs) were obtained from T_2 distributions using equation (A.9), with F_S value set at 2.

To determine the PSD and SSA, the conversion of the NMR amplitude into incremental pore volume normalized on the sample weight $V_{p,i}$ [cm^3/g], is required:

$$V_{p,i} = \frac{\emptyset_i}{\emptyset_{cum}} * \frac{V_p}{m} \quad (A.10)$$

where $\emptyset_i$ and $\emptyset_{cum}$ are NMR amplitude at each pore size and cumulative amplitude, respectively, V_p is the total pore volume [cm^3] of rock sample measured by NMR technique and m is the mass of rock specimen in gram. Subsequently, the procedure outlined in subchapter A.2.1 must be applied, to obtain the PSD and calculate the SSA using equations (A.4) and (A.7).

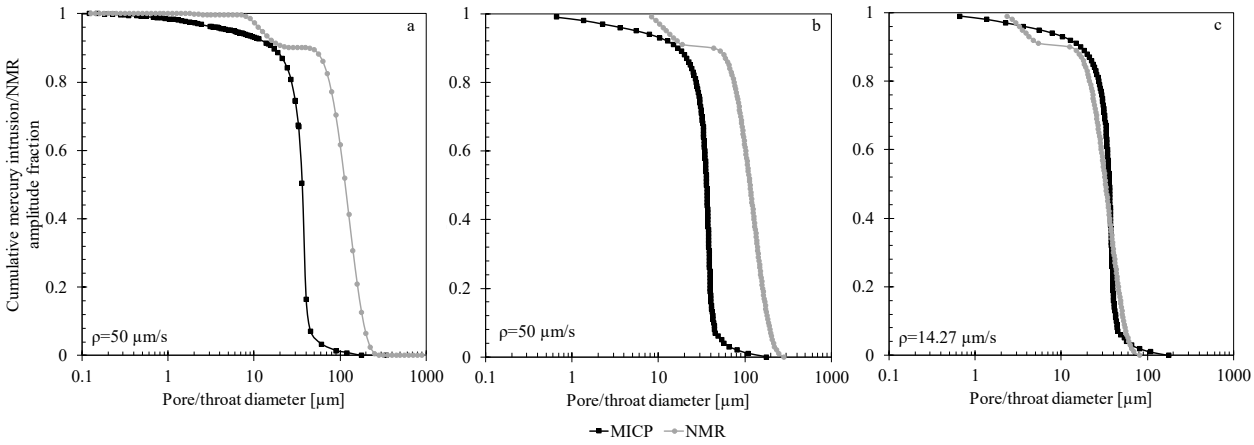

Figure A1. Surface relaxivity determination through the correlation of cumulative mercury intrusion fractions with cumulative NMR amplitude fractions in Bentheim rock specimens. Conversion of NMR T_2 data into pore diameters utilizing an arbitrary surface relaxivity value of 50 µm (a), interpolation of two datasets to compute pore diameters at uniform volume fraction intervals(b), and optimization of surface relaxivity to align NMR-derived pore diameters with those measured via MICP (c).

A.2.3 Scanning electron microscopy

SEM after low-angle Broad Ion Beam (BIB) polishing is a direct means to observe the 2D pore size, morphology, and spatial distribution of pores (Klaver, et al., 2015a). This approach enables the estimation of diverse petrophysical properties including porosity, SSA, and permeability. Several automated image analysis algorithms have been developed for image segmentation to differentiate pores from grains, and providing detailed pore-scale information including size and shape (ElHadidy et al., 2013; Kim et al., 2013; Leal-Egaña et al., 2011). Hojat et al. (2023) introduced an innovative automated method for detecting and quantifying pores employing the software *ImageJ*. The process involves the segmentation of images by an automated thresholding technique based on histogram analysis (Gonzalez & Woods, 2008; Schneider et al., 2012). While *ImageJ* offers 16 thresholding methods, the IsoData method proves particularly effective in segmenting the images. The subsequent phase involves isolating connected pores to facilitate their individual detection and measurement. This task is accomplished through implementing

morphological processes, specifically erosion followed by dilation. During erosion, pixels are added to the boundaries of non-porous areas using a 3x3 pixel structuring element. This results in the separation of connected pores, leading to the expansion of non-porous areas, thereby reducing pore areas. Furthermore, it eliminates noise and artefacts emerging from imperfect segmentation that are smaller than the structuring element. This ensures that the minimum detectable pore size remains constrained to dimensions of 3x3 pixels. To restore the pores to their original sizes, the dilation process is employed, removing pixels from the edges of pore areas and resulting in their enlargement (Bovik, 2009; Russ, 2006). Further details on this image analysis algorithm can be found in Hojat et al. (2023). The resulting pore statistics generated by the software enable quantifying the ratio between the total pore perimeter and the imaged area [m/m²]. Assuming the pore network resembles a bundle of capillary tubes, this ratio indicates the surface-to-volume ratio. This parameter can subsequently be transformed into a SSA through division by bulk density obtained from geometric measurements and sample weight.

A.2.4 X-ray micro-computed tomography

X-ray micro-computed tomography stands as a pivotal technique within geoscience, facilitating the non-destructive determination of three-dimensional rock microstructures down to micrometer scale. Notably, µCT directly observes pore and grain structures in porous media, producing greyscale images correlating with density. Merging these images yields three-dimensional datasets for qualitative and quantitative analysis, including phase volume fractions, pore and grain size parameters, tortuosity, and surface texture (Cnudde & Boone, 2013; Schepp et al., 2020).

Data analysis of tomographic images involves sequential tasks, often yielding variable outcomes due to system factors, user influence, and pre- and post-processing methods like grey-value segmentation, filtering for denoising of images and simulation algorithms. Quantitative characterization of pore space relies on applied segmentation methods, where volume elements (voxels) are assigned to pore or solid phases based on clustering similar attenuation values (Andrä et al., 2013; Chauhan et al., 2016; Iassonov et al., 2009). Despite the availability of numerous segmentation methods, the accurate identification and separation of phases remains complex. Techniques range from single or multiple threshold approaches to those utilizing local threshold values based on spatial information or intensity distribution gradients, such as the watershed algorithm and converging active contours (Sheppard et al., 2004; Vincent & Soille, 1991).

In this study, image enhancement and segmentation are performed using the commercial software package Avizo Fire 9.11. Prior to segmentation, images are denoised using a non-local means filter in 3D with standard settings (Buades et al., 2005) (Figure A2). Binarization is then performed using the multi-Otsu thresholding algorithm (Liao et al., 2001; Otsu, 1979) to separate the pixels of an input image into three different classes, each one obtained according to the intensity of the grey levels of (i) open pores, (ii) partly filled pores or micropores and (iii) grains (Figure A2). The method is modified by restricting the threshold search to the intensity range between zero and the largest peak within the grey-value histogram, which can be related to the quartz and/or feldspar grains in case of the examined sandstones to avoid misclassification by very dense materials such as pyrites. The lower threshold values yielding conservative estimates of porosity, surface area and pore size, which are chosen for all subsequent calculations. The threshold range is chosen to be conservative to ensure the real geometry of pores is retained, and to qualitatively and quantitatively assess only the pores clearly above the resolution limit of 4.036 µm. To enhance the accuracy of evaluation, a filtering process employing a 3x3 structuring element (Hojat et al., 2023) was implemented to eliminate noise and artefacts arising from imperfect segmentation. This process effectively removed features smaller than 12.11 µm, thereby establishing this threshold as the minimum pore size across all rock specimens.

The SSAs are calculated by performing the marching cubes algorithm to extract the surface mesh of the segmented pore space (van der Walt et al., 2014). The segmented images are loaded once again into Avizo Fire 9.11 to perform a watershed segmentation, i.e. separation of pores and grains. Thereof, a chamfer distance transform is applied on the binary images followed by an H-maxima filter on the masked distance map. The result of the H-maxima filter is used in combination with the complemented dataset of the chamfer distance map to obtain markers for subsequent watershed segmentation similar to the workflow proposed by Safari et al. (2021). For each individually labeled pore and grain (Figure A2), their respective equivalent diameters and surface areas are calculated. Herein, the equivalent diameter denotes the diameter of a hypothetical sphere possessing an equivalent volume to that of the segmented region under consideration.

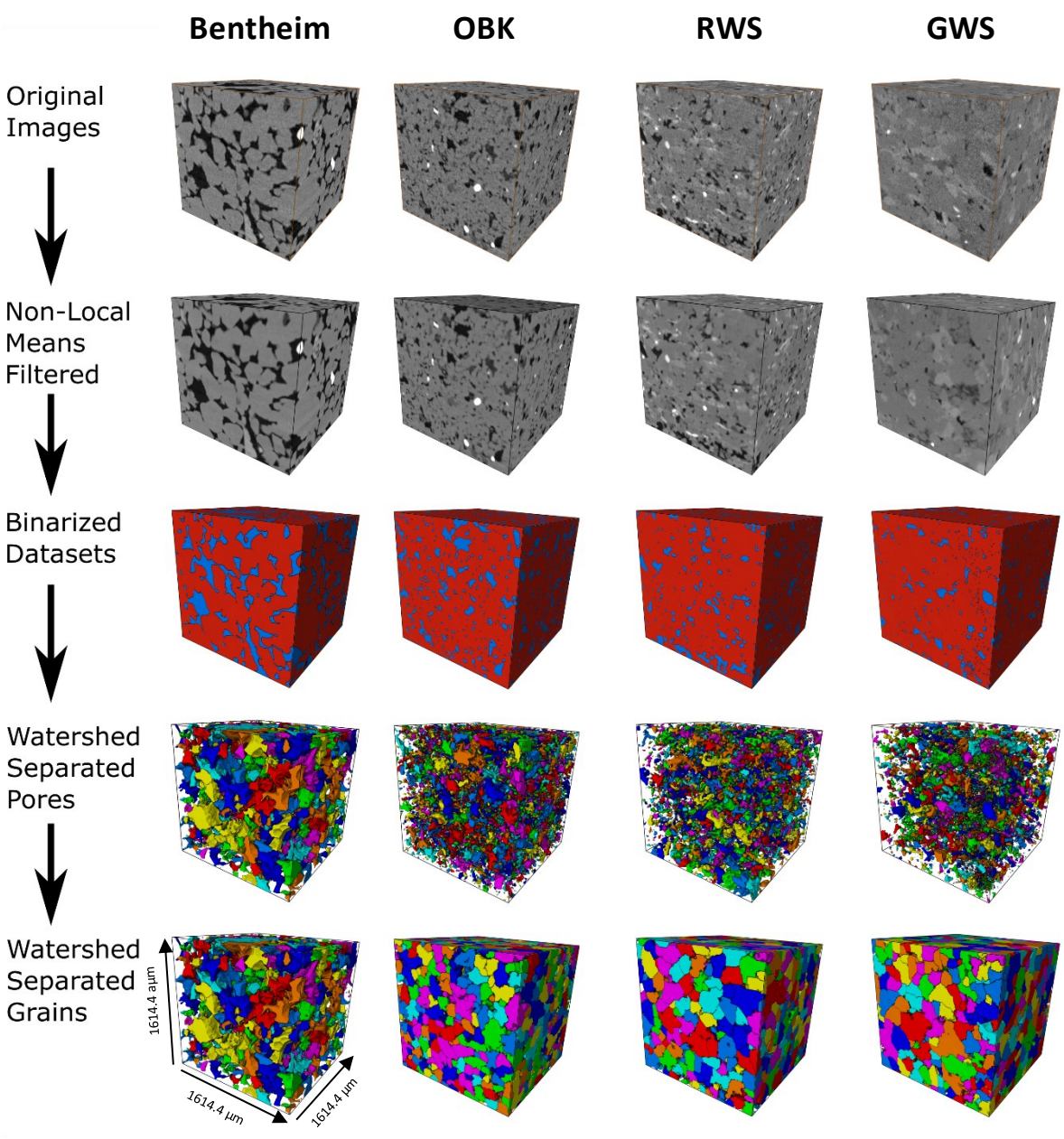

Figure A2. Schematic workflow designed for the extraction of pore and grain size distributions using µCT images. In the first step an edge-preserving non-local means filter is applied in three dimensions. Using global thresholding, the grey value images are segmented into binary images corresponding to open pores and grains. A Chamfer distance transform is applied on the binary images followed by a H-maxima filter on the masked distance map. This result is used in combination with the complemented dataset of the distance map for input of the marker-based watershed segmentation. The individually labeled pores and grains from the watershed algorithm will be used to obtain volumetric pore and grain size distributions by calculating the equivalent pore diameter of each label. The cubes have a dimension of 1614.4 µm on each side, corresponding to 400 voxels with a resolution of 4.036 µm.

7.2. Appendix B: Theoretical background (Chapter 4)

B.1 Mathematical model to determine the diffusion coefficient in water

Ratnakar and Dindoruk (2015) proposed a mathematical model for the pressure decay test aimed at determining the gas diffusion coefficient in liquids using a 1D transient-diffusion model. The study aligns with previous research on gas diffusion in liquids, making similar assumptions in deriving the analytical solution to the diffusion problem (Reza Etminan et al., 2013; Sheikha et al., 2005). These include a constant diffusion coefficient, isothermal conditions, negligible swelling of the liquid, negligible spatial concentration gradient in the gas phase, and no natural or induced convection.

As illustrated in Figure B1, the gas dissolves in water at the gas/water interface from the top, generating a concentration gradient along a singular direction (the x-axis). Therefore, the gas diffusion process can be described by Fick's second law of diffusion, which states (Crank, 1979; Fick, 1855; Ratnakar & Dindoruk, 2015):

$$\frac{\partial C(x,\ t)}{\partial t} = D\frac{\partial^2 C(x,t)}{\partial x^2} \tag{B.1}$$

where, $C(x,t)$ is the concentration of gas in the liquid phase [mol/m^3], and D is the gas diffusion coefficient [m^2/s]. The initial and boundary conditions considered for the diffusion problem are as follows:

$$C(x,0) = 0 \tag{B.2a}$$

$$V_g\frac{\partial \rho_g}{\partial t} = AD\frac{\partial C(h_L,t)}{\partial x} \tag{B.2b}$$

$$\frac{\partial C(0,t)}{\partial x} = 0 \tag{B.2c}$$

At the beginning of the experiment, the gas concentration in water is considered zero (equation (B.2a)). The interface boundary condition (at $x = h_L$) is defined based on mass conservation within the diffusion cell, where the rate of gas leaving the gas phase equals the rate of gas diffusion into the liquid. In equation (B.2b), V_g represents the gas phase volume, A the cross-sectional area of the gas-liquid interface, $\rho_g(t)$ the gas molar density at any given time [mol/m^3] and h_L the height of water in the diffusion cell [m] (Figure B1).

Gas density is dependent on gas pressure and can be determined by the real gas law, which is expressed as follows:

$$\rho_g(P,T) = \frac{PMw}{ZR(T+273.15)} \tag{B.3}$$

where P refers to the gas pressure [Pa], Mw the molecular weight [kg/kmol], Z the gas compressibility factor [-], R the universal gas constant, [$8.314 \cdot 10^3$ J/(kmol·K)], and T the temperature [°C]. The second boundary condition assumes a no-flow boundary at the bottom of the cell (equation (B.2c)). The gas concentration in water at the gas/water interface (C_{in}) is determined by the solubility of the specific gas in water which is related to gas density ($\rho_g \propto P$) with the proportionality of Henry's constant (H_{cc}) at constant temperature:

$$C(h_L,t) = C_{in}(t) = H_{cc}\rho_g(t) \tag{B.4}$$

Thus, the inner boundary condition can be formulated as a function of gas concentration in the liquid by combining equations (B.4) and (B.2b):

$$\frac{V_g}{H_{cc}}\frac{\partial C}{\partial t} = AD\frac{\partial C(h_L,t)}{\partial x} \tag{B.5}$$

The exact solution to equation (B.1), considering the initial and boundary conditions, was derived using the Laplace transform method and can be simplified for relatively long experimental times as follows:

$$\rho_g(t) - \rho_{g\infty} = \beta\exp(\gamma t), \quad \beta = \frac{2\rho_{g0}}{\left(1+\alpha H_{cc}+\frac{\lambda_1^2}{\alpha H_{cc}}\right)}, \quad \text{and} \quad \gamma = \frac{-\lambda_1^2 D}{h_L^2} \tag{B.6}$$

Here, subscripts ∞ and 0 denote the equilibrium and initial conditions for gas density [kg/m^3], respectively, β is the rate coefficient of pressure decay representing the driving force behind the dissolution process [kg/m^3], γ refers to the exponent factor indicating the rate of pressure decay at late times [1/s], α is the volume ratio of the liquid phase to gas phase, and λ_1 is the first root of the following equation:

$$\tan(\lambda_i) = -\frac{\lambda_i}{\alpha H_{cc}} \tag{B.7}$$

In cases where the values of αH_{cc} are small, an approximation for λ_1 can be expressed as:

$$\lambda_1 \to \frac{\pi}{2} + \frac{2}{\pi}\alpha H_{cc} \text{ with } \alpha H_{cc} \ll 1 \tag{B.8}$$

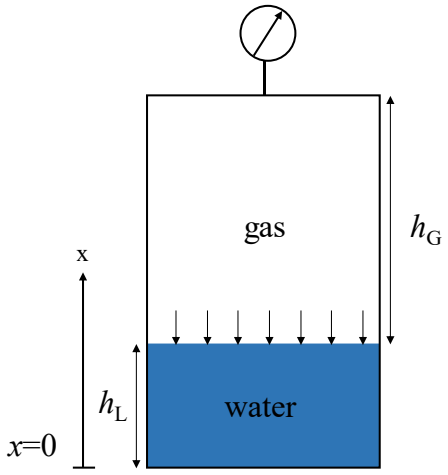

Figure B1. Physical model of gas diffusion in water during a pressure decay experiment. h_G and h_L denote the heights of gas and water in the diffusion cell, respectively (after Ratnakar and Dindoruk (2015)).

The late-transient solution (equation (B.6)) is only valid after transition time ($t_{tr} \geq \frac{1}{3\gamma}$). With the average diffusion coefficient of the gases studied in this research ($\approx 4.4 \cdot 10^{-9}$ m^2/s) and h_L of 0.03 m, the initial estimate for the transition time is approximately 7.6 hours, assuming that $\alpha H_{cc} \to 0$.

Prior to application of this model to the experimental data, the volumes of liquid (V_L) and gas (V_g) phases [cm^3] need to be determined as follows:

$$V_g = \frac{(P_{rc} - P_{eq})}{(P_{eq} - P_{ini})} V_{rc} \tag{B.9}$$

$$V_L = V_{dc} - V_g$$

where, P_{rc} and P_{ini} are the pressures in the reference and diffusion cells before gas expansion, respectively [Pa], P_{eq} is the initial pressure in the diffusion cell after gas expansion [Pa], and V_{rc} and V_{dc} represent the calibrated volumes of the reference and diffusion cells, respectively [m^3]. The parameter α can then be easily calculated by dividing V_L by V_g. Additionally, the heights of the gas (h_g) and liquid (h_L) columns [m] can be determined by dividing V_g and V_L by the cross- sectional area of the diffusion cell, which is calculated based on the measured cell geometry.

If the pressure decay experiment is conducted until equilibrium, the $\rho_{g\infty}$ can be determined using the pressure value at equilibrium. Nevertheless, it is feasible to assess the

experimental data prior to reaching equilibrium, using the following equation to determine $\rho_{g\infty}$:

$$\rho_{g\infty} = \frac{\rho_{g0}}{1+\alpha H_{cc}} \tag{B.10}$$

where Henry's constant can be obtained from published literature (Sander, 2015). Next, the evaluation of experimental data involves plotting $\ln(\rho_g(t) - \rho_{g\infty})$ against time, resulting in a linear relationship with a slope of γ and an intercept of $\ln(\beta)$, especially evident after the transition time. Subsequently, the experimental density data can be fitted to the model (equation (B.6)) using an optimization algorithm. This process employs the estimated $\rho_{g\infty}$, β, and γ as initial values to accurately determine their values and adjust the transition time accordingly. Once these three variables are determined, the diffusivity can be estimated using equation (B.6), given that the values of λ_1 and h_L are already known. Ratnakar and Dindoruk (2015) provide a comprehensive derivation of this mathematical model and the evaluation procedures.

B.2 Mathematical model to determine the effective diffusion coefficient in water-saturated rock

Li et al. (2006) introduced a physical model (Figure B2) elucidating the radial diffusion of gas through water-saturated rocks, subsequently formulating a mathematical model to determine the gas diffusivity. As illustrated in Figure B2, gas penetration into the water-saturated rock is constrained to occur solely along the radial direction, achieved by sealing the two end faces of the rock specimen.

To develop a mathematical model for gas diffusion in a water-saturated rock specimen, certain simplifying assumptions were established (Li et al., 2006). It was assumed that the gas concentration within the water on the surface of the rock specimen remained constant throughout the experimental duration. The degree of pressure loss was recognized to be influenced by both gas solubility and the volume of water occupying the pore space. Notably, the volume of water within the rock specimen's pores was found to be significantly lower, by one or two orders of magnitude, than the standard volumes typically employed in gas diffusivity assessments (10-20 mL).

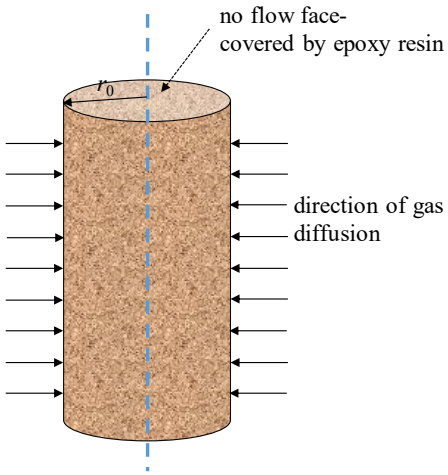

Figure B2. Physical model of gas diffusion into water-saturated rock specimens along radial direction during a pressure decay test. The two end faces of the rock specimen were sealed with epoxy resin (after Li et al. (2006)Li et al. (2006)). r_0 denotes the radius of the rock plug.

Consequently, variations in gas concentration at the gas/water interface during diffusivity tests on water were deemed essential to consider, whereas alterations in this parameter at the rock specimen's surface could be safely disregarded. Additionally, it was presumed that the effective diffusion coefficient of gas within the water-saturated rock specimen remained constant under dilute conditions. The rock was also assumed to exhibit homogeneity and isotropy, resulting in a uniform distribution of water throughout the sample. Furthermore, the potential effects arising from natural convection due to density differences in the liquid phase, liquid phase swelling resulting from gas dissolution, and water evaporation into the gas phase were considered negligible. Then, the rate of gas diffusion into water saturated porous media was determined to be proportional to its concentration gradient, as derived from the integration of Fick's law and the continuity equation (Crank, 1979; Li et al., 2006):

$$\frac{\partial C(t)}{\partial t} = \frac{D_{eff}}{r}\frac{\partial}{\partial r}\left(r\frac{\partial C}{\partial r}\right) \tag{B.11}$$

where, C denotes the gas concentration in the water-saturated porous medium [mol/m^3]; D_{eff} is the effective diffusion coefficient [m^2/s]; t the time [s]; and r is the radius of rock specimen [m]. The initial and boundary conditions for this physical model are as follows:

$$C = C_0 \text{ and } r(t) = r_0 \text{ with } t \geq 0 \tag{B.12a}$$

$$C = 0 \text{ and } 0 < r < r_0 \text{ with } t = 0 \tag{B.12b}$$

where C_0 denotes the gas concentration in the water at the surface of rock specimen, and r_0 the radius of rock specimen [m]. According to Henry's law, C_0 is directly proportional to the gas pressure at a constant temperature, as stated below:

$$P = H_{cc}C_0 \tag{B.13}$$

Then the solution to equation (B.11), is as follows:

$$\frac{C}{C_\infty} = 1 - \frac{2}{r_0}\sum_{n=1}^{\infty}\frac{\exp(-D_{eff}\alpha_n^2 t)J_0(r\alpha_n)}{\alpha_n J_1(r\alpha_n)} \tag{B.14}$$

here, $J_0(x)$ and $J_1(x)$ represent the first kind of Bessel function of zero and first order, respectively, and α_n are the positive roots of the following function:

$$J_0(r\alpha_n) = 0 \tag{B.15}$$

The quantity of gas that has diffused into the water-saturated porous medium can be derived from equation (B.14) and is expressed as (Crank, 1979; Li et al., 2006):

$$\frac{N}{N_\infty} = 1 - \sum_{n=1}^{\infty}\frac{4}{r_0^2\alpha_n^2}\exp(-D_{eff}\alpha_n^2 t) \tag{B.16}$$

where, N refers to the amount of gas diffused in water [mol] at time t, N_∞ is the maximum amount of gas that will eventually diffuse into water [mol].

The maximum gas concentration in water arises from gas dissolution at the surface of the rock specimen. Therefore, N_∞ can be determined by multiplying C_0 and the water volume within the porous media. According to the mass balance, the observed pressure reduction during the experiment can be attributed to the diffusion of gas molecules into the liquid phase. The relationship between pressure and the quantity of gas loss is defined by the real gas law:

$$N = \Delta n = \frac{\Delta P_g V_g}{ZRT} \tag{B.17}$$

where, Δn represents the amount of gas lost [mol], ΔP_g refers to the pressure drop [Pa], V_g denotes the gas phase volume (i.e., the sum of the reference cell and the diffusion volumes, excluding the bulk volume of the rock specimen) [m^3], Z is the gas compressibility, R is the universal gas constant [8.314 J/(mol·K)], and T is temperature [K].

Combining equations (B.17) and (B.16) yields

$$\Delta P_g = \frac{ZRTN_\infty}{V_g}\left(1 - \sum_{n=1}^{\infty}\frac{4}{r_0^2\alpha_n^2}exp(-D_{eff}\alpha_n^2 t)\right) \tag{B.18}$$

In this equation, the only variable that remains unknown is D_{eff}, which can be estimated by fitting the experimental ΔP_g with the model outlined in equation (B.18) (Li et al., 2006).

In addition, Li et al. (2006) have shown that for $\sqrt{\frac{D_{eff}t}{r_0^2}} < 0.1$, equation (B.18) can be approximated with high accuracy with the following relation:

$$\frac{N}{N_\infty} \approx 4\sqrt{\frac{D_{eff}t}{\pi r_0^2}} \tag{B.19}$$

Substituting this term into equation (B.13) yields

$$\Delta P_g = k_1\sqrt{t} \tag{B.20}$$

with

$$k_1 = \frac{4ZRTN_\infty}{r_0 V_g}\sqrt{\frac{D_{eff}}{\pi}} \tag{B.21}$$

equation (B.20) clearly demonstrates a linear relationship between the ΔP_g and $\sqrt{t}$, with the slope k_1. Thus, D_{eff} can be obtained from equation (B.21), based on the slope derived from the measured ΔP_g versus $\sqrt{t}$. This resultant value then serves as an initial estimate in equation (B.18), ultimately leading to a precise determination of D_{eff}.

B.3 Blank experiments

To investigate the baseline behavior of pressure transducers, a series of control experiments, referred to as blank experiments, were conducted using empty diffusion cells prior to initiating tests on water and water-saturated rock specimens. In these experiments, helium was injected into cells 1, 2, and 3 at a pressure of approximately 1.0 MPa, consistent with the pressure used in diffusion experiments. Observations revealed pressure drops of 0.0048, 0.0053, and 0.0047 MPa in cells 1, 2, and 3, respectively, with the majority of the decline occurring within the first 30 minutes (Figure B3 (a-c)). The reasons for this phenomenon remain unknown to the authors, but it is likely related to the Joule-Thomson effect, deficiencies of pressure transducers, gas diffusion into the membrane, or the capillary restrictions.

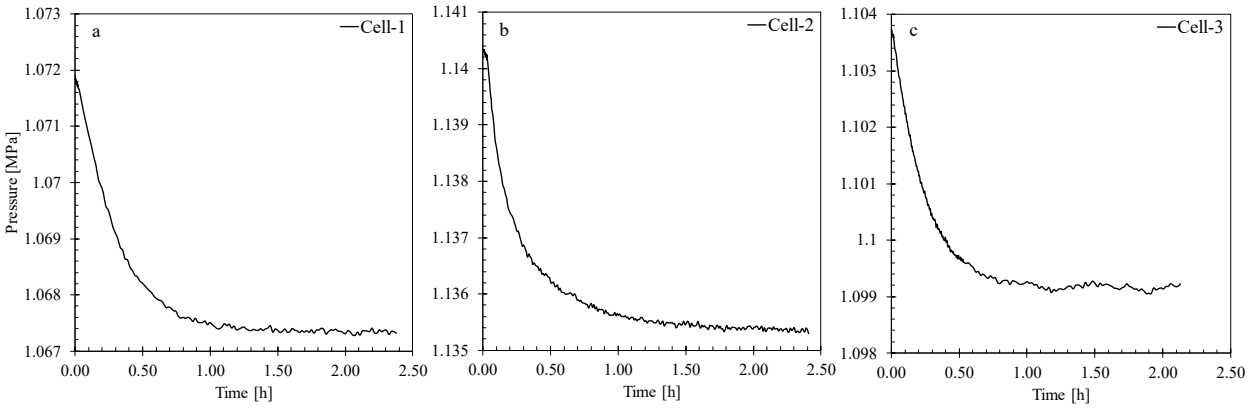

Figure B3. Pressure decays observed during the so-called blank experiments to investigate the pressure transducers reading in cell-1 (a), (b) cell-2 (b), and cell-3 (c). It was observed that substantial portion of pressure decay in each cell occurred within less than one hour.